ICCESEN-2019

6th International Conference on Computational and Experimental Science and ENgineering

Limak-Limra Hotel and Resort Kemer-Antalya-TURKEY

23-27 October 2019

Proceedings
of
ICCESEN-2019

EDITORS

Prof.Dr. İskender AKKURT

Dr. Kadir GÜNOĞLU

Dr. Hakan AKYILDIRIM

iccesen2019@gmail.com

2019.iccesen.org

Limak-Limra Hotel and Resort Kemer-Antalya-TURKEY
23-27 October 2019

Proceedings
of
ICCESEN-2019

Editors:
Prof.Dr. İskender AKKURT
Dr. Kadir GÜNOĞLU
Dr. Hakan AKYILDIRIM

i

Proceedings of ICCESEN-2019

6th International Conference on Computational and Eperimental Science and Engineering (**ICCESEN-2019**)

23-27 October 2019, Kemer-Antalya-TURKEY

Editors:

Prof. Dr. İskender AKKURT
　　Dr. Kadir GÜNOĞLU
　　Dr. Hakan AKYILDIRIM

Published : 24 December 2019
ISBN: 978-605-68728-1-5

TABLE OF CONTENTS

ii

iii

iv

FOREWORD

Dear Colleagues,

It is a great honor for me to host you all in **"6th International Conference on Computational and Experimental Science and Engineering (ICCESEN-2019)"** taken place at Limak-Limra Hotel and Resort, Kemer-Antalya-Turkey in the period of 23-27 October 2019. I thank you to all participants, invited speakers, all committe members and reviewers.

We are also happy to publish the proceeding of ICCESEN-2019. All papers have been reviewed by reviewers. I am hoping to meet you all in ICCESEN-2020.

Prof. Dr. İskender AKKURT

Chair for ICCESEN-2019
Editor for Proceedings of ICCESEN-2019

ORGANISATION COMMITTEE

Prof.Dr. Iskender AKKURT (Chair)	Suleyman Demirel University, Isparta -Turkey
Dr. Kadir GÜNOĞLU (secretary)	Isparta Uygulamalı Bilimler University, Isparta -Turkey
Dr. Hakan AKYILDIRIM	Suleyman Demirel University, Isparta -Turkey
Dr. Ahmet BEYCİOĞLU	Düzce University, Düzce -Turkey
Dr. Nilgün DEMİR	Uludag University, Bursa -Turkey
Dr. Nurdan KARPUZ DEMİR	Suleyman Demirel University, Isparta -Turkey
Dr. Özge Kozguş GÜLDÜ	Ege University,İzmir-Turkey
Dr. Ümit KARA	Suleyman Demirel University, Isparta -Turkey
Dr. Feride KULALI	Üsküdar University, Istanbul-Turkey
Dr. Zehra Nur KULUÖZTÜRK	Bitliseren University, Bitlis-Turkey
Dr. M. Fatih KULUÖZTÜRK	Bitliseren University, Bitlis-Turkey
Dr. Hüseyin Ozan TEKİN	Üsküdar University, Istanbul-Turkey

SCIENTIFIC COMMITTEE

Prof.Dr. Iskender AKKURT (Chair)	Suleyman Demirel University, Isparta –Turkey
Prof.Dr. Majid ABBASPOUR	Sharif University of Technology-Iran
Prof.Dr. Zahid Hussain ABRA	Quadi-E-Awam University, Sindh-Pakistan
Prof.Dr. Abdullah ALAMRI	King Saud University, Saudi Arabia
Prof.Dr. Nezam Mahdavi-AMIRI	Sharif University Iran
Dr. John R.M.ANNAND	Glasgow University, Glasgow-Scotland (UK)
Dr. Majda AOUITITEN	Abdelmalek Essaadi University-Morocco
Prof.Dr. Mohamed Kheireddine AROUA	University of Malaya-Malaysia
Dr. Rachid BELKADA	CRSTSE -Algeria
Dr. Radhey S BENIWAL	CSIR-NISCAIR, New Delhi 110012, India
Dr. Mahmoud Abdullah BENNASER	Kuwait University-Kuwait
Dr. Djoudi BOUHAFS	Centre de Recherche en Technologie -Algeria
Prof. Oleg BURDAKOV	Linköping University Linköping, Sweden
Dr. Yusuf CEYLAN	Selcuk University, Konya-Turkey
Prof.Dr. Lotfi CHOUCHANE	Weill Cornell MEdical College-Qatar
Dr. Manju D CHOUDHARY	Niscair-India
Dr. Nermin DEMİRKOL	Kocaeli University, Kocaeli –Turkey
Prof.Dr. İbrahim DİNÇER	University of Ontario Institue of Technology (UOIT)-Canada
Prof. Dr. Mitra DJAMAL	Institute Teknologi Bandung-Indonesia
Prof.Dr. Mahmut DOĞRU	Bitlis Eren University, Bitlis-Turkey
Prof.Dr. Mohammed Mostafa EL TOKHI	United Arab Emirates University-UAE
Dr. Zuhal ER	Istanbul Technical University, Istanbul-Turkey
Prof.Dr. Mustafa EROL	Dokuz Eylul University, İzmir-Turkey
Prof.Dr. Madjid FATHI	Dept. of EECS University of Siegen- Germany
Prof.Dr. Jan FELBA	Wroclaw University of Technology-Poland
Prof.Dr. S. Mostafa GHIAASIAAN	Mechanical/Nuclear Engineering, Georgia Tech USA
Prof.Dr. Mustafa GÜNAL	Gaziantep University, Gaziantep-Turkey
Prof. Dr. Amir HUSSAIN	University of Stirling- Scotland(UK)
Dr. Nabi IBADOV	Warsaw University of Technology-Poland
Prof.Dr. Fatma KARİPCİN	Nevşehir Hacı Bektaşi Veli University-Turkey
Prof.Dr. Hamdi Ş. KILIÇ	Selcuk University, Konya-Turkey
Dr. Menekşe V. KILIÇARSLAN	İstanbul Aydın University, Istanbul-Turkey

Prof.Dr. Ziya Erdem KOÇ	Selcuk University, Konya-Turkey
Prof. Dr. İsmail KOYUNCU	Istanbul Technical University, Istanbul-Turkey
Dr. Irida MARKJA	Polytechnic University,Tirana-Albania
Dr. F.Zümrüt Biber MÜFTÜLER	Ege University, Izmir-Turkey
Dr. Susan Shukur NOORI	Kirkuk University, Kirkuk-lraq
Prof.Dr. Ravindra NUGGEHALLI	New Jersey Institute of Technology-USA
Prof.Dr. İbrahim ÖRÜN	Aksaray University, Aksaray-Turkey
Prof.Dr. Necati ÖZDEMİR	Balıkesir University, Balıkesir-Turkey
Dr. Zeynep PARLAR	Istanbul Technical University, Istanbul-Turkey
Prof.Dr. Ioana G. Petrisor	ToxStrategies, Inc., Mission Viejo, CA
Dr. Tomasz PIOTROWSKI	Warsaw University of Technology, Warsaw-Poland
Prof.Dr. Javad RAHIGHI	AEOI, Tehran-Iran.
Dr. Abdelmadjid RECIOUI	University of Boumerdes-Algeria
Prof.Dr. Osman SAGDIÇ	Yıldız Technical University, Istanbul-Turkey
Prof.Dr. Miljko SATARIC	Faculty of Technical Sciences Novi Sad-Serbia
Prof.Dr. Saleh SULTANSOY	TOBB University, Ankara-Turkey
Dr. Naim SYLA	University of Prishtina-Kosova
Prof. Dr. Mustafa TAVASLI	Uludag University, Bursa-Turkey
Dr. Huseyin TOROS	Istanbul Technical University, Istanbul-Turkey
Prof.Dr. Ahmad UMAR	Najran University-Saudi Arabia
Prof.Dr. Gerhard-Wilhelm WEBER	Middle East Technical University Ankara-Turkey
Prof.Dr. Erol YAŞAR	Mersin University, Mersin-Turkey

INVITED SPEAKERS

Prof.Dr. Mansour H. ALMATARNEH

University of Jordan-JORDAN

Title: Computational Study of the Ozonolysis Reaction through Criegee Mechanism and Dissociation of Secondary Ozonide

Prof.Dr. Madjid FATHI

Dept. of EECS University of Siegen, GERMANY

Title: Unearthing the potential of smart health care applications – A digital transformation

Prof.Dr. Norani Muti Binti MOHAMED

University Teknologi Petronas-MALAYSIA

Title: Nanotechnology for Clean and Sustainable Energy Production

Prof.Dr. Ravindra NUGGEHALLI

New Jersey Institute of Technology-USA

Title: Thermal Radiative Properties of Materials – Fundamentals, Examples & Applications

Prof.Dr. Gerhard-Wilhelm WEBER

Poznan University of Technology-POLAND

Title: Social Entrepreneur Using Business Metrics: Migport Refugee Big Data Analytics - With a Note on Ability and Disability

Simulation of Rock Breaking Efficiency under Various Shapes of Impact Drilling Loads

Yandong Yang[1,2], Hualin Liao[1,2*], Jiansheng Liu[1,2], Jilei Niu[1,2]

[1] *China University of Petroleum (East China), School of Petroleum Engineering, Qingdao, China*

[2] *Ministry of Education, Key Laboratory of Unconventional Oil & Gas Development (China University of Petroleum (East China)), Qingdao, China*

*18266211690@163.com

ABSTRACT

It is demonstrated that if a dynamic load was applied above the drill bit, the penetration rate could be efficiently improved in percussive drilling. The objective of this research was to simulate the practical percussion drilling with various types of load, thereby proving a quite efficient and lower cost drilling as well as the exploration of hard formations. In this paper, a 3D physical rock and drill bit model was established to compare the drilling performance with the exponential, the rectangular, the triangular and the sinusoidal shape of impact load. In addition, the physical model was validated with experimental data. The results demonstrated that the drilling performance with the rectangular and sinusoidal loads was improved than the other shapes of impact loads at the same amplitudes. The research could provide a theoretical guidance for the design of down-hole percussion drilling tools.

KEYWORDS - *İmpact well drilling; energy transfer efficiency; rock breakage; incident stress wave*

1. INTRODUCTION

The essence of drilling is to solve the interaction problem between the drill bit and the rock, as well as to improve the drilling speed through the efficiency increase of rock breakage [1, 2]. Due to the various designs of rotary drilling tools as well as of working conditions, impact loads of various characteristics will be generated during impact [3, 4]. In addition to the experimental method, the finite element was implemented to simulate the rock breakage process [5, 6]. Compared to testing, the 3D simulation could deal with complicated boundary conditions. As an example, the ROP (rate of penetration) or displacement could be obtained under the specific types of dynamic load. Consequently, the rock breakage simulation was conducted with different types of dynamic load in this paper.

2. METHODOLOGY

2.1. Physical Model Definition

The physical model of bit and rock interaction was shown in figure1. In oil and gas drilling process, the drill bit which connected to the drill string was applied on the formation, the drill bit move forward through the drill collar deliver WOB on the drill bit. PDC drill bit was commonly used in the modern well drilling. Therefore, in this paper, a rock- PDC bit model was used to verify the theoretical analysis.

2.2. Governing Equations

The main constitutive models of rock model were the Mohr-Coulomb and the Drucker-Prager criteria, whereas the D-P criterion was from the M-C criterion.
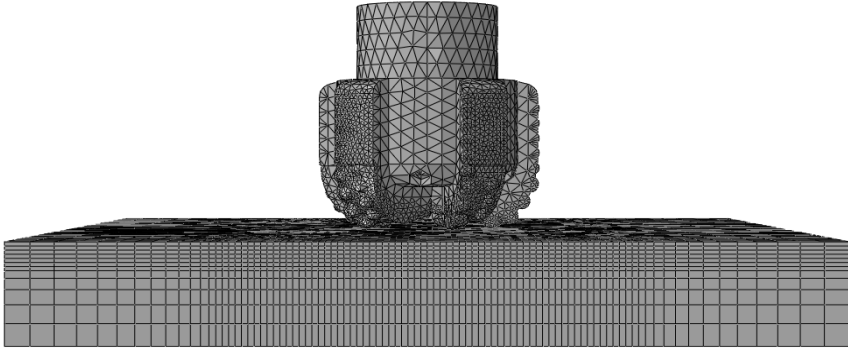
Figure 1 *Physical Rock Breaking Model of Rock-PDC bit*

$$f = \alpha I_1 + \sqrt{J_2} - K = 0 \tag{1}$$
$$I_1 = \delta_{ii} = \delta_1 + \delta_2 + \delta_3 = \delta_x + \delta_y + \delta_z$$
$$J_2 = \frac{1}{6}\left[\left(\delta_x - \delta_y\right)^2 + \left(\delta_y - \delta_z\right)^2 + (\delta_z - \delta_x)^2 + 6\left(\tau_{xy}^2 + \tau_{yz}^2 + \tau_{zx}^2\right)\right]$$

where, α, K (flowstress ratio) are the constant parameters related to the angle of friction φ (M-C) and c is cohension, β is angle of friction (D-P), δ_c is compression yield stress. In the three dimension.

$$tan\beta = \frac{6sin\varphi}{3-sin\varphi} \tag{2}$$
$$K = \frac{3-sin\varphi}{3+sin\varphi} \tag{3}$$
$$\delta_c = 2c\frac{cos\varphi}{1-sin\varphi} \tag{4}$$

The intermediate principal stress and the hydrostatic pressure were accounted for in the D-P criteria, whereas the D-P criterion overcome the M-C criterion weakness; therefore, the D-P criterion was applied in the simulation.,

3. RESULTS and DISCUSSION

In the percussive drilling, the impact energy was transmitted through the form of the stress wave, and the waveform of the stress energy was affect by the impact drilling tool, different tools corresponded to the different incident stress waves. In this paper, four various incident stress wave were discussed. In order to obtain the influence of the shape loaded above the bit on the ROP, WOB varied as sine, rectangle, triangle and exponent shape were applied on the bit, and the static load is 50kN, the amplitude of dynamic load are 10, 20, 30 and 40kN respectively, RPM is 104r/min, and frequency is 10Hz.

Figure 2 shows the penetration depth of sine, triangle, rectangle and exponent wave shaped loads. It can be seen that with the increasing of the impact load, the ROP increased as well; when the impact load is 0, that is, under the static load, the drilling velocity are same; however, when dynamic load were applied on the bit, the drilling velocity is higher than that under static load, it is indicated that drilling performance is excellent under the combination of static and dynamic load. In addition, generally, ROP under sine and rectangle shows similar performance, and better than

2
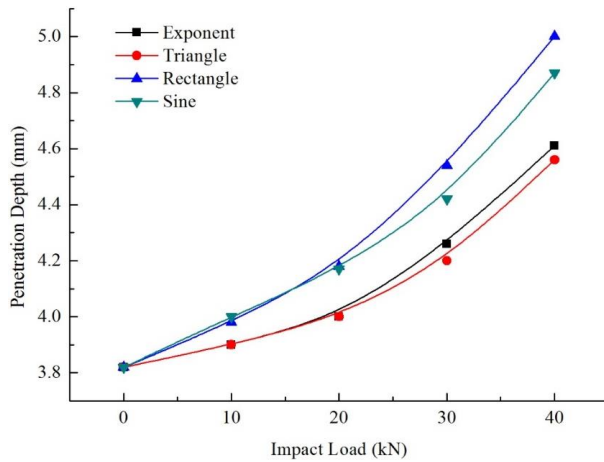
Figure 2 *Comparison of Drilling Velocity under Various Impact Load (Sine, Triangle, Rectangle and Exponent Wave Shape)*
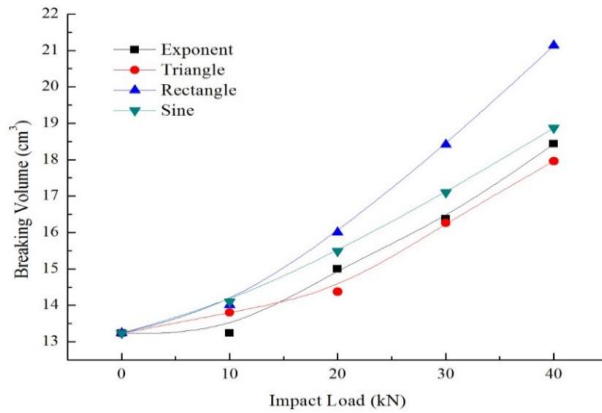
Figure 3 *Comparison of Rock Breaking Volume under Impact Load (Sine, Triangle, Rectangle and Exponent Wave Shape)*

that of exponent and triangle load apparently, and the higher impact load, the difference of drilling performance is more obvious. At the same time, drilling velocity under exponent and triangle shows similar tendency, however, the penetration depth is lower than that of sine and rectangle significantly.

4. CONCLUSION

A 3D simulation of rock breakage was conducted to investigate the rock breakage efficiency. The results of the study demonstrated that: different incident stress wave corresponded to a certain dynamic load shape, it is indicated that load shapes of the sine, triangle, exponent and rectangle shaped matched to the wave shape of incident stress. After the comparison of simulation and experimental results, it is indicated that the rock-bit interaction physical model is efficient and of less prediction error, and it can be used to predict and compare the drilling performance under sine, rectangle, triangle and exponent wave-shaped load. Theoretically analysis shows that the energy transfer efficiency of sine and rectangle load shows the similar performance, and the result

is highly in agreement with the simulation results. Therefore, the impact drilling too can be designed to generate a certain shape of load, for example, sine or rectangle.

REFERENCES
[1]. MA D, ZHOU D, DENG R. The computer simulation of the interaction between roller bit and rock; proceedings of the International Meeting on Petroleum Engineering, F, 1995 [C]. Society of Petroleum Engineers.
[2]. WU A, HARELAND G, LEI L. Computer Simulation and Analysis of Rock Breaking Process by Rock Bit Cutters; proceedings of the 48th US Rock Mechanics/Geomechanics Symposium, F, 2014 [C]. American Rock Mechanics Association.
[3]. LUNDBERG B, OKROUHLIK M. Efficiency of a percussive rock drilling process with consideration of wave energy radiation into the rock [J]. International Journal of Impact Engineering, 2006, 32(10): 1573-83.
[4]. LUNDBERG B. Microcomputer simulation of stress wave energy transfer to rock in percussive drilling; proceedings of the International Journal of Rock Mechanics and Mining Sciences & Geomechanics Abstracts, F, 1982 [C]. Elsevier.
[5]. REDDISH D, STACE L, VANICHKOBCHINDA P, et al. Numerical simulation of the dynamic impact breakage testing of rock [J]. International Journal of Rock Mechanics and Mining Sciences, 2005, 42(2): 167-76.
[6]. SAZID M, SINGH T. Two-dimensional dynamic finite element simulation of rock blasting [J]. Arabian Journal of Geosciences, 2013, 6(10): 3703-8.

Investigation of Istanbul Ayazma Coastal Sands In Terms of Natural Radioactivity

İskender AKKURT[1], Osman GÜNAY[2*] Kadir GÜNOĞLU[3]

[1] *Suleyman Demirel University, Science Faculty,Physics Department, Isparta-TURKEY*
[2] *Istanbul Okan University Vocational School of Health Services Istanbul, TURKEY*
[3] *Isparta University of Applied Sciences, Technical Vocational School, Isparta- TURKEY*
[*] *osman.gunay@okan.edu.tr*

ABSTRACT

All living things in the world have been living under the influence of natural radioactivity caused by long half-life radionuclides since the existence of the universe. The main source of this radioactivity is terrestrial radiation from the earth. Terrestrial radiation may vary according to the geological structure of each region. In this study, natural radioactivity levels of sand samples collected from different points of Ayazma coast in Istanbul were measured using gamma spectroscopy system containing NaI (Tl) detector. The average activity concentration values of ^{226}Ra, ^{232}Th and ^{40}K from the studied are 30.07 Bq/kg , 32.43 Bq/kg and 372.6 Bq/kg respectively.

KEYWORDS - *Natural radioactivity, Ayazma beach, Gamma spectroscopy,*

1. INTRODUCTION

Humanity has been directly or indirectly influenced by various radioactive sources throughout history. Well-known sources of this external ionizing radiation are cosmogenic irradiation and primitive natural radioactive elements based on the earth's crust. These two types of radiation are considered as the source of Naturally occurring Radioactive Substances (NORM). Radionuclides can be found in nature, air, soil and water. People are exposed to various types of radiation depending on the geographical conditions they live and the living standards in which they live. Investigating the risk of ionizing radiation to the public is still one of the most attractive subjects among scientists.[1,2] The most important terrestrial radiation sources which have been exist since the creation of earth are ^{40}K, ^{226}Ra, and ^{232}Th. All these three radionuclides; ^{40}K, ^{226}Ra, and ^{232}Th; have very long half-lives 4.47 x 109, 1.41 x1010 and 1.28x1010 years, respectively [3].

Environmental components, such as soil and sand, are often used in buildings where a large part of human life is spent, as they are the main source of human exposure to continuous radiation. In addition, these components allow the transport of radionuclides to other environmental factors such as water, air, sediment and biological systems. Therefore, environmental samples are an important component in assessing the radiological exposure of living things and in determining the level of environmental radioactivity. Therefore, determination of radionuclide activities in environmental formations such as stone, soil and sand, which have a wide usage area as building material, has gained importance especially for human health. [2]. Numerous studies have been conducted to determine the amount of natural radioactivity in sand samples in many regions around the World [4-11].

In this study, ^{40}K, ^{226}Ra, and ^{232}Th concentrations were measured by gamma spectrometer to determine the natural radioactivity levels of the sands collected from Ayazma beach in Şile-İstanbul.

2. MATERIAL AND METHOD

In this study, sand samples have been collected from Ayazma Beach. After collection of samples, they were crushed and dried until 100oC in an oven for about 24 h. The dried samples have been filled in a cup which is sealed tightly with a thick tape around its neck to limit any gas escape from

it, and stored for four weeks to get secular equilibrium to be achieved between 238U and its progeny [5].

The radioactivity concentrations of 226Ra, 232Th and 40K in sand samples were determined using a gamma ray spectrometry consists of a 3"x3" NaI(Tl) detector connected to Multi-Channel-Analyser (MCA). The spectrum is analyzed using the MAESTRO32 obtained from ORTEC. The schematic view of the experimental system has been shown in Figure 1.
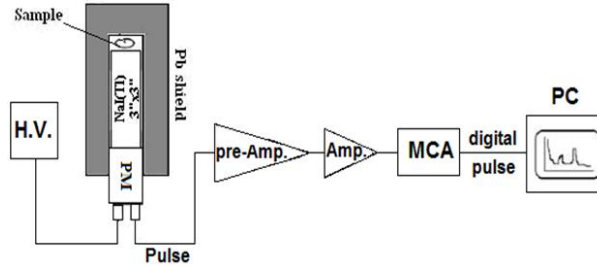
Figure 1. *Schematic view of gamma Spectrometer and electronic units*

Before measurement the system should be calibrated. This is done using ^{137}Cs and ^{60}Co radioactive sources, which produce γ-ray energy of 662, 1173 and 1332 keV, respectively. The γ-ray spectrum obtained from the mentioned source and related fit has been displayed in Figure 2.
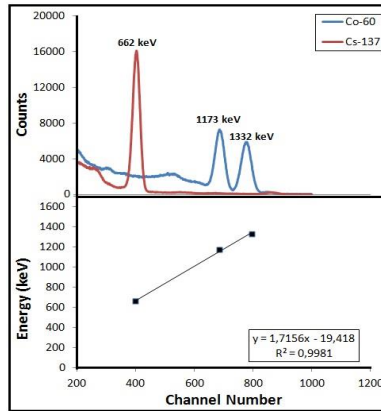
Figure 2. *The γ-ray energy spectrum obtained from ^{137}Cs and ^{60}Co sources (upper) and related fit channel versus energy (keV).*

The spectrum is analyzed using the MAESTRO32 obtained from ORTEC. The measurement was based on recording natural radioactivity quantities of three natural long-live elements: [226]Ra, [232]Th and [40]K which are considered the photopeaks at 1760, 2610 and 1461 keV respectively, in the natural γ-ray spectrum [4]. An exemplary spectrum obtained from the measurements is shown in Figure 3.

The activities for the natural radionuclides were calculated using the following relation [4]

$$A(Bq/kg) = \frac{N}{\varepsilon.\gamma.t.m} \tag{1}$$

6
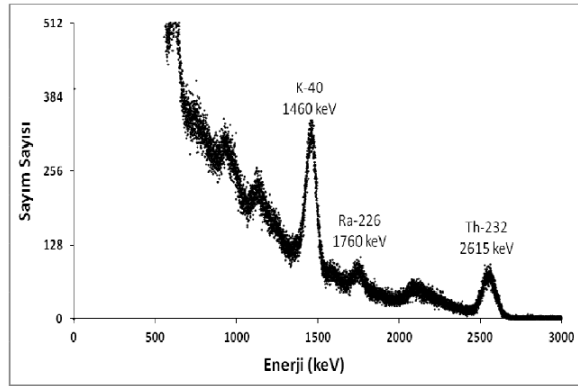
Figure 3. *Spectrum obtained from measurements.*

where A is the activity of the radionuclide in Bq/kg, N is the net peak area under the most prominent photo peaks calculated by subtracting the respective count rate from the background spectrum obtained for the same counting time. The net count rate in the measurement is calculated from the background subtracted area of prominent gamma ray peaks. ε is the detector efficiency of the specific gamma ray, γ the absolute transition probability of gamma decay, t the counting time (s) and m the mass of the sample (kg).

3.   RESULTS AND DISCUSSION

The measured activity concentrations of primordial radionuclides ^{226}Ra, ^{232}Th and ^{40}K in the sand samples collected from various locations in Ayazma Beach are illustrated in Figure 4 and 5.
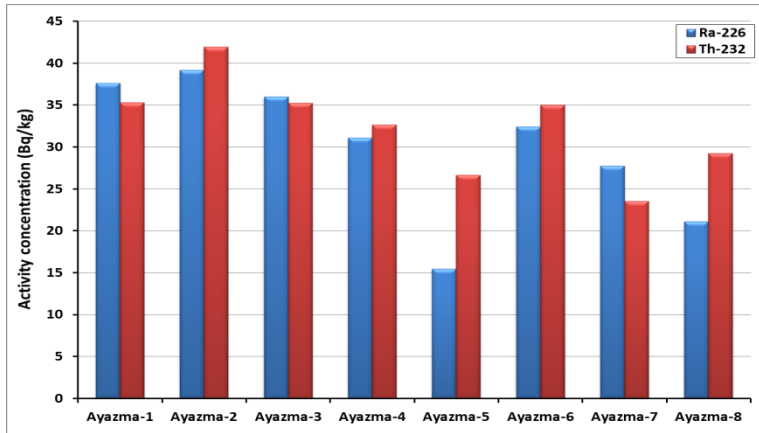
Figure 4. *The activity concentration of ^{226}Ra and ^{232}Th in sand samples*

It can be seen from Figure 4 that for the ^{226}Ra activity concentration, the smallest value was measured in the Ayazma-5 sample and the largest value was measured in the Ayazma-2 sample. For ^{232}Th activity concentration, the smallest value was measured in the Ayazma-7 sample and the maximum

7
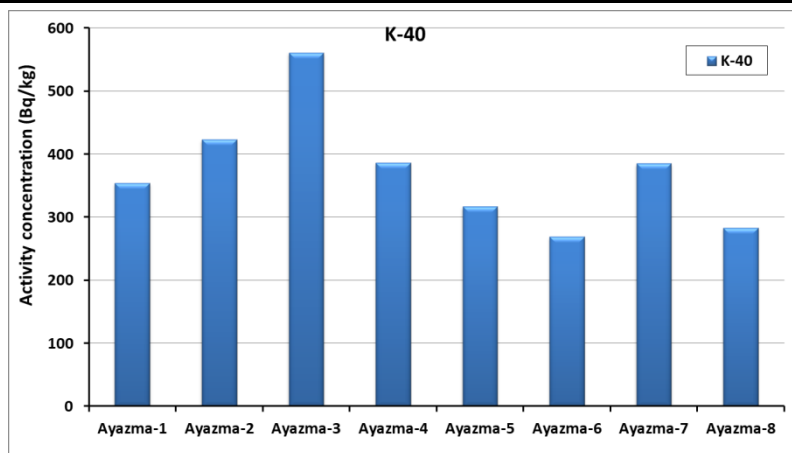
Figure 5. *The activity concentration of ^{40}K in gravel samples*

value was measured in the Ayazma-2 sample. It can be seen from Figure 5 that for ^{40}K activity concentration, the smallest value was measured in the Ayazma-6 sample and the largest value was measured in the Ayazma-3 sample.

The mean ^{226}Ra activity concentrations obtained for sand samples were lower than the world average stated in UNSCEAR 2000 reports, ^{232}Th activity concentrations were higher and ^{40}K activity concentrations were lower.

REFERENCES

[1]. UNSCEAR (2000) United Nations Scientific Committee on the Effects of Atomic Radiation. Report to the General Assembly, with scientific annexes, Sources and effects of ionizing radiation Annex B, New York. ,

[2]. Issa, S., Uosif, M. and Elsaman, R. (2013) Gamma radioactivity measurements in Nile River sediment samples. Turkish Journal of Eng. & Env. Sci. 37: 109 – 122. http://dx.doi.org/10.3906/muh-1207-21

[3]. UNSCEAR (1993) United Nations Scientific Committee on the Effects of Atomic Radiation. Report to the General Assembly, with scientific annexes, Sources, Effects and Risks of Ionizing Radiation Annex A, New York

[4]. Akkurt I. and Gunoglu,K., 2014. Natural Radioactivity Measurements and Radiation Dose Estimation in Some Sedimentary Rock Samples in Turkey. Science and Technology of Nuclear Installations Volume 2014, Article ID 950978

[5]. Akkurt, I., Oruncak, B., Gunoglu,K., 2010. Natural radioactivity and dose rates in commerciallyused marble from Afyonkarahisar – Turkey. International Journal of the Physical Sciences Vol. 5 (2), p:170-173.

[6]. Günay O., 2018 , Determination of Natural Radioactivity and Radiological Effects in some Soil Samples in Beykoz-Istanbul, European Journal of Science and Technology No. 12, pp. 9-14, April 2018 ISSN:2148-2683

[7]. İskender AKKURT, N. Ayten UYANIK, Kadir GÜNOĞLU "Radiation dose Estimation: An in vitro Measurement for Isparta-Turkey" IJCESEN 1-1(2015)1-4 DOI: 10.22399/ijcesen.194376

[8]. Seçkiner S., Akkurt, I., Günoglu K., 2017, Determination of 40K concentration in gravel samples from Konyaaltı Beach, Antalya. Acta Phys. Pol. A., Vol 132 (3-II), 1095-1097,doi: 10.12693/APhysPolA.132.1095.

8

[9]. Gandhi, S.M., Ravisankar, R., Rajalakshmi, A., Sivakumar, S., Chandrasekaran, A., Anand, P.D., 2014. Measurements of natural gamma radiation in beach sediments of North east coast of Tamilnadu, India by gamma ray spectrometry with multivariate statistical approach. J. Radiat. Res. Appl. Sci. 7 (1), 7–17.

[10]. Huang, Y., Lu, Xinwei, Ding, X.W., Feng, T., 2015. Natural radioactivity level in beach sand along the coast of Xiamen Island, China. Mar. Pollut. Bull. 91, 357–361.

[11]. Al-Ghamdi, H., Al-Muqrin, A., El-Sharkawy, A., 2016. Assessment of natural radioactivity and 137 Cs in some coastal areas of the Saudi Arabian gulf. Mar. Pollut. Bull. 104, 29–33.

Design and Experimental Research of Downhole Acoustic Wave Generator Device Based on Giant Magnetostrictive Transducer

Qing Wang[1*], Zhichuan Guan[1], Bo Zhang[2], Yongwang Liu[1]

[1] *School of Petroleum Engineering, China University of Petroleum (East China), Qingdao, China*
[2] *Tarim Oilfield, PetroChina, Korla, China*
*wq4967079@163.com

ABSTRACT

Effective generation of longitudinal wave and efficient transmission of acoustic energy in limited downhole space are prerequisites for stable and long-distance transmission of acoustic wave in drill string. So an efficient and reliable generator are of great significance for field application of downhole acoustic signal transmission technology. In this situation, based on the impact of acoustic radiation mode of giant magnetostrictive transducer on the acoustic propagation characteristics in drill string, a downhole acoustic generator is designed. The influence of acoustic radiation mode of transducer is analyzed. The result indicates that: Giant magnetostrictive transducer is an ideal downhole acoustic transducer. The transmission of downhole information by plane wave in drill string is very beneficial to the stability of acoustic signal and the signal quality of receiving end. When the center single point horn structure is used to radiate the acoustic wave, the ideal plane wave can be obtained in the drill string.

***KEYWORDS –** Acoustic wave, Transducer, Generating device.*

1. INTRODUCTION

The safety in the process of oil and gas drilling has always been the focus of petroleum scientists, and the fast and accurate transmission of downhole information is the premise of safe drilling[1]. Acoustic telemetry technology is a wireless transmission technology with acoustic wave as carrier and drill-string as transmission channel. It has been widely studied because of its advantages of low cost, high speed and easy directional transmission[2]. The downhole information acoustic telemetry system is the key to realize the field application of the technology, and the acoustic generator is the core component of the system, which mainly solves the conversion between the downhole electric energy and acoustic energy[3-6].

In this paper, a downhole acoustic generator is designed based on the giant magnetostrictive transducer, and the experimental research on the influence of transducer installation type on the acoustic transmission effect is carried out. According to the test results, it is a very effective way to transfer sound wave from transducer to drill string by using a horn. The parameters of acoustic horn in the generator are also designed. These results are helpful to reduce the attenuation of acoustic wave and realize the field application of acoustic telemetry technology.

2. DESIGN PROCESS

2.1. Transducer

The giant magnetostrictive transducer has the advantages of large strain, high output power, high controllability, compact structure and wide range of working temperature when generating longitudinal wave, which is the first choice of transducer used downhole. Its structure is shown in the figure 1. When the transducer is working, the pulse current generated by the pulse power supply is applied to the excitation coil of the transducer, and the giant magnetostrictive rod will expand and change under the action of alternating magnetic field, which will convert the electric energy into the mechanical vibration of a certain frequency, with the main frequency of 800 Hz and the working frequency band width of 20 Hz ~ 25 kHz.
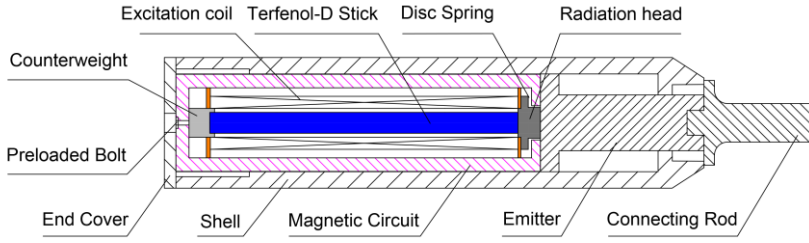
Transducer parameter
Length：350 mm Diameter：38 mm Weight：4.4Kg

Figure 1. *Structure of Giant Magnetostrictive Transducer*

2.2. Design of acoustic radiation mode

The mode of acoustic radiation refers to the mode in which the acoustic wave enters the drill string from the transducer, which determines the transmission efficiency and the propagation characteristics of the acoustic wave in the drill string. According to the characteristics of transducer and drill string section, two types of acoustic radiation are designed. Type 1 is a circumferential multi-point radiation mode, in which multiple transducers are uniformly distributed around the cross-section of the pipe string to transmit acoustic wave to the drill string; type 2 is a central single-point radiation mode, which uses the structural idea of the horn to install the transducer on the small end face of the horn at the axis of the drill string and the acoustic wave from the transducer is transmitted to the drill string through the horn.

The transmission of downhole information by plane wave in drill string is very beneficial to the stability of acoustic signal and the signal quality of receiving end. Therefore, in order to select the better type, the test device as shown in the figure 2 is designed to analyze the acoustic propagation effect of different transducer acoustic radiation modes.
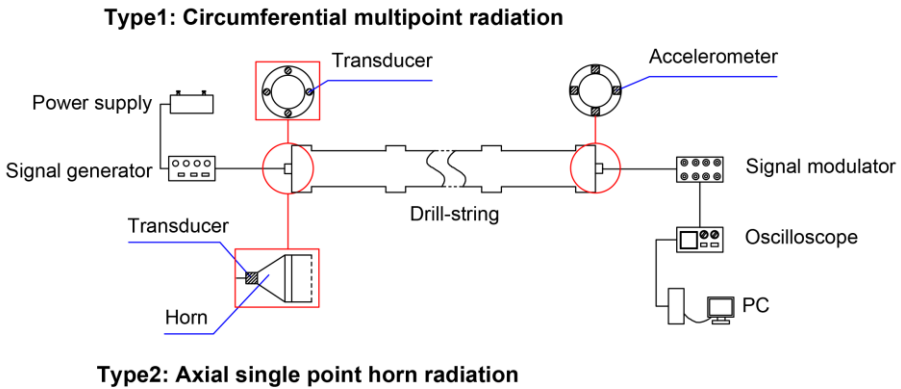
Figure 2. *Test Device of Acoustic Radiation Mode*

From the test results shown in Figure 3, using type 1 to obtain the difference between the amplitudes of the acoustic waves measured by the four accelerometers uniformly distributed on the same receiving surface of the receiving end is obvious. In comparison, the type 2 obtained at different receiving points of the receiving end does not have obvious waveform and amplitude. Differences can achieve better acoustic propagation effects. Therefore, Type 2 serves as a form of installation of the transducer in the downhole acoustic wave generating device.

11

a. Type 1   *b. Type 2*
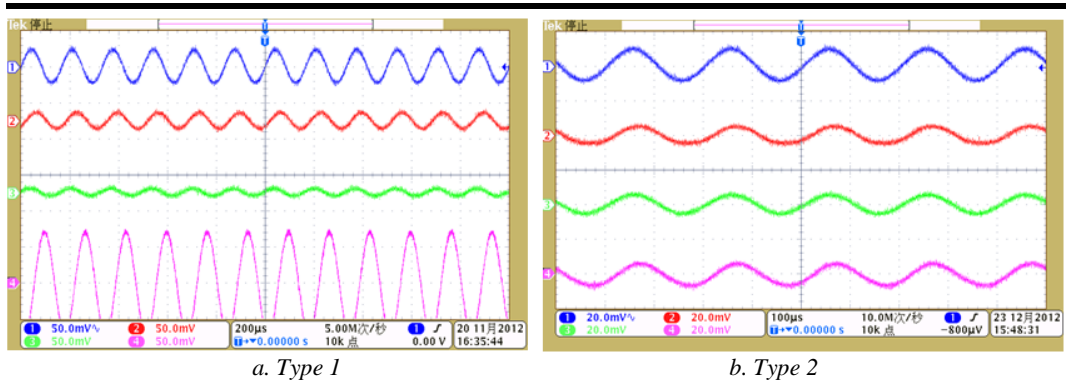
Figure 3. *Test Results*

2.3. Downhole acoustic wave generator device

According to the acoustic radiation mode of the designed giant magnetostrictive transducer, the downhole acoustic generator as shown in Figure 4 is designed. When the device is working downhole, the measured downhole information is transmitted to the encoding and transcoding circuit through the detecting instrument connecting tube to encode and transcode the signal, and then transmitted to the transducer driving circuit for amplification, and the transducer is driven to convert the electrical signal into acoustic signal radiation. Transfer into the drill string to achieve the occurrence of downhole information acoustic signals.
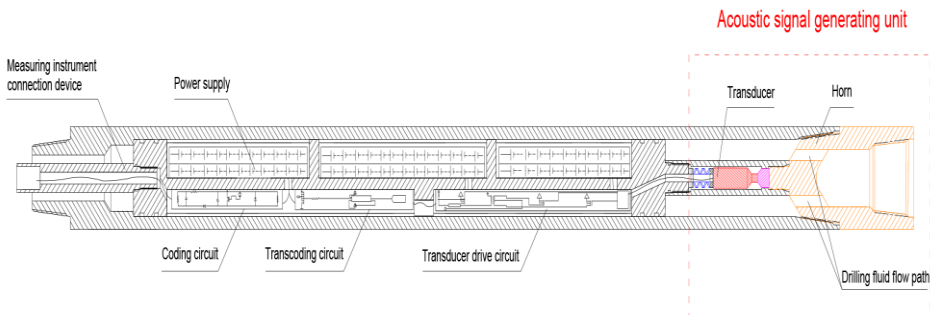
Figure 4. *Structure of Acoustic Wave Generator Device*

3.   CONCLUSIONS

Giant magnetostrictive transducer is an ideal downhole acoustic transducer. The transmission of downhole information by plane wave in drill string is very beneficial to the stability of acoustic signal and the signal quality of receiving end. When the center single point horn structure is used to radiate the acoustic wave, the ideal plane wave can be obtained in the drill string. Based on the results, a downhole acoustic generator is designed.

REFERENCES

[1]. Jiangshuai Wang, Gonghui Liu, et al. Study on Temperature Distribution in Wellbore during Drilling, International Conference on Computational and Experimental Science and Engineering (ICCESEN 2018), 12-16 October, 2018 Antalya-Turkey

[2]. Drumheller D. S. Acoustical properties of drill strings[J]. Journal of the Acoustical Society of America. 1989, 85(3): 1048-1064.

[3]. Dansen Shang, Jirui Hou, et al. Effect of Descending Viscosity Injection Pattern for Alkali-surfactant-polymer (ASP) Flooding on Enhanced oil Recovery, International Conference on

12

Computational and Experimental Science and Engineering (ICCESEN 2018), 12-16 October, 2018 Antalya-Turkey

[4]. Li Zhun, Xiaodong Wu, Guoqing Han. Performance of Multiple-fracture Horizontal Wells with Consideration of the Long-term Fracture Conductivity (ICCESEN 2018), 12-16 October, 2018 Antalya-Turkey

[5]. Hongwei Yang, Jun Li, Gonghui Liu. Why the Variable Gradient Drilling Approach Can Better Fit the Complex and Narrow Pressure Window in Ultra-deep Water Drilling? (ICCESEN 2018), 12-16 October, 2018 Antalya-Turkey

[6]. M. Lakestani, J. Manafian, Novel Dark. Singular and Combo Optical Solitons for Fokas-Lenells Equation[J]. Acta Physica Polonica A, 136(2019)214-224.

Simulation of the Sound Field in Marine Riser Annulus

Xiaohui Wang[1*], Zhichuan Guan[2]
[1] China University of Petroleum (East China), Qingdao, China
*wangxiaohuiupc@126.com

ABSTRACT

The deepwater drilling gas intrusion monitoring method based on gas-liquid two- phase flow identification of the riser is an ideal early monitoring method for gas intrusion and has great development potential. In this paper, the sound field in the air- liquid two-phase flow of the riser ring is studied in detail by numerical simulation method. Starting from the influence law of the drill pipe on the annulus sound field, the sound pressure level distribution on the probe placement (outer wall of the riser) is analyzed, and the possible placement position of the probe is determined according to the analysis result. The excitation pulse frequency is optimized by calculating the sensitivity field of the annulus.

KEYWORDS - *Gas-kick detection, Drill-pipe, Sound field.*

1. INTRODUCTION

The combination of wellhead device and blowout preventer for deepwater drilling is located under water and has a certain distance from the platform. As the water depth increases, the proportion of drilling fluid in the conduit above the blowout preventer will increase. At the same time, due to the low temperature and high pressure environment of the seabed, the equivalent size is still small when the gas invading the wellbore reaches the wellhead or even the riser, making it difficult to monitor the gas volume[1-4]. If the gas kick is not detected early, the gas entering the riser will be released quickly as the pressure is reduced, which may induce a serious blowout accident. Therefore, how to effectively achieve early monitoring and find that gas intrusion becomes the key to deepwater well control[5-8].

In this paper, the sound field in the air-liquid two-phase flow of the riser ring is studied in detail by numerical simulation method. The influence of the drill pipe on the sound field of the annulus is studied, and the distribution of sound pressure level on the probe placement (outer wall of the riser) is analyzed. Then, according to the analysis result, the possible placement position of the probe is determined. The excitation pulse frequency is optimized by calculating the sensitivity field of the annulus, thereby providing basic conditions for studying the influence of the gas content on the received signal.

Figure 1 *Complete view of experimental device*

14

2. EXPERIMENTAL MODEL

The experimental details have been shown in Fig.1.

3.   RESULTS

Firstly, the sound field distribution in the riser loop is numerically simulated. The influence of the intermediate drill pipe on the annulus sound field of the riser is analyzed by simulating the sound field distribution in the case of the annulus without the drill pipe and the drill pipe. The excitation source frequency is from 0.1. The MHz changes to 1MHz. The figure below shows the sound field distribution at different frequencies for both the drill pipe and the drill pipe.

Frequency/ MHz	Sound field distribution /dB	
	Without drillpipe	With drillpipe
0.1		
0.2		
0.6		
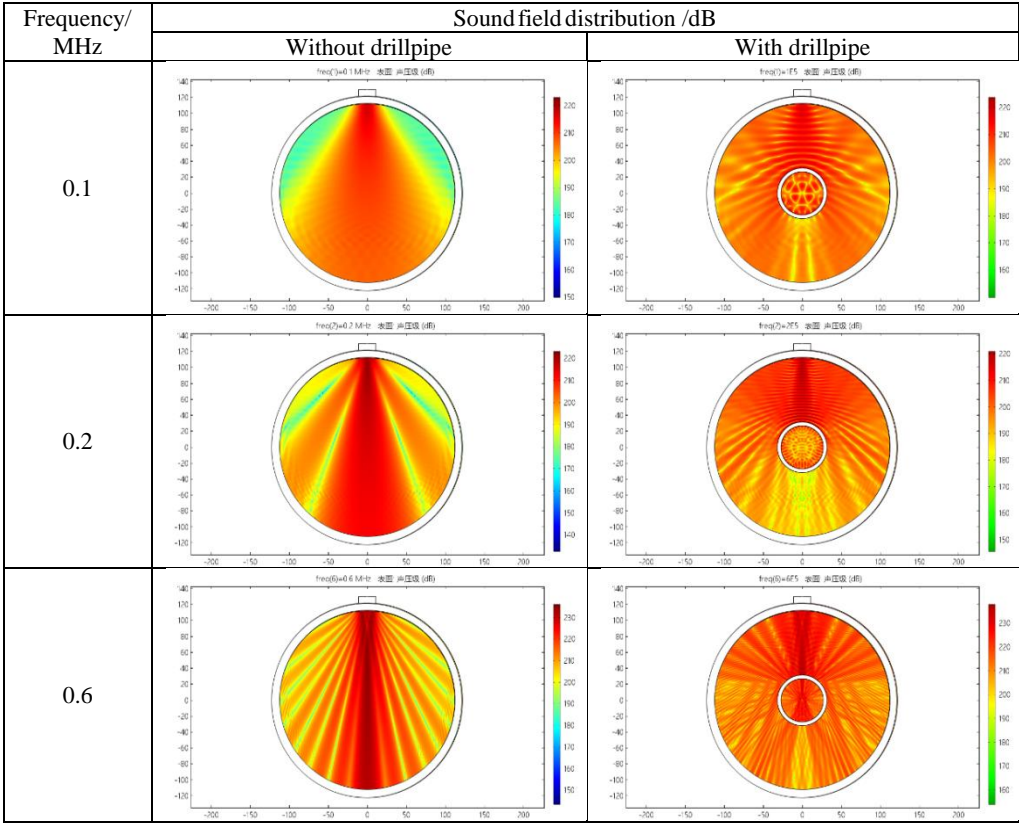
Figure 2 *Sound field within riser annulus under different frequency*

It can be seen from the figure that as the frequency increases, the beams in the annulus are more concentrated in the absence of the drill pipe and the drill pipe, the divergence angle becomes smaller, and the number of side lobes increases significantly. At the same time, the near field length is shortened and the directivity is enhanced. The energy of the sound field is mainly concentrated in the main lobe, and the side lobe is attenuated with respect to the sound pressure in the main lobe, which is oscillating.

The sound pressure in the annulus is symmetrically distributed with the center line as the axis of symmetry. Compared with no drill pipe, the drill pipe has obvious reflection effect on the sound wave when there is a drill pipe, that is, the drill pipe has a significant shielding effect on the propagation of the elastic wave, the sound pressure level is reduced in the region far from the

15

emission end, and the region near the emission end is drilled. The superimposed sound pressure level of the rod reflection sound field is significantly enhanced.

4   CONCLUSIONs

The sound field in the air-liquid two-phase flow of the riser ring is studied in detail by numerical simulation method. The sound pressure level distribution on the probe placement (outer wall of the riser) is analyzed, and the possible placement position of the probe is determined according to the analysis result. The excitation pulse frequency is optimized by calculating the sensitivity field of the annulus, thereby providing basic conditions for studying the influence of the gas content on the received signal.

REFERENCES

[1]. Avelar C S, Ribeiro P R, Sepehrnoori K., Deepwater gas kick simulation, Journal of Petroleum Science and Engineering, 67(2009)13-22. DOI: 10.1016/j.petrol.2009.03.001.

[2]. Jiangshuai Wang, Gonghui Liu, et al., Study on Temperature Distribution in Wellbore during Drilling, International Conference on Computational and Experimental Science and Engineering (ICCESEN 2018), 12-16 October, 2018 Antalya-Turkey

[3]. Chao Wang, Gonghui Liu, et al., Downhole WOB Measurement Error Owing to Temperature Variation, International Conference on Computational and Experimental Science and Engineering (ICCESEN 2018), 12-16 October, 2018 Antalya-Turkey

[4]. Sheng G. L., Su Y. L., Wang W. D. A new fractal approach for describing induced-fracture porosity/permeability/compressibility in stimulated unconventional reservoirs, Journal of Petroleum Science and Engineering, 179(2019)855-866. DOI:10.1016/j.petrol.2019.04.104.

[5]. Yang, Yingtao, Q. Wen., Numerical simulation of gas-liquid two-phase flow in channel fracture pack, Journal of Natural Gas Science and Engineering,43(2017)3-47. DOI:10.1016/j.jngse.2017.03.024.

[6]. M.Lakestani, J.Manafian, Novel Dark, Singular and Combo Optical Solitons for Fokas-Lenells Equation, Acta Physica Polonica A, 136(2019)214-224. DOI: 10.12693/APhysPolA.136.214

[7]. Hongwei Yang, Jun Li and Gonghui Liu, Why the Variable Gradient Drilling Approach Can Better Fit the Complex and Narrow Pressure Window in Ultra-deep Water Drilling? , International Conference on Computational and Experimental Science and Engineering (ICCESEN 2018), 12-16 October, 2018 Antalya-Turkey

[8]. Dansen Shang, Jirui Hou, Effect of Descending Viscosity Injection Pattern for Alkali-surfactant-polymer (ASP) Flooding on Enhanced oil Recovery, International Conference on Computational and Experimental Science and Engineering (ICCESEN 2018), 12-16 October, 2018 Antalya-Turkey

Explicit Relations for the Poly-Tangent Polynomials with a q-parameter

Burak KURT[*]

Department of Mathematics, Faculty of Education, University of Akdeniz , TR-07070 Antalya, TURKEY
* burakkurt@akdeniz.edu.tr

ABSTRACT

Recently, many mathematicians have studied in the area of the Bernoulli polynomials and numbers, the Euler polynomials and numbers, the poly-Bernoulli, poly-Euler and poly-Genocchi polynomials and numbers, the Tangent polynomials and the poly-Tangent polynomials. Bayad et al. [1] defined polylogarithms and poly-Bernoulli numbers. Hamahata investigated and proved poly-Euler polynomials. Ryoo investigated and defined the Tangent polynomials and numbers and poly-Tangent polynomials and numbers.

In this work, we introduce the poly-Tangent polynomials with a q-parameter. Furthermore, we prove the theorem for this polynomial.

***KEYWORDS –** Bernoulli numbers and polynomials, Poly-Bernoulli numbers and polynomials, Tangent polynomials.*

1. INTRODUCTION AND DEFINITIONS

The classical Bernoulli numbers and polynomials are defined the following generating functions, respectively;

$$\sum_{n=0}^{\infty} B_n \frac{t^n}{n!} = \frac{t}{e^t - 1}, \quad |t| < 2\pi \tag{1}$$

and

$$\sum_{n=0}^{\infty} B_n(x) \frac{t^n}{n!} = \frac{t}{e^t - 1} e^{xt}, \quad |t| < 2\pi. \tag{2}$$

The classical Tangent polynomials $T_n(x)$ are defined by the generating functions;

$$\sum_{n=0}^{\infty} T_n(x) \frac{t^n}{n!} = \left(\frac{2}{e^{2t} + 1} \right) e^{xt}, \quad |2t| < \pi \tag{3}$$

and
 The classical Tangent numbers T_n are defined by the generating functions;

$$\sum_{n=0}^{\infty} T_n \frac{t^n}{n!} = \left(\frac{2}{e^{2t} + 1} \right), \quad |2t| < \pi.$$

Let $k \in Z$ and k>1, then k-th polylogarithm function function is defined by (see [1], [4], [7])

$$Li_k(z) = \sum_{m=1}^{\infty} \frac{z^m}{m!}, z \in C, z > 1 \tag{4}$$

when k=1, $Li_1(z) = -\log(1 - z)$.

Kim et al. in [9] defined the poly-Bernoulli polynomials and the poly-Genocchi polynomials as

$$\sum_{n=0}^{\infty} B_n^{(k)}(x) \frac{t^n}{n!} = \frac{Li_k(1 - e^{-t})}{1 - e^{-t}} e^{xt}$$

and

$$\sum_{n=0}^{\infty} G_n^{(k)}(x) \frac{t^n}{n!} = \frac{2Li_k(1 - e^{-t})}{e^t + 1} e^{xt}$$

respectively.
The Stirling number of the second kind is defined as:

17

$$\sum_{n=0}^{\infty} S_2\,(n,m)\frac{t^n}{n!} = \frac{(e^t-1)^m}{m!} \tag{5}$$

The poly-Tangent polynomials $T_n^{(k)}(x)$ are defined by following generating functions by Ryoo [13]:

$$\sum_{n=0}^{\infty} T_n^{(k)}\,(x)\frac{t^n}{n!} = \frac{2Li_k(1-e^{-t})}{e^{2t}+1}e^{xt}, \tag{6}$$

and the poly-Tangent polynomials $T_n^{(k)}$ are defined using x=0, $T_n^{(k)}(0) \coloneqq T_n^{(k)}$ are called the poly-Tangent numbers.

The second kind weight Stirling numbers $S_2(n,m,x)$ are defined by Carlitz in [3] as

$$\sum_{n=0}^{\infty} S_2(n,m,x)\frac{t^n}{n!} = \frac{(e^t-1)^m}{m!}e^{xt}. \tag{7}$$

2. MAIN THEOREM

In this section, we give some basic identities and relations for the poly-Tangent polynomials with a q-parameter.

Definition The poly-Tangent polynomials and nıumbers with a q-parameter are defined the following generating functions, respectively:

$$\sum_{n=0}^{\infty} T_{n,q}^{(k)}\,(x)\frac{t^n}{n!} = \frac{2Li_k\left(\frac{1-e^{-qt}}{q}\right)}{e^{2tq}+1}e^{xt} \tag{8}$$

and

$$\sum_{n=0}^{\infty} T_{n,q}^{(k)}\frac{t^n}{n!} = \frac{2Li_k\left(\frac{1-e^{-qt}}{q}\right)}{e^{2tq}+1} \tag{9}$$

when n, k integer, $n \geq 0, k \geq 1$ and $q \neq 0$ real parameter.

Some special cases of $T_{n,q}^{(k)}(x)$ are following remarks.

Remark For q=1, $T_{n,q}^{(k)}(x)$ reduces to the poly-Tangent polynomials.

Remark When q=k=1, we obtain the classical Tangent polynomials.

Theorem The following relation holds true:

$$T_{n,q}^{(k)} + \sum_{m=0}^{n}\binom{n}{m}(2q)^m T_{n-m,q}^{(k)} = 2\sum_{m=0}^{n}\frac{1}{(m+1)^k}\frac{(-1)^j}{q^{m+1}}\sum_{j=0}^{m+1}\binom{m+1}{j}(-qj)^n \tag{10}$$

Proof By (9), we write as

$$e^{2qt}\sum_{n=0}^{\infty} T_{n,q}^{(k)}\frac{t^n}{n!} + \sum_{n=0}^{\infty} T_{n,q}^{(k)}\frac{t^n}{n!} = 2Li_k\left(\frac{1-e^{-qt}}{q}\right)$$

$$= 2\sum_{m=0}^{\infty}\frac{1}{(m+1)^k}\frac{(-1)^j}{q^{m+1}}\sum_{j=0}^{m+1}\binom{m+1}{j}e^{-qtj}(-1)^{m+1-j}$$

$$= \sum_{n=0}^{\infty}\left\{2\sum_{m=0}^{n}\frac{1}{(m+1)^k}\frac{(-1)^j}{q^{m+1}}\sum_{j=0}^{m+1}\binom{m+1}{j}(-qj)^n\right\}\frac{t^n}{n!}.$$

Comparing the coefficients of $\frac{t^n}{n!}$, we have (10).

Theorem The following relation holds true:

$$T_{n,q}^{(k)} + \sum_{m=0}^{n}\binom{n}{m}(2q)^m T_{n-m,q}^{(k)} = 2\left\{q^{-1}B_{n,q}^{(k)} - \sum_{m=0}^{n}\binom{n}{m}B_{n-m,q}^{(k)}(-1)^m q^{m-1}\right\} \tag{11}$$

Proof From (9), we write as:

18

$$\frac{2Li_k\left(\frac{1-e^{-qt}}{q}\right)}{\frac{1-e^{-qt}}{q}}\frac{q}{1-e^{-qt}} = \frac{2Li_k\left(\frac{1-e^{-qt}}{q}\right)}{e^{2qt}+1}e^{2qt} + 1$$

$$\frac{2}{q}\sum_{n=0}^{\infty} B_{n,q}^{(k)}\frac{t^n}{n!}(1-e^{-qt}) = \sum_{n=0}^{\infty} T_{n,q}^{(k)}\frac{t^n}{n!}(e^{2qt}+1)$$

$$\frac{2}{q}\left\{\sum_{n=0}^{\infty} B_{n,q}^{(k)}\frac{t^n}{n!} - \sum_{n=0}^{\infty} B_{n,q}^{(k)}\frac{t^n}{n!}\sum_{n=0}^{\infty}(-q)^n\frac{t^n}{n!}\right\} = \sum_{n=0}^{\infty} T_{n,q}^{(k)}\frac{t^n}{n!}\sum_{m=0}^{\infty}(2q)^m\frac{t^m}{m!} + \sum_{n=0}^{\infty} T_{n,q}^{(k)}\frac{t^n}{n!}$$

$$2\left\{\sum_{n=0}^{\infty} q^{-1}B_{n,q}^{(k)}\frac{t^n}{n!} - \sum_{n=0}^{\infty}\sum_{m=0}^{n}\binom{n}{m}B_{n-m,q}^{(k)}(-q)^{m-1}\frac{t^n}{n!}\right\}$$

$$= \sum_{n=0}^{\infty}\sum_{m=0}^{n}\binom{n}{m}T_{n-m,q}^{(k)}(2q)^m\frac{t^n}{n!} + \sum_{n=0}^{\infty} T_{n,q}^{(k)}\frac{t^n}{n!}.$$

By using Cauchy product and comparing the coefficients of $\frac{t^n}{n!}$, we have (11).

Corollary The following relation holds true:

$$2q^{-1}B_{n,q}^{(k)}(x) = \sum_{m=0}^{n}\binom{n}{m}\left\{(2q)^m T_{n-m,q}^{(k)}(x) + 2(-1)^m q^{m-1}B_{n-m,q}^{(k)}(x)\right\} + T_{n,q}^{(k)}(x).$$

Theorem The following relation holds true:

$$T_{n+m,q}^{(k)}(x) = \sum_{p=0}^{n}\sum_{r=0}^{m}\binom{n}{p}\binom{m}{r}v^{p+r}T_{n+m-p-r,q}^{(k)}(x) \tag{12}$$

Proof By (8), we write as:

$$\sum_{n=0}^{\infty} T_{n,q}^{(k)}(x)\frac{t^n}{n!} = \frac{2Li_k\left(\frac{1-e^{-qt}}{q}\right)}{e^{2qt}+1}e^{xt}. \tag{13}$$

We replace *t* by *t+u* in (13),

$$\sum_{m=0}^{\infty}\sum_{n=0}^{\infty} T_{n+m,q}^{(k)}(x)\frac{t^n}{n!}\frac{u^m}{m!} = \frac{2Li_k\left(\frac{1-e^{-q(t+u)}}{q}\right)}{e^{2q(t+u)}+1}e^{x(t+u)}. \tag{14}$$

In the last equation, we replace *x* by *v*, we get

$$\sum_{m=0}^{\infty}\sum_{n=0}^{\infty} T_{n+m,q}^{(k)}(v)\frac{t^n}{n!}\frac{u^m}{m!} = \frac{2Li_k\left(\frac{1-e^{-q(t+u)}}{q}\right)}{e^{2q(t+u)}+1}e^{v(t+u)} \tag{15}$$

By (14) and (15), we write

$$\sum_{m=0}^{\infty}\sum_{n=0}^{\infty} T_{n+m,q}^{(k)}(v)\frac{t^n}{n!}\frac{u^m}{m!} = e^{v(t+u)}\sum_{m=0}^{\infty}\sum_{n=0}^{\infty} T_{n+m,q}^{(k)}\frac{t^n}{n!}\frac{u^m}{m!} \tag{16}$$

Now by applying the following known series identities [19, p. 52, Eq.1.6 (2)]

$$\sum_{N=0}^{\infty} f(N)\frac{(x+y)^N}{N!} = \sum_{n,m=0}^{\infty} f(n+m)\frac{x^n}{n!}\frac{y^m}{m!} \tag{17}$$

in the right hand side of (16), we get

$$\sum_{m=0}^{\infty}\sum_{n=0}^{\infty} T_{n+m,q}^{(k)}(x)\frac{t^n}{n!}\frac{u^m}{m!} = \sum_{p=0}^{\infty}\sum_{r=0}^{\infty} v^{p+r}\frac{t^p}{p!}\frac{u^r}{r!}\sum_{m=0}^{\infty}\sum_{n=0}^{\infty} T_{n+m,q}^{(k)}\frac{t^n}{n!}\frac{u^m}{m!} \tag{18}$$

$$= \sum_{n=0}^{\infty}\sum_{r=0}^{\infty}\left\{\sum_{p=0}^{n}\sum_{r=0}^{m}\binom{n}{p}\binom{m}{r}v^{p+r}T_{n+m-p-r,q}^{(k)}(x)\right\}\frac{t^n}{n!}\frac{u^m}{m!}.$$

19

Finally, upon first replacing *n* by *n-p* and *m* by *m-r* by using the Cauchy product in the left hand side of the above equation (18) and comparing the coefficients of $\frac{t^n}{n!}$ and $\frac{u^m}{m!}$ On both sides of the resulting equation, we have (12).

REFERENCES
[1]. A.Bayad and Y. Hamahata, Polylogarithms and poly-Bernoulli polynomials, Kyushu. J. Math., 65 (2011), 15-34.
[2]. A.Bayad and T. Kim, Higher recurrences for Apostol-Bernoulli-Euler polynomials, Russ. J. of Math. Phys., 19(1), (2012), 1-10.
[3]. L. Carlitz, A note on Bernoulli and Euler polynomials of the second kind, Scripta Math., 25 (1961), 323-330.
[4]. M. Cenkci and T. Komatsu, Poly-Bernoulli numbers and polynomials with a q-parameter, J. Number Theory, 152 (2015), 38-54.
[5]. U. Duran, M. Acikgoz and S. Araci, Hermite based poly-Bernoulli polynomials with q-parameter, Advanced Stud. in Contemp., 28(2), (2018), 285-296.
[6]. U. Duran, M. Acikgoz, A. Esi and S. Araci, A note on the (p; q)-Hermite polynomials, App. Math. and Information Sciences, 12 (2018), 227-231.
[7]. Y. Hamahata, Poly-Euler polynomials and Arakawa-Kaneko type zeta functions, Functione et. App. Commentarii Mathematica, 51(1), (2014), 7-27.
[8]. D. S. Kim and T. Kim, Hermite and poly-Bernoulli mixed type polynomials, Advances in Diff. Equa., 2013.2013.343.
[9]. D. S. Kim and T. Kim, A note on poly-Bernoulli and higher order poly-Bernoulli polynomials, Russ. J. Math., 22(1), (2015), 26-33.
[10]. B. Kurt, Identities and relation on the poly-Genocchi polynomials with a q-parameter, J. Inequa. Special Func., 9(1), (2018), 1-8.
[11]. C. S. Ryoo, A note on the tangent numbers and polynomials, Adv. Studies Theor. Phs., 7 (9) (2013), 447-454.
[12]. C. S. Ryoo, T. Kim, R. P. Agarwal, A numerical investigation of the roots of q-polynomials, Inter. J. Comput. Math., 83 (2006), 223-234.
[13]. C. S. Ryoo, On poly-tangent numbers and polynomials and distribution of their zeros, Global Journal of Pure and Applied Mathematics, 12(5), (2016), 4411–4425.
[14]. R. Sanchez-Peregrino, Closed formula for Poly-Bernoulli numbers, Fibonacci Quart., 40(2002), 62-364.
[15]. H. M. Srivastava, Some generalization and basic (or q-) extension of the Bernoulli, Euler and Genocchi polynomials, Appl. Math. Inf. Sci., 5 (2011), 390-444.
[16]. H. M. Srivastava and H. L. Manocho, A treatise on generating functions, Halsted Press, John Willey and Suns, New York, Chichester, Brisbane and Toronto, 1984.
[17]. H. M. Srivastava and J. Choi, Series associated with the zeta and related functions, Kluver Academic Pub., Dordrect, Boston and London, (2001).

A New Class Of Modified Degenerate Bernoulli, Euler and Genocchi Polynomials

Burak KURT*

Department of Mathematics, Faculty of Education, Akdeniz University, Antalya, TURKEY
*burakkurt@akdeniz.edu.tr

ABSTRACT

Srivastava *et al.* in ([18]-[23]) proved some theorems and recurrences relation for Bernoulli, Euler and Genocchi polynomials. Also, they considered the Apostol-Bernoulli, Euler and Genocchi polynomials. Dolgy *et al.* in [4], H.-In. Known *et al.* in [5], Lim [1] defined and proved some relations for the modified degenerate Bernoulli polynomials $B_n^\alpha(x \mid \lambda)$ of order α, Euler polynomials $E_n^\alpha(x \mid \lambda)$ of order α and Genocchi polynomials $G_n^\alpha(x \mid \lambda)$ of order α, respectively.
In this work, we introduce and investigate to a further generalized the modified degenerate Bernoulli polynomials. We prove recurrence relations and some identities for these polynomials.

KEYWORDS – *Bernoulli numbers and polynomials, Modified Degenerate Bernoulli, Euler and Genocchi polynomials, The Degenerate Stirling numbers of the second kind.*

1. INTRODUCTION

The classical Bernoulli polynomials $B_n^{(\alpha)}(x)$ of order $\alpha \in C$, the classical Euler polynomials $E_n^{(\alpha)}(x)$ of order $\alpha \in C$ and the classical Genocchi polynomials $G_n^{(\alpha)}(x)$ of order $\alpha \in C$ are defined the following generating functions respectively ([20]-[23]),

$$\sum_{n=0}^{\infty} B_n^{(\alpha)}(x)\frac{t^n}{n!} = \left(\frac{t}{e^t-1}\right)^\alpha e^{xt} , \ |t| < 2\pi \tag{1.1}$$

$$\sum_{n=0}^{\infty} E_n^{(\alpha)}(x)\frac{t^n}{n!} = \left(\frac{2}{e^t+1}\right)^\alpha e^{xt} , \ |t| < \pi \tag{1.2}$$

and

$$\sum_{n=0}^{\infty} G_n^{(\alpha)}(x)\frac{t^n}{n!} = \left(\frac{2t}{e^t+1}\right)^\alpha e^{xt} , \ |t| < \pi. \tag{1.3}$$

The generalized Bernoulli polynomials $B_n^{[m-1]}(x)$, $m \in N$ are defined in a suitable neighbourhood of $t = 0$ by means of the generating function in ([1], [2], [17]);

$$\sum_{n=0}^{\infty} B_n^{[m-1]}(x)\frac{t^n}{n!} = \frac{t^m}{e^t-\sum_{l=0}^{m-1}\frac{t^l}{l!}} e^{xt}. \tag{1.4}$$

Recently, Kurt ([7], [8]) gave the generalized Bernoulli polynomials $B_n^{[m-1,\alpha]}(x)$ of order α, the generalized Euler polynomials $E_n^{[m-1,\alpha]}(x)$ of order α and the generalized Genocchi polynomials $G_n^{[m-1,\alpha]}(x)$ of order α are defined the following generating functions respectively;

$$\sum_{n=0}^{\infty} B_n^{[m-1,\alpha]}(x)\frac{t^n}{n!} = \left(\frac{t^m}{e^t-\sum_{l=0}^{m-1}\frac{t^l}{l!}}\right)^\alpha e^{xt}, \tag{1.5}$$

$$\sum_{n=0}^{\infty} E_n^{[m-1,\alpha]}(x)\frac{t^n}{n!} = \left(\frac{2^m}{e^t+\sum_{l=0}^{m-1}\frac{t^l}{l!}}\right)^\alpha e^{xt} \tag{1.6}$$

and

$$\sum_{n=0}^{\infty} G_n^{[m-1,\alpha]}(x)\frac{t^n}{n!} = \left(\frac{2^m t^m}{e^t-\sum_{l=0}^{m-1}\frac{t^l}{l!}}\right)^\alpha e^{xt} \tag{1.7}$$

21

Carlitz [3] defined degenerate Bernoulli polynomials are given by the generating function to be

$$\frac{t}{(1+\lambda t)^{\mu}-1}(1+\lambda t)^{\mu x} = \sum_{n=0}^{\infty} B_n(x|\lambda)\frac{t^n}{n!}, \; \mu t = 1 \qquad (1.8)$$

when $x=0$, $B_n(\lambda) = B_n(0|\lambda)$ are called degenerate Bernoulli numbers.
D. V. Dolget et. al. [4] defined the modified degenerate Bernoulli polynomials which are different from Carlitz's degenerate Bernoulli polynomials as follows

$$\frac{t}{(1+\lambda)^{\mu t}-1}(1+\lambda)^{\mu x t} = \sum_{n=0}^{\infty} B_{n,\lambda}(x)\frac{t^n}{n!}, \; \mu\lambda = 1 \qquad (1.10)$$

when $x=0$, $B_{n,\lambda} = B_{n,\lambda}(0)$ are called the modified degenerate Bernoulli numbers.
H.-In. Known *et al.* [5] defined the modified degenerate Euler polynomials as following generating functions

$$\sum_{n=0}^{\infty} E_{n,\lambda}(x)\frac{t^n}{n!} = \frac{2}{(1+\lambda)^{\mu t}+1}(1+\lambda)^{\mu x t}, \; \mu\lambda = 1 \qquad (1.12)$$

for x=0, $E_{n,\lambda} = E_{n,\lambda}(0)$ are called the modified degenerate Euler numbers.
Lim [11] defined the higher order degenerate Genocchi polynomials are defined the following generating functions

$$\sum_{n=0}^{\infty} G_{n,\lambda}^{(\alpha)}(x)\frac{t^n}{n!} = \left(\frac{2t}{(1+\lambda)^{\mu t}+1}\right)^{\alpha}(1+\lambda)^{\mu x t} \qquad (1.13)$$

For x=0, $G_{n,\lambda}^{(\alpha)} = G_{n,\lambda}^{(\alpha)}(0)$ are called the modified degenerate Genocchi numbers.
By these motivations in ([4], [5], [11]), we define generalized the modified degenerate Bernoulli polynomials $B_{n,\lambda}^{[m-1,\alpha]}(x)$ of order α, generalized the modified degenerate Euler polynomials $E_{n,\lambda}^{[m-1,\alpha]}(x)$ of order α and generalized the modified degenerate Genocchi polynomials $G_{n,\lambda}^{[m-1,\alpha]}(x)$ of order α the following generating functions, respectively

$$\sum_{n=0}^{\infty} B_{n,\lambda}^{[m-1,\alpha]}(x)\frac{t^n}{n!} = \left(\frac{t^m}{(1+\lambda)^{\mu t}-\sum_{h=0}^{m-1}\frac{t^h}{h!}}\right)^{\alpha}(1+\lambda)^{\mu x t}, \; \lambda\mu = 1 \qquad (1.14)$$

$$\sum_{n=0}^{\infty} E_{n,\lambda}^{[m-1,\alpha]}(x)\frac{t^n}{n!} = \left(\frac{2^m}{(1+\lambda)^{\mu t}+\sum_{h=0}^{m-1}\frac{t^h}{h!}}\right)^{\alpha}(1+\lambda)^{\mu x t}, \; \lambda\mu = 1 \qquad (1.15)$$

and

$$\sum_{n=0}^{\infty} G_{n,\lambda}^{[m-1,\alpha]}(x)\frac{t^n}{n!} = \left(\frac{2^m t^m}{(1+\lambda)^{\mu t}+\sum_{h=0}^{m-1}\frac{t^h}{h!}}\right)^{\alpha}(1+\lambda)^{\mu x t}, \; \lambda\mu = 1 \qquad (1.16)$$

Carlitz [3] defined degenerate Stirling numbers of the second kind as

$$\sum_{n=0}^{\infty} S(n,k|\lambda)\frac{t^n}{n!} = \frac{((1+\lambda t)^{\mu}-1)^k}{k!}, \; \lambda\mu = 1 \qquad (1.17)$$

Carlitz [3] introduced and investigated the degenerate Stirling, Bernoulli and Eulerian numbers. Srivastava *et al.* in ([18]-[23]) proved some theorems and recurrences relations for Bernoulli, Euler and Genocchi polynomials. Also, they considered the Apostol-Bernoulli, Euler and Genocchi polynomials. Bretti *et al.* ([1], [2]) and Natalini [17] defined and investigated *2D*-Bernoulli polynomials $B_n^{[m-1]}(x,y)$. Kurt in ([7], [8]) defined and gave some relations for the Bernoulli

22

polynomials $B_n^{[m-1,\alpha]}(x,y)$ of order α. Dolgy *et al.* [4], H.-In. Known *et al.* [5], Lim [1] defined and proved some relations for the modified degenerate Bernoulli polynomials $B_n^{(\alpha)}(x|\lambda)$ of order α, Euler polynomials $E_n^{(\alpha)}(x|\lambda)$ of order α and Genocchi polynomials $G_n^{(\alpha)}(x|\lambda)$ of order α, respectively.

2. EXPLICIT RELATIONS FOR THE GENERALIZED THE MODIFIED DEGENERATE BERNOULLI, EULER AND GENOCCHI POLYNOMIALS

In this section, we prove relations and some identities for these polynomials.

Theorem 1. For a fixed $m \in N$, let $B_{n,\lambda}^{[m-1,\alpha]}(x)$, $E_{n,\lambda}^{[m-1,\alpha]}(x)$ and $G_{n,\lambda}^{[m-1,\alpha]}(x)$ be the sequences of a new class of modified degenerate Bernoulli polynomials, a new class of modified degenerate Euler polynomials and a new class of modified degenerate Genocchi polynomials of order α, respectively. Then the following statements hold:

1. Special Values, for every $n \in N$

$$B_{n,\lambda}^{[m-1,0]}(x) = E_{n,\lambda}^{[m-1,0]}(x) = G_{n,\lambda}^{[m-1,0]}(x) = (x|\lambda)_n = \left(\frac{x\log(1+\lambda)}{\lambda}\right)^n$$

2. Summation Formulas

$$B_{n,\lambda}^{[m-1,\alpha]}(x) = \sum_k^n \binom{n}{k} B_{n-k,\lambda}^{[m-1,\alpha]} (x|\lambda)_k = \sum_k^n \binom{n}{k} B_{n-k,\lambda}^{[m-1,\alpha-1]} B_{k,\lambda}^{[m-1,1]}(x)$$
$$E_{n,\lambda}^{[m-1,\alpha]}(x) = \sum_k^n \binom{n}{k} E_{n-k,\lambda}^{[m-1,\alpha]} (x|\lambda)_k = \sum_k^n \binom{n}{k} E_{n-k,\lambda}^{[m-1,\alpha-1]} E_{k,\lambda}^{[m-1,1]}(x)$$
$$G_{n,\lambda}^{[m-1,\alpha]}(x) = \sum_k^n \binom{n}{k} G_{n-k,\lambda}^{[m-1,\alpha]} (x|\lambda)_k = \sum_k^n \binom{n}{k} G_{n-k,\lambda}^{[m-1,\alpha-1]} G_{k,\lambda}^{[m-1,1]}(x)$$

3. Difference Equations

$$B_{n,\lambda}^{[m-1,\alpha]}(x+1) - B_{n,\lambda}^{[m-1,\alpha]}(x) = n \sum_k^{n-1} \binom{n-1}{k} B_{k,\lambda}^{[m-1,\alpha]}(x) B_{n-1-k,\lambda}^{[0,-1]}$$
$$E_{n,\lambda}^{[m-1,\alpha]}(x+1) + E_{n,\lambda}^{[m-1,\alpha]}(x) = 2 \sum_k^n \binom{n}{k} E_{k,\lambda}^{[m-1,\alpha]}(x) E_{n-k,\lambda}^{[0,-1]}$$
$$G_{n,\lambda}^{[m-1,\alpha]}(x+1) + G_{n,\lambda}^{[m-1,\alpha]}(x) = 2 \sum_k^{n-1} \binom{n-1}{k} G_{k,\lambda}^{[m-1,\alpha]}(x) G_{n-1-k,\lambda}^{[0,-1]}$$

4. Integral Formal: For $m \in N$ and fixed α

$$\int_{x_0}^{x_1} B_{n,\lambda}^{[m-1,\alpha]}(x) \, dx = \left(\frac{t^m}{(1+\lambda)^{\mu t} - \sum_{h=0}^{m-1}\frac{t^h}{h!}}\right)^\alpha \int_{x_0}^{x_1}(1+\lambda)^{\mu x t} \, dx$$

$$= \left(\frac{t^m}{(1+\lambda)^{\mu t} - \sum_{h=0}^{m-1}\frac{t^h}{h!}}\right)^\alpha \frac{(1+\lambda)^{\mu x t}}{\log(1+\lambda)^{\mu t}}\Bigg|_{x_0}^{x_1}$$

$$= \sum_{k=0}^\infty (x|1)_k^{(-1)} \frac{t^k}{k!} \left\{\sum_{r=0}^\infty \left(B_{r,\lambda}^{[m-1,\alpha]}(x_1) - B_{r,\lambda}^{[m-1,\alpha]}(x_0)\right)\right\}\frac{t^r}{r!}$$

$$= \sum_{n=0}^\infty \sum_{k=0}^n \binom{n}{k}(x|1)_k^{(-1)} \left(B_{n-k,\lambda}^{[m-1,\alpha]}(x_1) - B_{n-k,\lambda}^{[m-1,\alpha]}(x_0)\right)\frac{t^n}{n!}.$$

Comparing the coefficients of both sides, we get

$$\int_{x_1}^{x_0} B_{n,\lambda}^{[m-1,\alpha]}(x) \, dx = \sum_{k=0}^n \binom{n}{k}(x|1)_k^{(-1)} \left(B_{n-k,\lambda}^{[m-1,\alpha]}(x_1) - B_{n-k,\lambda}^{[m-1,\alpha]}(x_0)\right).$$

5. Addition Theorem of the Argument: For $\alpha, \beta \in C, n \in N$;

$$B_{n,\lambda}^{[m-1,\alpha+\beta]}(x+y) = \sum_{k=0}^n \binom{n}{k} B_{n-k,\lambda}^{[m-1,\alpha]}(x) B_{k,\lambda}^{[m-1,\beta]}(y),$$
$$E_{n,\lambda}^{[m-1,\alpha+\beta]}(x+y) = \sum_{k=0}^n \binom{n}{k} E_{n-k,\lambda}^{[m-1,\alpha]}(x) E_{k,\lambda}^{[m-1,\beta]}(y)$$

and

$$G_{n,\lambda}^{[m-1,\alpha+\beta]}(x+y) = \sum_{k=0}^n \binom{n}{k} G_{n-k,\lambda}^{[m-1,\alpha]}(x) G_{k,\lambda}^{[m-1,\beta]}(y).$$

23

Theorem 2. There is the following relation for the generalized modified degenerate Bernoulli polynomials $B_{n,\lambda}^{[m-1,\alpha]}(x)$ of order α respectively;

$$B_{n,\lambda}^{[m-1,\alpha]}(1) - \sum_{h=0}^{\min(m-1,n)} \binom{n}{h} B_{n-h,\lambda}^{[m-1,\alpha]} = \frac{n!}{(n-m)!} B_{n-m,\lambda}^{[m-1,\alpha-1]}, \tag{2.1}$$

$$E_{n,\lambda}^{[m-1,\alpha]}(1) + \sum_{h=0}^{\min(m-1,n)} \binom{n}{h} E_{n-h,\lambda}^{[m-1,\alpha]} = 2^n E_{n-m,\lambda}^{[m-1,\alpha-1]}, \tag{2.2}$$

$$G_{n,\lambda}^{[m-1,\alpha]}(1) + \sum_{h=0}^{\min(m-1,n)} \binom{n}{h} G_{n-h,\lambda}^{[m-1,\alpha]} = 2^m \frac{n!}{(n-m)!} G_{n-m,\lambda}^{[m-1,\alpha-1]}. \tag{2.3}$$

The proof of this theorem can be easily obtain from (1.14), (1.15) and (1.16) respectively.

Theorem 3. There is the following relation between the generalized modified degenerate Bernoulli polynomials and generalized modified degenerate Euler polynomials

$$B_{n,\lambda}^{[0,\alpha]}\left(\frac{x+y}{2}\right) = 2^{-n} \sum_{k=0}^{n} \binom{n}{k} B_{n,\lambda}^{[0,\alpha]}\left(\frac{x+y}{2}\right) B_{n-k,\lambda}^{[0,\alpha]}(x) E_{k,\lambda}^{[0,\alpha]}(y). \tag{2.4}$$

Proof. From (1.14) and (1.15), we get

$$\sum_{n=0}^{\infty} B_{n,\lambda}^{[0,\alpha]}\left(\frac{x+y}{2}\right)\frac{(2t)^n}{n!} = \left(\frac{2t}{(1+\lambda)^{2\mu t}-1}\right)^{\alpha} (1+\lambda)^{2\mu t\left(\frac{x+y}{2}\right)}$$
$$= \sum_{p=0}^{\infty} B_{p,\lambda}^{[0,\alpha]}(x)\frac{t^p}{p!}\sum_{k=0}^{\infty} E_{k,\lambda}^{[0,\alpha]}(y)\frac{t^k}{k!}.$$

By using Cauchy product and equating the coefficients of $\frac{t^n}{n!}$, we have (2.4).

REFERENCES

[1]. G. Bretti, P. E. Ricci, Multidimensional extensions of the Bernoulli and Appell polynomials, Taiwan J. Math. 8(3) (2014) 415-428 Doi: 10.11650/twjm/1500407662.

[2]. G. Bretti, P. Natalini, P. E. Ricci, Generalization of the Bernoulli and Appell polynomials, Abstract Appl. Anal. 7 (2004) 613-623 Doi: 10.1155/S1085337504306263.

[3]. L. Carlitz, Degenerate Stirling, Bernoulli and Eulerian numbers, Utilas Math. 15 (1979) 51-88.

[4]. D. V. Dolgy, T. Kim, H.-In Known, J. J. Seo, On the modified degenerate Bernoulli polynomials, Advanced Studies in Contemp. 26 (2016) 203-209.

[5]. H.-In. Known, T. Kim, J. J. Seo, Modified degenerate Euler polynomials, Advanced Studies in Contemp. 26 (2016) 203-209.

[6]. T. Kim, D. S. Kim, H.-In Known, Some identities relating to degenerate Bernoulli polynomials, Filomat 30.4 (2016) 909-912 Doi: 10.2298/FIL1604905K.

[7]. B. Kurt, A further generalization of the Bernoulli polynomials and on the 2D-Bernoulli polynomials $B_n^{(2)}(x,y)$, Appl. Math. Sci. 4 47 (2010) 2315-2322.

[8]. B. Kurt, A further generalization of the Euler polynomials and on the 2D-Euler polynomials $E_n^{(2)}(x,y)$, Proc. Jangeon Math. Soc. 15 (2012) 389-394.

[9]. B. Kurt, Some relationships between the generalized Apostol-Bernoulli and Apostol-Euler polynomials, Turkish J. of Analysis and Number Theory 1 1 (2013) 54-58 Doi: 10.12691/tjant-1-1-11.

[10]. V. Kurt, Some symmetry identities for the Apostol-type polynomials related to multiple alternating sums, Advances in Diff. Equa. (2013) 2013.32 Doi: 10.1186/1687-1847-2013-32.

[11]. D. Lim, Some identities of degenerate Genocchi polynomials, Bull. Korean Math. Soc. 53 2 (2016) 569-579 Doi: 10.4134/BKMS.2016.53.2.569.

[12]. H. Lin, W. Wang, Some identities on the Bernoulli, Euler and Genocchi polynomials via power sums and alternate power sums, Discrete Math. 309 (2009) 3346-3363.

[13]. P. Hernandez-Lianos, Y. Quintana, A. Urieles, About extensions of generalized Apostol-type polynomials, Results Math. (2014) Doi:10.1007/s00025-014-0430-2.

[14]. Q.-M. Luo, The multiplication formulas for the Apostol-Bernoulli and Apostol-Euler polynomials of higher order, Integral Trans. Spec. Func. 20 (2009) 373-391 Doi: 10.1080/10652460802564324.

[15]. Q.-M. Luo, H. M. Srivastava, Some generalizations of the Apostol-Genocchi polynomials and the Stirling numbers of the second kind, Appl. Math. Comp. 217 (2011) 5702-5728 Doi: 10.1016/j.amc.2010.12.048.

[16]. Q.-M. Luo, H. M. Srivastava, Some relations between the Apostol-Bernoulli and Apostol-Euler polynomials, Comp. Math. Appl. 51 (2006) 631-642.

[17]. P. Natalini, A. Bernardini, A generalizations of the Bernoulli polynomials, J. Appl. Math. 9 (2003) 155-163 Doi: 10.1155/S1110757X03204101.

[18]. H. M. Srivastava, M. Garg, S. Choudhary, Some new families of generalized Euler and Genocchi polynomials, Taiwan J. Math. Phy. 15 (2010) 283-305 Doi: 10.11650/twjm/1500406175.

[19]. H. M. Srivastava, M. Garg, S. Choudhary, A new generalized Apostol-Bernoulli polynomials, Comp. Math. Appl. 20 (2016) 251-261.

[20]. H. M. Srivastava, J. Choi, Series associated with the zeta and related functions, Kluwer Academic 2001.

[21]. H. M. Srivastava, J. Choi, Zeta and q-zeta functions and associated series and integrals, Elsevier 2011.

Study on Production Decline Model of Dense Reservoir

Heng ZHANG[1*], Xiaodong WU[1], Kuo ZHAO[1], Mengshu Wang[2], Shuai JIANG[1]

[1] *China University of Petroleum(Beijing)/Oil and Natural Gas Engineering Department, Beijing, CHINA*
[2] *Beijing Zhongdu Grovis Logistics Limited Company/Planning Department，Beijing, CHINA*
*zhangheng4212@163.com

ABSTRACT

Analyzing and predicting the production performance of the well is of great significance for the management and reasonable control of oilfield production. The production decline model is a good method for analyzing and predicting reservoir changes in the oilfield. But for the compact reservoir and other unconventional oil and gas reservoirs, the production law of oil well is different from that of the conventional reservoir, and it is difficult to analyze and predict the production dynamic. Based on the MFF model, the production decline model of compact reservoir is established on the basis of the fractured horizontal well in compact reservoir. Using the production data of the horizontal well in the dense oil area of the Lucaogou Formation in Jimsar sag, the application effect of the Arps decreasing model and the new model are compared and evaluated, and the new model type is used to predict the production decline law of the actual well. The research shows that the use of Arps decline model to predict the production dynamic effect of dense oil well is not good. The new model can more accurately reflect the production decline law of compact reservoir oil well and forecast future production.

KEYWORDS - Compact reservoir, Production decline, Prediction model.

1. INTRODUCTION

Analyzing and predicting the production performance of the well is of great significance for the management and reasonable control of oilfield production. The production decline model is a good method for analyzing and predicting reservoir dynamics in the oilfield where production decline is in progress [1]. But for the compact reservoir and other unconventional oil and gas reservoirs, the production law of oil well is different from that of the conventional reservoir, and it is difficult to analyze and predict the production dynamic [2]. At present, Arps decline model (Arps,1945) is the most widely used among a series of mathematical models proposed at home and abroad to describe the law of production dynamics [3] analysis and prediction decline. However, it is generally found that the decline curve obtained by using Arps decline model deviates greatly from the actual production [4]. In recent years, some scholars have proposed a production decline model for analyzing oil well production dynamics for dense reservoirs [5]. Valko et al. (2010) proposed a SEPD model for tight gas and shale gas, Duong (2011) established an empirical model to reflect the production decline based on the linear flow stage in tight gas and shale gas wells, and Hong Yuan et al. (2013) established an MFF model for shale oil.

In this paper, the production decline model of tight reservoir was established based on MFF model for fracturing horizontal wells in tight reservoir, meanwhile considering flow within fractures, and the production decline rule of tight oil production wells in Lucaogou formation in Jimusaer sunken was analyzed and predicted.

2. MODEL ESTABLISHMENT

Considering the flow in the fracture, oil well production can be expressed as follows:

$$q_o = q_{o\max} \times t^y \tag{1}$$

Where, q_o is the monthly production, m^3; q_{omax} is the maximum monthly production, m^3; t is production time, month; y is the correlation coefficient, then

$$y = \frac{\log(q_o / q_{o\max})}{\log(t)} \tag{2}$$

It can be seen that y changes with the production time, which reflects that the reservoir property changes with the production of oil Wells.Through fitting, the calculation formula of y can be obtained:

$$y = \frac{a}{t} + b \tag{3}$$

Where, a and b are coefficients obtained by fitting y (calculated by formula 2) with t.

Thus, the calculation formula of cumulative output can be obtained:

$$N_p = \int_1^t q_{o\max} \cdot t^{\frac{a}{t}+b} dt \tag{4}$$

3.   MODEL VALIDATION

3.1. Classification of Horizontal Wells

Jimusaer sunken Lucaogou group of dense oil currently existing 16 fractured horizontal wells have been put into operation. Production performance of horizontal curve of the 14 production well which production time is longer is analyzed, the results found that horizontal well production performance fluctuation, the output of each well change trend and characteristic difference is obvious, thus the existing horizontal wells are classified.

The production stage with daily oil production more than 20 m^3/d was defined as high production stage; the production stage with daily oil production more than 10 m^3/d and less than 20 m^3/d was defined as middle production stage; and the production stage with daily oil production less than 10 m^3/d was defined as low production stage. The contribution rate of various wells to the accumulated oil production in high production stage, middle production stage and low production stage was calculated. According to the accumulated oil production and contribution rate, the classification method of horizontal wells in Lucaogou formation was determined, and the existing horizontal Wells in Lucaogou formation were divided into three categories:

 I class well: 3 years cumulative oil production is more than 9000t, contribution rate of middle and high production stage is more than 60%；Belong to I class well have JI 172_H, JHW018.

 II class well: 3 years cumulative oil production is more than 5000t and less than 9000t, contribution rate of middle and high production stage is more than 5% and less than 60%；Belong to II class well have JI 32_H, JI 36_H, JHW003, JHW020, JHW017, JI 251_H, JHW001, JHW019, JHW015 and JHW005.

III class well: 3 years cumulative oil production is less than 5000t, contribution rate of middle and high production stage is less than 5%；Belong to III class well have JHW016 and JHW007.

3.2. Production decline analysis

This paper respectively using the new established model and the Arps three regressive model to analyze production decline law of I class well and II class well(a total of 12 horizontal wells) in Lucaogou formation in Jimusaer sunken dense oil region.

JI 172_H was drilled and produced in July 2012, and reached the production peak in December 2012, and then entered the decline stage. Up to December 2017, a total of 61 months of decline period was experienced. Statistics and calculations were made based on monthly production, and the production decline analysis results are shown in the following figures:

27
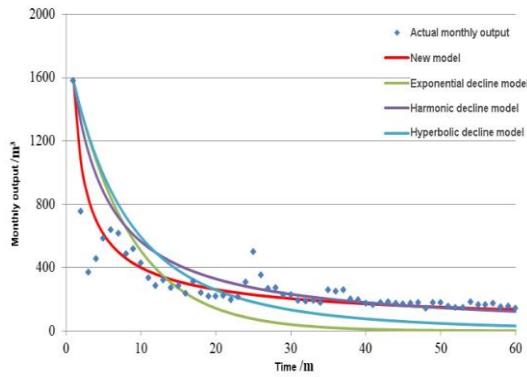
Figure 1 *Production decline analysis of JI 172_H well - monthly oil production curve comparison*
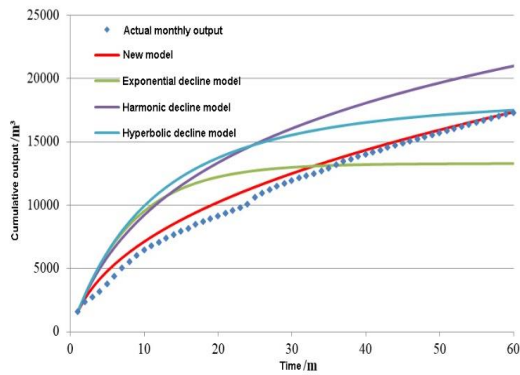
Figure 2 *Production Decline Analysis of JI 172_H well Cumulative Oil Production Curve Comparison*

JHW003 was drilled and produced in October 2013, and reached the production peak in November 2013, and then entered the decline stage. Monthly production was counted and calculated, and the production decline analysis results were shown in the following figures:
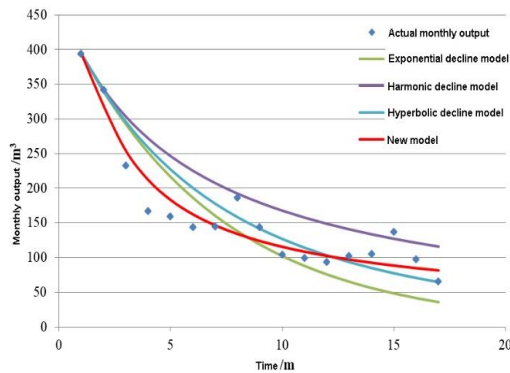
Figure 3 *Production Decline Analysis of JHW003 well - Monthly Oil Production Curve Comparison*

28
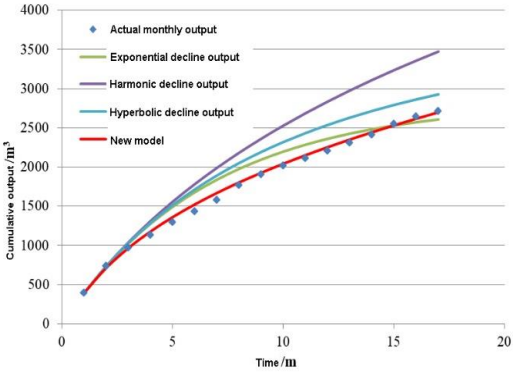
Figure 4 *Production Decline Analysis of JHW003 well - Cumulative Oil Production Curve Comparison*

The production decline analysis errors of 12 horizontal Wells under different decline models are shown in table 1.The results show that: for Ⅰ class wells, monthly output average relative error of exponential decline model, harmonic decline model hyperbolic decline model and new model is respectively: 63.33%, 27.715%, 47.61%, 15.61%, and the average error is respectively: 19.24%, 29.19%, 18.94% and 8.70%; for Ⅱ class well, monthly output average relative error of exponential decline model, harmonic decline model hyperbolic decline model and new model is respectively: 28.54%, 23.80%, 22.28%, 12.11%, and the average error is respectively: 9.02%, 11.66%, 7.76% and 3.76%.It can be seen from the comparison results that output obtained by the three Arps decline models is seriously deviated from the actual production situation.The new model can more accurately reflect the decreasing law of tight oil horizontal wells in Lucaogou formation in Jimusaer sunken and predict the future production.

This model was used to predict and evaluate the production decline of JHW025 tight oil horizontal well in Lucaogou formation in Jimusaer sunken.

JhHW25 well is a new fracturing horizontal well put into production in June 2017. It reached the peak production in September 2017, and then entered the stage of production decline. Using the existing production data of four months of decline, the undetermined coefficients a and b (Figure 4) are obtained by fitting according to formula (3), so as to predict the production decline rule of JHW025 well in the future, as shown in Figure 5.

$y = -1.1736/t - 0.5029$
$R^2 = 0.8366$
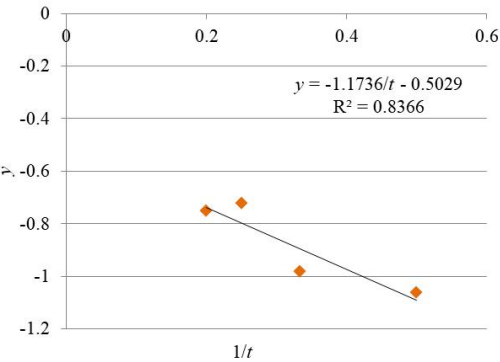
Figure 5 *Determination of the Coefficients a and b*

29
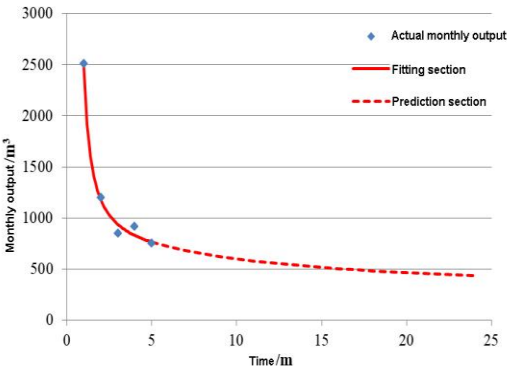
Figure 6 *Production Decline Analysis and Prediction of well JHW025*

Table 1 *Production Decline Analysis Error of 12 Horizontal Wells with Different Decline Models*

Category	Well no,	Error of monthly output（%）				Error of cumulative output（%）			
		Exponential decline	Harmonic decline	Hyperbolic decline	New model	Exponential decline	Harmonic decline	Hyperbolic decline	New model
Ⅰ class well	JHW 018	55.11	37.98	46.23	16.67	19.01	29.19	18.94	8.70
	JI 172_H	73.65	25.75	56.55	14.55	24.23	34.88	31.12	7.33
	average error	63.33	27.72	47.61	15.61	19.24	22.92	20.10	8.02
Ⅱ class well	JHW 001	16.46	17.18	18.41	10.21	5.75	3.32	3.60	2.20
	JHW 003	28.14	37.33	20.69	13.83	7.59	21.33	12.09	2.25
	JHW 005	18.17	35.77	18.45	14.83	4.68	3.74	4.25	5.14
	JHW 015	16.68	17.17	14.00	11.28	13.50	12.97	10.08	6.17
	JHW 017	39.70	38.95	37.49	11.45	15.55	28.79	20.41	3.96
	JHW 019	28.36	28.40	20.09	13.08	9.18	16.20	9.36	5.91
	JHW 020	30.12	16.15	24.24	12.41	7.53	4.23	5.82	3.34
	JI 32_H	34.88	19.35	24.96	12.86	8.62	13.48	7.33	3.30
	JI 251_H	44.09	17.67	28.48	11.70	12.81	8.54	5.78	2.65
	JI 36_H	16.75	25.11	11.12	9.41	3.89	13.22	6.33	2.71
	average error	28.54	23.80	22.28	12.11	9.02	11.66	7.76	3.76

30

4. CONCLUSION

(1) According to fracturing horizontal Wells in tight reservoir, the production decline model of tight reservoir was established based on MFF model, and the production decline law of tight oil horizontal wells in Lucaogou formation in Jimusaer sunken was analyzed and predicted.

(2) The Arps decline model is not good for predicting tight well performance of single stage. The new model takes the changes of reservoir properties with the production of oil wells into account, and can more accurately reflect the production decline law of oil Wells and predict the future production.

REFERENCES

[1]. Sinha S, Kumar R, Vega L, et al. Flow equilibration towards horizontal wells using downhole valves: 68635[R]. Houston: SPE, 2001

[2]. Ouyang L B. Practical consideration of an inflow-control device application for reducing water production: 124154[R]. Edmonton: SPE, 2009

[3]. Al-Khelaiwi F T, Davies D R. Inflow control devices: application and value quantification of a developing technology: 108700[R]. Houston: SPE, 2007

[4]. Coronado M P, Garcia L, Russell R, et al. New inflow control device reduces fluid viscosity sensitivity and maintains erosion resistance: 19811[R]. Houston: SPE, 2009

[5]. O. Jaripatke, D. Dalrymple. Water-Control Management Technologies: A Review of Successful Chemical Technologies in the Last Two Decades: 127806[R]. Edmonton: SPE, 2010

Calculation of Neutron Shielding Properties of Zeolite Concrete

Sameer Alobaidi[1*], Hakan Akyıldırım[1], Kadir Günoğlu[2], İskender Akkurt[1]

[1]*Süleyman Demirel University, Faculty of Science And Arts, Physics Department, Isparta,Turkey*

[2]*Isparta University of Applied Sciences, Technical Vocational School, Isparta, Turkey*

*rasul19847@yahoo.com

ABSTRACT

Neutron radiations of any energy are considered as one of the most difficult type to be shielded since they can penetrate long distances into materials. Therefore, investigating different materials by means of neutron shielding properties is an important objective. In this work, concretes containing zeolite mineral were tested experimentally and by Monte Carlo simulations using FLUKA code. The results form two methods were compared and a good aggreeement was observed.

***KEYWORDS** – Neutron, radiation shielding, zeolite, FLUKA*

1. INTRODUCTION

Concrete is one of the very fundamental materials of constructions utilized in a wide range from regular houses to even facilities those need extra attention for radiation protection, such as hospitals or power reactors. Therefore, it is an important objective to investigate different types of concretes containing various minerals as aggregate in terms of radiation shielding properties. In the present work, concretes with zeolite, which is also mined locally in Turkey, load are tested by means of fast neutron attenuation properties. The concrete types that are the subject of this study were previously studied by Akkurt et al. [1] in terms of gamma ray shielding capabilities.

Neutron is a massy neutral particle that can be a product of several natural and artificial nuclear processes such as radioactive decay of an unstable nucleus, fission and fusion. It is a highly penetrative particle because it is electrically neutral, and causes indirect ionizations in the material. Shielding capability of a material against neutrons is characterized by mainly two cross sections which are generally given in barn units: the macroscopic effective removal cross section of fast neutrons and the macroscopic thermal neutron cross section. Both parameters are highly dependent on the energy of incoming neutrons and the physical properties of the target. The total microscopic cross section (designated by σ_t) gives the probability of the interaction of neutron radiations with the medium traversed. It comprises two terms: the total microscopic scattering cross section (σ_s) and the microscopic absorption cross section (σ_a), as follows.

$$\sigma_t = \sigma_s + \sigma_a \tag{1}$$

In above equation σ_s includes inelastic and elastic scattering, and σ_a includes terms for nuclear fusion, nuclear spallation and neutrons capture. The total microscopic cross section given by Equation 1 is related to the macroscopic cross section (Σ_t, in cm^{-1}) as follows:

$$\Sigma_t = \sum_i N_i (\sigma_t)_i \tag{2}$$

Here, N_i is the number of nuclei per unit volume (in cm^{-3}) and $(\sigma_t)_i$ is the microscopic cross section of the element i. Equation 2 is the mixture rule written for neutron attenuation. When the attenuation is through a pure material, Σ_t simply becomes $N\sigma_t$, where N is the atomic density of that pure material [2, 3].

32

2. MATERIALS AND METHODS

2.1. Concretes

Three types of concretes including 0% (namely NZ0), 10% (namely NZ10) and 30% (namely NZ30) of zeolite mineral were investigated in the study. Detailed information on the other specifications of concretes, such as water to cement ratio, chemical compositions of cement and zeolite mineral and mixing proportions can be found in Ref. [1]. However, we give the chemical compositions of the concretes in weight fraction form in Table 1.

Table 1. Chemical compositions and densities of the concrete samples.

	CaO	MgO	NaO	Fe_2O_3	CO_2	SiO_2	H_2O	Al_2O_3	SO_2	ρ (g/cm³)
NZ0	0.394	0.110	0.004	0.005	0.315	0.127	0.074	0.010	0.005	2.476
NZ10	0.419	0.123	0.004	0.006	0.314	0.203	0.075	0.020	0.005	2.445
NZ30	0.343	0.095	0.003	0.008	0.253	0.247	0.078	0.040	0.005	2.154

2.2. Experimental study

Measurements were performed using the opportunities of the Gamma Spectroscopy Laboratuary in the Faculty of Science Arts – Süleyman Demirel University. Total macroscopic cross section (Σ_t) measurements were performed in accordance with the transmission technique. In this technique the exponential law is valid for neutrons as it is in photon attenuation. When incoming neutrons with intensity I_o interacts with the material of thickness *x,* some portion of the initial neutrons is attenuated by the material. If the attenuated intensity is called *I*, then the total macroscopic cross section can be calculated using the below exponential relation.

$$\Sigma_t = \frac{1}{x} ln \left(\frac{I_o}{I} \right) \tag{3}$$

Another significant parameter investigated in the present work is the mean free path (*mfp*, in cm) which is defined as the average distance that a neutron travels between two successive interactions. It is the inverse of the total macroscopic cross section as follows.

$$mfp = \frac{1}{\Sigma_t} \tag{4}$$

In the experiments a Californium252 spontenious source which emits 2.14 MeV fast neutrons was used. The detection system was a RadEye GN+ gamma – neutron detector provided from Thermo Scientific Company. Neutron cont-rate and neutron efficiency of the detector is 0, 1 to 1000 cps and 4.3 cps/20000 n/s (for Californium252), respectively. *I* and I_o intensities were determined in terms of neutron counts with and without concrete slabs between the source and the detector. Using Equation 3 and 4 total macroscopic cross sections and mean free path values were calculated. Arrangement of experimental study is as drawn in Figure 1.
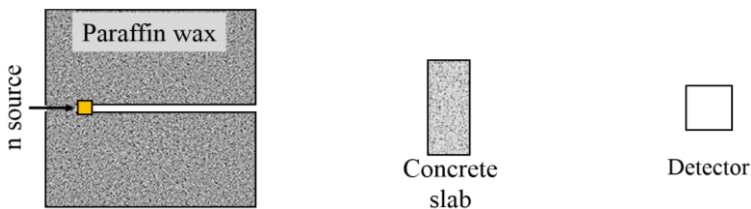
Figure 1. Sketch of the experimental arrangement.

33

2.3. Simulation study

Macroscopic cross sections of the zeolite concretes were estimated using FLUKA Monte Carlo code.

It is one of the well-known simulation codes in nuclear and high energy physics. It is a multipurpose code which can successfully transport about 60 particles ranging from elementary particles such as photons and neutrons to various heavy ions. So, it has a wide variety of application areas for which calorimetry, dosimetry, radiotherapy, accelerator physics and radiation shielding can be given as example [4, 5]. The simulations were performed with the version 2011.2c of FLUKA code on a UNIX operating system. Input files have been prepared to run simulations. FLUKA provides many options for simulations such as beam properties, geometry, material definition, physical settings, score options and primary radiation weight. Experimental configuration given in Figure 1 was used in simulations. Each option is represented by an input card which should be placed in a sequential order. 10^6 primary particles – which were neutrons with 2.14 MeV energy – were used to achieve a reasonable statistics and the code was run for 5 cycles in simulations. Results were read as primary/particle from USRBDX detector output files. Then Σ_t and *mfp* values were calculated by substituting *I* and I_o values into Equation 3.
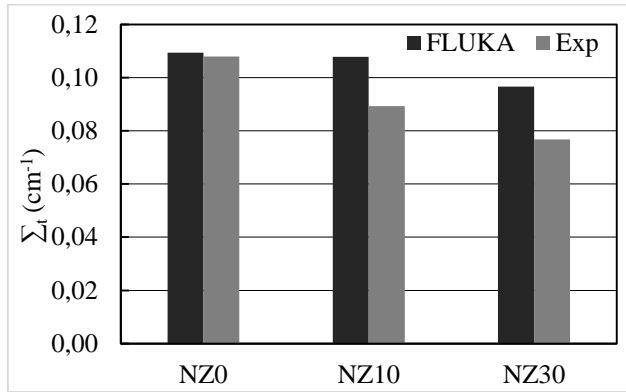
Figure 2. *Total macroscobic cross sections of zeolite concretes by experiments and simulaitons.*
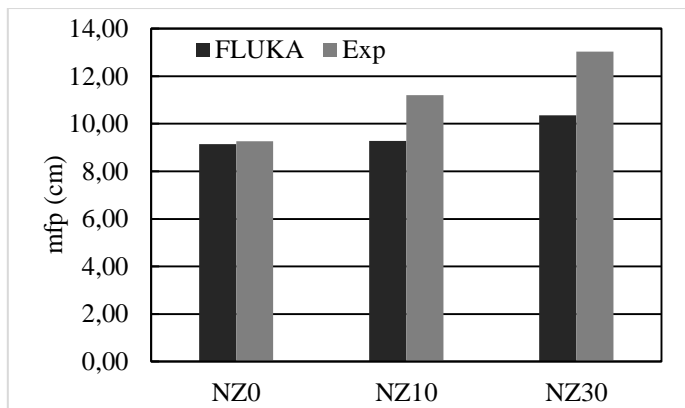
Figure 3. *Mean free path values of zeolite concretes by experiments and simulaitons.*

3.   RESULTS AND DISCUSSION

Experimental and simulation values of fast neutron total macroscopic cross sections and mean free paths are plotted in Figure 2 and 3, respectively. Maximum relative difference between experimental and simulation results is determined to be ~25% for NZ30 concrete. In general, it can be sais that results from the two methods are in good agreement. As can be seen from Figure 2 and 3, NZ0 is is the most, NZ30 is the least effective concrete type against neutrons of 2.14 MeV. Figure 3 shows that neutrons of this energy can penetrate more from NZ0 to NZ30. The most probable interaction type for fast neutrons is scattering with low - and medium - weight nuclei, such as Hydrogen. Water content of all concretes are almost the same (Table 1). So, the variation in total macroscopic cross sections can be ascribed to density effect. Because, greater density will increase the interaction probability of neutrons with concrete material. This can also explain the differences between NZ0 and NZ10 concretes with NZ30 concrete.

4. CONCLUSION

We conclude that increasing amount of zeolite mineral in the concrete decreases the shielding competence of the related concrete against fast neutrons of 2.14 MeV energy. This is most probably due the negative effect of zeolite mineral on concrete density. Also, it can be concluded from the results that FLUKA Monte Carlo code is an effective to be utilized in such shielding studies.

REFERENCES

[1] I. Akkurt et al., "Radiation shielding of concrete containing zeolite," Radiat. Meas., vol. 45, no. 7, pp. 827–830, 2010.
[2] T. Jaeger, Principles of radiation protection engineering. New York: McGraw-Hill Book Company, 1965.
[3] M. F. Kaplan, Concrete radiation shielding. New York: Wiley, 1989.
[4] A. Ferrari et al., "FLUKA: a multi-particle transport code," Cern. (2005), INFN/TC_05/11, SLAC-R-773, 2005.
[5] T. T. Böhlen et al., "The FLUKA Code: Developments and Challenges for High Energy and Medical Applications," Nucl. Data Sheets, vol. 120, pp. 211–214, 2014.

A Study of Scaling 3D Experiment on Cold Recovery after Steam Stimulation in Heavy Oil Reservoirs with Edge Water

Yanwei Wang[1*], Huiqing Liu[1], Zhangxin Chen[2], Xiaohu Dong[1]

[1] *China University of Petroleum, Beijing/Department of Petroleum Engineering, Beijing, China*

[2] *University of Calgary/Department of Petroleum and Chemical Engineering, Calgary, Canada*

* wangyanweicup@126.com

ABSTRACT

In the process of conventional thermal recovery in heavy oil reservoirs accompanied by edge water, the intrusion of edge water seriously affects the development effect, resulting in a large number of unutilized reserves. In this paper, parameters of KD521 block, a heavy oil reservoir with active edge water, are transformed into physical model parameters with similarity criteria firstly, and the process of cold recovery after steam stimulation is simulated by using a high temperature and high pressure three-dimensional experimental apparatus. Then, numerical models are established based on the physical simulation and history matching is conducted according to the production data. The water invasion rule and residual oil distribution and the influencing factors of chemical cold recovery were obtained. The results show that invasion of edge water causes the shape of the steam chamber formed by the steam to be asymmetric under the action of thermodynamics, and the development of the steam chamber, in turn, affects the invasion of edge water. By rationally utilizing the edge water energy and the new viscosity reducer to reduce the viscosity of heavy oil, heavy oil can be produced through the edge water pressure. The optimal viscosity reducer injection timing in the first-line and second-line wells is 80-85% and 85-90% water cut, respectively. The optimal injection rate is 10 mL/min, the production injection ratio is 1.2 and the injection mode is the long slug. The application of this technology on the field has achieved satisfactory oil recovery, providing an alternative for enhancing oil recovery in similar reservoirs.

KEYWORDS - *Heavy oil, Edge water, Steam stimulation, Cold recovery, Physical simulation.*

1. INTRODUCTION

With the gradual exhaustion of conventional oil, the development and utilization of heavy oil has attracted extensive attention, among which, heavy oil reservoirs with edge-water account for a large proportion of heavy oil resources [1,2]. Steam stimulation and steam flooding are generally used to develop such reservoirs, but the intrusion of the edge-water causes the steam thermal efficiency to drop rapidly, the water cut of the production well rises rapidly, and the development effect becomes worse [3]. The pressure of the formation at the end of steam stimulation is affected by active edge-water intrusion, which makes it difficult for the steam at the bottom of the well to reach the required dryness. At the same time, the oil wells after multiple rounds of steam stimulation have high water cut and small heating radius, which makes it difficult to form effective heat communication between wells, and the conditions for steam flooding are not achieved, so the development effect of steam flooding is also not satisfactory [4,5]. Currently, chemical flooding can be considered as a suitable enhanced oil recovery method for some heavy oil reservoirs where thermal and solvent-based methods face numerous technical, economic and environmental problems or poor development results [6]. The conversion of steam Stimulation to chemical flooding has been considered as one of the most promising methods to promote the development of heavy oil reservoirs with edge water.

2. EXPERIMENTAL EQUIPMENT AND PROCEDURE

2.1. Materials

The formation water is simulated by laboratory water with the same mineral composition. The density of the simulated water is 1.037 g/cm^3. The novel viscosity reducer, developed by Research Institute of Petroleum Exploration and Development, can achieve the high-efficiency viscosity reducing of heavy oil. The oil sample for laboratory experiments, obtained from KD521 block of Shengli Oilfield, has a viscosity of 8571 mPa·s at 50 °C and a density of 0.968 g/cm^3 at 25 °C.

2.2. Experimental Setup

The schematic of heavy oil reservoir with edge water simulation experiment is illustrated in Figure 1. The experimental device is composed of high temperature and high pressure three-dimensional physical model, monitoring system, edge water energy simulation system, data acquisition system and fluid injection and acquisition system.
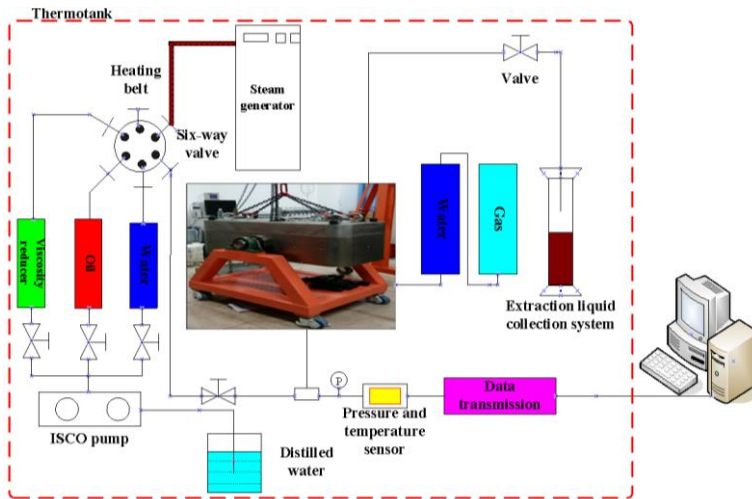
Figure 2. *Schematic diagram of three-dimensional physical simulation experiment.*

3. RESULTS AND DISCUSSION

3.1. Temperature profile analysis

The development characteristics of the experimental temperature profile are shown in Figure 2. The initial temperature field is not affected by the edge water and presents a relatively symmetrical shape. With the continuous injection of steam, the heating range of the reservoir around the well expands, the temperature gradually increases, and the flow capacity of crude oil around the production well increases. However, the edge water gradually invaded the production well, and the steam injection process was affected by the edge water, and the scope of steam heating was reduced. From the perspective of temperature profile, the vertical direction of the sag was the direction of edge water intrusion, and the position with a large temperature gradient around the well was the high water cut area.

37
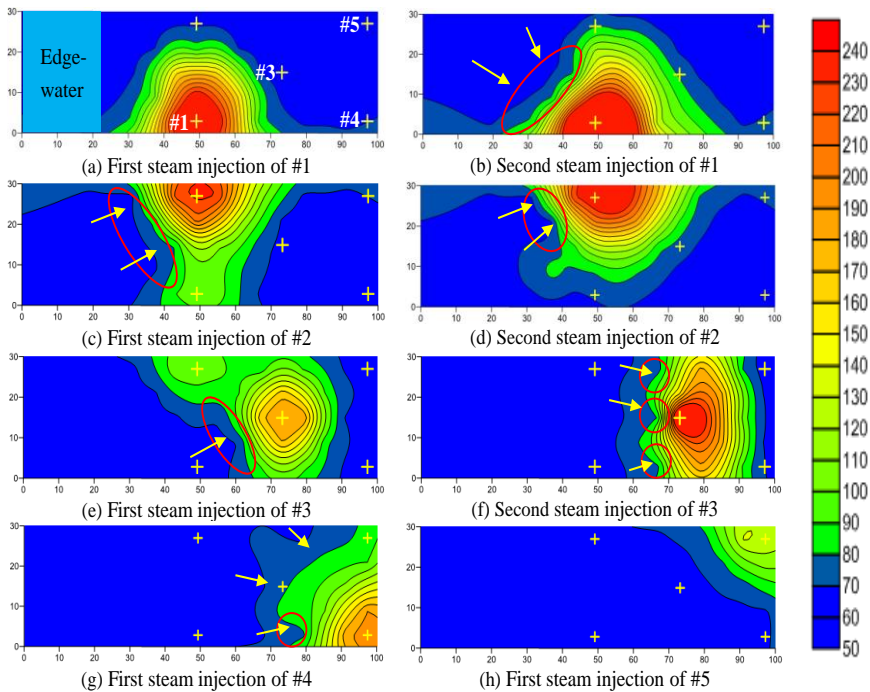
Figure 2. *Temperature profile at the end of steam injection (The arrow represents the main intrusion direction of edge-water, the circle represents the area with more edge-water).*

3.2. Residual oil analysis

Displacement of oil layer at different stages is shown in Figure 3. When the physical models were dismantled, it was found that the color of the oil sands that the steam had driven through the area became lighter, while the color of the oil sands that the viscosity reducer had swept through the area was grayish white, showing that the residual oil saturation after viscosity reducer injection is low.
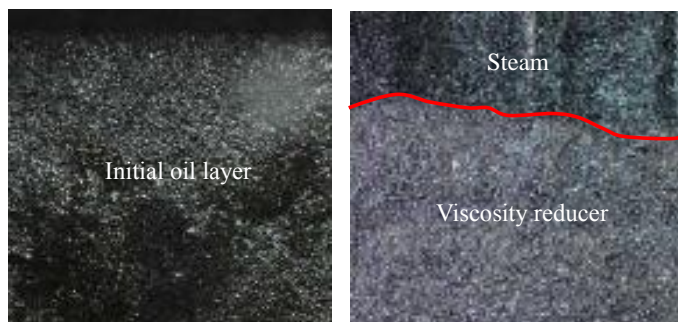
Figure 3. *Displacement of oil layer at different stages.*

3.3. Numerical simulation analysis

Figure 4 displays that the optimal viscosity reducer injection timing of the first-line and second-line wells is 80-85% and 85-90% water cut, respectively. The optimal injection rate is 10 mL/min, production injection ratio is 1.2, the water multiple is 8-10, and the injection mode is long slug.

38
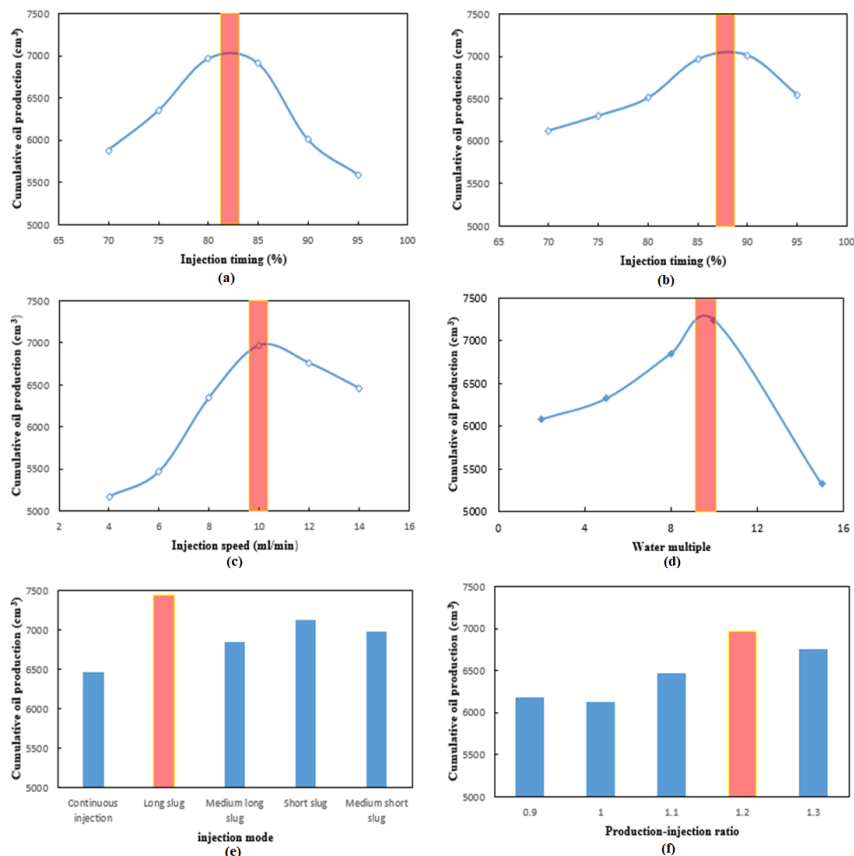
Figure 4. *Cumulative oil production under different parameters.*

4. CONCLUSION

1. Due to the influence of edge-water intrusion, the heating range of the oil layer by steam is asymmetric, and it is obviously shrinking. The heating range of the oil layer and the edge-water intrusion mutually influence and restrict each other.

2. The viscosity reducer plays the role of emulsification, viscosity reduction and slowing down edge-water intrusion. Combined with the law of water intrusion and reasonable utilization of water energy, it can achieve a better development effect.

REFERENCES

[1]. Dong X., Liu H., Chen Z., Wu K., Lu N., Zhang Q. Enhanced oil recovery techniques for heavy oil and oilsands reservoirs after steam injection, Applied Energy 239 (2019) 1190-1211. *DOI: 10.1016/j.apenergy.2019.01.244*

[2]. Mingda Dong, Xiang'an Yue. Effect of Surfactant Emulsification on High Water-cut Reservoir in Shengli Oilfield. International Conference on Computational and Experimental Science and Engineering **(ICCESEN 2018),** 12-16 October, 2018 Antalya-Turkey

[3]. Li X., Shi L., Li H., Liu, P., Luo, J., Yuan, Z. Experimental study on viscosity reducers for SAGD in developing extra-heavy oil reservoirs. Journal of Petroleum Science and Engineering, 166 (2018) 25-32. *DOI:10.1016/j.petrol.2018.03.022*

[4]. Pin Jia, Linsong Cheng, Yongchao Xue, Deqiang Wang and Suran Wang. Laboratory Investigation of High-speed and High-efficiency Development Mechanism of Sandstone

Reservoir. International Conference on Computational and Experimental Science and Engineering (ICCESEN 2018), 12-16 October, 2018 Antalya-Turkey

[5]. Wu Z., Liu H., Wang X., Zhang Z. Emulsification and improved oil recovery with viscosity reducer during steam injection process for heavy oil. Journal of Industrial and Engineering Chemistry, 61 (2018) 348-355. *DOI: 10.1016/j.jiec.2017.12.033*

[6]. Dansen Shang, Jirui Hou. Effect of Descending Viscosity Injection Pattern for Alkali-surfactant-polymer (ASP) Flooding on Enhanced oil Recovery. International Conference on Computational and Experimental Science and Engineering (ICCESEN 2018), 12-16 October, 2018 Antalya-Turkey

A New Coupling Model between Reservoir and Horizontal Well with ICDs

Gaoqiang Ma[*], Xiaodong Wu and Guoqing Han

China University of Petroleum-Beijing / Oil and Natural Gas Engineering Department, Beijing, China
*1240837759@qq.com

ABSTRACT

The Horizontal well technology has developed into an effective method for oil field to create huge economic benefits. For the development of reservoirs with edge-bottom water or water injection, water breakthrough in well is an inevitable problem in the middle and late stages of reservoirs development. Due to the uneven inflow profile of horizontal well, the process of water breakthrough is aggravated. It is a difficult problem to control early water breakthrough while taking advantage of horizontal well. Inflow Control Devices (ICDs) has been designed in response to early water breakthrough for horizontal well. A new method to solve the coupling flow between reservoir and horizontal well with ICDs was presented in this paper. The coupling process is transformed into interaction of different flow sections with nodal system analysis. Based on flow node unit of ICDs, the new coupling model is established. It can clearly depict the inflow profile of horizontal well with ICDs, which is conducive to evaluating the effect of water control by throttling and optimizing ICDs completion parameters. It plays a theoretical role for ICDs in piratical engineering applications.

KEYWORDS – *Horizontal well, The coupling model, ICDs, Water control, Nodal system analysis.*

1. INTRODUCTION

The bottom-water breakthrough has become a problem, which decreased the oil well production and reservoir ultimate recovery, and also increased the cost of water treatment and the risk of equipment corrosion at the same time.

As early as the 1980s, many scholars have carried on analysis of horizontal well productivity from an analytical perspective and gradually modified the analytic method. Dikken [1] has established the first semi-analytical coupling model between reservoir and horizontal well for calculating productivity, accounting for the influence of variable mass flow on coupling process in the horizontal wellbore. Ouyang [2][3] studied the flow rule of single-phase and multiphase in horizontal wellbore and improved the pressure loss model. The influence of wall friction, fluid velocity, wall inflow and outflow on pressure loss was considered in the coupling model. Luo [4] established a semi-analytical model to calculate the productivity index of a horizontal well with pressure loss along the wellbore. Vicente et.al [5] developed a fully implicit, three-dimensional simulator to simulate the transient pressure and flow rate behaviour of both the reservoir and the horizontal wellbore by numerical simulation method. Gui [6], Akim et al. [7], and Carvajal [8] et al. studied the coupling problem on the development of unconventional reservoirs by numerical simulation method. Wang [9] has studied the effects of capillarity and geomechanics on water loss in fracture-matrix system, and simulated multiphase flow and fluid distribution during shut-in and flow-back. Most of them focused on the description of reservoir flow characteristics without accounting for the influence of completion measures, wall fluid inflow and outflow on pressure loss in horizontal well.

Based on the flowing nodes unit, a flowing nodes network with ICDs is constructed. A new coupling model is established, which can more accurately and fast simulate the coupling process, evaluate the effect of water control and optimize ICD parameters.

2.   MATHEMATICAL MODEL FOR THE DYNAMIC COUPLING PROcESS

2.1. The Coupling Model

Under the action of coupling, it is necessary to study the influence of seepage in reservoir and variable mass pipe flow in the horizontal well on the entire production system. The node analysis method is adopted in this paper to discretize the entire system. As shown in Figure. 1, the flowing nodes unit of ICDs, recorded as the i-th flow nodes unit, sorted from left to right. The subscript r indicates the reservoir nodes, the subscript c indicates the completion nodes, the subscript t indicates the tubing nodes.
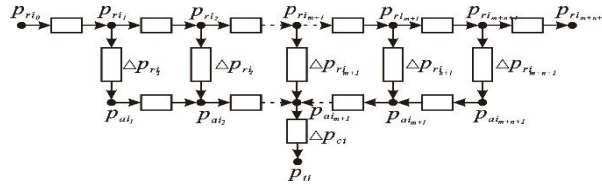
Figure 1. *Flowing nodes unit of ICDs.*

The nonlinear equations of flowing nodes unit are listed as follows:

$$F(k) = \begin{cases} \Delta p_{ri_k} + \sum_{j=k}^{m} \Delta p_{ai_j} + \Delta p_{ci} + p_{ti} - p_{ri_k} = 0, \ k = 1,2,\cdots,m \\ \Delta p_{ri_k} + \Delta p_{ci} + p_{ti} - p_{ri_k} = 0, \ k = m+1 \\ \Delta p_{ri_k} + \sum_{j=m+1}^{k-1} \Delta p_{ai_j} + \Delta p_{ci} + p_{ti} - p_{ri_k} = 0, \ k = m+2,\cdots,m+n+1 \end{cases} \quad (1)$$

Line source model have been used to evaluate pressure loss in the reservoir. The superposition principle and the Duhamel's principle have been used to deal with effects of internal and external boundaries on the model. Then pressure loss at any position (x, y, z) in reservoir with a horizontal wellbore at time t is as follow:

$$\sum_{j=1}^{N} Q_j^k A_{ij}(\Delta t) = \Delta p_r(t^k) - \sum_{m=1}^{k-1} \sum_{j=1}^{N} Q_j(t^m) \left[A_{ij}(k-m+1)\Delta t - A_{ij}(k-m)\Delta t \right] \quad (2)$$

$$A_{ij}(t) = \frac{1}{\emptyset C_t} \frac{1}{abhL} \int_0^t \int_{y_j}^{y_{j+1}} S_1(x_0, x_0, t) S_2(y_i, y, t) S_3(z_0, z_0, t) dy \, d\tau \quad (3)$$

Where, Q represents flowrate, S_1, S_2, and S_3 represents the Green function respectively.
Pressure loss of wellbore has been used to calculate the pressure loss of tubing by Eq. 4, the detail description of pressure loss model can be found in Ouyang [5][6].

$$\frac{dp_t}{dy} = -\frac{2f\rho U^2}{D} - \frac{2\rho}{A_t} q_{in} U \quad (4)$$

Where, A_t represents the cross-section area of tubing, D represents the inner diameter of tubing, f represents the friction factor, q_{in} represents the wall inflow rate per length, U represents the local velocity and ρ represents the fluid density.
The pressure loss of orifice/nozzle-based ICD is calculated by [10].

$$\Delta p_c = \frac{C_u \rho Q^2}{C_d^2 D_{ori}^4} \quad (5)$$

42

Where, C_u represents unit conversion factor, represents discharge coefficient for ICDs, and D_{ori} represents the inner diameter of orifice.

2.2. Solution of the Coupling Model

The coupling process between reservoir and horizontal well is a typical "grey-box" problem. The coupling model established above is exactly based on the flow law of the coupling process, and it is the coupling relationship among the flow variables at different time. Substituting the pressure loss and the boundary conditions, the multivariate function *F* becomes a unary function only with the variable q_{aa} and q_{at}, which greatly simplifies the problem. The mathematical relationship is as follows:

$$F(\Delta p_r, \Delta p_a, \Delta p_c, \Delta p_t, p_r, p_t) = 0 \xrightarrow{variables\ substitution} F(q_{aa}(t), q_{at}(t)) = 0 \qquad (6)$$

Where, q_{aa} represents flowrate form, and q_{at} represents flowrate from annulus to tubing. The Newton-Raphson method is adopted to solve the nonlinear equations in this paper. Set the time interval and loop in turn to get the solution of the coupling model at different times.

3. CASE STUDY

The proposed case studies had been developed to display the application of the new coupling model in practice. A case has been displayed here. A horizontal well with 500m length is centred in a boxed reservoir is used for the example. And the length, width and thickness of the boxed reservoir are 1500m, 1500m, and 30m respectively. Permeability in the three directions is 200mD, 200mD and 100mD. Specific well completion parameters are listed in Table.1.

Table 1. *This is the Style for Table Captions.*

Header	Value	Unit
Fluid density	961	kg/m^3
Fluid viscosity	1.0	cp
Compressibility	1.45×10^{-2}	MPa^{-1}
Well production	80	m^3/d
Inner diameter of tubing	0.1006	m
Outer diameter of tubing	0.114	m
Inner diameter of casing	0.127	m
Position of packer (start, end)	(100, 400)	m
Number of ICDs	15, 10, 5	1
Inner diameter of orifice	0.0508	m
Opening number of ICDs	5	1

Fig.2 display inflow rate distribution of the case at different times. As shown in the Fig.5, the inflow profile presents strong asymmetry due to mass flow in the tubing. With continuous production, the pressure wave propagates to the boundary. the influence of the boundary is gradually enhanced and plays a leading role and the inflow profile tends to be uneven over time.

1. CONCLUSION

The coupling problem is transformed into the interaction relationship between different flow sections by using node discretization. According to the flow characteristics of ICDs, the corresponding flowing nodes unit and network is extracted. And the new coupling model is established based on it.

43
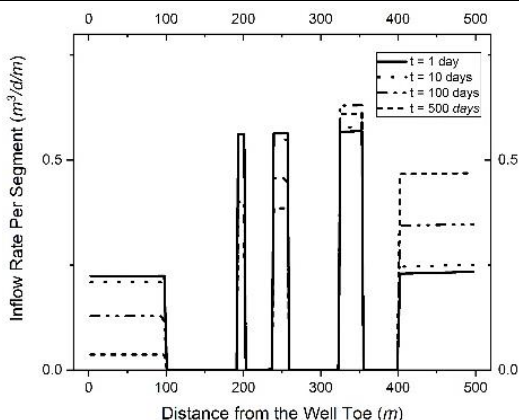
Figure 2. *Inflow rate distribution of the case at different times.*

Three cases of different ICDs completion types are carried out. The inflow profile changes little over time without packers. Conversely, the inflow profile becomes more uneven over time. Therefore, ICD parameters need to be pre-set on the ground. The new coupling model can provide theoretical support for further ICDs parameters optimization.

REFERENCES

[1]. Dikken, B. J. Pressure Drop in Horizontal Wells and Its Effect on Production Performance. Society of Petroleum Engineers, 1990. DOI:10.2118/19824-PA

[2]. Ouyang, L.-B. Single Phase and Multiphase Fluid Flow in Horizontal Well. PhD thesis, Stanford University, 1998.

[3]. Ouyang, L.-B., & Aziz, K. A Mechanistic Model for Gas-Liquid Flow in Pipes with Radial Influx or Outflux. Society of Petroleum Engineers, 1999. DOI:10.2118/56525-MS

[4]. Luo, W., Tang, C., and Feng, Y. A Semianalytical Model for Horizontal-Well Productivity with Pressure Drop Along the Wellbore. Society of Petroleum Engineers, 2018. DOI:10.2118/189973-PA

[5]. Vicente, R., Sarica, C., & Ertekin, T. Numerical Model Coupling Reservoir and Horizontal Well-Flow Dynamics: Transient Behaviour of Single-Phase Liquid and Gas Flow. Society of Petroleum Engineers, 2002. DOI:10.2118/77096-PA

[6]. Oliveira, R. 2011. Study of the Horizontal Wellbore and Reservoir Coupling. Society of Petroleum Engineers. DOI:10.2118/152372-STU

[7]. Gui, P., Cunha, L. B., and Cunha, J. C. S. A Numerical Two-Phase Flow Model Coupling Reservoir and Multi-Segment Horizontal Well. Society of Petroleum Engineers, 2007. DOI:10.2118/107989-MS

[8]. Carvajal, G. A., Saldierna, N., Querales, M., Thornton, K., & Loaiza, J. Coupling Reservoir and Well Completion Simulators for Intelligent Multi-Lateral Wells: Part 1. Society of Petroleum Engineers, 2013. DOI:10.2118/164815-MS

[9]. Wang, M., and Leung, J. Y. Numerical Investigation of Coupling Multiphase Flow and Geomechanically Effects on Water Loss During Hydraulic Fracturing Flow-Back Operation. Unconventional Resources Technology Conference, 2015. DOI:10.15530/URTEC-2015-2154838

[10]. Schlumberger. Eclipse User Manual. 2011.

Investigation on the Effects of Lean Zones on SAGD Performance in Oil Sands Reservoirs

Qichen Zhang, Huiqing Liu*, **Yisheng Liu, Yanwei Wang, Xiaohu Dong and Jiawei Gao**
China University of Petroleum, State Key Laboratory of Petroleum Resources and Prospecting, Beijing, China
*liuhq110@126.com

ABSTRACT

Steam-Assisted Gravity Drainage (SAGD) technique has been successfully applied to unlock the oil sands resources. However, the performance of SAGD is very sensitive to the geological condition such as lean zones, which greatly affect the steam chamber growth and oil production rate. In this study, the impact of lean zones in oil sands on SAGD performance is revealed by using physical and numerical simulation. Firstly, the operation and reservoir parameters were converted from field-scale to lab-scale based on the similarity criteria, and then three-dimensional physical simulation was conducted. Through analyzing the experiment data, the effects of lean zones on steam chamber growth and production performance were studied. Then, a history match was conducted based on the experimental data. Finally, the influences of lean zones parameters such as thickness of lean zones on SAGD performance were further analyzed. The physical results show that lean zones will accelerate the extension of steam chamber to both sides of the reservoir along the bottom of lean zones, accompanied by a stable and low oil rate. After steam breaks through the lean zones and reaches the top-layer, the oil rate rises rapidly. The water zone has a great impact on peak oil rate and plateau time. The numerical results show that the SAGD performance will be greatly affected by the thickness of lean zones and the distance from lean zones to injector mainly affects the shape of steam chamber and the increasing rate of oil recovery. The thicker the water zone, the lower the oil rate and ultimate oil recovery is, which causes lower heat efficiency during SAGD process.

KEYWORDS - *Steam-Assisted gravity drainage (SAGD), Lean zones, 3D physical experiment, Oil sands reservoirs.*

1. INTRODUCTION

The SAGD technology has been successfully applied to recover oil sands for decades [1-4]. However, this advantageous technology is being challenged facing to the complexity of reservoir heterogeneity such as zones with high water saturations. To understand the fluid flow behaviors and the heat loss to reservoirs with water zones, some studies have been conducted by experimental and numerical simulation. A detailed thermal reservoir numerical model is proposed by Fairbridge. J. K et al. [5] to study the performance of high-water saturation intervals during the SAGD process. In addition to, Xu et al. [6] established a simulation model with periodic lean zones for analyzing the influences of water intervals on steam chamber development and oil production. But these studies based on an ideal numerical simulation. The influences of lean zones on steam chamber development and oil production are not clearly understood. Therefore, in this paper, a 3D physical simulation is designed for investigating the effects of lean zones during SAGD process. Then, a lab-scale numerical model was established for analyzing the influence mechanism under different experimental parameters. Furthermore, the history matching of experimental results was conducted to validate the numerical model. Finally, the sensitivity analysis was performed and the impact mechanism of lean zones on SAGD performance were analyzed in detail.

45

2. EXPERIMENTAL AND NUMERICAL SIMULATION

2.1. Experiment design and results

Considering of the lab condition, the field-scale reservoir parameters was converted into the lab-scale based on the similarity criterion. The reservoir parameters were collected from the Long Lake project. Then a three-dimensional physical model was used to conduct the physical simulation, as shown in Fig. 1(a). The distribution of water zone was designed (Fig. 1(b)) and the apparatus for this experiment can be seen in Fig.1(c).

(a)   *(b)*   *(c)*
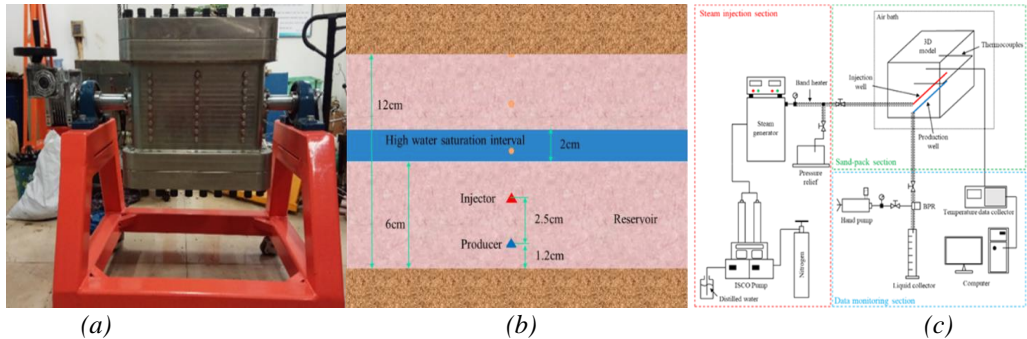
Figure 1. *Experiment design. (a) 3D physical model. (b) Schematic map of lean zone in oil sands. (c) Schematic of the experimental apparatus.*

2.2. Numerical model

The simulator used in this paper was the CMG-STARS. In order to simulate the real condition of experiment, the numerical model was built based on the lab-scale experiment. The grid number of the model was set at 25×25×29. The grid block size of reservoir part is 1.5cm×1.5cm×0.5cm.

As can be seen from Fig. 2, the comparison of the production performance for two designed experiments. The oil rate is lower and the water cut is obviously higher due to the impact of lean zone. Besides, the water zone has a large influence on the performance of oil recovery and instantaneous steam oil ratio (iSOR). The ultimate oil recovery is much lower compared with traditional SAGD. The iSOR increases rapidly at the early SAGD process keeps stable at a high level, which means the heat efficient is lower when the lean zone exists.

The Fig. 3 illustrates the profile of temperature distribution. It can be seen that the high water saturation zone has a great effect on development of steam chamber, especially during the early SAGD process.

(a)   *(b)*
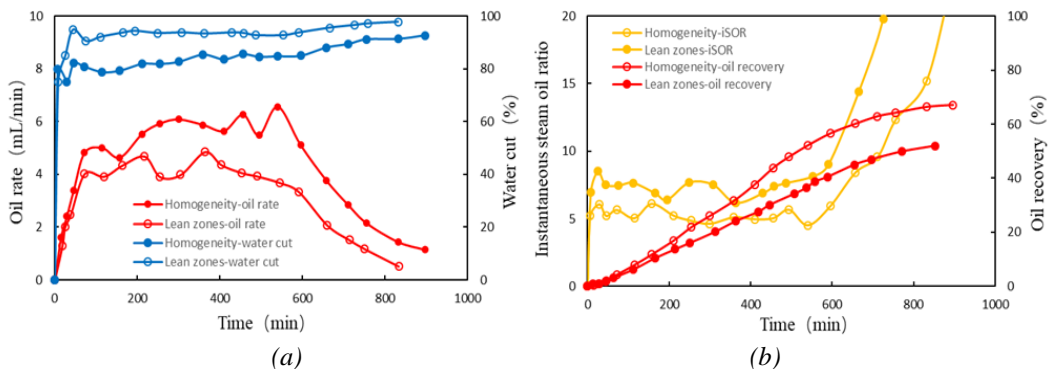
Figure 2. *Comparison of production performance between two experiments. (a) Oil rate and water cut curves. (b) Instantaneous steam oil ratio and oil recovery curves.*

46
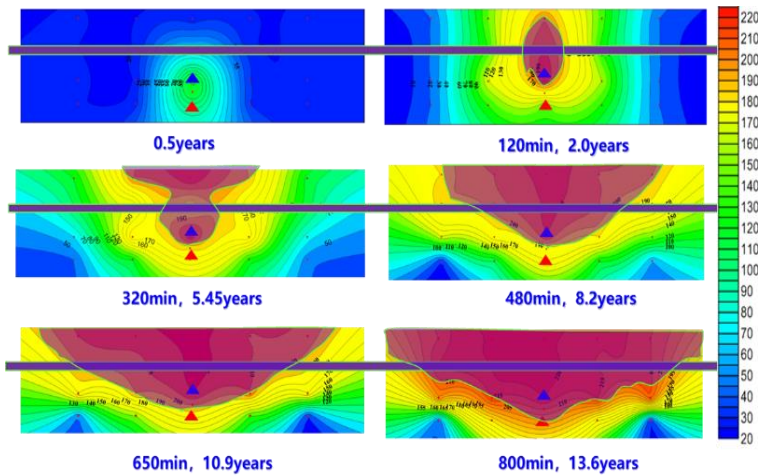
Figure 3. *Temperature profile for different times.*

2.3. History matching

Fig. 4 shows the comparisons of the experimental and numerical simulation results. Fig. 4(a) presents the oil rate and water cut and Fig. 4(b) shows the cumulative oil production. It can be seen that the numerical simulation results can match the experimental results well. Therefore, the numerical model is reliable for further study.

(a)   *(b)*
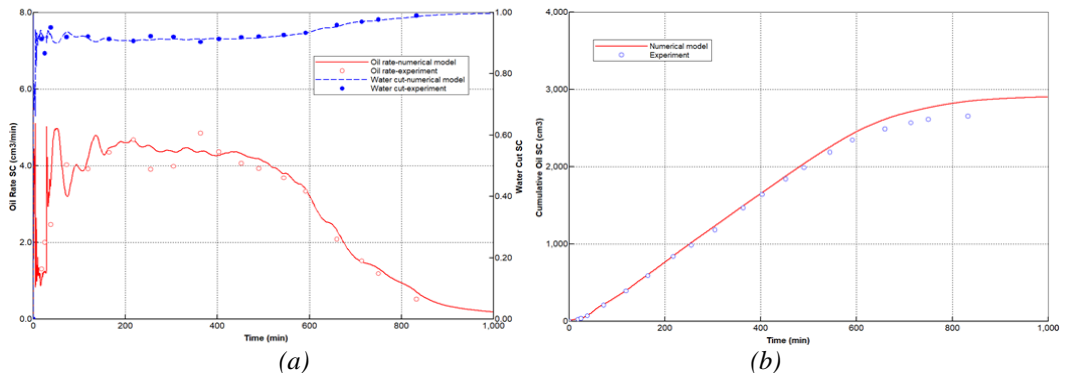
Figure 4. *History match. (a) Oil rate and water cut curves. (b) Cumulative oil production curves.*

2.4. Sensitivity analysis

Fig. 5(a) shows the oil rate curves for each simulation case. It can be seen that oil rate decreases with the increase of the thickness of lean zone and the thicker thickness of the lean zone, the greater the influence on oil rate. Besides, the first peak of oil production is lower when the thickness of high water saturation zone is thicker.

Fig. 5(b) shows that the comparison of oil recovery for different models. It can be seen that the oil recovery performance is obviously worse due to the existence of the lean zone. Furthermore, the thicker the lean zone, the lower the ultimate oil recovery. However, the impact of lean zone on oil recovery during early SAGD process is not obvious, when the thickness of lean zone is lower.

47

(a)   *(b)*
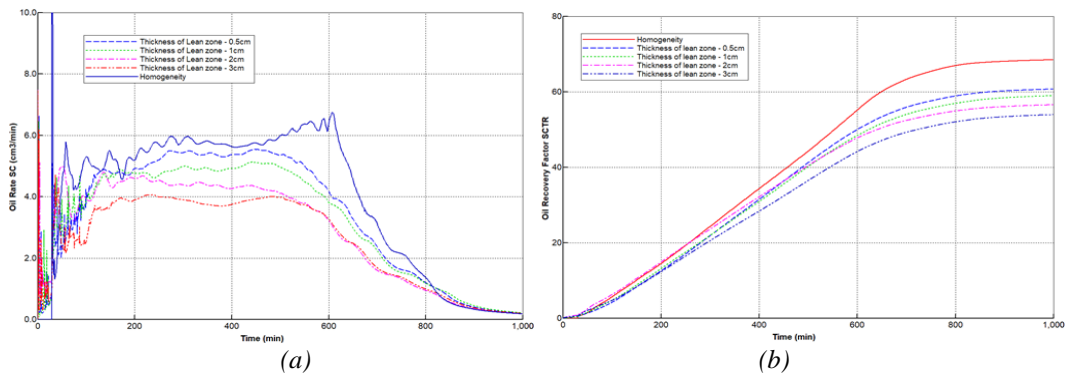
Figure 5. *Comparison of production performance for different numerical cases. (a) Oil rate curve. (b) Oil recovery curve.*

3. CONCLUSION

1. The lean zones can influence the development of steam chamber and production performance during the SAGD process.
2. The thickness of lean zone has a great impact on oil rate, especially during the steam chamber rising phase.
3. The existence of high-water saturation zone has an adverse effect on steam chamber expansion and the thicker the lean zone, the lower heat efficiency is when the steam encountering the water zone.

REFERENCES

[1]. S. Huang, M. Cao, Q. Huang, et al. Study on reaction equations of heavy oil aquathermolysis wi-th superheated steam, International Journal of Environmental Science and Technology (ICCES-EN 2017), Antalya-Turkey. DOI: 10.1007/s13762-018-1799-3

[2]. Dansen Shang, Jirui Hou. Effect of Descending Viscosity Injection Pattern for Alkali-surfactant-polymer (ASP) Flooding on Enhanced oil Recovery. International Conference on Computation-al and Experimental Science and Engineering (ICCESEN 2018), 12-16 October, 2018 Antalya-Turkey

[3]. K Liao, S. Zhang, X. Ma and X Sun. Numerical investigation of thermal fluid fracturing in low-mobility tight oil reservoirs. International Conference on Computational and Experimental Science and Engineering (ICCESEN 2018), 12-16 October, 2018 Antalya-Turkey

[4]. I.D. Gates, N. Chakrabarty. 2006. Optimization of Steam Assisted Gravity Drainage in McMurr-ay Reservoir. J Can Pet Technol 45 (9): 54-62. PETSOC-06-09-05. DOI: 10.2118/06-09-05

[5]. Fairbridge, J. K., Cey, E., & Gates, I. D. (2012). Impact of intraformational water zones on SAG-D performance. Journal of Petroleum Science and Engineering, 82, 187-197. DOI: 10.1016/j.petrol.2012.01.013

[6]. Xu, J., Chen. Z. J., Cao, J., & Li, R. (2014). Numerical Study of the Effects of Lean Zones on S-AGD Performance in Periodically Heterogeneous Media. In SPE Heavy Oil Conference Canada. Society of Petroleum Engineers. DOI: 10.2118/170138-MS

Hydrate Risk Assessment in Deepwater Gas Wells During Well-Cleanup Stage Before Production: A Case Study of Deepwater Gas Well Production in The South China Sea

Wenyuan Liu[1]*, Jinqiu Hu[1], Huan Ma[4], Fengrui Sun[2], Zheng Sun[3] and Hongyang Chu[4]

[1] *China University of Petroleum, Department of Safety Engineering, Beijing, China*
[2] *University of Texas at Austin, Department of Petroleum and Geosystems Engineering, Austin, USA*
[3] *Texas A&M University, Department of Petroleum Engineering, College Station, USA*
[4] *China University of Petroleum, Department of Petroleum Engineering, Beijing, China*
* Wenyuan_liu@126.com

ABSTRACT

Well-cleanup stage is an important part in the completion test of deep water gas wells, and it is also a key stage of hydrate risk prevention in wellbore. Unreasonable well cleaning and blowout release can easily lead to hydrate formation and blockage in the pipe string, and sometimes bringing huge economic losses for deepwater gas well testing. Therefore, it is very important for safe and efficient deep water gas well testing to accurately predict the hydrate formation risk in wellbore and to reasonably formulate effective hydrate control measures during well-cleanup stage. In this paper, based on PIPESIM software, sensitivity analysis of the factors affecting hydrate formation conditions is carried out, including natural gas composition, exhaust gas-liquid ratio, reservoir temperature and pressure, formation water salinity, condensate oil-gas ratio, inhibitors type and content, and the influence of temperature and pressure on hydrate formation is analyzed. Then, taking a deep-water gas well in South China Sea as an example, the temperature-pressure distribution field in the wellbore during blowout stage are simulated, and the critical conditions of hydrate formation in the wellbore during well-cleanup stage of deep-water gas wells are determined based on hydrate phase equilibrium curve, so as to provide theoretical guidance for reasonable test of blowout release system. It is concluded that reasonable control of blowout volume, wellhead pressure and formulation of completion fluid with certain salt inhibitors can effectively avoid the hydrate formation risk during blowout process. The implementation of quantified blowout release system can ensure the safety of deep water test and reduce economic input.

KEYWORDS - *Deepwater, Well-cleanup stage; Hydrate-risk assessment.*

1. INTRODUCTION

Well cleaning is an important stage in the testing process of deep-water gas wells. This stage is to return the wellbore and formation near wellbore fluid by induced blowout before oil and gas well testing and production. In the process of blowing-out, gas and water coexist in the wellbore string and the combined effect of temperature and pressure in the wellbore often lead to the hydrates formation in the string, especially near the mud line of the seabed [1]. The formation and deposition of hydrate will directly reduce the pipe flow channel and affect the blowout process of deep-water gas wells. When blowout is released with high productivity, it may also cause pipe string rupture due to pressure trapping in the wellbore [2].

At present, scholars from all over the world have done some research on hydrate risk prediction and prevention in the process of drilling and production of deep-water gas wells. However, there are insufficient studies on hydrate risk prediction and prevention in the process of deepwater gas wells well cleaning stage. Wang et al. (2008) established a prediction model for hydrate formation area in deep water drilling process [3]. The model consists of multiphase flow control equation, temperature field equation and hydrate formation equation. Later, Wang et al. (2018) proposed a prediction method of gas hydrate formation area in deep water gas wells by combining the

wellbore temperature field equation and hydrate phase equilibrium equation [4]. In view of the problem of hydrate blockage during deep water gas well testing. Liu et al. (2018a) have established a quantitative evaluation model for the risk of hydrate deposition in wellbore for deep water gas wells testing [5]. In addition, Liu et al. (2018b) analyzed the risk of hydrate formation and blockage under different flow patterns, considering the multi-phase flow pattern in wellbore during the blowout period of gas well cleaning and combining the formation conditions and sedimentary characteristics of hydrate [6]. It provides a theoretical basis for hydrate prevention in deep water gas well cleanup stage.

Methods for conducting research include theoretical methods, experimental methods, and software simulation methods [7-11]. This study is based on PIPESIM software. Aiming at the well-cleanup stage of deep water gas well, the influence of temperature and pressure on hydrate formation is analyzed. Then the temperature-pressure field of wellbore and the formation of hydrate in wellbore are analyzed by the method of temperature-pressure field coupling. Taking a deep water gas well as an example, the critical conditions of hydrate formation during backflow are analyzed. Finally, economic and effective measures for hydrate risk prevention and control during well cleaning stage are put forward.

2. THE FORMATION OF NATURAL GAS HYDRATE

When a certain gas composition and gas-liquid ratio are available, appropriate temperature and pressure are needed to generate hydrate. Fig. 1 shows the phase diagram of gas hydrate under a certain composition, and Fig. 2 shows the phase equilibrium curve (temperature-pressure) of gas hydrate.
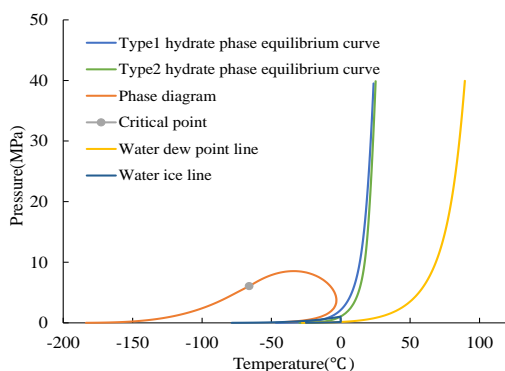
Figure. 1. *The phase diagram of natural gas under a certain composition.*
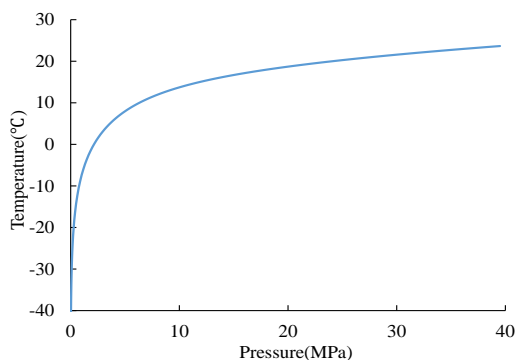
Figure. 2. *The phase equilibrium curve (temperature-pressure) of hydrate under a certain natural gas composition.*

Natural gas hydrate is easy to form under high pressure and low temperature. With the increase of ambient temperature, the pressure required for hydrate formation is higher. On the contrary, the external pressure environment is higher, and the temperature range for hydrate formation is enlarged. That is to say, hydrate can be formed at higher temperature, but in the high pressure area, the temperature-pressure curve tends to be flat, that is, the pressure increases. The increase of critical temperature of hydrate formation decreases.

3. RISK ASSESSMENT OF HYDRATE FORMATION IN DEEPWATER GAS WELLS—TAKING A SOUTH CHINA SEA DEEP WATER GAS WELL AS AN EXAMPLE

The following is an example of a deepwater gas well. The related data of a deepwater gas well are shown in Table 1. The composition of natural gas is shown in Table 2.

50

***Table. 1.** Basic data for deepwater gas wells.*

Parameter	Value
Seawater depth	1300m
Internal diameter of riser	482.6mm
Casing depth	3400m
Casing size	9-5/8″~36″
Formation pressure	39MPa
Formation pressure coefficient	1.2MPa/100m
Formation temperature	89℃
Geothermal gradient	3.87℃/100m
Sea surface temperature	20℃
Total amount of completion fluid	1380m³
Completion fluid density	1.3g/cm³
Condensate oil-gas ratio	50g/m³
Salinity of formation water	0

***Table. 2.** Natural gas composition.*

Components	Content（%）
CH_4	88
C_2H_6	5,4
C_3H_8	0,56
$i-C_4H_{10}$	0,3
$n-C_4H_{10}$	0,45
$i-C_5H_{12}$	0,13
$n-C_5H_{12}$	0,11
C_6^+	0,1
N_2	3,1
CO_2	1,85

Next, through the analysis of the well cleaning and blowout release system, the critical condition of no hydrate formation is obtained.

(1) Hydrate formation can be avoided by controlling wellhead pressure below 11.7 MPa or releasing gas volume above 20 mmscf/d under original formation pressure.
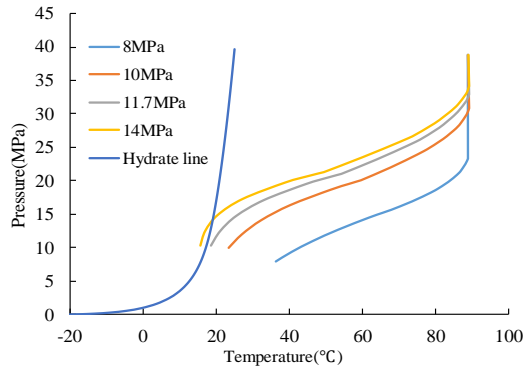
***Figure. 3.** Hydrate formation conditions under different wellhead pressures*

It is found that with the increase of wellhead pressure, the wellbore temperature-pressure curve moves to the upper left step by step. When wellhead pressure is 11.7 MPa, the temperature-pressure curve intersects with the hydrate line, indicating that hydrate will not be formed. When wellhead pressure increases further, hydrate will be formed. When the wellhead pressure is 11.7 MPa, the amount of gas released is 20 mmscf/d, so controlling the wellhead pressure below 11.7 MPa or the amount of gas released above 20 mmscf/d can completely avoid hydrate formation.

51

(2) The difficulty of hydrate formation increases with the decrease of formation pressure.
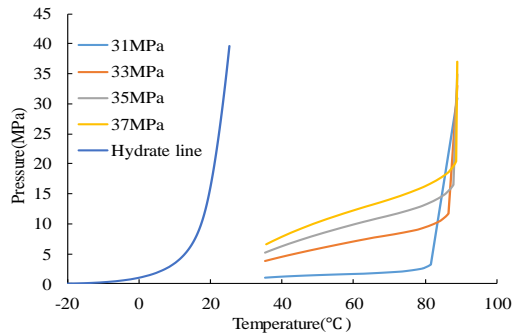
Figure. 4. *Hydrate formation conditions under different formation pressures (25mmscf/d).*

When the injection volume is fixed at 25 mmscf/d, with the formation pressure decreasing gradually, it can be found that the average pressure in the wellbore decreases gradually, and the wellbore temperature-pressure curve is more and more lower. However, the temperature in the wellbore is higher as a whole due to the large injection volume, and the high temperature inhibits the formation of hydrate. It can be found that hydrate will not be formed when the bottom hole pressure is 37 MPa, 35 MPa, 33 MPa and 31 MPa. With the decrease of formation pressure, the gas well will not be able to maintain 25 mmscf/d for blowout. The temperature-pressure curve is shown in Fig. 5.
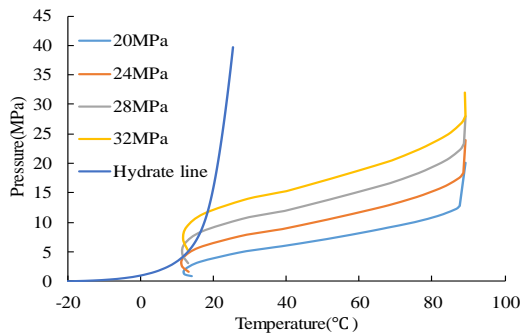
Figure. 5. *Hydrate formation conditions under different formation pressures (15mmscf/d).*

(3) The formation of hydrate can be effectively inhibited by using the completion fluid formula containing a certain amount of salts.
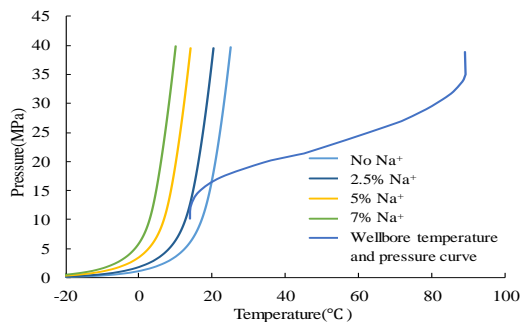
Figure. 6. *The influence of different sodium salt content in completion fluid on hydrate formation.*

52

Adding a certain amount of sodium or potassium salts to the completion fluid can stabilize the wellbore and balance formation pressure. At the same time, these salts are salt inhibitors that inhibit hydrate formation. In order to evaluate the inhibiting effect of salt content on hydrate formation, this paper analyses the situation when the discharge volume is 15 mmscf/d. The results are shown in Fig. 6. With the increase of salt content, the hydrate line shifts to the left gradually, indicating that the more difficult hydrate is to be formed, and it can effectively inhibit the hydrate when the content is more than 2.5%.

4. HYDRATE CONTROL MEASURES

At present, there are many methods to prevent and control wellbore hydrate. The following are widely used:

1. Hydrate injection inhibitor method.
2. The surface of the tubing is coated with an anaerobic layer.
3. Insulation and insulation method.
4. Downhole gas nozzle throttling method.

The above methods can play a certain role in hydrate prevention and control, but if only blindly using inhibitors, the effect of hydrate prevention and control can be achieved, but it will cause economic losses due to the use of inhibitors in large quantities. Although the methods of coating the surface of tubing with anaerobic layer, heat insulation, and downhole gas nozzle throttling can play the role of hydrate prevention and control, the effect of prevention and control is limited, and also require huge economic investment.

In view of safety and economy, several countermeasures which are helpful to the prevention and control of hydrate are put forward.

1. Adopt a reasonable discharge system. Reasonable control of injection pressure or output.
2. In the completion process before gas well testing, the formation of wellbore hydrate and the formation of flow barrier can be effectively avoided by preparing and using a certain salinity or hydrate inhibitor, and the amount of hydrate inhibitor in the later stage can be reduced.

5. CONCLUSION

1. Natural gas composition, temperature and pressure environment, formation water salinity, condensate oil gas ratio, inhibitor type and content have different effects on gas hydrate formation. In particular, H2S content in natural gas components has the greatest influence on hydrate formation. For deep water gas wells, methanol is the best choice of hydrate inhibitors.
2. For a specific deep-water gas well, the critical conditions for hydrate formation and blowout release system can be determined.
3. Reasonable blowout release system can economically and effectively reduce the hydrate risk in the well-cleanup stage of deep-water gas wells.
4. Hydrate formation can be avoided by controlling wellhead pressure or gas flow rate and configuring completion fluid with certain salinity during well cleanup (blowout release) stage.

REFERENCES

[1]. Arrieta, V. V., Torralba, A. O., Hernandez, P. C., García, E. R. R., Maia, C. T., & Guajardo, M.. Case History: Lessons Learned From Retrieval of Coiled Tubing Stuck by Massive Hydrate Plug When Well Testing in an Ultradeepwater Gas Well in Mexico. SPE Production & Operations, (2011) 26(04), 337–342. DOI:10.2118/140228-pa

[2]. Reyna, E. M., & Stewart, S. R. Case History of the Removal of a Hydrate Plug Formed During Deep Water Well Testing. SPE/IADC Drilling Conference. (2001). DOI:10.2118/67746-ms

[3]. WANG, Z., SUN, B., CHENG, H., & GAO, Y. Prediction of gas hydrate formation region in the wellbore of deepwater drilling. Petroleum Exploration and Development, (2008) 35(6), 731–735. DOI:10.1016/s1876-3804(09)60103-8

[4]. Wang, Z., Zhao, Y., Zhang, J., Wang, X., Yu, J., & Sun, B. Quantitatively Assessing Hydrate-Blockage Development During Deepwater-Gas-Well Testing. SPE Journal. (2018). DOI:10.2118/181402-pa

[5]. Liu, W., Hu, J., Li, X., Sun, F., Sun, Z., & Zhou, Y. Research on evaluation method of wellbore hydrate blocking degree during deepwater gas well testing. Journal of Natural Gas Science and Engineering, (2018) 59, 168–182. DOI:10.1016/j.jngse.2018.08.027

[6]. Liu, W., Hu, J., Li, X., Sun, Z., Sun, F., & Zhou, Y. Research on hydrate formation and prevention during deepwater gas wells cleanup stage. Petroleum Science and Technology, (2018) 36(22), 1928–1949. DOI:10.1080/10916466.2018.1519575

[7]. M. Saadsaoud, A.H. Ahmed, Z. Er, Z. Rouabah, Experimental Study of Degradation Modes and Their Effects on Reliability of Photovoltaic Modules after 12 Years of Field Operation in the Steppe Region. ICCESEN 2016. (2017) 132, 930-935. DOI: 10.12693/APhysPolA.132.930

[8]. H. Ahmad Mukifza, H.B. Awang, S. Yusof, E.M. Farid. Experimental Analysis of Titanium Dioxide Synthesis from Synthetic Rutile Waste using a Moderate Acid Concentration and Temperature. ICCESEN 2016. (2017) 132, 833-835. ICCESEN 2016. DOI: 10.12693/APhysPolA.132.833

[9]. M. Ozsoy, C. Kurnaz. An Optimization Study of a Hydraulic Gear Pump Cover with Finite Element Method. ICCESEN 2016. (2017) 132, 944-948. DOI: 10.12693/APhysPolA.132.944

[10]. A. Bouguerra, R. Labbani. Simulation of Carbon Ions Interactions with Monocrystalline Silicon Targets. ICCESEN 2014. (2015) 128, B67-70. DOI: 10.12693/APhysPolA.128.B-67

[11]. B. Mukanova, T. Mirgalikyzy. Simulation of the Electric Field of a Point Source on the Relief Surface. ICCESEN 2014. (2015) 128, B142-144. DOI: 10.12693/APhysPolA.128.B-142

The Flow Pattern And Pressure Gradient Of Gas-Liquid Two Phase Flow In The Vertical Pipe With Rotary Inner Boundary

Shuzhe SHI*, Xiaodong WU, Ziyao ZHONG

Oil and Natural Gas Engineering College, China University of Petroleum, China

ABSTRACT

As there is pump and rod in the well, the interference of gas-liquid two phase flow will lead to the changes of flow pattern and pressure gradient, which is important to the production's optimization. So, In order to study flow pattern and pressure gradient's changes of gas-liquid two phase flow along the pipe with a rod, use a partially transparent plexiglass pipe containing a screw pump, the pipe has an inner diameter of 88.9mm and length of 7m. Conducting the experiments in different rotation rate, Obtaining the flow pattern transition of bubble flow to slug flow when the pump is working; Comparing to the rodless flow pattern transition model, obtained the modified flow pattern transition model with the rotation rate of 30r/min, 60r/min, 90r/min. Based on the beggs-brill method, adding a rotational resistance coefficient $f(\beta)$, fitting the experimental data, modify the variations of pressure gradient with different rotation rate in the pipe and get the pressure gradient formula of different rotational rate. The results showed that: (1) At the same liquid superficial velocity, the transition of bubble flow to slug flow occurred earlier in rodless pipe; (2) The modified beggs-brill method can reflect the influence of rotational rate on pressure drop well, as the rotational rate increases, frictional resistance increases at the same time, but the degree of increase is small; (3) As the increase of gas superficial velocity, the total pressure gradient drops, and the drop rate of pressure gradient decreases gradually.

KEYWORDS - *Screw Pump Rotation, Gas Liquid Two-Phase Flow, Flow Pattern Transition, Frictional Pressure Drop*

1. INTRODUCTION

In the process of oil and gas production, the study of two-phase flow plays a key role in the optimization of production. The changes of gas liquid two-phase flow velocity and void fraction make the two-phase mixture shows different flow patterns, and these different flow patterns along the pipeline will interfere the pressure gradient and the mixture density, etc.

A large number of experiments were conducted by Duns-Ros [1] in 1960s, and the transitional boundaries of different flow patterns in rodless wellbore were given. They also had the formula of void fraction and pressure gradient of different flow patterns.

Orkiszewski [2] analyzed the old methods with field data in 1967. He made a detailed inspection of the methods with field data, chose a better method for different flow pattern. He combined with the results of his experiments, then the equations of two-phase pressure drop in the vertical pipeline and the transitional boundaries of different flow patterns were given.

At the beginning of 1970s, Aziz, Govier and Fogarasi [3] gave the flow pattern along the pipeline into following types: bubble flow, slug flow, transition flow, annular flow and mist flow. In the same time, he had the transitional boundaries of different flow patterns, and he puts forward a new method to calculate the pressure gradient.

At the beginning of 1980s, Taitel-Bornea-Dukler [4] made the mechanism of different flow patterns' transition as a starting point, he analyzed and predicted conditions of flow pattern transition, and obtained the model to describe flow pattern's change, which was used to draw the flow pattern regime.

At the same time, based on the previous scholars' research, Chen Jialang [5],[6] had obtained the "drag coefficient method" for calculating the pressure drop of gas-liquid two-phase flow in a pipe

55

according to the field data. Subsequently, he got the "flow pattern calculation method" to calculate the pressure drop of the oil, gas and water flow in the pipe.

In the middle of 1980s, through the experimental study, Caetano [7],[8] detailedly described the various types of annulus flow, at the same time he changed the Taitel's transition model of the vertical pipe flow pattern in the annular pipe, obtained the eccentric and concentric annular flow pattern regime in vertical pipeline.

At the beginning of 1990s, Ansari [9] and other scholars obtained the flow pattern identification methods of gas-liquid two-phase flow. They studied the the characteristics of each flow pattern and obtained the model to depict the characteristics of bubble flow, slug flow and annular flow.

After 1990s, many Chinese scholars have also studied two-phase flow models and mechanisms of pressure drop, obtained a lot of achievements [10]-[13], many of their mechanisms adopted Hasan, Kabir, Ansari's theory.

For a long time, the scholars were doing experiments of rodless gas-liquid two-phase flow and annular two-phase flow in different pipe angles. In the oil field, there normally are rod pump and screw pump in wells, so the research of the annular flow with rotating inner boundary is very rare, we need to focus on gas liquid two-phase flow in the wellbore with rotational rod. In the actual screw pump wellbore, when analyzing the gas liquid two-phase annular flow, it is necessary to consider the rod's influence, that is to say, the rotating inner boundary. The difference to the normal annular flow is: when there is the gas-liquid two-phase flow of rotating inner boundary, the changes of rod diameter, rotational rate, gas and liquid velocity will lead to the difference of gas-liquid two-phase average density and void fraction, which would affect the flow pattern and pressure gradient. Zhang Jun [14] and other scholars' studies suggested that the diameter ratio(N) of inner and outer boundaries has bigger effect on single-phase flow pattern, and the effect is more obvious as N becomes larger. But now there is no relations of rod rotating rate to flow pattern and pressure drop. This experiment research obtains the gas-liquid flow pattern and pressure in the pipeline as the rotating rate change, when have the determined diameter ratio.

The rotating inner boundary of the gas-liquid two-phase flow experiment research on the different flow patterns between rod rotating condition and the rodless condition in a vertical pipeline, we also modify the flow pattern regime. When the rod rotating at the rate of 30r/min, 60r/min, 90r/min, bringing in the flow resistance coefficient in the beggs-brill method, and modifying this method to calculate the change of pressure gradient in the pipeline more accurately.

2.   THE DEVİCE AND METHOD OF THE EXPERIMENT

The experiments adopt single layer simulation pipe, there are 8 temperature sensors and 4 pressure measuring points from the top to the bottom. The diameter of pipe is 88.9mm. There is a rod which has the diameter of 30mm, it's effective length is 7m, and install a top drive screw pump motor to rotate the rod. Arranging a one-meter transparent section in the middle of the pipe to observe, and the other sections are stainless steel. Experiments were carried out at room temperature, the variation range of gas volume flow rate is 0m3/h-40m3/h, the variation range of liquid volume flow rate is 0m3/h-5m3/h. The experimental device flow diagram is shown in Fig. 1.

The water circulation system is mainly composed of a buffer tank, a liquid storage tank, an injection pump and valves.

The gas circulation system is mainly composed of an air compressor, an air tank and pressure a regulating valve.

The data collected by data collecting system which are gas flow rate, liquid flow rate, temperature, and pressure.
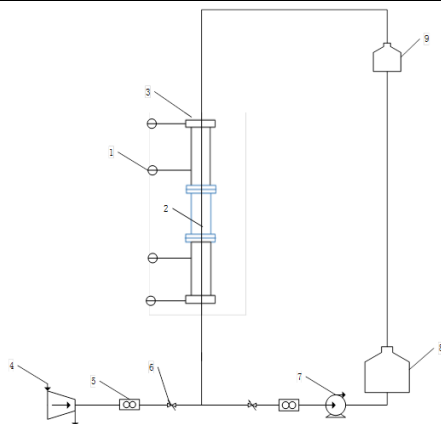
Figure 1: the changeable inner boundary pipe flow experimental device. (1-pressure sensor; 2-rod; 3-partly visible pipe; 4-air compressor; 5-volumetric flow meter; 6-valve; 7-centrifugal pump; 8-liquid storage tank; 9-buffer tank.)

The experiment process: Inspecting if the pipeline and valve's switch are normal or not; Starting the pump to fill water into the wellbore, maintain a constant rate of liquid flow; Start the screw pump at a certain velocity, then switch on the air compressor, regulate the pressure regulating valve, and change the gas flow gradually; Start collecting data when the two-phase flow rate and pressure are reached a relatively stable state; At the same time, observing and recording flow patterns in different conditions, when reach the maximum gas flow rate, stop the circulation, change the rotational rate of screw pump then repeat the above operations. At last according to the experimental data of each group, draw the transitional boundary charts of different flow patterns and pressure drop charts under different rotational rate respectively. Analyzing the transitional boundary of different flow patterns and the pressure drop under different rotational rate, and then obtain the experimental results.

3. THE RESULT AND ANALYSIS OF THE FLOW PATTERN EXPERIMENT
In the vertical annulus ascending pipeline, the flow patterns are divided into Bubble flow, Slug flow, Churn flow and Annular flow. In the actual well, the bubble flow and slug flow are the most common flow and they have more practical meaning, the rest of flow patterns is relatively rare. Therefore, the experiments are mainly composed of bubble flow and slug flow.

Bubble flow: Generally believed that when the liquid flow rate is low, gas is divided into discontinuous small bubbles by liquid. When the liquid flow rate increases gradually, bubbles combined with each other consist of larger bubbles. A homogeneous mixture is formed in the annular cross section of the pipe. The dispersed bubbles usually exhibit two states, which are spherical bubbles and cap shaped bubbles.

Slug flow: when the gas flow rate increases, so does the void fraction. The bubbles grow big and move upward, they combine with each other and form slug bubbles, the bubbles' diameter close to the diameter of the pipe, the liquid phase is presented as liquid film, which is located around the bubbles and move downward along the pipe.

When the void fraction is 0.25-0.3, the Taylor bubbles consist of slug; In this experiment, there is a screw pump in the pipe. When the rotational rates of the pump were 30r/min, 60r/min, 90r/min respectively, we observed the transition process of bubble flow to slug flow. According to the data observed and measured in the experiment, it is found that the void fraction when the bubble flow transfer to slug flow is approximately 0.29. Therefore, it is taken as the transitional boundary, and the transitional void fraction is 0.25 in Kelessidis's [15] research.

57

Taitel established that the velocity of the small bubbles in the liquid is U∞, which is equal to the slippage velocity US between the gas and liquid when the liquid velocity is small. According to the formula of slippage velocity, the relation between slippage velocity and void fraction is:

$$U_\infty = U_s = \frac{U_{SG}}{\alpha} - \frac{U_{SL}}{1-\alpha}. \tag{1}$$

The velocity of single bubble move upward in the pipe is:

$$U_\infty = 1.53 \left[\frac{(\rho_L - \rho_G)g\sigma}{\rho_L^2} \right]^{0.25}. \tag{2}$$

The gas and liquid velocity are $U_G = \frac{U_{SG}}{\alpha}$, $U_L = \frac{U_{SL}}{1-\alpha}$. Because the gas velocity equals to the sum of the liquid velocity and bubble velocity, the transfer equation from bubble flow to slug flow in rodless pipe is:

$$U_{SL} = 3.0 U_{SG} - 1.1475 \left[\frac{(\rho_L - \rho_G)g\sigma}{\rho_L^2} \right]^{0.25}. \tag{3}$$

Based on the void fraction, the modified transfer equation in a pipe with a screw pump is:

$$U_{SL} = 2.45 U_{SG} - 1.086 \left[\frac{(\rho_L - \rho_G)g\sigma}{\rho_L^2} \right]^{0.25}. \tag{4}$$

$U_{SG,}$ U_{SL}--gas and liquid superficial velocity, m/s.
According to the experimental data and theoretical model, this paper compares the transitional boundaries from bubble flow to slug flow with different rotational rate of rodless pipe and screw pump pipe, then draws the transitional diagrams. As shown in Fig. 2, 3 and 4, which are the contrast of modified transitional model against Caetano's model (air-water) and experimental data when the screw pump works at the rate of 30r/min, 60r/min, 90r/min.
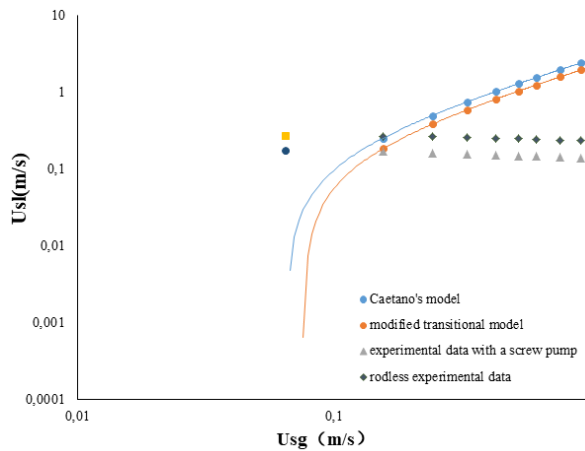
Figure 2: The contrast of modified transitional model with Caetano's model (air-water) and experimental data when 30r/min

58
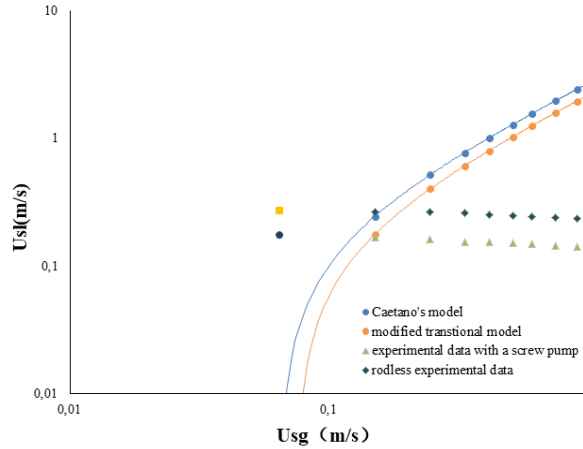
Figure 3: *The contrast of modified transitional model with Caetano's model (air-water) and experimental data when 60r/min*
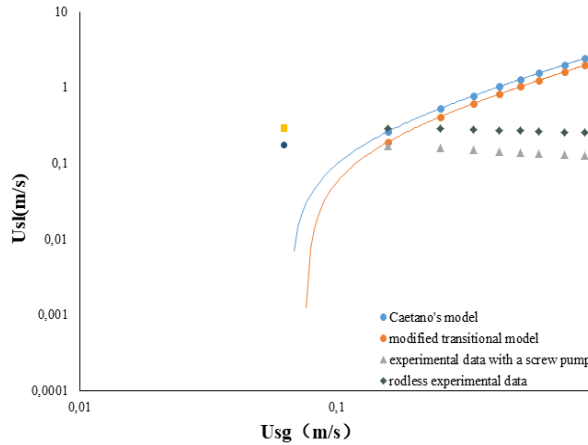
Figure 4: *The contrast of modified transitional model with Caetano's model (air-water) and experimental data when 90r/min*

The horizontal axis is the superficial velocity of gas, the vertical axis is the superficial velocity of liquid, blue and orange curves were caetano's model and modified transitional model respectively, left area of the curve is the bubble flow, right area of the curve is slug flow. According to the data from these diagrams, the caetano's model and the modified model have the same trend, but each point on the curve is different obviously, mainly due to the difference of the void fraction caused by rotation of screw pump; There is also the difference of the transitional boundaries between a rodless pipe and a pipe with a screw pump can be seen: At the same superficial velocity of liquid, the transition from bubble flow to slug flow in the rodless pipe is earlier.

4.   THE RESULT AND ANALYSIS OF PRESSURE DROP EXPERIMENT
In the two-phase flow process of the actual wellbore, getting accurate pressure variation in the wellbore has very important influence on the optimization of oil and gas wells and rod selection, it also plays a positive role in improving and stabilizing the production. When calculating the

59

pressure gradient, the beggs-brill [16] method is adopted. The method can be used to calculate the gas liquid two phase pressure in the wellbore of all kinds of angles. In the case of screw pump, using hydraulic diameter instead of pipe diameter to calculate the pressure gradient. The rotational resistance coefficient is introduced by regression analysis, it is calculated by least square method combined with experimental data. Finally, we could obtain the modified beggs-brill method which could be used in the pressure calculation of existence of rod in a pipe.

Due to the existence of gas in the gas-liquid two-phase flow experiment, the measured instantaneous pressure and flow rate data are unsteady, so calculate with average value of the measured data to reduce the error. We measured the pressure data when the screw pump rotates at the rate of 0r/min, 30r/min, 60r/min, 90r/min. Comparing the pressure gradient's variation of different rotational rate, and find out the relationship between them, then modify the beggs-brill equation. The modified one would be applied in actual situation better.

There are 4 pressure measuring points from the bottom to the bottom on the wellbore. The pressure measuring point 1 is located at the outlet of the pipe, which can be considered that connected with the atmosphere. The other 3 measuring points are arranged downward sequently. In the experiment, we measured pressure data of each pressure measuring point at different rotating rates with different liquid and gas flow rates respectively.

The frictional pressure formula of beggs-brill method is:

$$\left(\frac{dP}{dz}\right)_{friction} = \lambda \frac{v^2}{2D_h}\rho. \tag{5}$$

In the experiment, because there is a screw pump, the frictional resistance is represented by a rotational resistance coefficient f(β), which can reflect the influence to the pressure caused by the rod rotation and inner surface area's augment.

$$\left(\frac{dP}{dz}\right)_{friction} = f(\beta)\lambda \frac{v^2}{2D_h}\rho. \tag{6}$$

β is rotational rate.
The modified begs-brill equation by eqn. (6) is:

$$-\frac{dP}{dz} = \frac{[(1-H_L)\rho_G+H_L\rho_L]gsin\theta+f(\beta)\lambda\frac{v^2}{2D_h}\rho}{1-\{[(1-H_L)\rho_G+H_L\rho_L]vv_{sg}\}/p}. \tag{7}$$

Making the bottom pressure as beginning, calculate the pressure under different flow rate from top to bottom (a total of 3 pressure points), then fitting the experimental data, genetic algorithm was used to determine the rotational resistance coefficient   f(β)=β^a=β^(-0.587). Calculation had achieved convergence criterion, making the error between experimental data and the calculated data as small as possible. Then comparing the experimental pressure data and the pressure calculated by the model.

Figure 5, 6, 7 present the pressure curve calculated by begs-brill method, pressure curve calculated by modified method and experimental pressure curve at the rotational rate of 90r/min. Figure 8, 9, 10 present pressure curve calculated by begs-brill method, pressure curve calculated by modified method and experimental pressure curve at the rotational rate of 60r/min. Figure 11,12,13 present pressure curve calculated by begs-brill method, pressure curve calculated by modified method and experimental pressure curve at the rotational rate of 90r/min.

60
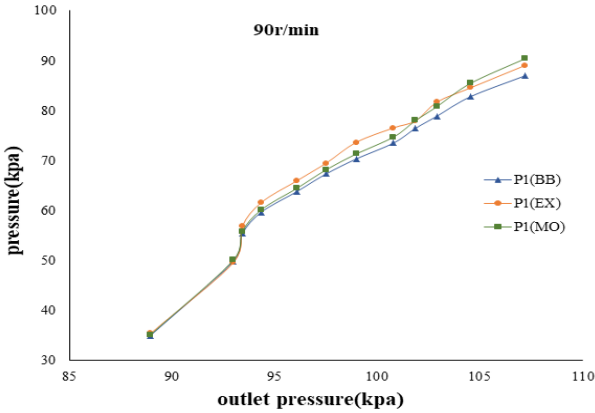
Figure 5: *the contrast of the beggs-brill pressure curve, modified formula pressure curve and experimental pressure curve at the first point when 90r/min (BB represents pressure calculated by begs-brill, EX represents experimental data, MO represents pressure calculated by modified formula)*
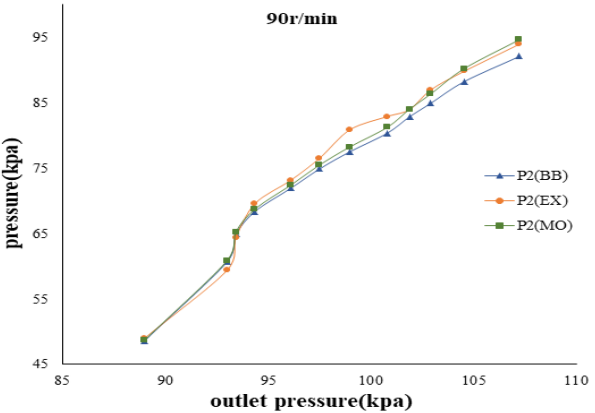
Figure 6: *the contrast of the beggs-brill pressure curve, modified formula pressure curve and experimental pressure curve at the second point when 90r/min*
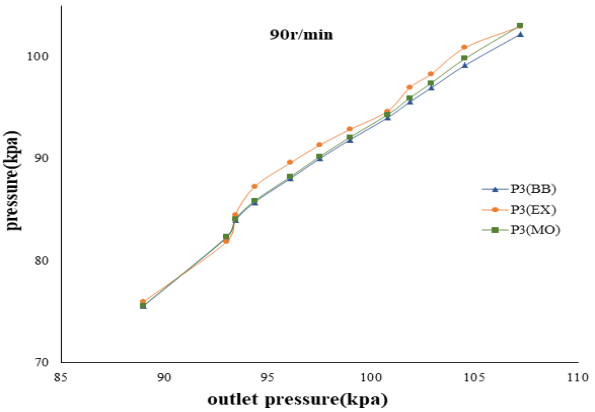
Figure 7: *the contrast of the beggs-brill pressure curve, modified formula pressure curve and experimental pressure curve at the third point when 90r/min*

61
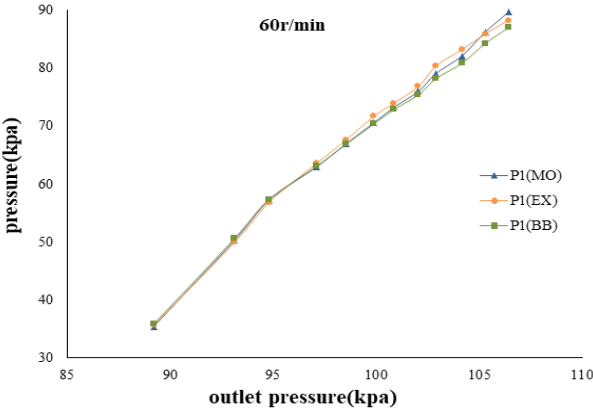
Figure 8: *the contrast of the beggs-brill pressure curve, modified formula pressure curve and experimental pressure curve at the first point when 60r/min*
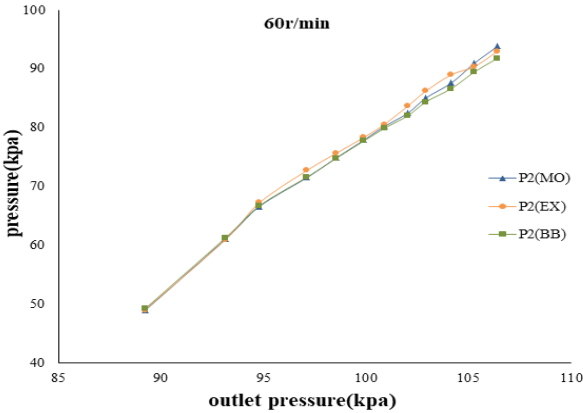
Figure 9: *the contrast of the beggs-brill pressure curve, modified formula pressure curve and experimental pressure curve at the second point when 60r/min*
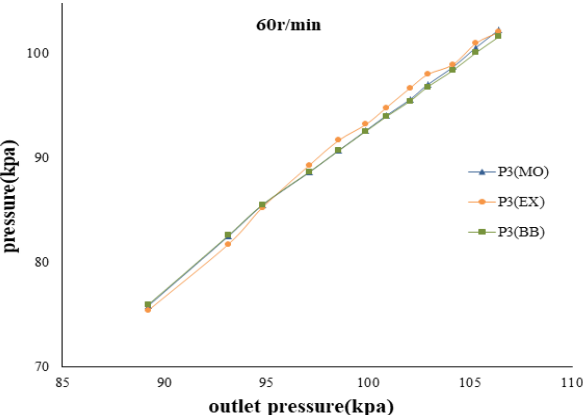
Figure 10: *the contrast of the beggs-brill pressure curve, modified formula pressure curve and experimental pressure curve at the third point when 60r/min*

62
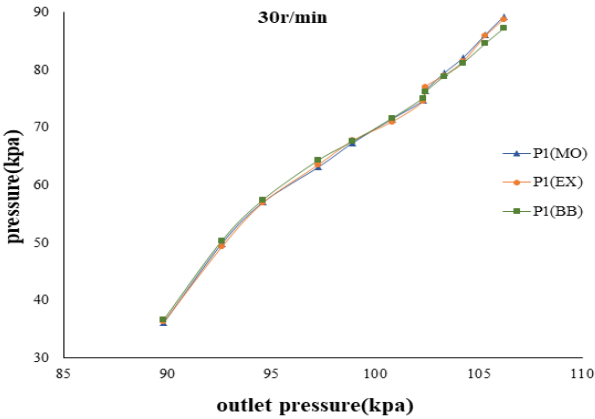
Figure 11: *the contrast of the beggs-brill pressure curve, modified formula pressure curve and experimental pressure curve at the first point when 30r/min*
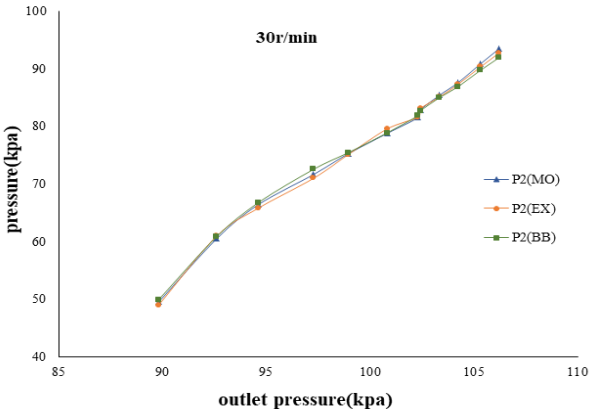
Figure 12: *the contrast of the beggs-brill pressure curve, modified formula pressure curve and experimental pressure curve at the second point at the third point when 30r/min*
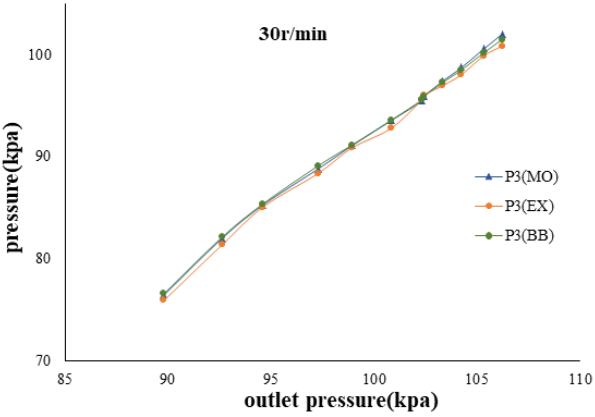
Figure 13: *the contrast of the beggs-brill pressure curve, modified formula pressure curve and experimental pressure curve when 30r/min*

63

After the calculation and analyzing, we obtained the following conclusions: Due to the increased area between gas-liquid mixture and the rod, the rotational resistance coefficient f(β) becomes larger as the rotational rate increases gradually, then compare with the experimental data, it is found that the error is relatively small (as shown in Table.1). For higher rotational rate, the error between the modified beggs-brill method and the experimental data is small, but the error between the beggs-brill method and the experimental data is rather big. When there is a lower rotational rate, the modified beggs-brill method and beggs-brill method have few differences, and the error is also small. The above conclusions indicate that the modified formula is more suitable for high rotational rate. When the rotational rate is relatively low, the rotational resistance coefficient is small, and influence on the calculation results can be neglected.

Table 1: *the maximum error and average error of the modified BB method when rotational rate are 30r/min, 60r/min and 90r/min*

Rotational rate \ error	Maximum error	Average error
30r/min	2.19%	0.78%
60r/min	2.84%	1.22%
90r/min	4.52%	1.94%

Putting the pressure gradient curve and superficial gas velocity curve in the same graph, we could compare the pressure gradient changes as superficial gas velocity increases, when the screw pump works at different rotational rate. It can be seen that as the superficial gas velocity increases, pressure gradient decreases gradually, and the pressure gradient decreasing speed becomes smaller; As the screw pump rotational rate becomes higher, the pressure gradient is relatively larger, but the difference between these pressure gradients is small.
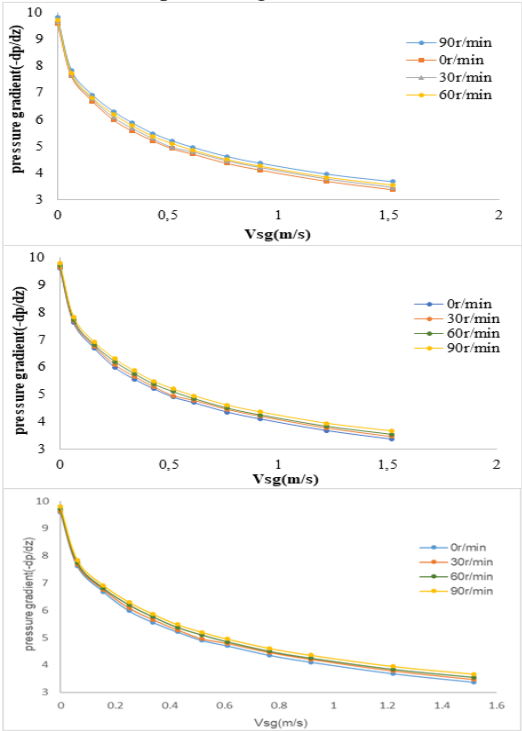
Figure 14: *the variation of the pressure gradient with different superficial gas velocity under different rotation rate*

64

5. CONCLUSION

1. When the rod's rotating speed respectively are 0r/min, 30r/min, 60r/min and 90r/min, it can be seen that under the same liquid superficial velocity, the gas superficial velocity is lower when the transition of bubble-flow convert to slug flow occured in the rodless pipe model. At the same time, according to the experimental data, the modified model shows better performance for the boundary of flow pattern transition.

2. Because of the inner boundary effect caused by the rod, the frictional resistance compared with rodless wellbore has obvious increasement. Using the coefficient of f (β) to reflect the change of the frictional resistance due to the increase of rotational speed, and fitting the formula, then the relationship between β and rotational speed is obtained. Compared with the experimental data, it is found that the error is small, so the fitting formula has a good performance;

3. As the rotational speed of the screw pump increases, the frictional pressure drop gradually increases, but the increase amplitude of the friction pressure drop is small;

4. The total pressure gradient decreases as the increase of gas superficial velocity, and the decrease amplitude of pressure gradient is gradually reduced, and the decrease degree of total pressure drop also decreases with the increase of gas superficial velocity.

REFERENCE

[1]. Duns H., Ros N.C.J. Vertical Flow of Gas and Liquid Mixtures in Wells[C]. Proc. 6th.World Petroleum Congress, 1963: 451-465.

[2]. Orkiszewski J. Predicting Two-Phase Pressure Drops in Vertical Pipes[J]. Journal of Petroleum Technology, 1969: 829-838.

[3]. Aziz K., Govier G.W., Fogarasi M. Pressure Drop in Wells Producing Oil and Gas[J]. Journal of Petroleum Technology, 1972: 38-47.

[4]. Taitel, Y., Barnea,D.,and Dukler, A.E. Modelling Flow Pattern Transitions for Steady upward Gas- Liquid Flow in Vertical Tubes[J]. AIChE Journal, 1980,26(3): 345-354.

[5]. CHEN Jialang. Two-phase flow in pipes[M]. Beijing; Petroleum Industry Press,1989.

[6]. CHEN Jialang. Petroleum gas liquid two phase flow[M]. Beijing; Petroleum Industry Press: 1-58,1988.

[7]. Caetano, E. F., O. Shoham, and J. P. Brill. Upward Vertical Two-Phase Flow Through an Annulus—Part I: Single-Phase Friction Factor, Taylor Bubble Rise Velocity, and Flow Pattern Prediction. Journal of Energy Resources Technology 114.1:1-13,1992.

[8]. Caetano, E. F., O. Shoham, and J. P. Brill. Upward Vertical Two-Phase Flow Through an Annulus—Part II: Modeling Bubble, Slug, and Annular Flow. Journal of Energy Resources Technology 114:1.1:14-30, 1992.

[9]. Ansari A. M., Ansari A. M. A comprehensive mechanistic model for upward two-phase flow[J]. Spe Production & Facilities, 9:2(2):143-151, 1994.

[10]. HAN Hongsheng, CHEN Jialang, Flow Regularity of Gas Liquid Two Phase Slug Flow to Plug Flow[J]. Natural Gas Industry,9(1): 42~44, 1989.

[11]. ZHENG Cheng. Gas Liquid Two Phase Slug Flow Pressure Drop in Vertical Tube[J]. Chemical Engineering,24(4) :59~63,1996.

[12]. ZHANG Jun, JIN Youhuang, CHEN Tingkuan, WEI Aijun. Evaluation of the Several Models for Predicting the Rise Velocity of Taylor Bubbles through the Stagnant Liquid in a Vertical Annulus[J]. Journal of Xi'An Petroleum University,13(6):50-53, 1998.

[13]. LI An, WAN Banglie, LOU Haoliang. A Summary of Present Studies on Gas Liquid Two Phase Flow In Vertical Tubes[J]. Oil Drilling & Production Technology, 22(4): 45~47,2000.

[14]. ZHANG Jun, LUO Tiqian, CHEN Tingkuan. Single phase flow experimental study in a vertical concentric annular tube with inner tube rotation[J]. Oil Drilling & Production Technology, 24(1):1-5, 2002.

[15]. Kelessidis V. C., Dukler A. E. Modeling flow pattern transitions for upward gas-liquid flow in vertical concentric and eccentric annuli[J]. International Journal of Multiphase Flow, 15(2):173-191, 1989.

[16]. ZHANG Qi, Principle and design of oil production engineering[M]. Dongying Shandong: China University of Petroleum Press: 23~32, 2004.

Determination of the Gamma-Ray Attenuation Coefficient of Magnetite Aggregate Concretes

Faez WAHEED*[1], Kadir Günoğlu[2], Hakan AKYILDIRIM[1] İskender AKKURT[1]

[1] *Suleyman Demirel University, Isparta-Turkey*
[2] *Isparta Applied Science University, Isparta- Turkey*
*faez_radiophysics@yahoo.com

ABSTRACT

With the use of radiation in many areas in daily life, radiation protection has gained great importance in terms of human health and the environment. Time, distance and shielding are three basic rules of radiation protection. The most effective of these three rules is shielding. In this study, the gamma attenuation coefficient for magnetite aggregate concretes were measured using a gamma spectrometer containing a NaI (Tl) detector and MCA at 0.835 MeV. The obtained experimental results were compared using the FLUKA Monte Carlo code and XCOM.

KEYWORDS: *Gamma ray attenuation, magnetite, gamma spectrometer, FLUKA*

1. INTRODUCTION

The radiation was widely used around the world in medical treatments as well as the application in thousands of usage throughout developed societies. The major sources of radiological dose to the public are natural and medical sources of radiation. Any source of radiation, as with most hospital radiation sources and some industrial processes can be entirely shielded to protect workers and the public (Akkurt, 2013c; Akkurt, 2010). FLUKA is one of the most preferred simulation codes. It uses the Monte Carlo technique to simulate transportation and interaction with the matter of about 60 particles over a wide energy range with high accuracy (Waheed, 2018).

2. MATERIALS and METHODS

2.1. Gamma Spectrometer System

The gamma spectrometer consists of a detector type 3"x3" NaI(Tl) detector by ORTEC Inc., with a resolution of 7.45 % for 0.662 MeV (measured experimentally). counting electronic system (high voltage, preamplifier, amplifier 16384-channel Multichannel Analyses (MCA)), and a PC (where software was installed) to record data (Akkurt, 2011). In order to reduce the background level of the system, the detector is shielded using lead shielding on all sides. Figure 1 shows a schematic description of this spectrometer that was used in this study (Akkurt, 2015).
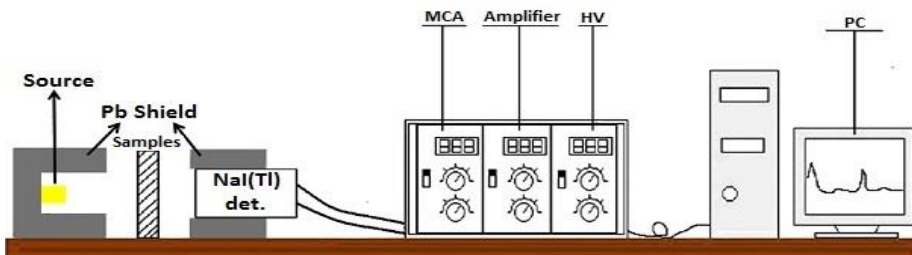
Figure 1. *Schematic view of the experimental system setup*

2.2. The FLUKA simulations

The simulation of the NaI(Tl) detector by FLUKA code should be modeled with the best possible accuracy. The geometry of FLUKA simulation exactly to the practical measurement properties, the

67

physical volume, the mother volume, and sensitive volume were implemented in the word accordingly using (FLUKA 2011.2 x 7, July 2019). (Ferrari, 2005), the description of the interaction of the incident particles is importance during prepare the input file (Joel, 2018). Figure 2. Illustrate practical geometry, side, and pack shielding and covered all by lead shielding to illumination background, Figure 3. Illustrate the geometry structure related to selection configuration.
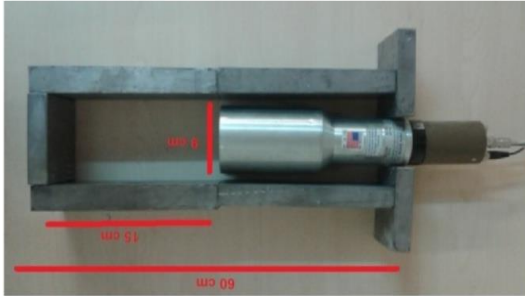
Figure 2. *The experimental configuration.*
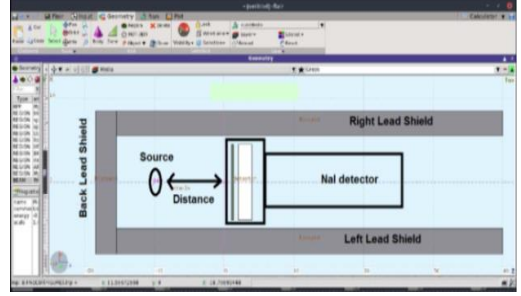
Figure 3. *FLUKA simulation geometry*

3. RESULTS

The linear attenuation coefficient of magnetite aggregate concretes by using two methods during experimentally, and by using the FLUKA Code program. The result was obtained using gamma-ray energy 0.835 MeV.
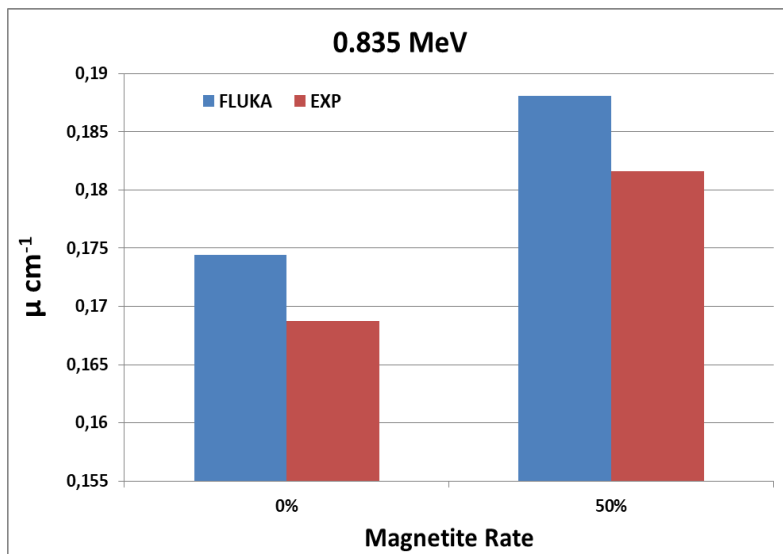
Figure 4. Linear attenuation coefficient for 0.835 MeV

4. CONCLUSIONS

Depending on the linear attenuation coefficient results, the adding Magnetite Aggregate Concretes seem to be better attenuator values. The content of elements with high atomic masses contributes to the attenuation capability of concrete. This concretes compounds in a positive way. From this point of view, it can be stated that the chemical property of a Magnetite Aggregate Concretes has a

68

strong effect on radiation shielding properties. FLUKA are powerful tools to be used in such radiation shielding studies.

REFFERENCE.
[1]. Akkurt, I., Tekin, H., O., & Mesbahi, A. (2015). Calculation of detection efficiency for the gamma detector using MCNPX. Acta Phys. Pol. A, 128(2-B), 332-334.
[2]. Akkurt, I., Günoğlu, K., Çelik, A., Karakas, M., S ., 2013c . Determination of Gamma Ray Attenuation Coefficients of AL-4% Cu/B4c Metal Matrix Composites at 662, 1173,and 1332 KeV.Bulletin of Materials Science August 2014, Volume 37, Issue 5, pp 1175-1179 First online: 20 September 2014.
[3]. Akkurt, I., Calik, A., Akyıldırım, H., 2011. The boronizing effect on the radiation shielding and magnetization properties of AISI 316L austenitic stainless steel. Nuclear Engineering and Design 241, 55–58.
[4]. Akkurt, I ., Akyildirim, H., Mavi, B., Kılınçarslan, Ş., Basyigit, C., 2010. Photon Attenuation Coefficients Of Concrete Includes Barite In Different Rate ,Annals of Nuclear Energy (Impact Factor: 0.96). 07/2010; 37 (7): 910-914. DOI: 10.1016 / j.anucene.2010.04.001.
[5]. Ferrari, A., Sala, P. R., Fasso, A., & Ranft, J. (2005). FLUKA: A multi-particle transport code (Program version 2005) (No. INFN-TC-05-11).
[6]. Joel, G. S. C., Maurice, N. M., Jilbert, N. M. E., Ousmanou, M., & David, S. (2018). Monte Carlo method for gamma spectrometry based on GEANT4 toolkit: Efficiency calibration of BE6530 detector. Journal of environmental radioactivity, 189, 109-119.
[7]. Waheed, F., Q., Akyildirim, H., Günoğlu, K., Akkurt, İ., 2018. The Importance of the Buildup Factor for NaI(Tl) Detector System. 5thinternational Conference on Computational And Experimental Science And Engineering (ICCESEN-5), ISBN:978-605-68728-0-8, 12-16 October 2018, Antalya-Turkey, 298-300

.

Experimental Study on Relative Permeability Curves in the Whole Process of High-salinity Water Flooding and the Followed Low-salinity Water Flooding

Su Wenbo[1], Liu Yuetian[1*], Kong Xiangming[1], Fu Jia[1], Zhang Junru[1], Ren Xingnan[1]

1. State Key Laboratory of Petroleum Resources and Prospecting, China University of Petroleum(Beijing), Changping, Beijing102200, China

[*]lyt51s@163.com

ABSTRACT

Considering the fact that low salinity water flooding(LSWF) can significantly improve oil recovery after carrying out high salinity water flooding(HSWF) to a certain water content. The oil-water relative permeability curves were determined by a constant-speed unsteady-state method during the whole process with HSWF to a certain water content about 80%, 90%, 100% followed by LSWF. The results showed that when LSWF was carried out after HSWF, the oil-water relative permeability curves have been changed obviously. The water relative permeability and water content decreased first and then increased, meanwhile that the oil phase relative permeability increased first and then decreased; With the same permeability level, the earlier transferred to LSWF, the greater change of oil-water relative permeability during LSWF, the larger the span of two-phase region, and the higher ultimate recovery.

KEYWORDS - *High salinity water flooding, Low salinity water flooding, Relative permeability curves; Transfer time of low salinity water flooding.*

1. INTRODUCTION

LSWF, as a hot enhanced oil recovery (EOR) technology in recent years, has gained more and more attention due to its high potential in enhancing oil recovery beyond conventional (high salinity) water flooding. The current study on the relative permeability curve of LSWF only aims at the secondary oil recovery stage, figuring out the difference between HSWF and LSWF[1-3]. There is no study on determining the relative permeability during the whole process from HSWF to LSWF. In order to obtain the oil-water relative permeability curves, we have selected the artificial core parallel samples with different levels of permeability and used the non-steady-state method to measure the relative permeability of the whole procedure. The results have great value for the development of LSWF and its application in oilfields.

2. EXPERIMENT

The experimental device is mainly composed of three modules: injection system, model body, flow and pressure measurement system. Since the clay minerals are of great influence on LSWF[4], the cores used in the experiment are specially designed quartz sand epoxy cemented cores, which core rich in clay minerals. The average permeability of the cores is 1.48D. The physical properties of the cores are shown in Table 1. The composition and salinity fo the saline are shown in Table 2. The oil/water relative permeability was determined by the unsteady method with a constant velocity. The experimental data were processed by JBN method[5].

3. RESULTS AND ANALYSIS

When core A1 is flooded by high salinity water (FW) to a water content of 80%, then flooded with low salinity water (FW-100) until no oil flows out. The curve of the relative permeability of the whole process is shown in Figure 1. After the water salinity changes, the water content decreases and then rises, the oil relative permeability increases and then decreases, the water relative.

70

Table1 *Petrophysical parameters of the artificial cores*

No.	Diameter, mm	Length, mm	Porosity, %	Water-measured permeability, μm^2
A-1	25.30	82.16	30.5	1.475
A-2	25.30	82.14	30.7	1.482
A-3	25.30	82.08	30.8	1.493

Table2 The ion concentration and salinity of the brines

Brines	Ion concentration(mg/L)							Salinity (mg/L)
	Na^+	Ca^{2+}	Mg^{2+}	K^+	HCO_3^-	SO_4^{2-}	Cl^-	
FW	75009.6	13626.8	1748.0	1170.9	422.7	1116.7	145134.9	238460.5
FW-100	750.1	136.3	17.5	11.7	4.2	11.2	1451.3	2384.6

permeability decreases and then increases. The oil relative permeability has a larger change than the water relative permeability. When cor A2 is flooded with high salinity water (FW) to a water content of 90%, then flooded with low salinity water (FW-100) until no oil flows out. The curve of the relative permeability of the whole process is shown in Figure 2. Overall, the change of water content and oil-water relative permeability in Figure 2 is similar to that in Figure 1. The difference is that, when the water content reaches 90%, the oil-water relative permeability has smaller change in the LSWF stage than that with water content of 80%, and the residual oil saturation of the former is less than that of the latter.
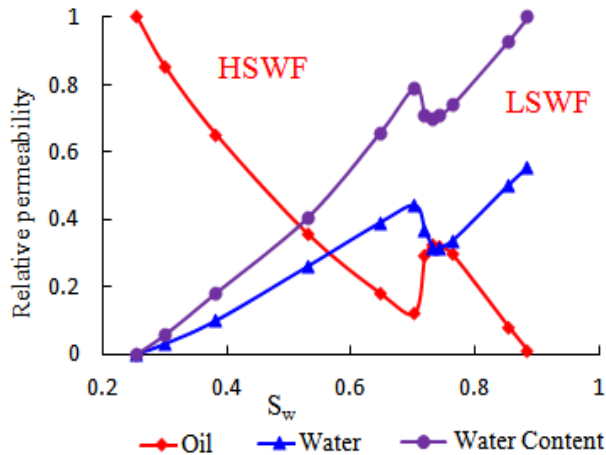
Fig.1 The oil-water relative permeability curves in core A1 of the full term of low salinity water flooding after high salinity water flooding reaching to 80% of water-cut

When cor A2 is flooded with high salinity water (FW) to a water content of 100%, then flooded with low salinity water (FW-100) until no oil flows out. The oil/water relative permeability curve is shown in Figure3. Overall, the change of water content and oil-water relative permeability in Fig.3 is similar to Fig.1 and Fig.2. However, when the water content reaches 100%, the water content and oil-water relative permeability have the smallest change, comparing to 80% and 90% water content, and the final residual oil saturation is also less than that when the water content is 80% and 90%. The performance of oil production is the worst.

71
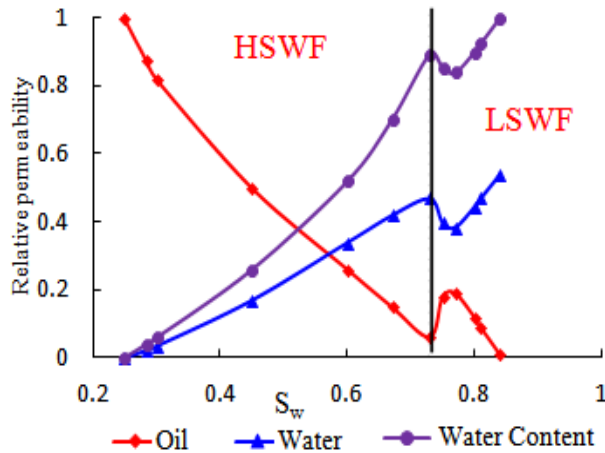
Fig.2 The oil-water relative permeability curves in core A2 of the full term of low salinity water flooding after high salinity water flooding reaching to 90% of water-cut
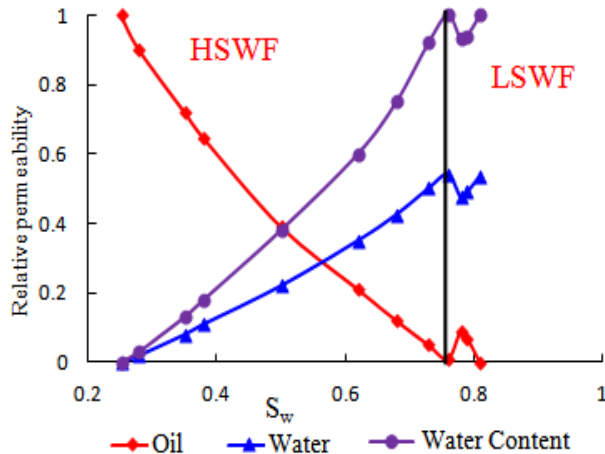
Fig.3 The oil-water relative permeability curves in core A3 of the full term of low salinity water flooding after high salinity water flooding reaching to 100% of water-cut

4. CONCLUSION

(1) When HSWF until the water content reaches a certain level and transferred to LSWF, the oil-water relative permeability curve changes significantly. The oil relative permeability increases and then decreases, and the water relative permeability decreases and then increases.

(2)When the cores have the same permeability level, the earlier of the change of water salinity brings about the greater variation of the oil-water relative permeability, the larger oil-water co-infiltration area, and a larger recovery factor. Therefore, early transfer of LSWF is conducive to improve ultimate recovery.

REFERENCES
[1]. E. Bilgic, Y. Durgut, Effect of waveform model on sensitivity values of transducers used in mechanical dynamic measurements, Acta Physica Polonica A 128 (2015) B-267. DOI: 10.12693/AphysPolA. 128. B-267

72

[2]. G. Xueli, L. Jun. International Conference on Computational and Experimental Science and Engineering (ICCESEN 2017), 4-8 October, 2017 Antalya-Turkey

[3]. Z. Wenkuan, L. Yuetian. International Conference on Computational and Experimental Science and Engineering (ICCESEN 2017), 4-8 October, 2017 Antalya-Turkey

[4]. Z. Ziyao,W. Xiaodong. International Conference on Computational and Experimental Science and Engineering (ICCESEN 2018), 12-16 October, 2018 Antalya-Turkey

[5]. D. Jingchen, Yang Shenglai. International Conference on Computational and Experimental Science and Engineering (ICCESEN 2017), 4-8 October, 2017 Antalya-Turkey

Validation and Modification of Simplified Local Density Model for Theoretical Adsorption Simulation

Xiaojun Wu[1,2]*, Zhengfu Ning[1,2]*, Zhilin Cheng[1,2], Qing Wang[1,2], Heng Zhang[1,2], Rongtong Qi[3], Liang Huang[1,2] and Wentong Zhang[1,2]

[1] *State Key Laboratory of Petroleum Resources and Prospecting, China University of Petroleum (Beijing), Beijing, PR China*

[2] *Department of Petroleum Engineering, China University of Petroleum (Beijing), Beijing, PR China*

3 Guangzhou Marine Geological Survey, Guangzhou, PR China

*xiaojun_wu@outlook.com, nzf@cup.edu.cn

ABSTRACT

Simplified local density (SLD) model is a widely accepted and utilized model for the adsorption experiments of activated carbon, coal and gas shale. However, its accuracy has not been ensured considering that specific surface area, slit-pore size, and solid-solid interaction energy all need regressions for the utilization of SLD model on experimental samples, due to the uncertainty of the physical properties. The accuracy could not be determined considering too many regressed parameters and the regressions are various in different literatures. Therefore, it is necessary to validate the SLD model by molecular simulation (MS) results without parameter regression instead of experimental results, and figure out its applicability on theoretical adsorption simulation, which is meaningful for the better acceptation and application of SLD model.

In SLD model, the parameters (i.e., specific surface area, slit-pore size, and solid-solid interaction energy) all utilize the same data with MS, and as the most common treatment, the correction parameter (Λ_b) for co-volume modification in Peng-Robinson equation of state (PR EOS) is set as -0.2. At the fixed condition (pore width 1.12 nm, temperature 298 K, pressure interval 0-20 MPa), by comparing the methane adsorption density of SLD and MS, the deviation varies with pressure and is 19.02 % at 20.327 MPa. It indicates that the original SLD model with a typical value of Λ_b is inappropriate for theoretical adsorption simulation. Based on the SLD model, at the fixed pressure, the calculated adsorption possesses a negative relationship with Λ_b. Herein, based on the positive correlation of deviation with pressure, Λ_b could be expressed as the positive exponential function of pressure. With the new expression, the average absolute percent error (AAD) of SLD model is reduced from 24.96 % to 5.87 %. Therefore, the SLD model with the new expression of Λ_b is accurate enough for theoretical adsorption simulation, which makes sure that SLD model is totally applicable to theoretical adsorption study and prediction, in addition to the conventional experimental data interpretation.

KEYWORDS - *Simplified local density (SLD) model, Peng-Robinson equation of state, Theoretical adsorption.*

1. INTRODUCTION

SLD-PR model is an efficient and popular tool for experimental adsorption interpretation and the pore characterization. But SLD-PR model's accuracy on theoretical adsorption simulation is unknown, which restricts the model's ability to be as acceptable as MS[1, 2], and density functional theory (DFT)[3]. Herein, we validated and modified the SLD-PR model for an accurate theoretical adsorption simulation. In our research, only excess adsorption was considered.

2. MODEL VALIDATION AND MODIFICATION

2.1. The SLD model

SLD adsorption model is the combination of PR EOS and fluid-wall interaction potential model. The adsorbed density at a particular position of the pore could be calculated firstly. And by

74

integral, the adsorption in a pore could be obtained. The detailed expressions of SLD model could refer to our previous paper[4].

2.2. The novel expression of dynamic Λ_b

Based on the GCMC data and parameter values, the common utilized typical values for Λb, 0 and -0.2, are both inappropriate for theoretical adsorption in SLD model (Fig.1).
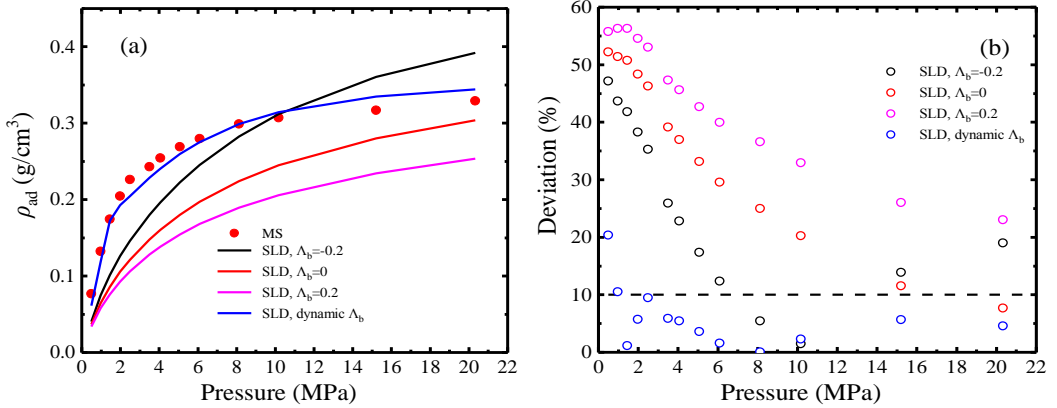
Figure 3. *The SLD simulation with different Λ_b values. (a) absolute adsorption, (b) the deviations for with different Λ_b values*

By curve fitting (Fig. 2), a dynamic Λ_b could be obtained for ensuring the theoretical adsorption accuracy of SLD model. The formula could be obtained as below.

$$L_b = 0.14\ln\left[p/(9.5p_c)\right] \tag{1}$$

Where, p and p_c are pore pressure and critical pressure, separately. By comparing the adsorption curves of SLD model with different values of Λ_b, the dynamic Λ_b ensures the accuracy of SLD model for theoretical adsorption (Fig. 1a). Except the extemely low
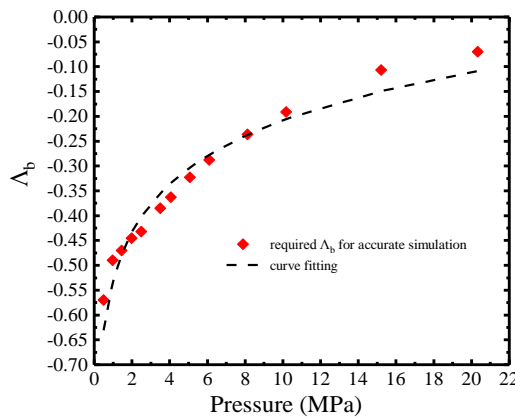
Figure 2. *Curve fitting for dynamic Λ_b*

75

pressure, the deviations of adsorption value at different pressure are all much lower than 10% , shown in Fig. 1b.

2.3. Discussion

Controlled by the fixed fluid-solid interaction (Fig. 3a), at 20.327 MPa, lower value of Λ_b results in larger adsorbed density distributions (Fig. 3b). It indicates that, the adsorption possesses negative relationship with the value of Λ_b. The impact of Λ_b on correction is that the positive and negative values could make the adsorption value to be lower and larger than the original adsorption value, separately.
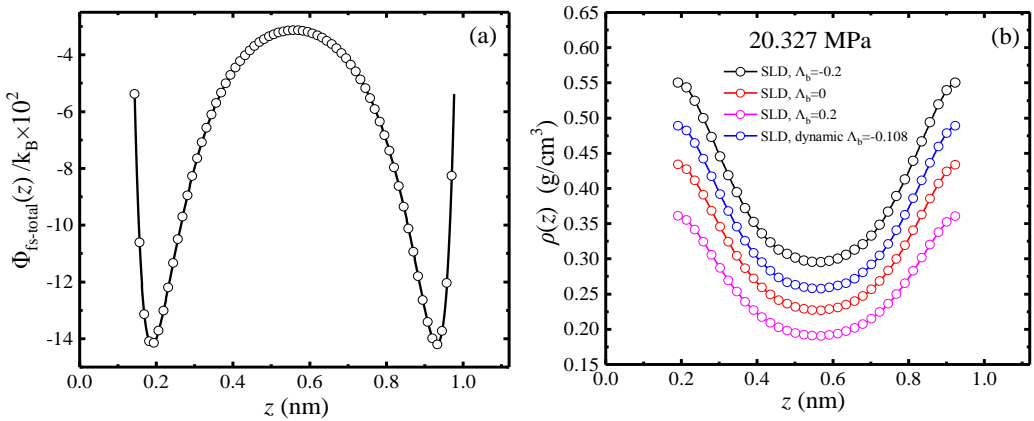
Figure 3. *The effect of Λ_b on density distribution. (a) the fluid-wall interaction potential. (b) the density distributions for different Λ_b values at 20.327 MPa.*

With the dynamic Λb or the fixed Λb (zero), in the pore, the adsorbed density minimum has positive relationship with pressure, same as the relationship of bulk density and pressure. However, for the adsorbed density distribution calculated by the SLD model with dynamic Λb, the adsorbed density maximum arises with pressure at first and then declines, which could be explained by the effect of bulk density and is consistent with the previous research, proving the correctness of dynamic Λb.
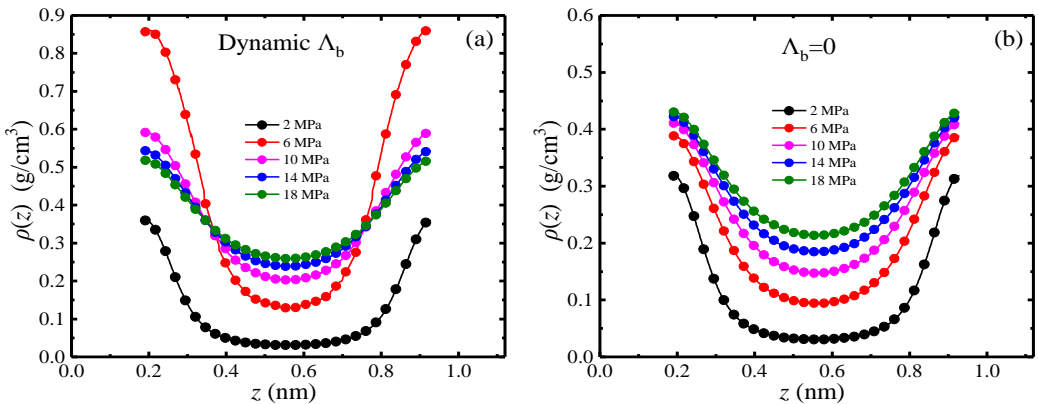
Figure 4. *The effect of pressure on density distribution for two different kinds of Λb values. dynamic Λb, (b) $\Lambda b=0$.*

76

For further validation of dynamic Λb, shown in Fig. 5, the adsorptions in the pores with various wall properties were utilized. The SLD model with the fixed Λb (zero) presents inaccurate adsorption curves, while the adsorption curves obtained by the SLD model with the dynamic Λb fit well with the MS data. The validation underlines the necessity of dynamic Λb.
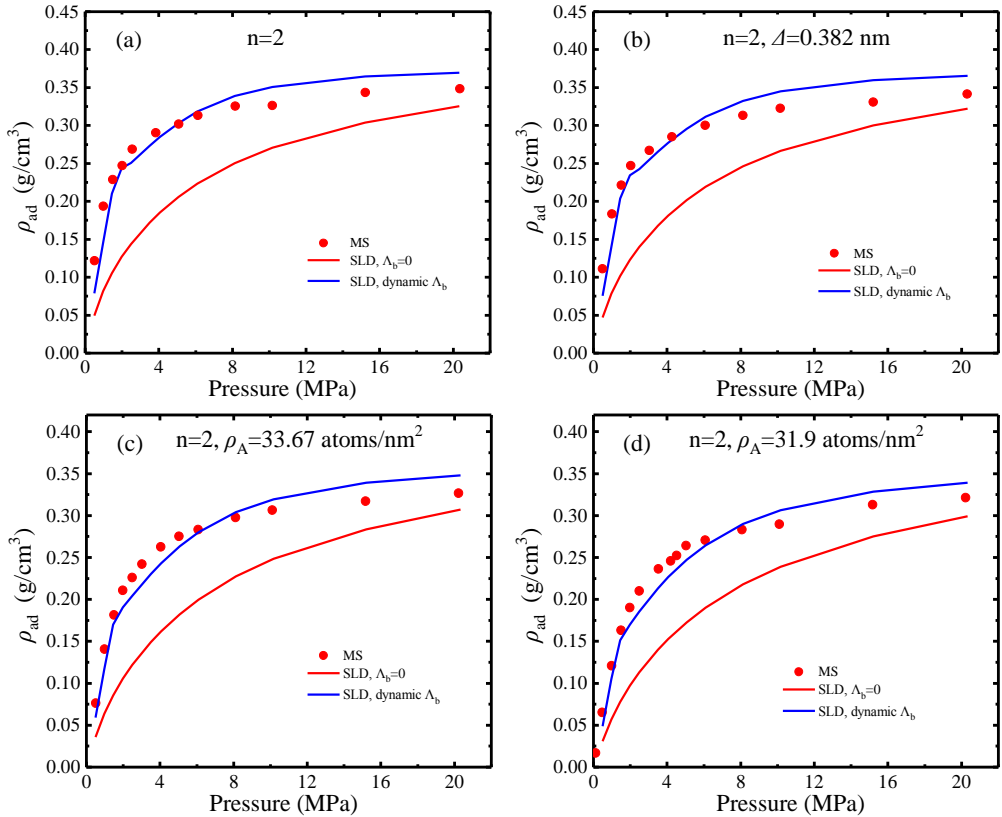
Figure 5. *Further validation of modified SLD model with dynamic Λ_b value at different wall properties.*

3. CONCLUSION

With the dynamic Λ_b, the SLD model could be as accurate as MS method, for theoretical adsorption. The dynamic Λ_b could reveal the correct effect of bulk density on excess adsorbed density that the maximum density arises with pressure at first and then declines. For the pore with various properties, the dynamic Λ_b is still appropriate for theoretical adsorption.

REFERENCES

[1]. L. Huang, Z. Ning, Q. Wang, H. Ye, Z. Chen, Z. Sun, F. Sun, H. Qin, Enhanced gas recovery by CO 2 sequestration in marine shale: a molecular view based on realistic kerogen model, Arabian Journal of Geosciences 11(15) (2018) 404. http://dx.doi.org/10.1007/s12517-018-3762-5

77

[2]. R. Song, M. Cui, Molecular simulation on competitive adsorption mechanism of CH 4/CO 2 on shale kerogen, Arabian Journal of Geosciences 11(15) (2018) 403. http://dx.doi.org/10.1007/s12517-018-3750-9

[3]. H. Agrawal, A. Mishra, Evaluation of initiating system by measurement of seismic energy dissipation in surface blasting, Arabian Journal of Geosciences 11(13) (2018) 345. http://dx.doi.org/10.1007/s12517-018-3683-3

[4]. X. Wu, Z. Ning, G. Han, Q. Wang, Z. Zhong, R. Qi, Z. Cheng, L. Huang, Modified SLD model for coalbed methane adsorption under reservoir conditions, Arabian Journal of Geosciences 12(18) (2019) 562. http://dx.doi.org/10.1007/s12517-019-4763-8

The Potential of Cold-Water Damage on a High Pour Point Reservoir after Long-Term Injection

Mibang WANG[1*], Shenglai YANG[1], Zuhao ZHENG[1], Jing WEN[2], Jichang ZHANG[2], Qicheng LIU[2], Quanzheng MA[1]

[1] *State Key Laboratory of Petroleum Resources and Prospecting, Beijing, China*
[2] *PetroChina Liaohe Oilfield Company, Panjin, Liaoning, China*
* zgsydxwmb@163.com

ABSTRACT

High pour point oil is a kind of temperature sensitive reservoir. After long-term cold waterflood development, it is necessary to evaluate the degree or potential possibility of cold-water damage. In this study, the oil-water relative permeability curves, oil recovery and oil components under different displacement PV number at different temperatures were studied by using live oil and artificial-made 1m long cores under the current formation pressure (12 MPa). The results show that the decrease of temperature will lead to the decrease of flow capacity of crude oil and injection water, the increase of residual oil saturation and the decrease of oil recovery. Most importantly, the retention of heavy components in the pores of the formation is deepened at low temperature. It is suggested that the development plan should be changed and the injection temperature should be increased to reduce the impact of cold damage. This study is helpful to deepen the understanding of the cold damage phenomenon of high pour point oil and reduce the adverse effects of long-term low-temperature water injection.

KEYWORDS - *High pour point oil reservoir; Oil-water relative permeability; retention of heavy components.*

1. INTRODUCTION

The crude oil with wax content more than 20% and the pour point (PPT) higher than 40 ℃ is called high PPT oil [1-3]. The high PPT oil reservoir is extremely sensitive to temperature. When the temperature is lower than the wax appearance temperature (WAT), the precipitated wax crystals increase the viscosity of the crude oil to make the flow capacity worse; and at the same time deposit in the pores and the throat, reducing the reservoir permeability and porosity. Eventually, the oilfield production will decrease and the water injection pressure will increase, this phenomenon is called 'cold-water damage' [4-6]. It is generally confirmed that there is no 'cold damage' in the high PPT oil field where the difference between WAT and formation temperature is more than 10 ℃, such as the s84 field studied in this paper. However, after a long period of cold-water injection development, some phenomena show that the oil field is experiencing cold damage. The main purpose of this paper is to use the long core displacement experimental device to obtain the accurate oil-water relative permeability curve and oil displacement efficiency, at the same time, to obtain the migration rule of heavy components in the core, and then to evaluate the potential of cold damage.

2. MATERIALS AND EXPERIMENTAL PROCEDURE

The live oil sample used in the experiment was compounded by dead oil collected from the ground wellhead and dissolved gas. The dead oil sample has the characteristics of high PPT (49 ºC), high WAT (61.5 ºC), mediate viscosity (5.84 cP at 100 ºC), high wax content (55.18%). A total of 1m long artificial core is used in the experiment, and about 3% clay is added, which can be more realistic simulation of reservoir damage.

The experimental equipment mainly includes ISCO pump, long core holder, back pressure valve (BPV) and incubator, and the experimental flow chart is shown in Figure 1. The experimental

79

process includes: a) The core samples were evacuated for 1 h and then saturated with formation water for 1h under 75 ℃ and 2MPa (BPV) ; b) The 3 PV of kerosene was injected through the core under 2MPa (BPV) until no water was produced to achieve the immobile water, then gradually pressurize the system to 12 MPa (BPV); c) the kerosene was displaced with 2 PV of live oil to achieve initial oil saturation under 12MPa (BPV); d) reduce the temperature of the incubator to the design temperature and keep it constant for 12 h, and then use formation water to displace the live oil until no oil production in the outlet. Record the oil production, water production and the pressure difference between the upstream and downstream in the process. It should be noted that the displacement speed of the whole experimental process is 0.2 ml / min
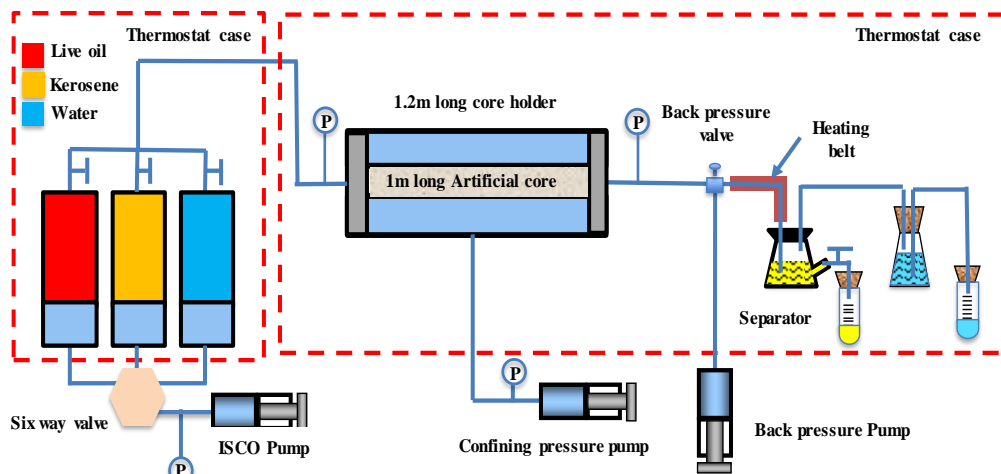
Figure 4. *Schematic diagram of the experimental apparatus.*

3. RESULTS AND DISSCUSSION

3.1. Effect of temperature on the oil-water relative permeability

As shown in Figure 2(a), temperature has a great influence on the shape of relative permeability curve. With the decrease of experimental temperature, Kro and Krw both decreased; the residual oil saturation increased significantly, and the relative permeability of water phase corresponding to the residual oil saturation decreased. All this phenomenon indicating that the water cut increased rapidly, and the effect of water flooding became worse. In addition, the two-phase co-flow region is narrowed, and the isotonic point corresponds to the left shift, indicating that the core wettability changes from water wet to oil wet[7]. Obviously, viscosity effect is the most important reason. When the temperature is lower than 50 ℃, the viscosity of crude oil increases exponentially as shown in Figure 2(b). At 39 ℃, the viscosity is nearly 70 times higher than at 65 ℃.

3.2. Changes of recovery

Moreover, as shown in Figure 2(v), the recovery and water free recovery can be significantly increased by increasing temperature. Therefore, it is necessary and urgent to improve the water injection temperature for the current reservoir development.

3.3. Changes of oil composition

Further, table 3 shows the composition of oil samples under different temperatures and injection PV 0f water drive. It clearly shows that the lower the temperature is and the larger the PV number is,

80
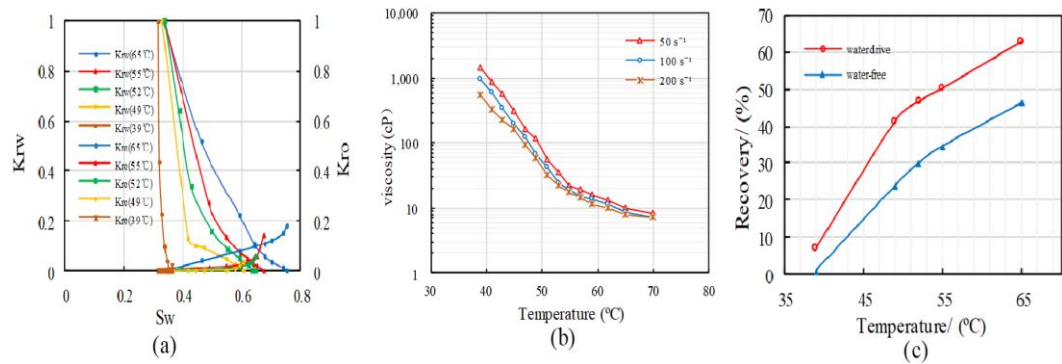
***Figure** 2. Experimental curve: (a) Comparison of live oil-water relative permeability curves at different temperatures; (b) Viscosity of crude oil at different shear rates under 12MPa; (3) Displacement efficiency at different temperatures.*

the lower the saturation content is, which means the greater the retention of heavy components in the core. It also means that if no action is taken, the retention degree of heavy components in the reservoir will continue to deepen, and the degree of cold damage will be increase.

***Table 1.** This is the Style for Table Captions.*

Temperature/ºC	Injected PV	Asphaltene	resins	aromatics	saturation
55	0.3PV	0.37	5.74	11.26	82.63
	0.6PV	0.51	6.04	11.77	81.68
	0.9PV	0.66	6.34	12.86	80.14
52	0.3PV	0.77	5.48	12.12	81.63
	0.6PV	0.74	6.64	12.18	80.44
	0.9PV	0.69	6.71	13.17	79.43
49	0.3PV	0.83	6.73	14.22	78.22
	0.6PV	0.72	7.46	14.58	77.24
	0.9PV	0.67	8.31	15.97	75.05
39	0.3PV	0.73	7.32	14.21	77.74
	0.6PV	0.68	7.84	15.28	76.20
	0.9PV	0.63	8.28	16.27	74.82
Original		0.31	5.4	10.12	84.17

4. CONCLUSION

In this paper, the possibility of cold damage in S84 high PPT oil field is evaluated by long core experiment in laboratory. It is found that with the decrease of temperature, the relative permeability of oil phase and water phase will decrease, the residual oil saturation will increase, the oil recovery will decrease, and the deposition of wax crystal on the rock indicates that the wettability will turn to oil wetness. The most important thing is that the movement rate of heavy components in crude oil decreases at low temperature, and the retention degree in the reservoir increases, which will increase the impact of cold damage. In general, the degree of cold injury of S84 is slight at present, but the production system needs to be changed, and the water injection temperature needs to be increased to reduce the impact of cold injury

REFERENCES

81

[1]. Z. Wei, Z. Tang, O. Orodu. Case study of the impact of cold and hot waterflooding performance by simulation and experiment of high pour point oil reservoir, Liaohe Oilfield, North-East China, SPE (2010), 128873. DOI:10.2118/128873-MS

[2]. Wang, Y., Liu, Y. & Sun, L. Arab J Geosci (2019) 12: 297. DOI :https://doi.org/10.1007/s12517-019-4413-1.

[3]. Song, L., Ning, Z. & Duan, L. Arab J Geosci (2018) 11: 472. DOI : https://doi.org/10.1007/s12517-018-3842-6

[4]. R. K. Romeu, C. N. Khalil, A Rabinovitz, Paraffin Precipitation in the Formation in Dom Joao Field, Brazi. SPE,21108-MS, 1990. DOI:10.2118/21108-MS

[5]. Zheng, W., Liu, Y., Huang, J. et al. Arab J Geosci (2018) 11: 640. DOI : https://doi.org/10.1007/s12517-018-3965-9.

[6]. Huang, S., Yao, Y., Zhang, S. et al. Arab J Geosci (2018) 11: 285. DOI : https://doi.org/10.1007/s12517-018-3639-7

[7]. Lu Wang, Yongming He, Hao Chen, et al. Experimental investigation of the live oil-water relative permeability and displacement efficiency on Kingfisher waxy oil reservoir, Journal of Petroleum Science and Engineering, 2019 178: 1029-1043. DOI : https://doi.org/10.1016/j.petrol.2019.04.027

Experimental Study on Gas Phase Flow Characteristics and Influencing Factors in Low-Permeability-Tight Gas Reservoirs

Jianxun Chen[1], Shenglai Yang[1]*, Cheng Zou[1], Qingyan Mei[2], Yuan Zhou[2], Yuxiang Zhang[1]

[1] State Key Laboratory of Petroleum Resources and Prospecting, China University of Petroleum (Beijing), Beijing 102249, China

[2] Exploration and Development Research Institute of Southwest Oil & Gas Field Company, PetroChina, Chengdu 610041, China

* yangsl2021@163.com

ABSTRACT

After long-term development, low permeability-tight gas reservoir faces the problems of complex water relationship and low productivity. Firstly, X-ray CT is used to analyze the micro pore structure of cores; secondly, the experiments of gas-phase single-phase and gas-water two-phase flow are carried out under different conditions to analyze the influence of pore structure and water saturation on gas-phase flow. The results show that the gas flow characteristics and gas well productivity are mostly affected by pore structure, secondly by water saturation, and relatively little by temperature and pressure. The reservoirs with fractures are easy to form high permeability channel, which makes the relative permeability of gas phase increase and the water drive efficiency decrease. Compared with laboratory conditions, under high temperature and pressure conditions, the increase of gas water viscosity ratio results in the increase of relative permeability of gas phase and the decrease of water drive efficiency. The existence of water phase increases the resistance of gas phase flow and obviously reduces the conductivity and permeability of the reservoir. Controlling water saturation and improving reservoir conductivity can effectively improve gas well productivity. This study has a certain guiding significance for the analysis of gas phase flow, the adjustment of production plan and the application of numerical simulation in low permeability-tight sandstone gas reservoir.

KEYWORDS – *Low-permeability gas reservoir, Types of cores, Gas-water flow, Experimental condition, Flow characteristics*

1. INTRODUCTION

As an important part of oil and gas resources, low permeability-tight gas reservoirs are widely distributed in the world [1-3]. After long-term development, gas reservoir will enter water production period, how to improve gas well productivity becomes difficult.

Previous studies have found that pore structure and water have an important influence on gas phase flow [4,5]. There are some differences between the characteristics of gas-water two-phase permeability measured under laboratory conditions and reservoir conditions [5].

Taking Xujiahe Formation sandstone gas reservoir in the central Sichuan Basin of China as the target block to analyze the gas flow characteristics and optimize the plan to improve productivity of water-bearing gas reservoir.

2. METHOD OF EXPERIMENTS

2.1. Core samples

The experiment cores are natural cores from the target block. The cores with diameter of about 2.5 cm are used for gas flow experiments. The full diameter cores with diameter of 6.5 cm are used for gas-water two-phase flow experiments. The physical properties of cores are shown in Table 1. According to the observation of core surface, if there is fracture on the core surface, it is fracture-pore type, otherwise it is pore type.

Table 1. *Some parameters of natural cores in experiments.*

Core samples	Length (cm)	Diameter (cm)	Porosity (%)	Permeability ($\times 10^{-3} \times \mu m^2$)	Core types
K1	4.239	2.559	6.64	0.32	Pore
K2	4.192	2.534	9.34	0.19	Pore
K3	4.254	2.539	6.34	0.14	Pore
K4	4.424	2.549	9.19	0.06	Pore
L1	4.126	2.560	7.36	0.24	Fracture-pore
L2	4.207	2.549	10.83	0.19	Fracture-pore
L3	4.297	2.559	4.98	0.07	Fracture-pore
W1	9.454	6.604	7.44	0.27	Fracture-pore
W2	8.990	6.586	7.13	1.26	Fracture-pore
W3	8.766	6.564	6.87	0.08	Pore
W4	6.422	6.552	8.48	0.15	Pore

2.2. Experimental conditions

The temperature is 90 ℃, the overburden pressure is 45 MPa, and the pore pressure is 30 MPa under reservoir conditions. The temperature is 25 ℃, the overburden pressure is 9 MPa, and the pore pressure is 6 MPa under laboratory conditions.

2.3. Experimental methods

The high temperature and pressure experiments system is adopted, and the flow chart is shown in Figure 1. Firstly, the pore core and fracture-pore core are scanned by CT at the resolution 1 micron. Secondly, gas flow experiments are carried out in irreducible water cores and dry cores under reservoir conditions. The method is to keep the inlet pressure 30MPa constant, gradually reduce the outlet pressure to 24MPa in steps of 0.2MPa, and record the stable gas flow rate under different pressure differences. Finally, the unsteady state method of gas driving water is used to carry out the gas-water two-phase flow experiment under reservoir conditions and laboratory conditions.
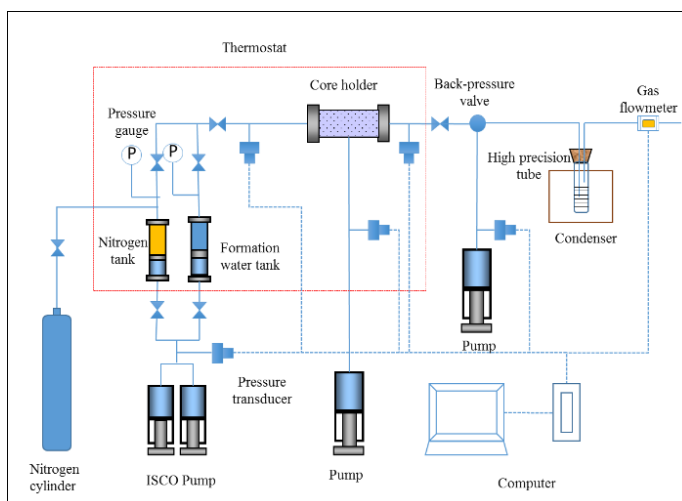
Figure 1. *Flow chart of gas flow experiment*

84

3.   RESULTS AND DISCUSSION

3.1. Pore structure characteristics

The pore distribution of porous core (Fig. 2a) is relatively dense, but the connectivity between pores is relatively poor, and the permeability is relatively low. The pore distribution of fracture pore core (Fig. 2b) is relatively heterogeneous; although the direct pore connectivity is poor, the fracture connectivity is strong and the permeability is relatively high. Therefore, the degree of fracture development and pore connectivity are the main factors affecting permeability.
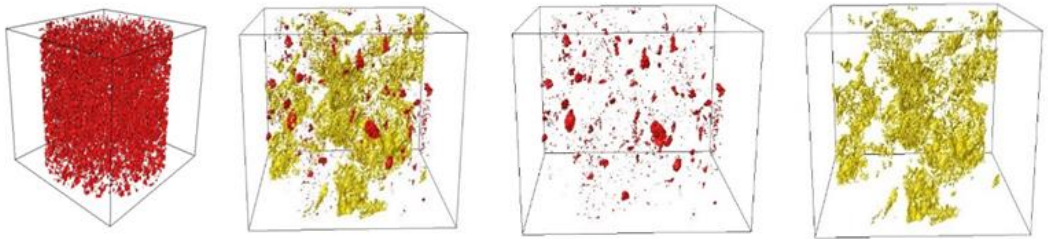
Figure 2. *Pore network models (a: Pore type; b: Fracture-pore type; c: Pores in Fracture-pore; d: Fractures in Fracture-pore)*

3.2. Gas phase flow characteristics

According to Figure 3, with the increase of pressure difference, the characteristics of gas phase flow is from linear flow to high-speed non Darcy flow in dry cores.
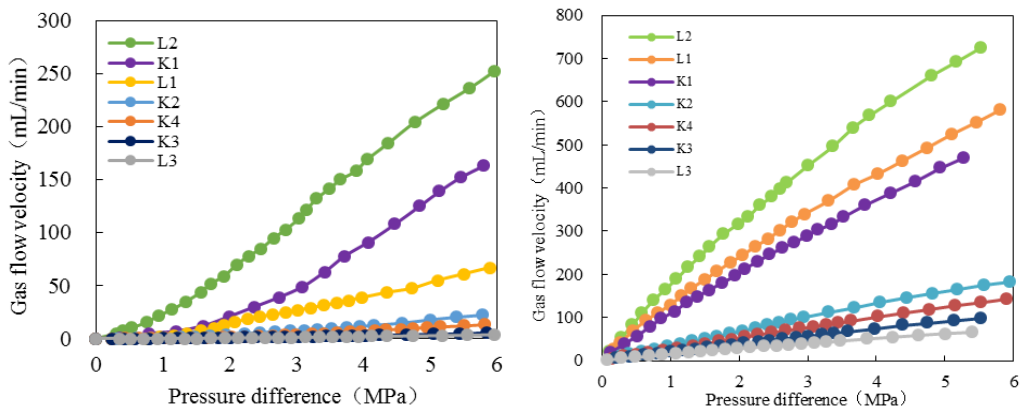
Figure 3. *Gas phase flow characteristics (a: Irreducible water cores; b: Dry cores)*

There is an obvious starting pressure for the gas phase flow in the irreducible water cores; the gas phase flow changes from non Darcy flow to linear flow with the increase of pressure difference. Experiments show that the existence of water phase increases the resistance of gas phase flow, reduces the gas phase flow capacity, and leads to the gas well productivity reduction.

3.3. Gas-water two-phase flow characteristics

According to Figure 4, the trend of relative permeability of water phase in four types of cores is similar. Under the same water saturation, the relative permeability of gas phase in fractured core is higher. So, fractures can improve the conductivity of the reservoir.

85
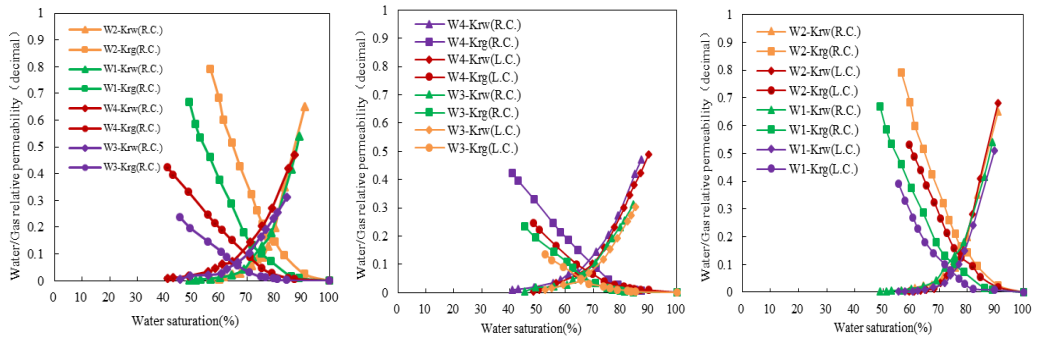
Figure 4. *Gas-water two-phase flow characteristics (a: Reservoir condition; b: Pore cores under different conditions; c: Fracture-pore cores under different conditions)*

Under the reservoir conditions, the efficiency of gas drive water is higher, so the irreducible water saturation is lower. And the gas phase relative permeability is high under the same water saturation. Therefore, the relative permeability measured under reservoir conditions is more practical.

4. CONCLUSION

Reservoir permeability is mainly affected by fracture development and pore connectivity. Water phase can reduce the flow capacity of gas phase. Fracture can improve the conductivity of reservoir. Controlling water saturation and improving reservoir permeability are effective ways to improve gas well productivity.

REFERENCES

[1]. El Tokhi, M., B. El Din Mahmoud Amin, and H. Arman. Geochemical Characters of the Gabbroic Rocks in Ophiolite Sequences of North Hatta Area, United Arab Emirates. Acta Physica Polonica A 130.1 (2016): 17-22. *DOI : 10.12693 / APhysPolA.130.17.*

[2]. Ding, Jingchen, et al. Dynamic threshold pressure gradient in tight gas reservoir and its influence on well productivity. Arabian Journal of Geosciences 11.24 (2018): 783.

[3]. Zheng, Wenkuan, et al. Study on the optimal development method for offshore buried hill fractured reservoirs. Arabian Journal of Geosciences 11.20 (2018): 640.

[4]. Kara, Ü., H. O. Tekin, and I. Akkurt. Computed tomography routine examinations and the related risk of cancer. Thorax 249 (2016): 120. *DOI: 10.12693/APhysPolA.130.409.*

[5]. Zhou, Chao, X. D. Wu, and Hui Li. Influence of in-situ stress distribution on selection of fracturing fluid backflow technology (ICCESEN 2015), 14-19 October, 2015 Antalya-Turkey. *DOI: 10.12693/APhysPolA.130.347.*

Determination of Radiation Shielding Properties of Pumice Aggregate Concretes using GAMOS

Aycan ŞAHİN[1]*, Kadir GÜNOĞLU[2], İskender AKKURT[3]
[1] Akdeniz University, Vocational School of Health Services, Antalya-TURKEY
[2] Isparta University of Applied Sciences, Technical Vocational School, Isparta- TURKEY
[3] Suleyman Demirel University, Science Faculty,Physics Department, Isparta-TURKEY
*aycansahin@akdeniz.edu.tr

ABSTRACT

The photon attenuation coefficient results of pumice aggregate concretes were calculated for 662 keV energy by using GAMOS Monte Carlo code. In order to test the validity of this code, the values of the calculated photon attenuation coefficients were compared with the previously published experimental data. As a result of this comparison, the values calculated using GAMOS Monte Carlo code are in good agreement with the experimentally measured values. Therefore, GAMOS simulation is an alternative technique for determining the shielding performance of concrete.

KEYWORDS: photon attenuation, pumice, GAMOS

1. INTRODUCTION

Radiation has been used for many years in the field of health research and treatment, industrial irradiation and space research. The increasing use of radiation has also made the issue of radiation protection important. Against the stochastic and deterministic effects of ionizing radiation, the importance of various protective materials increased in line with the protection principles. In the laboratory, radiation protection of many materials has been studied. However, these studies can be done with a limited number of energy. This study employs Monte Carlo method to estimate mass attenuation coefficient. This method is used for radiation transport purposes and utilizes probability distributions and random numbers to approximate such related quantities as flux, energy deposition, dose, etc. There are many MC-based codes. (Fluka, EGS etc.)

Gamos (Geant4-based Architecture for Medicine-Oriented Simulations) is a Geant4-based code system. This Monte Carlo simulation software compiled from Geant4 provides great convenience for applications in the field of medical physics, as it does not require C ++ knowledge, has a comprehensive command language, and is easy to use. In addition, the GAMOS project has reached more than a thousand users worldwide and the reliability of the code has been verified by researchers working on various radiation applications with the support of literature. [1-3]

In this study, linear attenuation coefficient of pumice doped concretes in different ratios were calculated by using GAMOS program for 662 keV gamma energy. The results obtained from the simulation were compared with the experimental results.

2. MATERIAL AND METHOD

In this study, a variant of the famous Monte Carlo package Geant 4 called GAMOS (version 5.1.0) was employed for modeling the geometry of the problem as well as estimating the interaction of source photons [1-3]

Normal aggregate and pumice were used as aggregate in concrete production. Pumice was used in fractions 0, 50 and 100% in concrete which are tagged as N, NP and P, respectively. The linear attenuation coefficient of N,P,NP concretes for 662 keV which were computed GAMOS and the obtained values were compared with the measurement result [4].

The photon was modeled as a point source in a cube of 2 mm directed as a parallel beam toward a collimator having a 0.5 cm opening and made of lead. The beam passed the 0.5 cm thick absorber before reaching the detector which was described as NaI(Tl) material.

All the materials in the problem geometry were placed in a cube of air with 100 cm side. A total of three different samples as shown in Table were investigated in this study, all of which contained a known proportion of pumice.

In radiation protection, the thickness of the protective agent to be used and the radiation absorption property are important. For this we need to know the density of the material.

The photon attenuation coefficients have been evaluated by comparing I and I0, which are the count rates measured by the detector, respectively, with and without the absorber of thickness x.

$$\mu = \frac{1}{x}\ln\left(\frac{I_0}{I}\right)$$

(1)

3.   RESULTS AND DISCUSSION

The linear attenuation coefficient of the concrete produced using pumice and normal aggregate in different ratios as aggregate was calculated by using GAMOS, which is a Monte Carlo simulation code. The simulation results (G) obtained are shown in Figure 1 together with the experimental results (Exp) found in the literatüre [4].
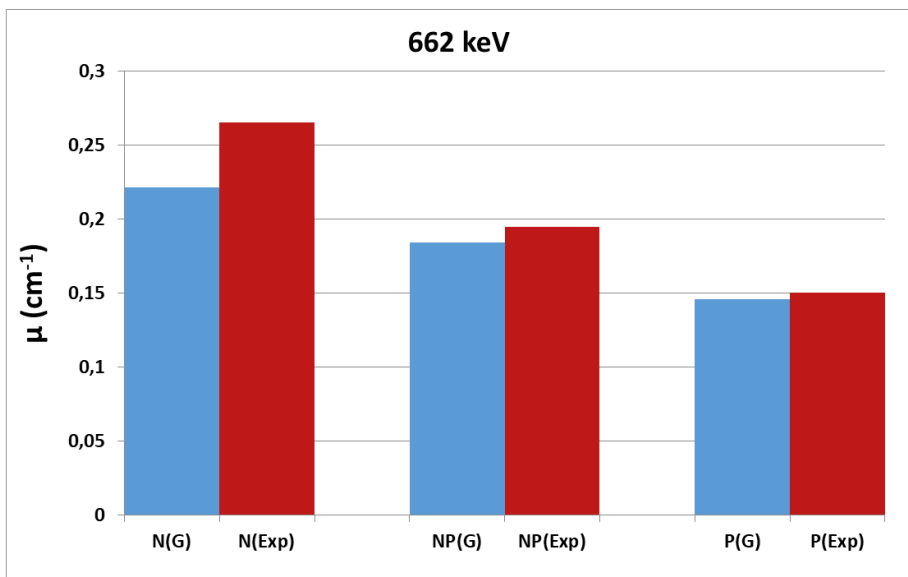
Figure 1. *Simulation and experimental linear attenuation coefficients*

In Figure 1 it can be seen that there is a good agreement between experimental and calculated results. In addition, both experimental results and simulation results showed that the attenuation coefficient decreased with increasing pumice ratio.

REFERENCES

[1]. Agostinelli, S. et al., Geant4 - A Simulation Toolkit, Nucl. Instrum. Meth. A 2003; 10.1016/S0168-9002(03)01368-8

88

[2]. Arce P, Rato P, Canadas M. and Lagares, JI. GAMOS: A GEANT4-based easy and flexible framework for nuclear medicine applications. 2008 IEEE Nuclear Science Symposium and Medical Imaging Conference (2008 NSS/MIC), 2008; 10.1109/NSSMIC.2008.4775023.

[3]. Geng, J.P., Cao, T.G., Li, D.F., An, H.L., Han, Y.R., Li, J., Hu, J.S., Li, N.N., Zhan, Y., 2014. Calculation of the physical and microdosimetric parameters of electron and alphaparticle radiation using Monte Carlo simulations. Chin. Phys. Lett. 31(038701_1–038701_3).

[4]. A.B. Chilton, J.K. Shultis, R.E. Faw, Principles of Radiation Shielding, Prentice-Hall, Englewood Cliffs, 1984.

[5]. Akkurt I., Akyıldırım H., "Radiation Transmission of Concrete Including Pumice For 662, 1173 And 1332 keV Gamma Rays" Nuclear Engineering And Design. 252 (2012) 163-166, DOI: 10.1016/j.nucengdes.2012.07.008

Electrochemical Performance of Graphene Supported MnO₂ and Fe₂O₃ Nanocomposites for Supercapacitors Application

Jolita Jablonskiene* **Juratė Vaiciuniene, Giedrius Stalnionis, Audrius Drabavičius, Loreta Tamasauskaite-Tamasiunaite, Eugenijus Norkus**

Center for Physical Sciences and Technology, Vilnius, Lithuania
*jolita.jablonskiene@ftmc.lt

ABSTRACT

In this study, we report a simple approach for preparation of the graphene (GR) or carbon (C) supported manganese(IV) and iron(III) oxides (denoted as MnO_2-Fe_2O_3/GR or MnO_2-Fe_2O_3/C) using microwave-assisted synthesis. Scanning electron microscopy (SEM) has been used for the characterization of morphology, structure and composition of the prepared nanocomposites. Electrochemical performance has been evaluated using cyclic voltammetry.

It was found that the highest specific capacitance (C_s) was achieved at the MnO_2-Fe_2O_3/GR electrode. Moreover, the retention for the graphene supported MnO_2-Fe_2O_3 was estimated to be 37.14 % compared with that of the carbon supported MnO_2/C, Fe_2O_3/C and MnO_2-Fe_2O_3 suggesting a great potential for supercapacitors.

KEYWORDS - *Supercapacitors, Graphene, Manganese, Iron*

1. INTRODUCTION

With the increasing desire for the clean, safe and renewable energy sources, supercapacitors have attracted significant attention as one type of efficient energy storage device due to their high power density, long cycling stability, fast charge-discharge rate and superior safety in the modern electronics [1]. MnO_2 as one kind of pseudocapacitive materials is especially attractive due to its low cost, nontoxicity, and high theoretical capacitance [2]. Fe_2O_3 is an environmentally friendly, low cost, non-toxic and stable electrode material [3].

Herein, we demonstrate a facile microwave irradiation method for the synthesis of graphene or carbon supported MnO_2-Fe_2O_3 nanocomposites with the aim to apply them as material for supercapacitors.

2. EXPERIMENTAL

The MnO_2-Fe_2O_3/GR nanocomposite was prepared by microwave-assisted heating. In a typical experiment, 0.2 g of $KMnO_4$, 0.5 g of $FeSO_4 \cdot 7H_2O$ and 0.1 g of graphene powder were dispersed in the 20 ml of deionized water. The obtained reaction mixture was put into a microwave reactor Monowave 300 (Anton Paar) for 5 min at a temperature of 150 °C. The precipitate was filtered out, washed with water and dried in a vacuum oven at a temperature of 80 ˚C for 4 h.

The morphology and composition of the prepared catalysts were characterized using an SEM-focused ion beam facility (Helios Nanolab 650) equipped with an EDX spectrometer (INCA Energy 350 X-Max 20). Mn and Fe loadings in the prepared samples were estimated using an ICP optical emission spectrometer Optima 7000DV (Perkin Elmer).

The electrochemical performance of the MnO_2/C, Fe_2O_3/C, MnO_2-Fe_2O_3/C and MnO_2-Fe_2O_3/GR was tested by cyclic voltammetry (CV) using a Zennium electrochemical workstation (ZAHNER-Elektrik GmbH & Co.KG). The prepared nanocomposites coated on the glassy carbon electrode (GCE) with a geometric surface area of 0.07 cm² were employed as working electrodes, a Pt sheet as a counter electrode, and an Ag/AgCl/KCl electrode was used as reference. The working electrodes were prepared as follows: the 10 mg of the prepared nanocomposites were dispersed ultrasonically in a 0.1 ml of 2 % of polyvinylidene fluoride (PVDF) in an N-methyl-2-pyrrolidinone (NMP) solution for 1 h. Then, 5 µL of the prepared suspension mixture was pipetted

90

onto the polished surface of a GCE and dried in an oven for 2 h at a temperature of 80 ˚C. Cyclic voltammograms (CVs) were recorded in a 1 M Na_2SO_4 solution at different scan rates between 10 and 200 mV s^{-1} at ambient temperature. The measuring potential range was from 0.05 to 1.10 V. All solutions were deaerated by argon for 15 min prior to measurements.

Specific capacitance (C_s, F g^{-1}) was calculated from CV measurements. The mass of the prepared nanocomposites was 0.5 mg.

3. RESULTS AND DISCUSSION

Figure 1 shows the representative SEM images of synthesized MnO_2/C (a), Fe_2O_3/C (b), MnO_2-Fe_2O_3/C (c) and MnO_2-Fe_2O_3/GR (d) nanocomposites. As evident from Fig. 1a, the formation of spherical MnO_2 nanoparticles as well as small clusters, which are made up of small spherical nanoparticles with average diameter of 50-70 nm is identified in the prepared MnO_2/C nanocomposite. The analogous view is observed for Fe_2O_3 nanoparticles of ca. 100-170 nm in size (Fig. 1b). Whereas, in the case of MnO_2-Fe_2O_3 nanocomposite, which was deposited on C (Fig. 1c) or GR (Fig. 1d), the nanotube-like structure with completely unoccupied spheres is formed. The assemblies of MnO_2-Fe_2O_3 particles in size of 250-300 nm are determined in the prepared nanocomposites (Fig. 1 c, d).
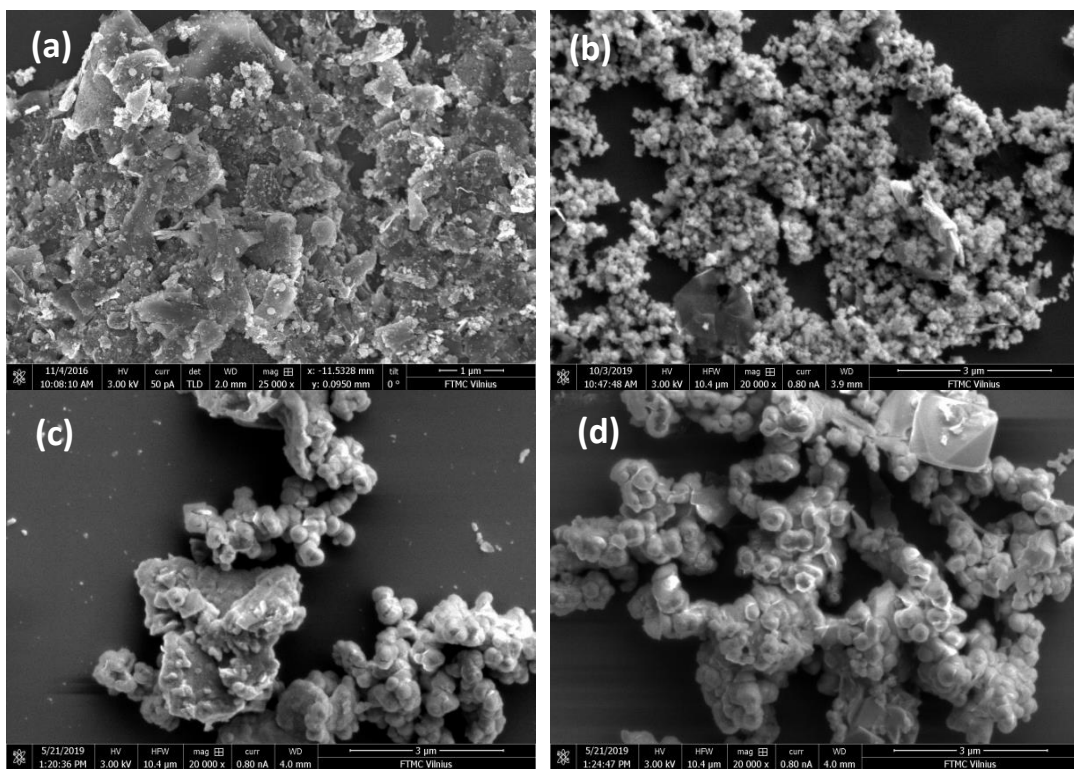
Figure 1. SEM images of MnO₂/C (a), Fe₂O₃/C (b), MnO₂-Fe₂O₃/C (c) and MnO₂-Fe₂O₃/GR (d).

3.1. Electrochemical performance of individual electrodes

Figure 2a shows electrochemical performance of the MnO_2/C, Fe_2O_3/C, MnO_2-Fe_2O_3/C and MnO_2-Fe_2O_3/GR electrodes evaluated in an aqueous 1 M Na_2SO_4 electrolyte at a scan rate of 10 mV s^{-1} in the potential window of 0.05 to 1.10 V vs. SHE. In all the cases quasi-rectangular shape

91

of CV curves is defined. The graphene based MnO_2-Fe_2O_3 nanocomposite shows a superior behaviour when compared to that observed for MnO_2/C, Fe_2O_3/C and MnO_2-Fe_2O_3/C electrodes.
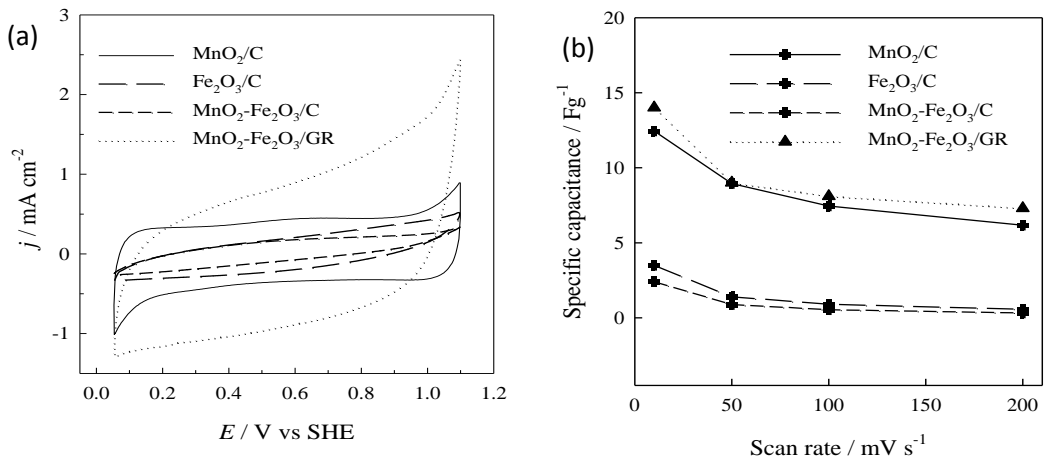
Figure 2. *(a) CVs of MnO$_2$/C, Fe$_2$O$_3$/C, MnO$_2$-Fe$_2$O$_3$/C and MnO$_2$-Fe$_2$O$_3$/GR recorded in a 1 M Na$_2$SO$_4$ solution at a scan rate of 10 mV s^{-1}. (b) Specific capacitance at different scan rates.*

However, when C support was used the significant decrease in the current value for MnO_2-Fe_2O_3/C nanocomposite is observed. Moreover, this value is much lower when compared to that determined for MnO_2/C alone. The voltammetric responses of the MnO_2/C, Fe_2O_3/C, MnO_2-Fe_2O_3/C and MnO_2-Fe_2O_3/GR electrodes at a scan rate of 10 mV s^{-1} are presented in Fig. 2a. C_s values for the same electrodes are 12.45, 3.5, 2.5 and 14 F g^{-1}, respectively (Fig. 2b). Meanwhile, C_s values at a scan rate of 200 mV s^{-1} are 6.17, 0.57, 0.33 and 7.2 F g^{-1} for the same electrodes and correspond to the retention of 50, 16.3, 13.2 and 51.4 %, respectively.

4. CONCLUSION

It was found a simple approach for the preparation of the graphene (GR) or carbon (C) supported manganese (IV) and iron (III) oxides using microwave-assisted synthesis. The synthesized MnO_2-Fe_2O_3/GR nanocomposite has the nanotube-like structure with completely unoccupied spheres. The highest specific capacitance of 14 F g^{-1} at a scan rate of 10 mV s^{-1} has been achieved at the MnO_2-Fe_2O_3/GR electrode as compared with that of MnO_2/C, Fe_2O_3/C and MnO_2-Fe_2O_3/C. It suggests a great potential as the electrode material for supercapacitors.

REFERENCES
[1]. A.Burke, J. Power Sources, 91 (2000) 37. DOI: 10.1016/S0378-7753(00)00485-7
[2]. N. Yu, H. Yin, W. Zhang, Y. Liu, Z.Y. Tang, M.Q. Zhu. Adv. Energy Mater. 6 (2016) 1501458. DOI: 10.1002/aenm.201501458.
[3]. W. Tian, X. Wang, C. Zhi, T. Zhai, D. Liu, C. Zhang, D. Golberg, Y. Bando, Nano Energy. 2 (2013) 754–763. DOI: 10.1016/j.nanoen.2013.01.004.

Carbon Supported Manganese(IV)-Cobalt(II/III) Oxides Nanoparticles for High-Performance Electrochemical Supercapacitors

Jolita Jablonskiene[*], Dijana Simkunaite, Juratė Vaiciuniene, Giedrius Stalnionis, Vitalija Jasulaitiene, Audrius Drabavicius, Loreta Tamasauskaite-Tamasiunaite, Eugenijus Norkus

Center for Physical Sciences and Technology, Vilnius, Lithuania
*jolita.jablonskiene@ftmc.lt

ABSTRACT

The MnO_2-Co_3O_4/C nanocomposites with lamellar and spherical shape nanoparticles (denoted as MnO_2-Co_3O_4/C-1 and MnO_2-Co_3O_4/C-2, respectively) have been prepared using a simple one-step microwave-assisted method. Scanning electron microscopy (SEM), transmission electron microscopy (TEM) and inductively coupled plasma optical emission spectroscopy (ICP-OES) have been used for the characterization of morphology, structure and and composition of the synthesized nanocomposites, whereas, electrochemical performance of the prepared nanocomposites has been evaluated using cyclic voltammetry (CV).

It was determined that morphology and structure have a significant influence on the electrochemical performance of the MnO_2-Co_3O_4/C nanocomposites. A high specific capacitance (C_s) of 661.32 F g^{-1} at a scan rate of 10 mV s^{-1} in a 1 M Na_2SO_4 solution has been obtained for the MnO_2-Co_3O_4/C-2 nanocomposite that has spherical shape nanoparticles. Moreover, it significantly outperforms the MnO_2-Co_3O_4/C-1 nanocomposite that has lamellar nanoparticles.

KEYWORDS - Supercapacitors, nanocomposites, Graphene, Manganese, Cobalt

1. INTRODUCTION

Supercapacitors have gained increasing attention due to their high power density, long cycle life, fast charge/discharge rate and are seriously viewed as potential candidates of next-generation energy storage devices [1, 2]. They are especially valued for lightness and flexibility determining their large-scale of possible applications ranging from consumer electronic or portable devices like mobile phones, computers, and memory back-up systems to hybrid electric vehicles or even large industrial machinery, for defense and military or space equipment [3].

The key issues in the developing of practical supercapacitors are the selection and fabrication of electrode materials in order to achieve a high energy density. Based on the different energy storage principles, supercapacitors are generally categorized into electrochemical double-layer capacitors using carbon materials and pseudocapacitors using metal oxides as active materials. Among the emerging electrode materials for pseudocapacitors, nanoscaled transition metal oxides or mixed metal oxides such as MnO_2, Co_3O_4, NiO, Fe_3O_4 and V_2O_5 are the most attractive materials, because they are featured by high theoretical specific capacitances, which are based on fast and reversible redox reactions with the electrolyte ions [3].

Herein, we demonstrate a facile microwave-assisted irradiation method for the synthesis of carbon supported MnO_2-Co_3O_4 nanocomposites with the aim to apply them as material for electrochemical supercapacitors.

2. EXPERIMENTAL

The MnO_2-Co_3O_4 nanocomposite supported on carbon was prepared in two different ways by the microwave-assisted heating. In the first way, 0.2 g of $KMnO_4$, 0.369 g of $Co(NO_3)_2 \cdot 7H_2O$ and 0.1 g of carbon powder were dispersed in the 20 ml of deionized water. The obtained reaction mixture was put into a microwave reactor Monowave 300 (Anton Paar) for 5 min at a temperature of 150 °C. The precipitate was filtered out, washed with water and dried in a vacuum oven at a temperature of 80 °C for 4 h. The prepared nanocomposite was labelled as MnO_2-Co_3O_4/C-1. In

the second way, 0.2 g of $KMnO_4$, 0.01 g of Co_3O_4 and 0.1 g of carbon powder were dispersed in the 20 ml of deionized water. The synthesis of nanocomposite was carried out at the same conditions. The prepared nanocomposite was labelled as MnO_2-Co_3O_4/C-2. Notably, Co_3O_4 was prepared by annealing of $Co(NO_3)_2 \cdot 7H_2O$ in air atmosphere in the muffle furnace at a temperature of 400 °C.

The morphology and composition of the prepared catalysts were characterized using an SEM-focused ion beam facility (Helios Nanolab 650) equipped with an EDX spectrometer (INCA Energy 350 X-Max 20). A shape and size of catalyst particles were examined using a transmission electron microscope Tecnai G2 F20 X-TWIN equipped with an EDX spectrometer with an r-TEM detector. For microscopic examinations, 10 mg of sample was first sonicated in 1 ml of ethanol for 1 h and then deposited on the Ni grid covered with a continuous carbon film. Mn and Co loadings in the prepared samples were estimated using an ICP optical emission spectrometer Optima 7000DV (Perkin Elmer).

The electrochemical performance of the MnO_2-Co_3O_4/C was tested using a Zennium electrochemical workstation (ZAHNER-Elektrik GmbH & Co.KG). The prepared nanocomposites coated on the glassy carbon electrode (GCE) with a geometric surface area of 0.07 cm^2 were employed as the working electrode, a Pt sheet as a counter electrode, and an Ag/AgCl/KCl electrode was used as reference. The working electrodes were prepared as follows: the 10 mg of the prepared nanocomposites were dispersed ultrasonically in a 0.1 ml of 2 % of polyvinylidene fluoride (PVDF) in an N-methyl-2-pyrrolidinone (NMP) solution for 1 h. Then, 5 μL of the prepared suspension mixture was pipetted onto the polished surface of a GCE and dried in an oven for 2 h at a temperature of 80 ^{o}C.

Cyclic voltammograms (CVs) were recorded in a 1 M Na_2SO_4 solution at different scan rates between 10 and 200 mV s^{-1} at ambient temperature. The measuring potential range was from 0.05 to 1.10 V. All solutions were deaerated by argon for 15 min prior to measurements.

3.   RESULTS AND DISCUSSION

SEM analyses have been performed to probe the surface structural identities of MnO_2-Co_3O_4/C samples prepared by the microwave-assisted heating method (Fig. 1a, b). As evident from Fig. 1a, the MnO_2-Co_3O_4/C-1 nanocomposite has a spatial layer of irregularly shaped lamellar nanostructures of ca. 10-50 nm in size. Meanwhile, in the case of MnO_2-Co_3O_4/C-2 nanocomposite, the spongy and porous frost-like three-dimensional surface is observed (Fig. 1b). The widely sprayed branches range from several to hundred nm in size.

More detailed microstructural information of the synthesized MnO_2-Co_3O_4/C nanocomposites has been provided by TEM analysis and are shown in Fig. 1 (c, d). The obtained data are in line with those determined by SEM analysis. In the case of MnO_2-Co_3O_4/C-1 nanocomposite, tapered nanowires and nanosheets are almost uniformly distributed on the surface (Fig. 1c). Moreover, the aggregated spherical nanostructures composing of oblong branches are seen in the prepared MnO_2-Co_3O_4/C-2 nanocomposite (Fig. 1d).

It has been determined that the Mn loadings in the prepared nanocomposites are ca. 0.013 and 0.021 mg cm^{-2} respectively.

Electrochemical performance of the MnO_2-Co_3O_4/C electrodes was evaluated in an aqueous 1 M Na_2SO_4 electrolyte. Figure 2a shows the CV curves of MnO_2-Co_3O_4/C-1 and MnO_2-Co_3O_4/C-2 at a scan rate 10 mVs^{-1} in the potential window of 0.05 to 1.1 V vs. SHE. CV curves present quasi-rectangular shape. C_s values for the same electrodes are 87.9 and 661.32 F g^{-1}, respectively (Fig. 3b).
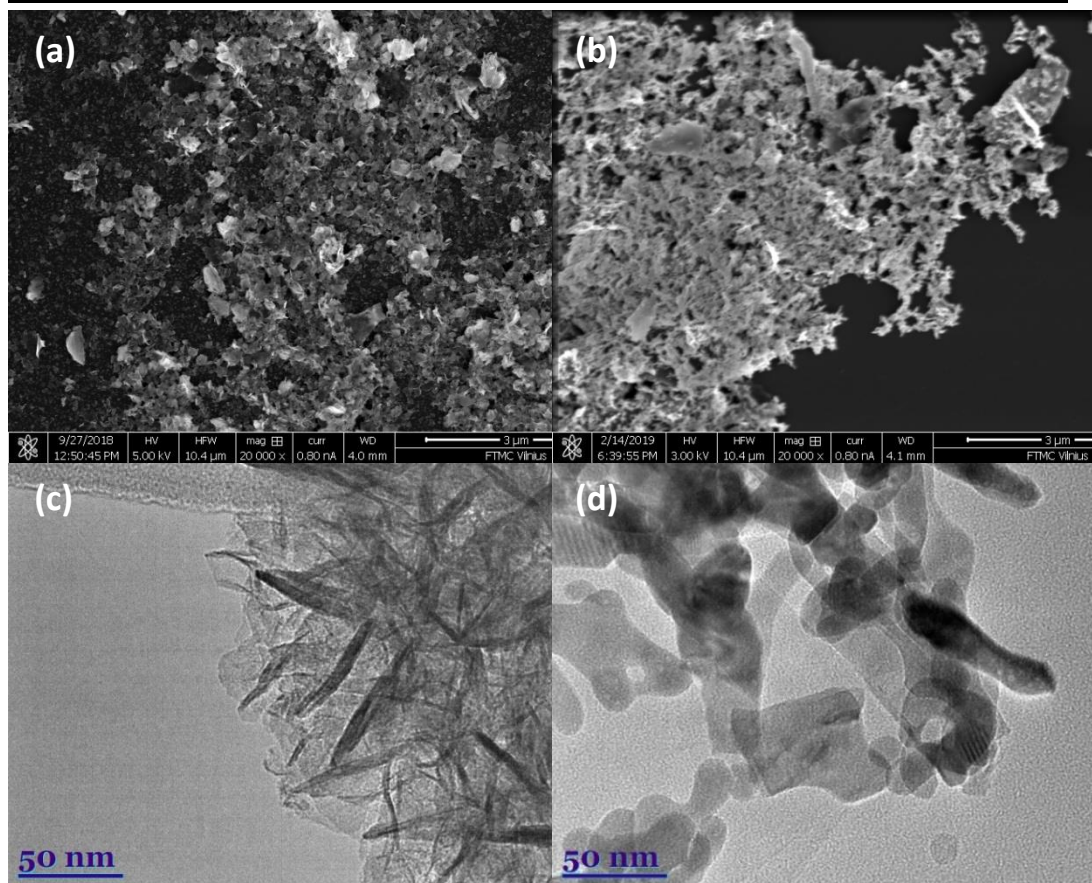
Fig. 1. *SEM and TEM images of MnO₂-Co₃O₄/C-1 (a, c) and MnO₂-Co₃O₄/C-2 (b, d).*
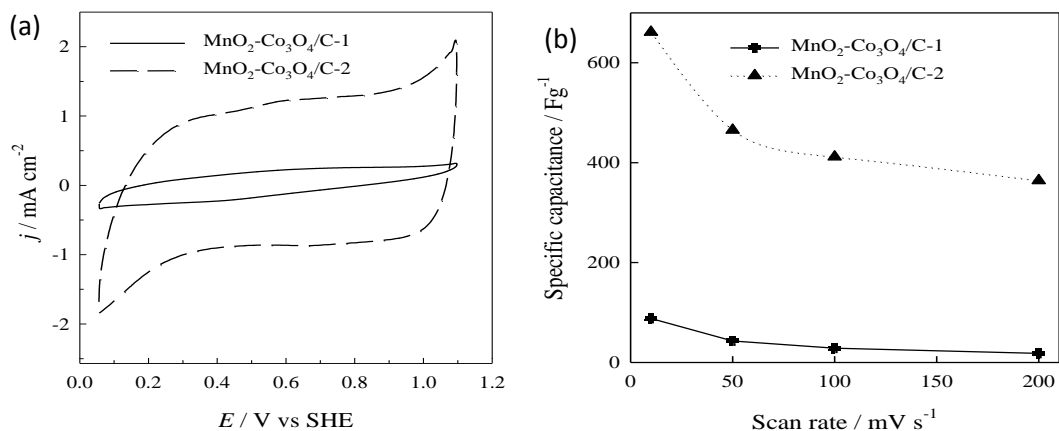
Fig. 2. *(a) CVs of MnO₂-Co₃O₄/C-1 and MnO₂-Co₃O₄/C-2 (b) in a 1 M Na₂SO₄ solution at a scan rate of 10 mV s⁻¹. (b) Specific capacitance at different scan rates.*

95

Meanwhile, C_s values at a scan rate of 200 mV s^{-1} are 18.3 and 364.10 F g^{-1} for the same electrodes and correspond to the retention of 20.7 and 55.1 %, respectively.

4. CONCLUSION

It was found a simple approach for the preparation of the carbon (C) based manganese (IV) and cobalt (II/III) oxides using microwave-assisted synthesis. The synthesized MnO_2-Co_3O_4 nanocomposites have lamellar and spherical shape nanoparticles. The highest specific capacitance of 661.32 F g-1 at a scan rate of 10 mV s-1 has been achieved at the MnO_2-Co_3O_4/C-2 electrode as compared with that of MnO_2-Co_3O_4/C-1.

The MnO_2-Co_3O_4 nanocoposites are expected to be a promising candidate to be used for electrochemical capacitors.

REFERENCES

[1]. F. Wang, X. Wu, X. Yuan, et al., Chem. Soc. Rev., 46, (2017) 6816–6854
[2]. C. Liu, X. Yan, F. Hu, et al., Adv. Mater., 30, (2018) 1705713
[3]. Poonam, K. Sharma, A. Arora, S. K. Tripathi, J. Energy Storage, 21 (2019) 8011-825

Effects of Emulsification Capability and Interfacial Tension of Chemical Flooding Agents on Oil Displacement Efficiency in Ultra-low Permeability Reservoirs

Yabing Guo[1,2], Xiangan Yue[1,2]*, Jie Dong[3], Lijuan Zhang[1,2]

[1]*State Key Laboratory of Petroleum Resources and Prospecting , Beijing , 102249 , China*
[2]*Key Laboratory of Petroleum Engineering Ministry of Education , Beijing , 102249 , China*
[3]*College of Petroleum , China University of Petroleum-Beijing at Karamay , Karamay, 834000, China*
yuexa@139.com

ABSTRACT

Emulsification capability and interfacial tension (IFT) are two key parameters of surfactant solutions. However, the relevance between emulsification capability and IFT was still not well understood, as well as their contributions to oil displacement efficiency in ultra-low permeability reservoirs. Aiming at these problems, we used emulsification index (an experimental parameter which quantify the emulsification capability) to investigate the effect of IFT on the emulsification capability. From comprehensive analysis of experimental test results of three typical surfactant solutions, we found that there was no significant correlation between emulsification index and IFT. And then, we carry out oil displacement experiments. The experimental results showed that the additional oil displacement efficiency of surfactant solutions with large emulsification index were significantly higher than the surfactant solution with small emulsification index. The observation results of the produced fluid in the oil displacement experiments also showed that surfactant solution with large emulsification index easily emulsified crude oil in the displacement process, and formed emulsion in-situ. Due to the plugging effect of emulsions in pore throats, the subsequent fluid entered the lower permeability zones which had a large amount of residual oil and displaced more crude oil. Therefore, when screening chemical flooding agents for ultra-low permeability reservoirs, we should pay more attention to emulsification capability.

KEYWORDS - *ultra-low permeability, emulsification capability, IFT, oil displacement efficiency.*

1. INTRODUCTION

Owing to the low porosity and low permeability of ultra-low permeability reservoirs [1-4], the efficiency of conventional water flooding, is commonly poor, usually 20%‑30%. In addition, many problems, such as high injection pressure, and serious water breakthrough, tend to occur along with water flooding. After water flooding, there are still a lot of residual oil in the reservoir, such as oil film, dead end oil, cluster oil, oil droplet, et al [5]. Chemical flooding is one of the promising technologies. IFT reduction and emulsification are the two main mechanisms to enhanced oil recovery by chemical flooding [5-10]. And also researchers pay increasingly close attention to chemical flooding of ultra-low permeability reservoirs.

Due to the pore structure and size of ultra-low permeability reservoirs are different from middle-high permeability reservoirs, the chemical flooding agents screening of low permeability reservoirs should pay more attention to emulsification capability. In the actual chemical flooding process, one of the main mechanism of emulsification improved microscopic oil displacement efficiency is through high displacement efficiency of residual oil. On the other hand, the emulsion formed in reservoir pores can effectively block high conductivity channels and thus improved sweep efficiency. However, the contributions of emulsification capability and IFT to the oil displacement efficiency still remains controversial.

In view of the problems above, this paper investigated the correlation between IFT and emulsification capability by the evaluation of IFT and emulsification capability of three typical

97

surfactant solutions. And then carry out oil displacement experiments to study the contributions of emulsification and IFT to oil displacement efficiency

2. EXPERIMENTAL SECTION

2.1. Experimental materials

The cores used in oil displacement experiments were artificial homogeneous cylindrical cores with the size of 2.5cm × 30cm, and the permeability were 10 ×10-3μm2. The exterior of core samples are shown in Figure 1 and the properties are shown in table 1. The oil used in the experiment was crude oil of CQ oil field .And the water was simulated formation water, whose parameters are highly similar to the formation water of CQ oil field. The properties of simulated formation water was shown in Table 2. The experimental surfactant is a compound mixture of betaine surfactant, anionic surfactant and auxiliary agent.

Figure 1. *The exterior of the core samples.*

Table 1. *The properties of three artificial cores.*

No.	Diameter(cm)	Length(cm)	Permeability($\times 10^{-3}\mu m^2$)	Porosity(%)
10-1	2.51	30.0	10.12	23.53
10-2	2.50	30.1	10.38	22.73
10-3	2.48	30.0	9.98	22.14

Table 2. *Properties of simulated formation water.*

Ca^{2+}	Mg^{2+}	$Na^{+}+K^{+}$	SO_4^{2-}	Cl^-	HCO_3^-	Total salinity mg/L
13258	512	16929	453	50637	119	81910

2.2. Emulsification capability evaluation

Dynamic emulsified oil ratio curves of the three surfactant solutions were measured by the high temperature emulsification characterizer [10].

2.3. Interfacial tension evaluation

Dynamic IFT curves of the three surfactant solutions were measured by the JJ2000B rotating droplet IFT measuring instrument.

2.4. Oil displacement procedure

The experimental procedure for the oil displacement experiment was, first, water flood to reach irreducible water saturation and then conduct surfactant flooding. The schematic diagram of oil displacement is shown in Figure 2.

3. RESULTS AND DISCUSSIONS

3.1. Correlation between emulsification capability and IFT

98
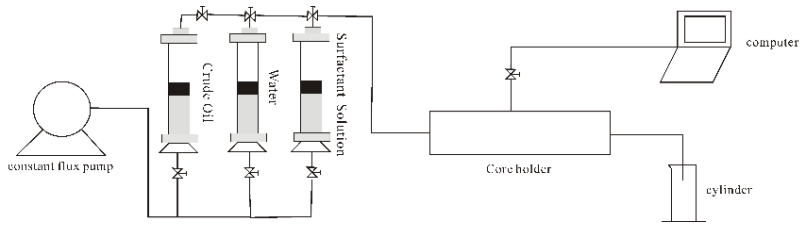
Figure 2. *Schematic diagram of oil displacement experiment*
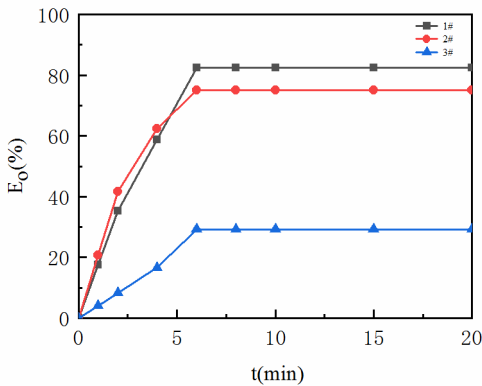
Figure 3. *Dynamic emulsified oil ratio curves.*   **Figure 4.** *Dynamic IFT curves.*
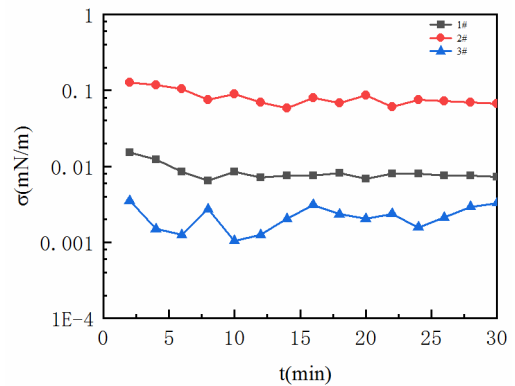
The dynamic emulsified ratio curves and dynamic IFT curves of the three typical surfactant solutions were shown in Figure 3 and Figure 4.

As shown in Figure 3, the emulsified oil ratio monotonously increases with the emulsification time until reaching the equilibrium emulsified ratio. The emulsification index calculated by the emulsified oil rate data[10], which the emulsification index of 1#, 2#, 3# surfactant solutions were 0.706, 0.667, 0.244, respectively. Comparing the emulsification index of three surfactant solutions, the emulsification capability were significantly different. Among them, the emulsification capability of 1# surfactant solution was the strongest, whereas that of 3# surfactant solutions was the weakest. The bigger the emulsification index, the stronger the emulsification capability.

Comparing the alternate trend of emulsified oil ratio and IFT of the three surfactant solutions, it was found that emulsification capability does not increase with decreasing of IFT. In other words, there is no significant correlation between emulsification capability and IFT.

3.2. Results of oil displacement experiments

The oil displacement results and experimental dynamics of the three surfactant solutions were shown in Table 3 and Figure 5.

Comparing the oil displacement efficiency results of three surfactant solutions, we can see that the surfactant solutions (1#, 2#) with strong emulsification capability have higher additional oil displacement efficiency than the surfactant solution (3#) with weak emulsification capability. And also, we can see that both emulsification capability and IFT have effects on the oil displacement efficiency, but the contributions are different. Emulsification capability is the main control factor. Comparing the water cut curves of the three surfactants in Figure5, we can see that surfactants with strong emulsification capability can easily form emulsions in-situ when migrated in the porous.

99

Table 3. *Results of oil displacement experiments*

N0.	Permeability ($\times 10^{-3} \mu m^2$)	Surfactant injection (PV)	Oil displacement efficiency of water flooding (%)	Total oil displacement efficiency (%)	Addition oil displacement efficiency (%)
10-1	10.12	0.6PV1#	41.30	54.79	13.49
10-2	10.38	0.6PV2#	40.17	52.18	12.01
10-3	9.98	0.6PV3#	39.24	45.99	6.75

(a) 1#   **(b) 2#**   **(c) 3#**
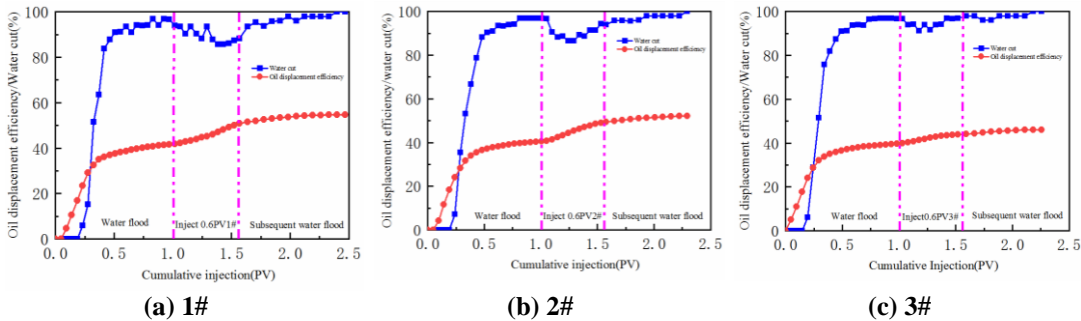
Figure 5. *Experimental dynamics of different core displacements*

(a) 1#   **(b) 2#**   **(c) 3#**
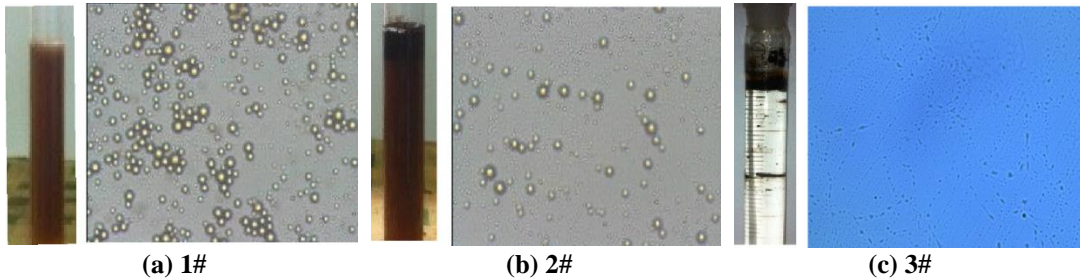
Figure 6. *Pictures of the produced fluid and corresponding micrograph during the surfactant flood.*

media. The observation of emulsification phenomenon in Figure 6 also verified the result. The formed emulsion blocked the water flow channels, and forcing the subsequent fluid to change flow direction, which drive the residual oil in lower permeability zones

4. CONCLUSION

(1) Comparing the emulsification index and IFT of the three surfactant solutions, it was found that there is no significant correlation between emulsification capability and IFT.

(2)The results of oil displacement experiments showed that, the additional oil displacement efficiency of surfactant solutions with stronger emulsification capability were significantly higher than that of surfactant solution with ultra-low IFT and weak emulsification capability.

(3)Comparing the oil displacements results, it was found that emulsification capability is the main factor of oil displacement efficiency in ultra-low permeability reservoirs.

REFERENCES

100

[1]. Feng, H. S., Kang W. L., Zhang, L. M., et al. Experimental study on a fine emulsion flooding system to enhanced oil recovery for low permeability reservoirs. Journal of Petroleum Science and Engineering, 171 (2018) 974-981. Doi: 10.1016/j.petrol.2018.08.011.

[2]. Wang, Q., Yang, S. L., Han, H. S., et al. International Conference on Computational and Experimental Science and Engineering (ICCESEN 2018), 12-16 October, 2018 Antalya-Turkey.

[3]. Cheng, T. T., Hou, J. R., Yang, Y. L., et al. International Conference on Computational and Experimental Science and Engineering (ICCESEN 2018), 12-16 October, 2018 Antalya-Turkey.

[4]. Cheng, Z. L., Ning, Z. F., Zhao, H. W., et al. A comprehensive characterization of north china tight sandstone using micro-CT, SEM imaging, and mercury intrusion. Arabian Journal of Geosciences, 12 (2019) 407. Doi: 10.1007/s12517-019-4568-9

[5]. Li, K. X., Jing, X. Q., Qu, D. Pore-level investigations on the oil displacement mechanisms of a viscoelastic surfactant in porous media. Journal of Petroleum Science and Engineering 173 (2019) 748–757. Doi.:10.1016/j.petrol.2018.09.086

[6]. Shang, D. S., Hou, J. R. International Conference on Computational and Experimental Science and Engineering (ICCESEN 2018), 12-16 October, 2018 Antalya-Turkey.

[7]. Dong, M. D., Yue, X. A. International Conference on Computational and Experimental Science and Engineering (ICCESEN 2018), 12-16 October, 2018 Antalya-Turkey.

[8]. Li, W. T., Wei, F. L., Xiong, C. M., et al. A novel binary compound flooding system based on DPG particles for enhancing oil recovery. Arabian Journal of Geosciences, 12 (2019) 256. Doi: 10.1007/s12517-019-4297-0

[9]. Shang, D. S., Hu, J. R. Effect of emulsifying property of an alkaline-surfactant-polymer system without ultra-low interfacial tension on enhanced oil recovery. Arabian Journal of Geosciences, 12 (2019) 543. Doi: 10.1007/s12517-019-4709-1

[10].Guo, Y. B., Yue, X. A., Fu, J. Y., et al. Relevance between emulsification capability and interfacial tension of chemical flooding agents. Energy & Fuels, 32 (2018) 12345-12350. Doi: 10.1021/acs.energyfuels.8b03110.

Developing Effectiveness Evaluation of Volcanic Reservoir: A Case Study of Che47 Carboniferous Reservoir

Xiangming Kong[*], Yuetian Liu, Xuanyi Song, Wanli Xu and Wenbo Su
China University of Petroleum (Beijing), Department of Petroleum Engineering, Beijing, China
*conist369@163.com

ABSTRACT

Due to uneven development of natural fracture, the well productivity of volcanic reservoir varies greatly, furthermore, the development effectiveness is affected by several factors such as fracture distribution and bottom water development. Reasonable evaluation of development effectiveness and analysis of influencing factors are of great importance for development optimization. In this article, 5 evaluation indices are screened at first, then evaluation criteria are divided by K-means cluster analysis, and development effectiveness evaluation model of volcanic reservoir is established by fuzzy judgment to evaluate the development effect of production wells. Principal Component Analysis (PCA) is used to analyze the main factors affecting the development effect, an evaluation system for the development effectiveness of volcanic reservoir is established step by step. The influence of factors on the production distribution and development effect is clarified, thus the production law of volcanic reservoir is studied. Development effect of single well in Che47 Carboniferous reservoir is evaluated in this study, the wells are classified to 5 types, thus well location distribution map of development effectiveness is analysed to find the characteristic of production distribution. Geological and engineering factors of different wells such as fracture growth level, perforation distance from the original water-oil contact, perforation thickness and lithology are compared for studying the influence law of each factor on development effect. The well with good development effect is mainly located in the fracture development area with suitable water-avoidance height, that is, the fracture and water-avoidance height play a synergistic role. The main factors determining the development effect are the degree of fracture development, perforation thickness and water-avoidance height. The evaluation system of single well development effect of volcanic reservoir is established to summarize production distribution characteristics of fault-block volcanic reservoir and analyze production laws and influencing factors, providing guidance for well location deployment and development optimization.

KEYWORDS- *Volcanic Reservoir, Fuzzy Judgment, Development Effectiveness Evaluation System, Production Law.*

1. INTRODUCTION

Che47 carboniferous reservoir is one of the lithologic reservoirs in the northwest margin of Junggar basin [1,2] and has dual medium reservoir stratum with large difference in production [3,4]. In order to understand the development law of volcanic reservoir, based on the current production performance of the reservoir, the development evaluation index and evaluation standard of volcanic reservoir are determined by the actual production data statistics, reservoir engineering analysis and various statistical methods, and then the development effect evaluation system is established by using the fuzzy comprehensive evaluation theory, and the development effect of single well is evaluated, and the production control factors are analyzed, providing suggestions and guidance for the follow-up development of the reservoir [5-8].

2. METHODOLOGY
2.1. Analysis of Geological and Engineering Parameters

Principal Component Analysis is used to figure out the main factor among geological and engineering parameters. We can acquire the weight of various parameters to evaluate the degree of influence, the analysis result is shown in Table 1 and Figure 1.

Table 1. Total variance interpretation.

Composition	Initial eigenvalue			Sum of the extracted loads			Sum of squares of rotating load		
	Total	Percentage of variance	Cum %	Total	Percentage of variance	Cum %	Total	Percentage of variance	Cum %
1	2.278	32.537	32.537	2.278	32.537	32.537	2.001	28.579	28.579
2	1.363	19.466	52.003	1.363	19.466	52.003	1.505	21.499	50.078
3	1.177	16.816	68.820	1.177	16.816	68.820	1.312	18.742	68.820
4	0.798	11.406	80.226						
5	0.638	9.120	89.345						
6	0.533	7.616	96.961						
7	0.213	3.039	100.00						
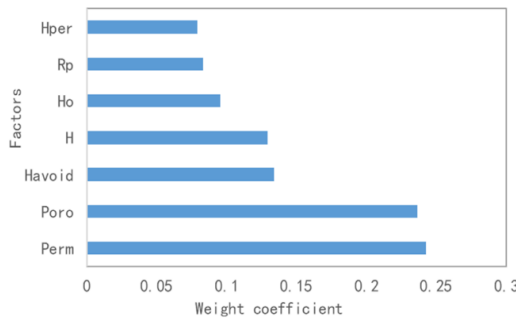
Figure 1. Weight coefficient of Factors
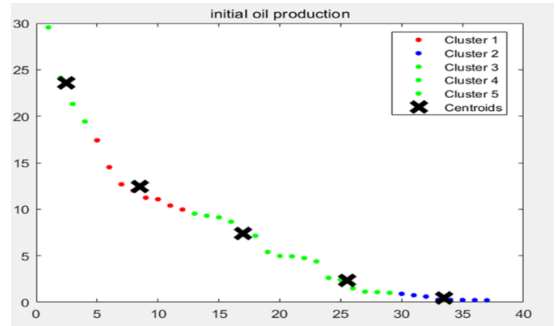
Figure 2. K-means cluster analysis result.

Table 2. Evaluation indices value range.

Evaluation Criteria	Great	Good	Medium	Weak	Poor
Initial Oil Production(t/d)	≥15.964	8.891~15.964	4.569~8.891	0.959~4.569	≤0.959
Stable Production Coefficient	≥2.177	0.997~2.177	0.795~0.997	0.528~0.795	≤0.528
Daily Average Oil Production(t/d)	≥14.18	5.146~14.18	3.521~5.146	1.672~3.521	≤1.672
Production Time Efficiency(%)	≥78.52	52.145~78.52	31.898~52.145	13.052~31.898	≤13.052
Water Cut After 1 Year(%)	≤3.494	3.494~12.962	12.962~29.945	29.945~53.908	≥53.908

2.2. Development Effect Evaluation System

According to industry standards and development practice, 5 evaluation indexes of development effect are selected, and evaluation criteria are divided by K-means cluster analysis.

3.   RESULTS

After establishing evaluation system of development effect of volcanic reservoir, 38 wells in Che47 Carboniferous reservoir is evaluated by fuzzy judgment, which are classified to 5 types. In order to find the differences among 38 single wells, average value of several parameters of different types of wells are compared, Figure 4 shows that well type is relevant to three major geological and engineering parameters. Perforation thickness of reservoir has positive influence on development effect, while fracture development degree has synergistic effect with water-avoidance height.

103
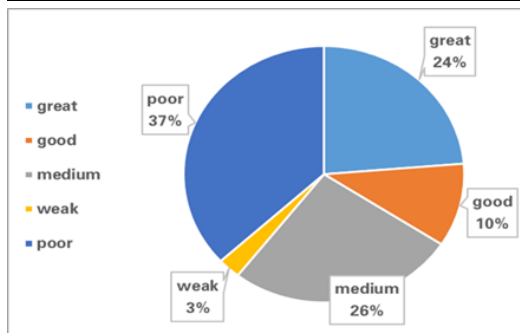
Figure 3. *Developing effectiveness evaluation result.*
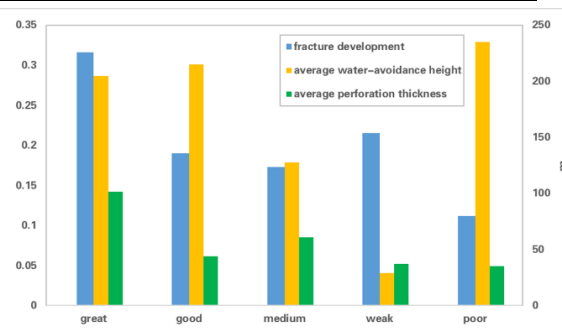
Figure 4. *Developing effectiveness evaluation result.*

4. CONCLUSION

(1) Well development effectiveness of volcanic reservoir is affected by geological and engineering factors comprehensively, fracture development index, perforation thickness and water-avoidance height are critical among them.

(2) Well with good development effect is mainly located in the fracture development area with suitable water-avoidance height, the fracture and water-avoidance height play a synergistic role.

REFERENCES

[1] Y. Lu, P. Jianguo, T. Kaijun, et al. Application of volcanic seismic reservoir to oil and gas exploration of Carboniferous in Hongche fault belt in Junggar basin[J]. Lithologic Reservoirs, 2010, 22(4): 25-30.

[2] Y. Weijiang, D. Yufang, Z. Shuncun, et al. Formation of Carboniferous reservoir in Hongche fault belt, northwestern margin of Junggar basin[J]. Natural Gas Geoscience, 2010, 21(6):917-923.

[3] C. Yan, L. Ruilan, W. Zehua, et al. 3D quantitative fracture model of igneous rock reservoir in Chepaizi oilfield[J]. Journal of Southwest Petroleum University(Natural Science Edition), 2008, 30(2): 54-56.

[4] L. Ruilan, W. Zehua, S. Youguo, et al. Geological modelling of dual porosity igneous reservoir in Chepaizi oilfield in Junggar basin[J]. Xinjiang Petroleum Geology, 2008, 29(4): 482-484.

[5] W. Deqiang, C. Linsong. International Conference on Computational and Experimental Science and Engineering (ICCESEN 2017), 4-8 October, 2018 Antalya-Turkey.

[6] H. Jianshu, L. Yuetian. International Conference on Computational and Experimental Science and Engineering (ICCESEN 2017), 4-8 October, 2017 Antalya-Turkey.

[7] L. Zhun, W. Xiaodong. International Conference on Computational and Experimental Science and Engineering (ICCESEN 2018), 12-16 October, 2018 Antalya-Turkey.

[8] H. Liang, N. Zhengfu. International Conference on Computational and Experimental Science and Engineering (ICCESEN 2017), 4-8 October, 2017 Antalya-Turkey.

104

Measurement of Natural Radioactivity Levels in Some Soil Samples from Çekmeköy-İstanbul

Kadir GÜNOĞLU[1], Osman GÜNAY[2*], Yusuf CEYLAN[3], İskender AKKURT[4]

[1] Isparta University of Applied Sciences, Technical Vocational School, Isparta- TURKEY
[2] Istanbul Okan University Vocational School of Health Services Istanbul, TURKEY
[3] Selçuk University, Science Faculty,Physics Department,Konya-TURKEY
[4] Suleyman Demirel University, Science Faculty,Physics Department, Isparta-TURKEY
* osman.gunay@okan.edu.tr

ABSTRACT

Radiation from natural radioactive isotopes which are present in the earth crust since its formation and the cosmic rays with very high energy are the natural ionizing radiations. Natural radioactive isotopes are found in soil, rocks, water, air, vegetation, building material, food in small amounts and irradiate us from outside as well as from inside of our body. In this study, 226Ra, 232Th and 40K concentrations were measured by gamma spectrometry system to determine the natural radioactivity levels of soil samples collected from Çekmeköy district in Istanbul.

KEYWORDS: Natural radioactivity, Ayazma beach, Gamma spectroscopy,

1. INTRODUCTION

Humans are exposed to radiation from both natural and artificial sources in their living environments. Knowing the level of natural radioactivity in any region is important not only for people to recognize the natural radioactivity levels of their habitats, but also to detect any possible changes in radioactivity levels. Significant contributions to environmental radiation are due to radioactive elements such as 238U, 232Th and 40K. Uranium and thorium concentrations in soils are high in local areas and cosmic rays are more intense at high altitudes [1]. External exposure due to natural environmental radioactivity and gamma radiation is largely dependent on geological and geographic conditions and appears at different levels in the territory of any area in the world [2].

The main purpose of environmental radiation measurements is to determine the type and dose of radiation that people receive from environmental sources and to assess the risk to be posed. In this, the environmental concentrations of radionuclides, which constitute natural sources of radiation, and the effect of radiation on biological systems, particularly in humans, need to be determined. In addition, the relationship between the radionuclides in the environment and the dose of radiation received by humans from these sources should also be determined. Only after such an investigation can it be decided whether a region is suitable for living in terms of natural radiation.

In this study, 226Ra, 232Th and 40K concentrations were measured by gamma spectrometer to determine the natural radioactivity levels of some soil samples collected from Çekmeköy-İstanbul. The results were compared with the accepted standard values.

2. MATERIAL AND METHOD

In this study, soil samples have been collected from Çekmeköy-İstanbul. After collection of samples, they were crushed and dried until $100^{o}C$ in an oven for about 24 h. The dried samples have been filled in a cup which is sealed tightly with a thick tape around its neck to limit any gas escape from it, and stored for four weeks to get secular equilibrium to be achieved between ^{238}U and its progeny [4].

The radioactivity concentrations of ^{226}Ra, ^{232}Th and ^{40}K in soil samples were determined using a gamma ray spectrometry consists of a 3"x3" NaI(Tl) detector connected to Multi-Channel-

105

Analyser (MCA). The spectrum is analyzed using the MAESTRO32 obtained from ORTEC. The schematic view of the experimental system has been shown in Figure 1.
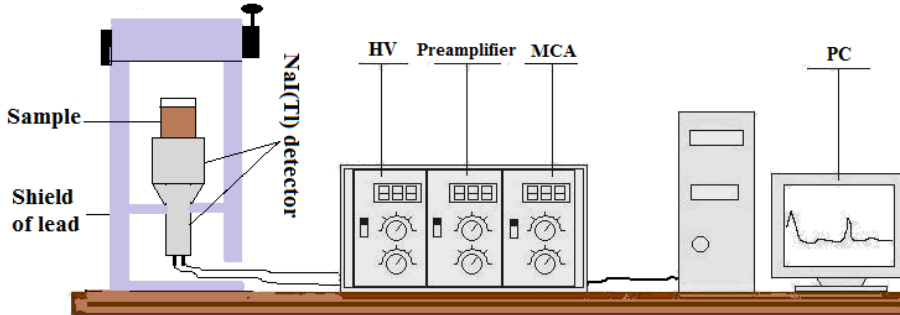
Figure 1. *Schematic view of gamma Spectrometer and electronic units*

The spectrum is analyzed using the MAESTRO32 obtained from ORTEC. The measurement was based on recording natural radioactivity quantities of three natural long-live elements: ^{226}Ra, ^{232}Th and ^{40}K which are considered the photopeaks at 1760, 2610 and 1461 keV respectively, in the natural γ-ray spectrum [3].

The activities for the natural radionuclides were calculated using the following relation [3]

$$A(Bq/kg) = \frac{N}{\varepsilon.\gamma.t.m}$$

(1)

where A is the activity of the radionuclide in Bq/kg, N is the net peak area under the most prominent photo peaks calculated by subtracting the respective count rate from the background spectrum obtained for the same counting time. The net count rate in the measurement is calculated from the background subtracted area of prominent gamma ray peaks. ε is the detector efficiency of the specific gamma ray, γ the absolute transition probability of gamma decay, t the counting time (s) and m the mass of the sample (kg).

3. RESULTS AND DISCUSSION

The measured activity concentrations of primordial radionuclides ^{226}Ra, ^{232}Th and ^{40}K in the soil samples collected from various locations in Çekmeköy-İstanbul are illustrated in Figure 4 and 5.

106
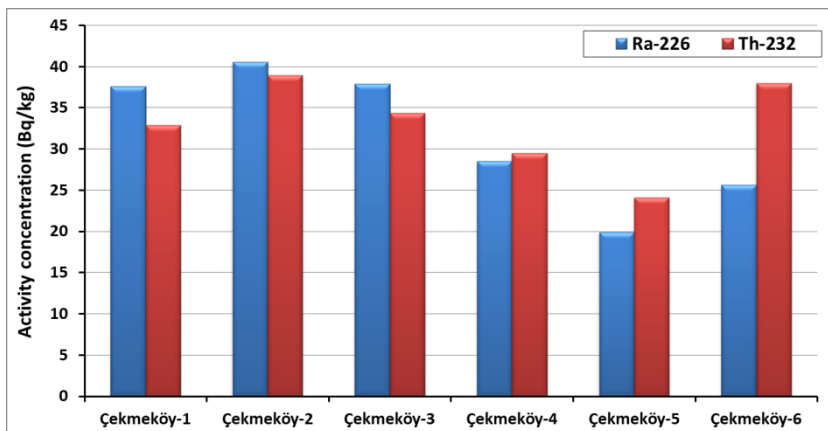
Figure 4. *The activity concentration of ^{226}Ra and ^{232}Th in soil samples*
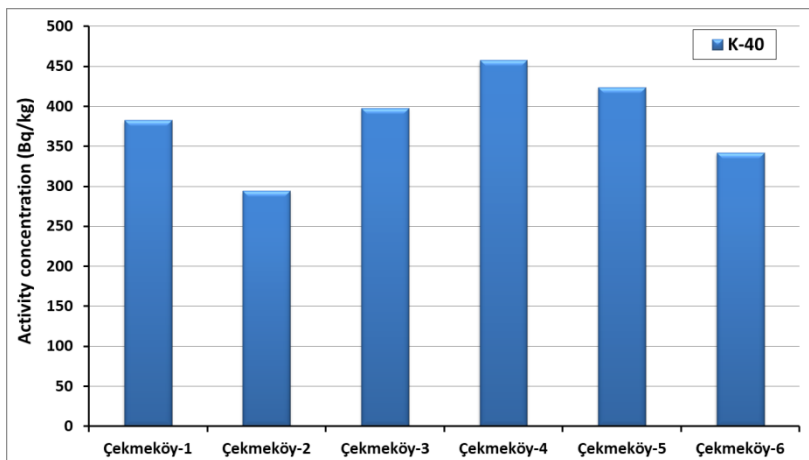
Figure 5. *The activity concentration of ^{40}K in gravel samples*

In this table, it can be seen the activity variation for these samples. The radioactivity of natural radionuclides is evaluated after measuring by comparing results with worldwide average values in natural soil. The worldwide average value of ^{226}Ra, ^{232}Th and ^{40}K in the normal soil is 35, 30 and 400 Bq/kg, respectively [5]. It can be seen that activity concentration of 40K for Çekmeköy-4 and Çekmeköy-5 samples are more than the worldwide average value, activity concentration of 226Ra for Çekmeköy-1, Çekmeköy-2 and Çekmeköy-3 samples more than the worldwide average value and activity concentration of ^{232}Th for Çekmeköy-1, Çekmeköy-2, Çekmeköy-3 and Çekmeköy- 6 samples more than the worldwide average value.

REFERENCES

[1]. Anagnostakis M. J; E.P. Hinis, S.E. Simopoulos, et al. Natural Radioactivity Mapping of Greek Surface Environment International, 1996, Vol. 22, Suppl. 1, S3- S8, Editor: J.P. McLaughlin, E.S. Simopoulos, F. Steinhäusler.

[2]. Ravisankar, R., Chandrasekaran, A., Vijayagopal, P., et al. Natural radioactivity in soil samples of Yelagiri Hills, Tamil Nadu, India and the associated radiation hazards, Radiation Physics and Chemistry, 2012, 81, 1789-1795.

[3]. Akkurt I. and Gunoglu,K., 2014. Natural Radioactivity Measurements and Radiation Dose Estimation in Some Sedimentary Rock Samples in Turkey. Science and Technology of Nuclear Installations Volume 2014, Article ID 950978

[4]. Akkurt, I., Oruncak, B., Gunoglu,K., 2010. Natural radioactivity and dose rates in commerciallyused marble from Afyonkarahisar − Turkey. International Journal of the Physical Sciences Vol. 5 (2), p:170-173.

[5]. UNSCEAR (2000) United Nations Scientific Committee on the Effects of Atomic Radiation. Report to the General Assembly, with scientific annexes, Sources and effects of ionizing radiation Annex B, New York. ,

Ulnar Nerve Deep Terminal Branch, Macroscopic and Morphometric Study

Hamzaoui Bahia, Yabka Assia and Bensalem Hind
Medical School, anatomy laboratory Blida and constantine, Algeria.
*mazari.bahia@gmail.com

ABSTRACT

The deep branch of the ulnar nerve, larger than the superficial branch, is exclusively muscular. It originates on the lateral side of the pisiform bone. This communication explains the variable innervation of the short flexor of the thumb and the variable repercussion of the opposition of the thumb and the sign of Froment respectively of the ulnar nerve and the median nerve. An anatomical study has allowed us to specify that the deep branch of the ulnar nerve travels to the lower surface of hamatum hamulus in a dense fibro-muscular environment.

KEYWORDS- *ulnar nerve, deep branch, macroscopic and morphometric study.*

1. INTRODUCTION

The hand is the upper limb terminal organ. A wonderful tool, capable of performing innumerable actions thanks to its two essential fonctions: grasping and touching. It is the instruments instrument according to "ARISTOTE » [1]. The hand is a real tool of sensation and manipulation. These two functions are made possible by the nerves that collect information from outside and inside. Three of these nerves are terminal branches of the brachial plexus: median and ulnar nerves are both motor and sensory, the radial nerve is only sensory. [2]. **The ulnar nerve:** The ulnar nerve is one of the major brachial plexus branches. It is a mixed nerve, coming from the medial cord of the brachial plexus (C8-T1) [3]. At the wrist, the ulnar nerve and artery enter a fibro-osseous tunnel formed between the the pisiform and hamate hook called distal ulnar canal or Guyon's canal. Within Guyon's canal, at the distal edge of the pisiform or in other cases above the pisiform, the the ulnar nerve bifurcates into superficial (sensitive) and deep(motor) branches.
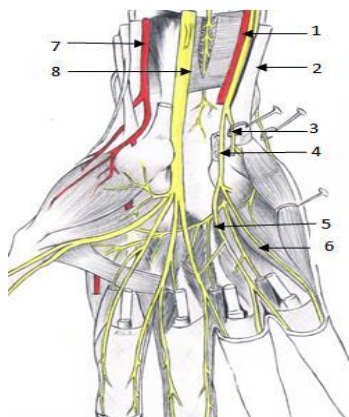
Figure 1. *Ulnar nerve superficiel branch (illustration from Testut modified). 1: Ulnar vasculo-nervous package. 2: flexor carpi ulnaris tendon. 3: Deep ulnar nerve branch. 4: Superficial ulnar nerve branch. 5: 4th space common digital nerve. 6: Fifth digit medial. 7: Radial artery. 8: Median nerve.*

2. MACROSCOPIC AND MORPHOMETRIC STUDY OF THE OF THE ULNAR NERVES DEEP BRANCH.

Hamatum hamulus in the deep palmar region. It crosses forward the deep palmar arterial arch. It ends in the Adductor Pollicis. [4]. This communication explains the variable innervation of the Flexor pollicis brevis muscle and the variable impact of the opposition of the thumb and the sign of Froment respectively of the ulnar nerve and the median nerve. An anatomical study allowed us to specify that the deep branch of the ulnar nerve travels to the lower surface of hamatum hamulus in a dense fibro-muscular environment. (Figure 2).
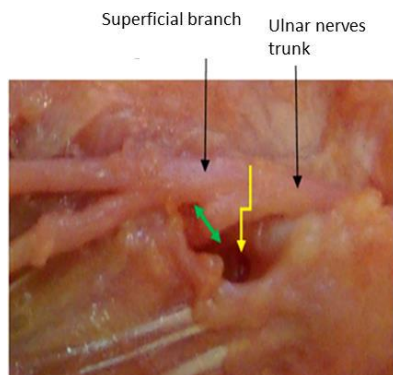
Figure 2. *Deep branch at the entrance to the piso-hamulian orifice. High magnification. Green arrow represents the width of the deep branch. Yellow broken arrow represents the piso-hamulian hiatus.*

In our dissection work we found that the position of the deep branch with respect to the main trunk of the ulnar nerve is variable ; it is located on the posteromedial face of the trunk en 18 cases (Figure 2), on the medial side en 4 case and on the posterior side en 6 cases. The deep branch of the ulnar nerve is larger than the superficial one. It is exclusively
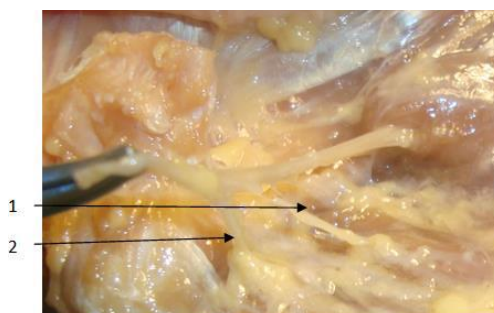
Figure 3. *Branches for the two most medial dorsal and ventral interossei. 1: Ventral and palmar branches of the 3rd interosseous space.*
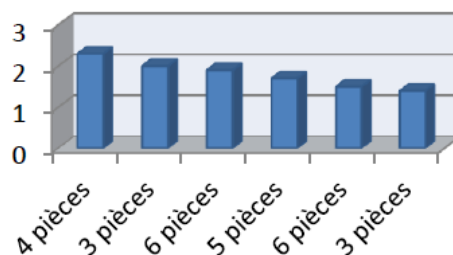
Figure 4. *Graphic representation of the width of the deep branch of the ulnar nerve.*

3. THE DEEP MEDIO-ULNAR ANASTOMOSIS OF RICHE CANNIEU

This anastomosis is formed by a netting of the twig that the deep branch of the ulnar nerve provides to the medial (deep) head of the flexor brevis at the level of the thenar eminence. This net crosses the tendon of the flexor pollicis longus and unites with the branch which the median sends to the lateral head of the flexor brevis, this branch of the adductor pollicis can be followed up to the medial (deep) head of the flexor brevis. In photo 4, Opponens digiti minimi muscle has been resected. The superficial terminal branches of the ulnar nerve have been removed in order to better see the deep motor branch.

4. RESULTS OF THE MACROSCOPIC STUDY OF THE DEEP BRANCH

Measurement D represents the width of the deep branch before entering the piso-hamulian hiatus, 1.8 ± 0.11 (2.3-1.4) mm.

5. DISCUSSION

Our dissections reveal that the deep branch passes to the dorsal side of the arch of the hypothenar muscles and in depth of these muscles and on the surface of the Opponens digiti minimi. On the contrary, the superficial branch passes to the surface of the origin of the abductor digiti minimi muscle and the Flexor digiti minimi brevis muscle. The distribution of muscle branches is more variable. Anatomically, systematization is difficult, it is only by stimulation on living subjects that we can define the true innervation. It is therefore deduced that several branches of the deep branch of the ulnar nerve are intended for the hypothenar muscles and a compression at this level frequently causes a motor deficit of the whole region. At the end of these results we found that despite the clinical interest of the ulnar nerve and its branches in the ulnar canal, only a few morphometric details have been described in the literature and the diameters of the terminal branches of the ulnar nerve have not been measured. The knowledge of the anastomosis of Riche Cannieu is very important while doing an electrophysiological study, otherwise there is a big risk for an erroneous diagnosis. There is one case reported by Saperstein and King on the coexistence of neuropathy of the deep branch of the ulnar nerve and Riche Cannieu's anastomosis misdiagnosed as a motor neuropathy. [5] Tamagawa et al. reported a case of bilateral carpal tunnel syndrome in which there was a paradoxical retention of the abductor muscle of the left thumb that was found to be due to Riche Cannieu's anastomosis. [6]

The clinical presentation of Riche Cannieu's anastomosis can take three forms:

- All the muscles of the hand can be innervated by the ulnar nerve.
- The motor innervation is dominated by the ulnar nerve.
- Some muscles innervated by the median nerve may be innervated by the ulnar nerve.

6. CONCLUSION

At the level of the canal, the ulnar nerve divides at the middle part of the canal, about 6 mm from the distal pole of the pisiform, into two branches, a sensitive superficial branch and a deep motor branch, which originates from the dorsal surface of the trunk. from the ulnar nerve, it passes under the deep distal hiatus of the canal. It is fixed by the fibrous arch of the hypothenar muscles on its palmar face, the piso-hamulian ligament and the hamatus hamulus on its dorsal surface. These anatomical relationships with the deep branch can be considered as a compression site. We performed a series of dissections of 28 balmy and fresh hands at the laboratory of anatomy and organogenesis University of Brussels. These dissections allowed us to make a study of the hand and particularly a macroscopic and morphometric study of the deep branch of the ulnar nerve.

The knowledge of the territories of sensory and motor innervation is clinically useful.

REFERENCES

[1].Aristote, Les parties des animaux 10, 687 b. éd. Les belles lettres, trad. P. Louis. p. 136. 137. Par Tubiana R. Traité de chirurgie de la main tome 4. Edit Masson 1991 p.316.

[2].Bonnel F, Mansat M. Nerfs périphériques. Anatomie et pathologie chirurgicale tome I, membre supérieur, embryologie du plexus brachial. edit Masson1989- p 20-37

[3].Kamina P. Précis d'Anatomie Clinique. Edit Maloine 2002. Tome I page 339-345.

[4].F.Bonnel, M. Mansat. Nerfspériphériques. Anatomie et pathologie chirurgicales. Tome I membresupérieuréditionMasson 1990. p. 138-145.

[5].King RB. Motor neuron presentation of an ulnar neuropathy and Riche-Cannieu anastomosis. Electromyogr Clin Neurophysiol. 2000 ;40(2) :119-122.

[6].Tamagawa C, Shiga K, Ohsima Y, Tokunaga D, Nakagawa M. Riche-Cannieu anastomosis and a paradoxical preservation of the thenar muscles.

Ultrasound Study of Aneurysm of the Ulnar Artery Compressing the Trunk of the Ulnar Nerve at the Wrist, about a Clinical Case

Hamzaoui B, Yabka A, Amrane CY
Laboratory of Anatomy Faculty of Medicine of Blida and Constantine Algeria
* mazari.bahia@gmail.com

ABSTRACT

We report a clinical case of thrombosed aneurysm of the ulnar artery. It is an infrequent and poorly understood pathology that is regularly associated with hypothenarhammer syndrome, found specifically in manual workers and athletes exposed to repeated manual trauma.

KEYWORDS- *Aneurysm - Ulnar artery – Thrombosis- Doppler ech.*

1. INTRODUCTION

The aneurysms of the arteries of the hand are most often of traumatic etiology. The false aneurysms of the arteries of the hand follow acute trauma, repeated microtrauma (hypothenar hammer syndrome) are responsible for true aneurysms [1]. Von Rosen. S. was the first to describe post-mortem trauma syndrome in the hypothenarian region, and ulnar artery aneurysm in the off-road cyclist [2]. Conn J.J et al in 1970 describe for the first time the hypothenar hammer syndrome or Hammer hypothenar Anglo-Saxon syndrome [3]. We report a clinical case of thrombosed aneurysm of the ulnar artery. This is an infrequent pathology and poorly known, regularly associated with hypothenar hammer syndrome, found specifically in manual workers and athletes exposed to repeated manual trauma.
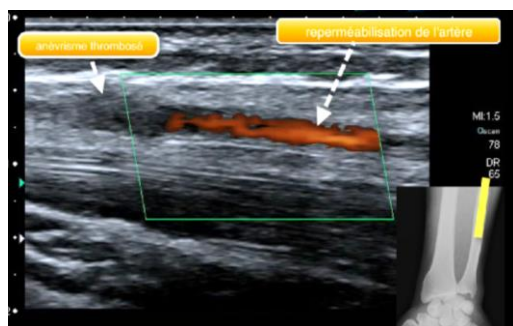
Figure 1. Ultrasound image of the right wrist, axial section showing thrombosis at the ulnar artery level. (Ain Naadja Military Hospital Algeria 2016)

Figure 2. Longitudinal ultrasonographic section showing the reversal of the ulnar artery at the distal quarter of the ulnar diaphysis. The aneurysm sits next to the distal radial shaft but the thrombosis is extended from the aneurysm to the distal.

2. OBSERVATION

Patient aged 29, with no particular antecedents, nurse by profession and athlete at the same time, consults for pain in the hypothenar region, the little finger and the ring finger following a sports injury on the right wrist that occurred 5 days before the first consultation. The clinical examination shows a pale purplish appearance of the integuments, and a difference of temperature (coldness) of the concerned region compared to the rest of the hand, there was no motor disorders [4].

111

The necessary course of action was ultrasound surveillance. The one-month control did not show a large clinical and radiological evolution. A control ultrasound showed the presence of aneurism compressing the trunk of the ulnar nerve, we proceeded to the resection of the thrombosis and the operative follow-ups were good. (Figures 1, 2).
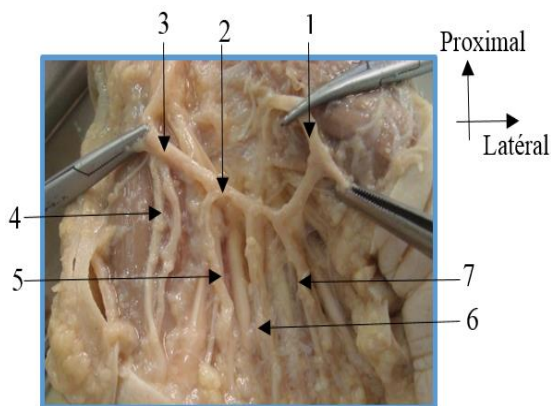
***Figure 3.** Embalmed left hand, superficial arterial palmar arch.*

3. DISCUSSION

The compression of the ulnar nerve at the wrist is a rare pathology, much less common than its compression at the elbow. The only noticeably noticeable difference between ulnar nerve injuries in the elbow and wrist is whether or not the muscles of the forearm innervated by this nerve are affected. In the ulnar canal, the ulnar nerve is surrounded by adipose tissue, is separated from the canal surfaces, and is never really compressed by the fibrous structures. The only elements that can lead to compression of the nerve are the aneurysm of the ulnar artery and the anterior synovial cysts. At the level of the wrist, the ulnar nerve is placed within the ulnar vessels and divides into its terminal branches : one superficial and the other deep. At the level of the wrist, the ulnar nerve is placed within the ulnar vessels and divides into its terminal branches : one superficial and the other deep (Figure 3).

4. CONCLUSION

The aneurysm of the ulnar artery remains a rare pathology. The presence of a mass in the hypothenar eminence, of soft consistency following direct or repeated trauma of paresthesia of signs of ischemia and a test Allen's positive is suggestive of the diagnosis. Doppler ultrasound can confirm the diagnosis. Surgical indication remains the treatment of choice because of the risks of embolic complications.

REFERENCES

[1].Journal des maladies vasculaires, volume 39 num 6 pages 426-429. Dec 2014 faux anévrisme traumatique chez un adolescent.

[2].Von Rosen. S. fut le premier à faire une description du syndrome consécutif à des traumatismes de la région hypothénarienne, et l'anévrisme de l'artère ulnaire chez le cycliste tout terrain.

[3].Conn J.J et al en 1970 décrivent pour la première fois le syndrome du marteau hypothénarien ou Hammer hypothénar syndrome des anglo-saxons.

[4].Military hospital radiology department Ain Naadja Algiers 2018

The Numerical Simulation Study on Percolation Characteristics and Displacement Mechanism of Fractured Reservoir

Hao Zheng[1,2*], Huiqing Liu[2], Qichen Zhang[2], Qu Ziyi[3]
[1]CNOOC International Limited, Beijing, PR China
[2]College of Petroleum Engineering, China University of Petroleum, Beijing, PR China
[3]CCDC Geological Exploration and Development Research Institue, Sichuan, PR China
* Zhenghao2@cnooc.com.cn

ABSTRACT

The author has studied the percolation characteristics and displacement mechanism of fractured reservoir by double media numerical simulation in detail, as well as made sensitivity analysis of the impact of development effect. The results show that the rock stress sensitivity is the key to decide fractured reservoir development strategy, including the development model, the ability to maintain reservoir pressures, the recovery of matrix system and fracture system. The crossflow between matrix system and fracture system is very difficult to occur in natural energy sufficient or artificial water to maintain reservoir pressure. It only appears in the development process of reducing reservoir pressure. Regarding the matrix system, capillary pressure dialysis is the most important percolation characteristics and displacement mechanism. Its recovery ratio may reach over 4%. Regarding the fracture system, the displacement process depends on the external driving pressure differential and is pipe flow. Its recovery ratio may reach over 75%.

KEYWORDS - *fractured reservoir; percolation characteristics; displacement mechanism; double medium; numerical simulation.*

1. INTRODUCTION

With the permeability of several Darcy and the porosity of generally less than 1%, the fracture system is formed by large cracks and caves. The width of the cracks is more than 10 um and the caves are connected to cracks. Since the reservoir space is full of crude oil, the oil saturation is close to 100%. Considering the existence of caves, the porosity of fracture system is also less than 2%.

Matrix system is composed of different sizes of rocks divided by cracks with the width of less than 10 um and permeability less than $10 \times 10\text{-}3um2$. Generally the porosity of matrix system is between 2% and 5% due to its smaller pore throat and higher irreducible water saturation, which are basically above 30%.Due to their different types of reservoir space characteristics, the percolation characteristics and displacement mechanism of matrix system are quite different from that of fracture system.

2. NUMERICAL SIMULATION STUDY
2.1. The establishment of fractured reservoir model

Without edge and bottom water, the reserves of matrix in the model is about 621.3×10^4 m^3 and the reserves of fracture is 207.2×10^4 m^3 with a total of is 828.5×10^4 m^3. It is assumed that the model includes five horizontal Wells, 4 production wells and 1 injection well. The essential parameters of reservoir are shown in Table 1.

2.2. Sensitivity Analysis
(1) The natural energy development

Without edge-bottom water and artificial water injection, the development of fractured reservoir mainly depends on elastic energy of rock and fluid. Since oil is single-phase flow under the ground

113

where water flooding process doesn't happen, the percolation characteristics are like pipe flow in the fracture system and channeling between matrix system and fracture system.

Table 1. Parameters table of one fractured reservoir in Bohai bay

Type	Parameter	Value
Reservoir characteristics	Matrix porosity，%	5.72
	Matrix permeability，mD	1
	Fracture porosity，%	1.08
	Fracture permeability，mD	465
	Reservoir temperature，℃	75
	Midpoint of pay zone，m	1760
	Reservoir pressure，MPa	17.7
	saturation pressure，MPa	12.6
Fluid characteristics	Oil density，g/cm^3	0.80
	Oil viscosity in reservoir，mPa.s	2.36
	Volume factor of formation oil，m^3/m^3	1.172
	Initial solution gas-oil ratio，m^3/m^3	35

1) Rock stress analysis
Compared with fracture system, the conductivity of matrix system is smaller and oil supply system of that is slower which lead to its smaller pressure drop. At the same time, due to its smaller compressibility and lower delivery rate, the oil supply rate of matrix system is much slower than that of fracture system. Thus, rock deformation has great influence on development effect and enough attention should be paid in the process of oilfield development and numerical simulation study on strong rock stress sensitivity of fractured reservoir.

2) The channeling capacity analysis
From numerical simulation results, it can be seen that the recovery of fractured reservoirs will gradually become bigger as shape factor grows. The reason is that the bigger shape factor will make percolation ability enhance and increase crude oil from matrix to fracture, which then lead to the recovery of matrix system increase while the recovery of fracture system doesn't change much. But the recovery of fracture system is still greater than that of matrix system. It's important to note that because the shape factor of channeling function comes from geological statistics and stochastic modeling, much attention should be paid in numerical simulation research, especially in history matching.

(2) The artificial water injection development
As mentioned, different from conventional sandstone reservoir, there may be rock stress sensitivity in the development of fractured reservoir by natural depletion. In such cases, it is very necessary to inject water to maintain reservoir energy and prevent cracks and pore throats from closing. Otherwise, large number of remaining oil cannot be produced. Therefore, researches are made to find how percolation characteristics and displacement mechanism of matrix system and fracture system affect the development effect by the way of water injection.

1) The Analysis of fluid channeling

114

From the simulation results, we can find that the overall recovery of each case is around 19% with different shape factors, among which, the recovery of fracture system is above 75% while the recovery of matrix system is almost zero. The reason is that pressure of matrix system and fracture system are both the original reservoir pressure so that channeling between them doesn't happen. Only in the condition of natural energy shortage or lack of artificial water injection, can the channeling between matrix and fracture happens. Therefore, for fracture reservoir simulation, especially evaluating matrix system and fracture system separately, just considering channeling will not be able to make objective analysis on the producing degree, the recovery degree and the contribution to the overall recovery of matrix system.
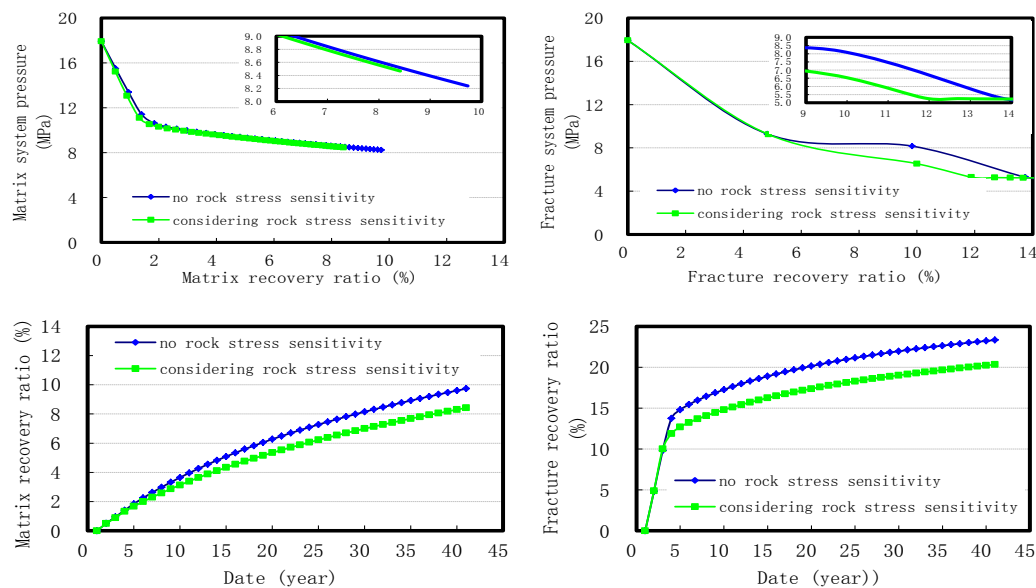
Figure 1. *The rock stress analysis between matrix and fracture*
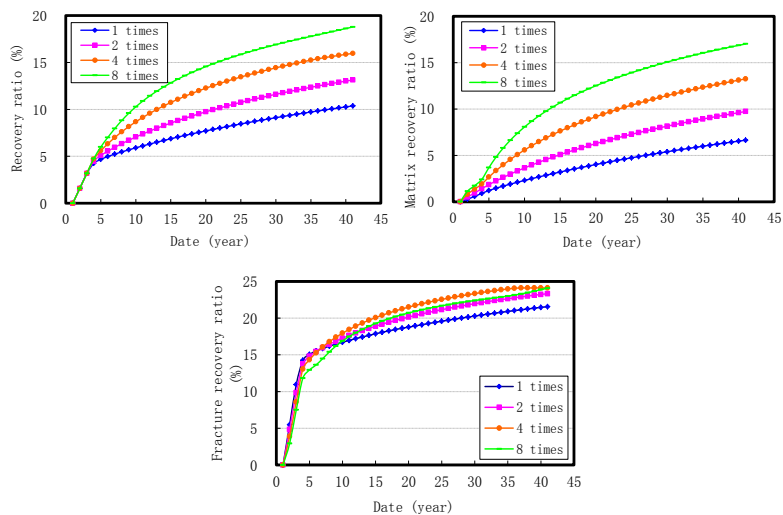
Figure 2. *The channeling capacity analysis of fracture reservoir*

115
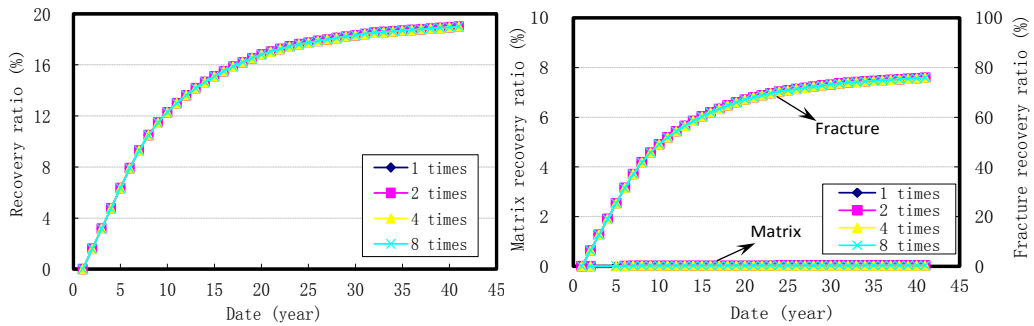
Figure 3. *The channeling capacity analysis of fracture reservoir*

2) The analysis of imbibition by capillary force

From the numerical simulation results it can be seen that the overall recovery of reservoir increases when considering imbibition effect. The main reason was that part of oil from matrix system can be produced by imbibition effect while the recovery of fracture system has little change although the recovery of fracture system can reach 75%. The imbibition recovery can reach above 4%. Since most of crude oil stores in matrix system, the overall recovery of reservoir mainly depends on matrix system in fractured reservoir. Therefore, the key factor to enhance overall recovery of fractured reservoir is to improve the recovery of matrix system while the imbibition effect in this process can't be ignored.
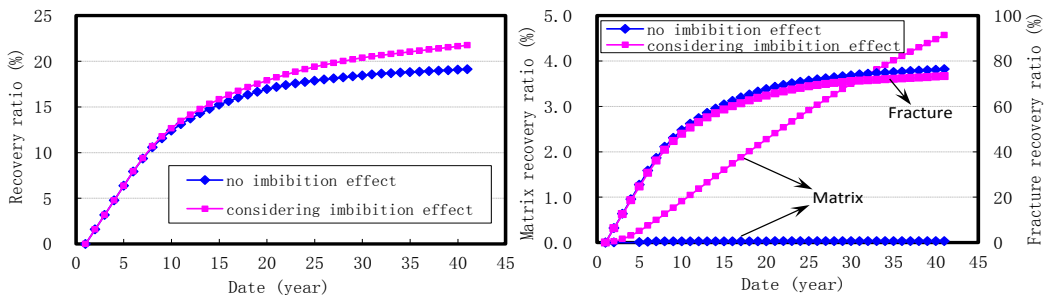
Figure 4. *The analysis of imbibition by capillary force on fracture reservoir*

CONCLUSION

(1) Rock stress sensitivity is the key for the development of fractured reservoir, which determines the way of development, the maintenance ability of pressure and the recovery of matrix system and fracture system.

(2) The fluid channeling between matrix system and fracture system will not happen under the condition of plenty of edge-bottom water or water injection to keep pressure balance. When reservoir pressure is not balanced, fluid channeling will happen and the effect of which depends on the fracture growth level. Because fractured reservoir is so complex that there is a big uncertainty which should be highly valued in the process of practical production and numerical simulation.

(3) For matrix system, imbibition is the main percolation characteristic and displacement mechanism with the recovery of 4%. For fracture system, the driving force mainly comes from the external differential pressure. Flow type looks like pipe flow which makes recovery efficiency can reach above 75%.

This paper has presented the improved power control of DFIG used in wind turbine by the Artificial Intelligence (AI) techniques control, after modelling the wind turbine and the DFIG in

116

the d and q axis, we have established the indirect vector control of DFIG based on stator flux oriented, then the ANNs is synthesized and compared to a FL controller. We have also presented the performance of the ANNs and FL and comparisons between them, the robustness of the controllers are evaluated and allows us to have a decoupling between active and reactive power thus independent control. The simulation results show that the control strategy ANNs is much more efficient compared to FL, it also improves the performance of the power DFIG, and ensure some important strength despite the variation of the parameters of the DFIG and the simplicity of its design. The use of ANNs has many advantages.

The proposed controller ensures fast and accurate dynamic response with excellent steady-state performance.

We can conclude that the ANNs is an improved controller for DFIG power.

We remark that the proposed ANNs are able to associate between the advantages given by Neural Network and Fuzzy Logic systems, which was predictable.

REFERENCES

[1]Kazemi h,Merrill L S,Jr K L Porterfield.Numerical Simulaition of Water-oil Flow in Naturally Fractured Reservoir[G].SPE 5719,1976:317-326.

[2]Kai Liao, Shicheng Zhang, Xinfang Ma, et al. Numerical investigation of thermal fluid fracturing in low-mobility tight oil reservoirs. International Conference on Computational and Experimental Science and Engineering (ICCESEN 2018), 12-16 October, 2018 Antalya-Turkey.

[3]Suran Wang, Linsong Cheng, Shijun Huang, et al. A Novel Approach for Production Data Analysis of Fractured Carbonate Wells during Transient Flow Regime. International Conference on Computational and Experimental Science and Engineering (ICCESEN 2018), 12-16 October, 2018 Antalya-Turkey.

[4] Pin Jia, Linsong Cheng, Yongchao Xue, et al. Laboratory Investigation of High-speed and High-efficiency Development Mechanism of Sandstone Reservoir. International Conference on Computational and Experimental Science and Engineering (ICCESEN 2018), 12-16 October, 2018 Antalya-Turkey.

[5] Du Dianfa, Chen Yueming, Wang Lushan, et al. A study on water invasion behavior of buried hill reservoir. OGRT, 2000, 7(3):42-45.

A New Method for Studying the Theoretical Relationship Curve between the Water Cut and the Recovery Percent

Yuejie Wang[1,2*], Huiqing Liu[2]
[1]Tianjin Branch of CNOOC Ltd, Tianjin，PR China
[2]School of Petroleum Engineering, China University of Petroleum, Beijing, PR China
*wangyj7@cnooc.com.cn

ABSTRACT

The relative permeability curves methods cannot accurately describe the relationship curve between water cut and recovery percent. In view of this problem, this paper established the theoretical formula of recovery percent in water-free stage and water cut increasing rate in water production stage, by using the stream tube model, based on nine-spot well pattern of the homogeneous reservoir. On this basis, a new method was proposed to analysis the theoretical relationship curve between water cut and recovery percent.

KEYWORDS - *water cut, recovery percent, water-free stage, water cut increasing rate.*

1. INTRODUCTION

The relation curve between water cut and recovery percent is usually used for the evaluation of oilfield development effect. Stream tube method and relative permeability method are the two methods for the establishment of theoretical curve. Relative permeability method is commonly used for the establishment of water cut and recovery percent due to its simple formula and procedure. However the theoretical curve can not describe the water-free production period. In this paper, a new method was proposed to analysis the theoretical relationship curve between water cut and recovery percent.

2. METHODOLOGY

For nine-spot well pattern of the homogeneous reservoir, seepage field can be divided into two types of units. Two phase seepage in the stream tube can be expressed as follows:

$$\int_0^\zeta A(\zeta)\,\mathrm{d}\zeta = \int_0^t \frac{\Delta q f_w'(S_w)}{\phi}\,\mathrm{d}t \tag{1}$$

Percolation resistance of a stream tube can be described as:

$$r(i) = \frac{\int_{r_w}^{\zeta_1}\dfrac{1}{A_i(\zeta)\dfrac{K_{rw}}{\mu_w}}\mathrm{d}\zeta}{K} + \frac{\int_{\zeta_1}^{\zeta_2}\dfrac{1}{A_i(\zeta)\left(\dfrac{K_{ro}}{\mu_o}+\dfrac{K_{rw}}{\mu_w}\right)}\mathrm{d}\zeta}{K} + \frac{\int_{\zeta_2}^{l_i-r_w}\dfrac{1}{A_i(\zeta)\dfrac{K_{ro}}{\mu_o}}\mathrm{d}\zeta}{K} \tag{2}$$

The flow rate of a stream tube can be described as:

$$\Delta q(i) = Q\frac{1}{r(i)}\frac{1}{\displaystyle\sum_{i=1}^n \frac{1}{r(i)}} \tag{3}$$

118

The distribution of water saturation in each stream tube can be cooperatively solved by Equation1, Equation2 and Equation3. Considering 5 factors (water oil mobility ratio, water index, oil index, irreducible water saturation and residual oil saturation).

2.1. Recovery percent of water-free stage
2.1.1.   Study on the influence factors
There was a typical power function relationship between recovery percent and water oil mobility ratio under the condition that other 4 factors keeps invariant. Similarly, recovery percent respectively has a linear relationship with water index, oil index, irreducible water saturation and residual saturation under the condition that other 4 factors keeps invariant.

2.1.2.   Establishing relationship between recovery percent and influence factors
The relationship between recovery percent of water-free stage and 4 influence factors can be expressed as Equation (4).

$$R_0 = b_0 + b_1 n_w + b_2 n_o + b_3 S_{wi} + b_4 S_{or} \tag{4}$$

The value of four coefficients have a linear relationship with water oil mobility ratio. the relation curve between coefficient b2 and water oil mobility is as shown in Figure 1.
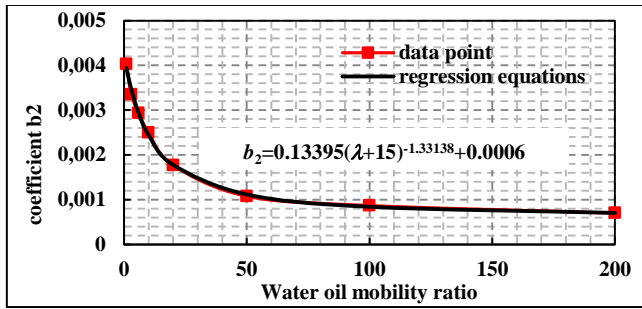
Figure 1. The relation between coefficient b2 and water oil mobility ratio.

The theoretical relation between recovery percent of water-free stage and five influence factors was established (Equation (5)).

$$\begin{aligned}
R_0 &= \left(0.17967\lambda^{-0.48301} - 0.015\right) \times 100 + \left(0.08486(\lambda+15)^{-0.56316} + 0.016\right)n_w \times 100 \\
&+ \left(0.13395(\lambda+15)^{-1.33138} + 0.0006\right)n_o \times 100 - \left(0.25064(\lambda+3)^{-0.64349} + 0.024\right)S_{wi} \times 100 \\
&- \left(0.34470(\lambda+0.11)^{-0.30747} + 0.011\right)S_{or} \times 100
\end{aligned} \tag{5}$$

2.2. Water cut increasing rate of water production stage

2.2.1.   Establishing the relation between $\overline{S_w}$ and S_w
Based on the distribution of water saturation solved by numerical simulation, out-let water saturation and average water saturation were analyzed. There is a linear relationship between out-let water saturation and average water saturation with different water oil mobility ratio. The linear relationship can be expressed as Equation (6).

$$\overline{S_w} = aS_w + b \tag{6}$$

Relation between the coefficient a of equation (6) and water oil mobility ratio was established (Equation (7)).

$$a = a_1 \ln \lambda + a_2 \tag{7}$$

$$a_1 = (0.0116 \ln n_w - 0.0489) \ln n_o - 0.088 \ln n_w + 0.1971 \tag{8}$$

$$a_2 = (-0.126 \ln n_w + 0.1469) \ln n_o + 0.2647 \ln n_w + 0.4406 \tag{9}$$

2.2.2.   Establishing the calculation formula of water cut increasing rate

According to the definition of water cut increasing rate, the calculation formula can be described as Equation (10).

$$f_w' = \frac{df_w}{dR} = \frac{f_{w(i)} - f_{w(i-1)}}{R_{(i)} - R_{(i-1)}} \tag{10}$$

The relationship between recovery percent and average water saturation can be expressed as Equation (11)

$$R = \frac{\overline{S_w} - S_{wi}}{1 - S_{wi}} \tag{11}$$

Based on fraction flow equation, water cut increasing rate can be expressed as Equation (12).

$$f_{w0}' = \frac{f_{w(i)} - f_{w(i-1)}}{\frac{S_{w(i)} - S_{w(i-1)}}{1 - S_{wi}}} \tag{12}$$

Substituting Eq.(7) , Eq.(8), Eq.(9), Eq.(11) and Eq.(12) into Eq.(10), a new calculation formula of water cut increasing rate was established (Equation(13)).

$$f_w' = \frac{1}{a} \frac{f_{w(i)} - f_{w(i-1)}}{\left(\frac{S_{w(i)} - S_{w(i-1)}}{1 - S_{wi}} \right)} = \frac{1}{a_1 \ln \lambda + a_2} f_{w0}' \tag{13}$$

2.3. Establishing the relation between water cut and recovery percent

Based on the theoretical formula of recovery percent of water-free stage and water cut increasing rate of water production stage, the theoretical relation curve was established. The solution procedure are as follows:

1）Water-free stage：calculate recovery percent of water-free stage R_0 ,when $R \le R_0$, *fw=0*;

2）Water production stage($R > R_0$)：

①   Determine the water cut steps Δf_w ($\Delta f_w = 0.1\%$)；

②   Solving water cut of the first step:

③   Solving average water cut of the first step：

Solving the water cut increasing rate of the first step by Equation (13)；

120

④   Solving the recovery percent of first step：

⑤   Repeating steps ②～⑤, the theoretical relation curve between water cut and recovery percent can be established.

As can be seen from figure 2, with the increase of formation oil viscosity, the shape of relation curve are changing from "concave type" to "S type" and "convex shape". The variation of curve shape is consistent with field performance, and can characterize the water cut rising rule of different reservoirs.

3.   FIELD APPLICATION

By plotting the field data and theoretical relation curve between water cut and recovery percent into at the same figure, we can evaluate the development effect of waterflooding reservoir according to the difference between field data and theoretical value. This method has been applied to many water flooding reservoirs and the evaluation results are consistent with field performance. The theoretical curve between water cut and recovery percent of the sample reservoir was established and was compared to field data (Figure 3).Theoretical curve has the same trend with field data, which proves the validity of this method.
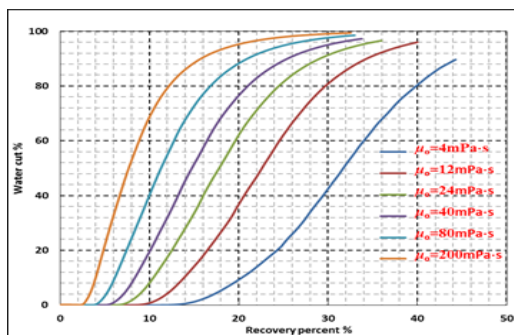
Figure 2. *Theoretical relation curve between water cut and recovery percent.*
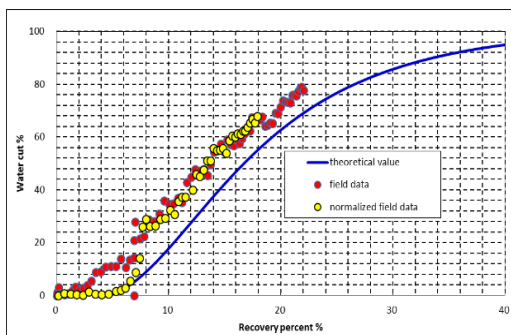
Figure 3. *The relation curve between water cut and recovery percent.*

4.   CONCLUSION

There is an approximate linear relationship between out-let water saturation and average water saturation and based on which a new method for calculating theoretical water cut increasing rate was proposed. Based on the theoretical recovery percent of water-free stage and water cut increasing rate of water production stage, a new method for solving the relation between water cut and recovery percent was proposed which solves the problems of traditional relative permeability method.

REFERENCES

[1] Mingda Dong, Xiang'an Yue .Effect of Surfactant Emulsification on High Water-cut Reservoir in Shengli Oilfield (ICCESEN 2018), 12-16 October, 2018 Antalya-Turkey.

[2] Kai Liao, Shicheng Zhang, Xinfang Ma, et al. Numerical investigation of thermal fluid fracturing in low-mobility tight oil reservoirs. International Conference on Computational and Experimental Science and Engineering (ICCESEN 2018), 12-16 October, 2018 Antalya-Turkey.

[3] Suran Wang, Linsong Cheng, Shijun Huang, et al. A Novel Approach for Production Data Analysis of Fractured Carbonate Wells during Transient Flow Regime. International Conference on Computational and Experimental Science and Engineering (ICCESEN 2018), 12-16 October, 2018 Antalya-Turkey.

[4] Pin Jia, Linsong Cheng, Yongchao Xue, et al. Laboratory Investigation of High-speed and High-efficiency Development Mechanism of Sandstone Reservoir. International Conference on Computational and Experimental Science and Engineering (ICCESEN 2018), 12-16 October, 2018 Antalya-Turkey.

[5] Mingda Dong, Xiang'an Yue .Effect of Surfactant Emulsification on High Water-cut Reservoir in Shengli Oilfield(ICCESEN 2018), 12-16 October, 2018 Antalya-Turkey.

[6] Fan Zheyuan,Yuan Xiangchun,Liao Rongfeng and Shu Qinglin. (2005) 'Common problems and solutions in plotting theoretical curves of water-cut vs.recovery percent of reserves', Oil & Gas Geology,Vol.26,No.3,pp.384-387.

[7] Feng Qihong, Lv aimin and Yu Hongjun.(2004) 'A new method for evaluating waterflooding development effectiveness', Journal of the University of Petroleum, Vol.28,No.2,pp.58-60.

[8] Zhang Hongyou, Deng Qi, Mu Chunrong, Bie Mengjun and Zhang Yanhui.(2015) 'A new method for computing the increased rate of water cut for waterflooding sandstone reservoirs-a correction of fractional flow equation method', China Offshore Oil and Gas, Vol.27,No.3,pp.79-83.

A Study of Intermittent Pumping Design for Low Production Oil Wells in Ordos Basin in China

Ye Meng[1,2*], Xiangfang Li1[2], Minxia He1[2], Mingjie Jiang[3]

[1]*MOE Key Laboratory of Petroleum Engineering, China University of Petroleum Beijing, Beijing, China*

[2]*State Key Laboratory of Petroleum Resources and Prospecting, China University of Petroleum Beijing, Beijing, China*

[3]*Nanpu Oilfield Operation Distric of Jidong Oilfield Company, China National Petroleum Corporation, Tanghai, China*

*825346094@qq.com

ABSTRACT

In Ordos Basin of China, intermittent pumping has been applied to low production oil wells of a certain low-permeability reservoir. However, due to being short of well testing data and monitoring equipment downhole, also restricted to financial considerations, pumping work system has been made just by artificial experience. Studies in this article reveals that the pumping unit work system being used now has a low pumping efficiency and economic benefit, which would probably have a deficit when water cut increases or oil price decreases. Based on the situation of the low-permeability reservoir, a productivity formula coupling formation flow and fluid column pressure in wellhole is established, which can predict the dynamics of formation liquid production rate and liquid level in wellbore when short of monitoring equipment and well testing data, different from former methods that depend on these equipment or data to analyse intermittent pumping work system. A software is developed, which can contrast and analyse oil production and profit of multiple pumping unit working parameters, in order to optimize the intermittent pumping work system. Meanwhile, profit regions are predicted with various oil price and water cut. Additionally, mechanical safety check is considered in the software, to make sure that pumping unit work system will operate safely.

KEYWORDS – *intermittent pumping, productivity equation, software development, economic benefit.*

1. INTRODUCTION

As oil and gas resources being developed worldwide, conventional reservoirs that with good geological conditions have been becoming fewer. Therefore, unconventional reservoirs have drawed attention of petroleum workers, and relevant researches have also been carried out. At present, unconventional oil and gas resources account for a great proportion in both proven oil reserves and undeveloped reserves in China, which plays a significant role to promote the ability of oil production self-sufficiency in China[1-6]. Due to the low permeability of formation, oil wells in low-permeability reservoirs usually have a low productivity, and artificial lift has become the major production method, among which reciprocal sucker rod pump is the majority. While during the production, people find that pump displacement frequently exceeds the deliverability of formation, and liquid level in wellbore will decrease, which can easily lead to decline of pump efficiency, even dry pumping, aggravation of friction between sucker rod and wellbore, also waste of electric power. By now about 70% oil wells in Ordos Basin of China are under the condition that pump displacement mismatches deliverability of formation [7].

For low production wells, though the pumping parameters have been set to their limits (maximum stroke and minimum frequency, etc.), continuous pumping method still has a pump displacement over deliverability of formation, therefore intermittent pumping has been brought forward [8]. When pump efficiency declines to a low level due to the liquid level decreases in wellbore, the pumping unit will be shut down. On the one hand, fluid inside formation will have time to flow

into wellbore and increase the liquid level; on the other hand, mechanical wear can be reduced and electric power can be saved during shut down. When pump efficiency has increased to a certain level due to the liquid level rises, pumping unit will run again. During shut down, however, the flowing bottomhole pressure will increase as the liquid level rises in wellbore, resulting in formation liquid production rate reducing, which in turn can also slow down the rising of liquid level in wellbore [9]. This means that formation liquid production rate has a coupling relationship with the height of liquid level in wellbore.

At present, there has been quite some researcher about intermittent pumping of low production wells. However, these researches are almost based on the data of well testing, which have already known the dynamics of liquid production rate and flowing bottomhole pressure [10-16]. Furthermore, monitoring equipment and automatic regulatory system are installed, so that real time data of dynamics of oil wells can be recorded, and pumping parameters will be adjusted automatically and quickly [17-19]. For some reservoirs that mainly consist of low production wells, however, whether lots of frequent well testing or installing automatic regulatory system, it will be quite limited due to financial concerns. Also, some fields make work plans of intermittent pumping just by work experience, which is obviously unscientific.

Based on the situation of a certain low-permeability reservoir in Ordos Basin in China, a productivity formula coupling formation flow and fluid column pressure in wellhole is established, which can predict the dynamics of formation liquid production rate and liquid level in wellbore when short of monitoring equipment and well testing data. A model including tax, electric charge, sewage treatment fee, etc, is built, combined with running and shutdown time, reasonable pumping work plans can be optimized. Sucker rod mechanical strength is also considered, and the safety of multi-parameter pumping plans will be secured. At last, a software is developed, which can contrast and analyse oil production and profit of multiple pumping work plans, and predict profit regions with various oil price and water cut, so that intermittent pumping work system will be opitimized.

2. PRODUCTIVITY FORMULA COUPLING FORMATION FLOW AND FLUID COLUMN PRESSURE IN WELLBORE

2.1. Assumptions

A reservoir with supply boundaries that is in the middle and later periods of development, will have relatively stable (minor variations) production rate and water cut of oil wells, and formation pressure. Several formation pressure tests will be conducted within a few months, and the variation of formation pressure is usually not obvious in a month or two. Meanwhile, field workers will have a lot of water cut tests within a month, which turns out that water cut doesn't change much.

The idea of differential can be taken into consideration, that each water cut test or formation pressure test is conducted with a interval of less a month to another test, which can be considered as a time infinitesimal compared to the life of reservoir development (more than 20-30 years). Within each time infinitesimal, the flow in formation can be viewed as steady flow, and oil and water can be viewed as a pseudo single-phase liquid as the water cut almost doesn't change. When a new test has been conducted, the new data will be used in research of next time infinitesimal.

2.2. Productivity Formula Derivation

The flow in formation can be viewed as steady flow within a time infinitesimal, so here take Dupuit formula:

$$Q = \frac{2\pi Kh(p_e - p_{wf})}{\mu\left(\ln\dfrac{r_e}{r_w} + S\right)} \cdot 10^{-6} \tag{1}$$

124

where Q is formation liquid production rate, m3/s; K is formation permeability, 10-3μm2; h is formation thickness, m; pe is supply boundary pressure, MPa; pwf is flowing bottomhole pressure, MPa; μ is fluid viscosity, mPa·s; re is supply boundary radius, m; rw is wellbore radius, m; S is skin factor.

During pumping unit shut down, as fluid in formation flows into wellbore, the liquid level in casing-tubing annulus will rise, resulting in fluid column pressure increasing. Here take the fluid column pressure as dominant factor that generates flowing bottom hole pressure, and consider casing pressure as atmosphere. Therefore, within each time infinitesimal, the variable is flowing bottomhole pressure pwf in Eq.(1).

Rewrite flowing bottomhole pressure pwf into the height of fluid column in casing-tubing annulus, and Dupuit formula of moment t is:

$$Q = \frac{2\pi Kh(p_e - \rho g H \cdot 10^{-6})}{\mu\left(\ln\dfrac{r_e}{r_w} + S\right)} \tag{2}$$

where H is height of fluid column in casing-tubing annulus, m; g is acceleration of gravity, 9.8 m/s^2.

As shown in Figure 1, liquid level increases by *ΔH* in casing-tubing annulus within time *Δt*, and Dupuit formula of moment *t+Δt* is:

$$Q' = \frac{2\pi Kh[p_e - \rho g(H + \Delta H)\cdot 10^{-6}]}{\mu\left(\ln\dfrac{r_e}{r_w} + S\right)} \tag{3}$$
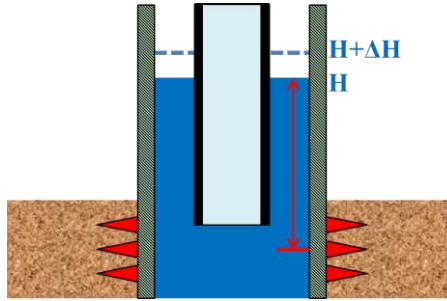
Figure 1. *Liquid Level Increases by ΔH within Time Δt in Casing-Tubing Annulus*

Variation of formation liquid production rate ΔQ from moment t to moment t+Δt can be obtained by Eq.(3)-Eq.(2):

$$\Delta Q = Q' - Q = -\frac{2\pi Kh}{\mu\left(\ln\dfrac{r_e}{r_w} + S\right)} \cdot \rho g \Delta H \cdot 10^{-6} \tag{4}$$

125

When $\Delta t \to 0$, there is $\Delta H \to 0$, according to the definition of differential, the derivative of formation liquid production rate Q with respect to height of liquid level H can be written as follow:

$$\lim_{\Delta H \to 0} \frac{\Delta Q}{\Delta H} = \frac{dQ}{dH}$$

which is:

$$\frac{dQ}{dH} = -\frac{2\pi Kh}{\mu \left(\ln \frac{r_e}{r_w} + S \right)} \cdot \rho g \cdot 10^{-6} \tag{5}$$

Due to formation fluid flowing into casing-tubing annulus during time dt, the liquid level will rise by dH. According the schematic figure (0), the volume of fluid produced within time dt equals the shadow area that is encompassed by the curve of $Q(t)$ and the t axis.
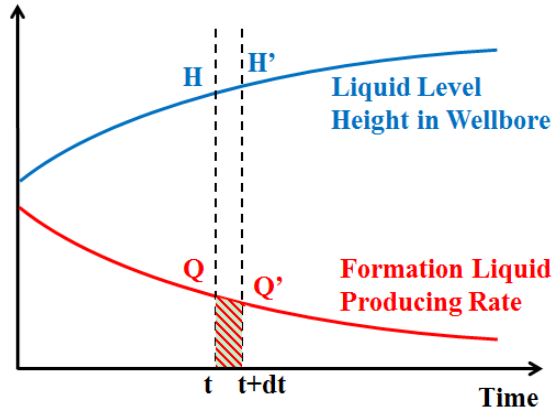
Figure 2. *Dynamics of Formation Liquid Producing Rate and Liquid Level Height During Well Shutdown*

As the time variable dt is quite tiny, a bit of curve of $Q(t)$ can be viewed as a straight line, so the shadow area can be viewed as a trapezoid:

$$\frac{(Q + Q') \cdot dt}{2} = Ac \cdot dH \tag{6}$$

where Ac is cross section area of casing-tubing annulus, m². Considering $\Delta Q \approx dQ$, Eq.(6) can be rewritten into:

$$\frac{(Q + Q + dQ) \cdot dt}{2} = Ac \cdot dH \tag{7}$$

Substitute Eq.(7) into Eq.(5), and rearrange:

$$dQ = -C \cdot Qdt - \frac{C}{2} \cdot dQdt \tag{8}$$

126

where

$$C = \frac{2\pi Kh}{\mu\left(\ln\frac{r_e}{r_w} + S\right)} \cdot \frac{\rho g \cdot 10^{-6}}{Ac}$$

The item of $dQdt$ can be omitted because it is infinitesimal of higher order. Separate variables of Eq.(8) and integrate:

$$\int_{Q_0}^{Q} \frac{dQ}{Q} = -C\int_{t_0}^{t} dt$$

where Q_0 is formation liquid production rate at initial moment (already known), m^3/s; t_0 is initial moment, s. Integrate and rearrange:

$$Q = \exp\left[\ln Q_0 - C(t - t_0)\right] \tag{9}$$

where

$$C = \frac{2\pi Kh}{\mu\left(\ln\frac{r_e}{r_w} + S\right)} \cdot \frac{\rho g \cdot 10^{-6}}{Ac}$$

And Eq.(9) is the productivity formula coupling formation flow and fluid column pressure in wellhole.

3. SOFTWARE DEVELOPMENT OF INTERMITTENT PUMPING WORK SYSTEM OPTIMIZING

3.1. Production Pattern of Oil Well

When liquid level in wellbore declines below point B that preset as a pump submergence, shut down the pumping unit. During the shutdown, liquid level in wellbore rises as formation fluid flows in, which increases flowing bottomhole pressure and decreases formation liquid production rate as well as the rising speed of liquid level. When liquid level reaches point A, start pumping unit. Fluid in wellbore is being extracted until liquid level declines below point B again, shut down pumping unit, and it comes the next cycle period.

The running and shutdown time of pumping unit can be altered by changing the preset pump submergences of point A and B. Electric energy fee, that pumping unit consumes during running time, will be calculated by the sum of multiple running time.

3.2. Analysis of Oil Sale Profit

After being dewatered, some of the produced oil is used for the field energy supply, and the rest is for sell. The proportion that oil for sell to total produced oil is called commodity rate. Some of saleroom is used for paying taxes, and some is for sewage treatment fee and other costs. The rest

127

of saleroom is viewed as sale profit in this article, which can be used for paying salaries, financial accumulation and investment on field development.
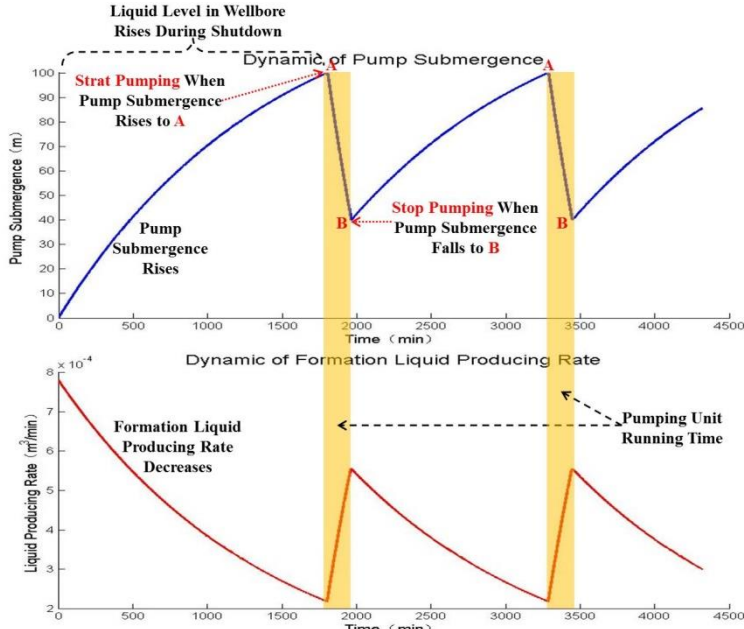
Figure 3. *Dynamics of Formation Liquid Producing Rate and Pump Submergence During Running Time and Shutdown.*

$$S = Q_t \cdot R_{com} \cdot P \cdot (1 - T_{ax}) - F_{elec} \cdot T_{open} - Q_t \cdot f_w \cdot F_{wat}$$

where S is sale profit, RMB; Q_t is oil production, ton; R_{com} is commodity rate, fraction; P is oil price, RMB/ton; T_{ax} is composite tax rate, fraction; F_{elec} is average electric energy charge, RMB/min; T_{open} is sum of pumping unit running time, min; f_w is water cut of oil well, fraction; F_{wat} is sewage treatment fee, RMB/ton.

3.3. Load and Fatigue Strength Check of Sucker Rod
(1) Upstroke and Maximum Load of Sucker Rod
Sucker rod generates maximum load Pmax during upstroke, including weight of sucker rod, weight of fluid column that lifted by pump, inertial load of sucker rod and fluid column, and kinds of friction (downward).

$$P_{max} = W_{rod} + W_{fluid} + I_{rod} + I_{fluid} + F_f$$

(2) Downstroke and Minimum Load of Sucker Rod
Sucker rod generates minimum load Pmin during downstroke. Inertial load of sucker rod and friction become upward which can counteract some weight of sucker rod, and so does buoyancy of sucker rod when it goes into the fluid in wellbore. As sucker rod is not lifting fluid, weight and inertial load of fluid column no more exist.

128

$$P_{\min} = W_{rod} - F_{buo} - I_{rod} - F_f$$

(3) Fatigue Strength Check of Sucker Rod

Maximum and minimum stress of sucker rod can be calculated by its maximum and minimum load respectively. And its fatigue strength will be checked by drawing modified Goodman plot [20].

4. INTERMITTENT PUMPING WORK SYSTEM OPTIMIZING AND ECONOMIC BENEFIT RESEARCH

A low-permeability reservoir X in Ordos Basin of China now is implementing intermittent pumping due to the low productivity of oil wells. Considering the amount of well (over 400), it is not realistic on finance that installing monitoring equipment downhole or conducting well testing frequently for all the wells. Therefore, the field made an intermittent pumping work system by working experience, that pumping unit runs for 5.5 hours and shut down for 6.5 hours in a single work cycle period, meaning 2 cycles per day. This empirical method is a conservative way to make sure that fluid stored in wellbore would be extracted completely. However, it is inevitable that dry pumping will happen, and some electric energy is wastes. This work is aiming at optimizing intermittent pumping work system through altering pumping parameters and plan prediction, and without extra investment on equipment of oil wells.

4.1. Software Introduction and Parameter Settings

Figure 4 shows the software interface of intermittent pumping work system optimizing of low production oil well, including formation parameters, fluid parameters, casing and tubing parameters, pumping unit and mechanical parameters, pumping unit working parameters, simulation run, plotting buttons, and output. In the section of simulation run, simulating production time and economic parameters can be selected. After the simulation run ends, according to the dynamic curves of formation liquid production rate and liquid level in wellbore, some production cases can be predicted, and some parameters that not accurately obtained can also be estimated, such as the pump submergence when pumping unit restarts (as known as point B). Parameters of reservoir X and other main parameters are as shown in Table 1.
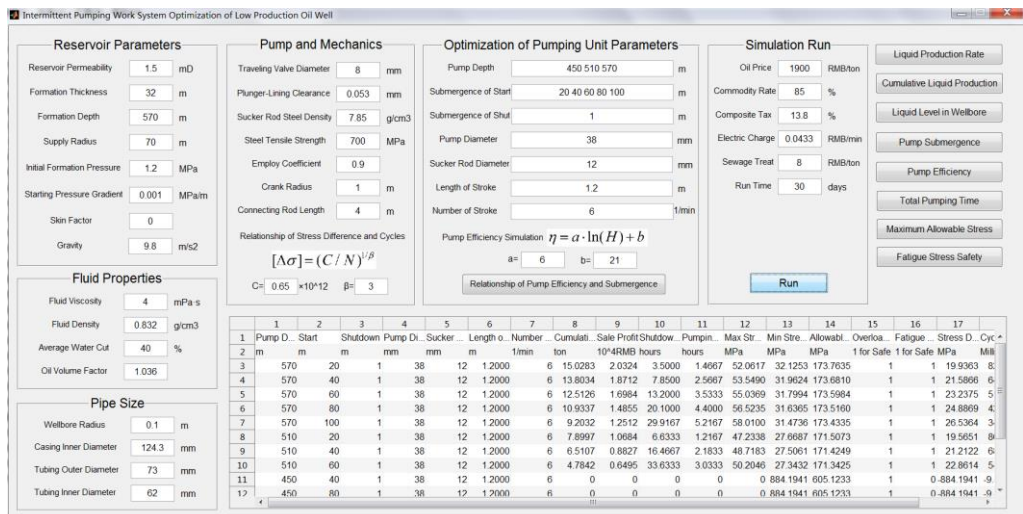
Figure 4. The Software Interface of Intermittent Pumping Work System Optimization of Low Production Oil Well

129

***Table 1.** Main Parameter Setting of Simulation*

Formation Permeability	$1.5 \times 10^{-3} \mu m^2$
Formation Thickness	32m
Formation Average Depth	570m
Formation Initial Pressure	1.2MPa
Fluid Viscosity	4mPa·s
Fluid density	$0.832g/cm^3$
Average Water Cut	40%
Pump Depth	450m
Oil Price	1900RMB/ton

4.2. Influences of Intermittent Pumping Work System on Cumulative Oil Production and Profit

(1) Influences of Pumping Duration on Oil Production and Profit

The intermittent pumping work system implemented at present in reservoir X is 5.5 hours for pumping and 6.5 hours for shutdown. However, this plan is just made by working experience, and not contrasted with 24-hour-pumping plan (continuously pumping whole day) for actual outcomes. By the software mentioned above, it is easy to obtain the pumping and shutdown durations of various pumping work systems. Here take the pumping duration as a representative of pumping work systems to research their outcomes.

Pumping work systems can be sorted into three types: ①preset pump depths for pumping unit start time and shutdown time, corresponding to its pumping and shutdown duration respectively, and the pumping unit will operate automatically according to it; ②the present pumping work system of reservoir X, that 5.5 hours for pumping and 6.5 hours for shutdown; ③24-hour-pumping work system, which has not been optimized at all. Figure 5, Figure 6 and Figure 7 show the simulation results of oil production and profit that three types of pumping work systems in various water cut periods.

Generally speaking, oil production and profit decrease gradually as the pumping duration increases. In fact, a longer pumping duration means a higher liquid level in wellbore when pumping unit starts to run, meaning it will take a longer time of shutdown to store fluid in wellbore. The higher the average of liquid level is, the lower the average of formation liquid production rate will be, resulting in the final oil production and profit reduce. With the same liquid production rate, the rising of water cut means less oil and less profit; meanwhile, sewage that needed treatment will get more, and sewage treatment fee increasing also reduces profit.

The 24-hour-pumping plan has the most oil production at all pump depths. This is because that fluid produced from formation can be extracted immediately and no fluid column exists in wellbore. Therefore, flowing bottomhole pressure almost stays the lowest, meaning formation liquid production rate can maintain the highest. The present plan (5.5 hours for pumping and 6.5 hours for shutdown), however, has a overmuch pumping duration than that actually needed, which is about 1 to 2 hours, and also occupies the time of shutdown, during which formation pressure in vicinity of well could recover somewhat. Thus, the cycles of present plan is less than those of optimized plans, and the oil production is almost the least. In the aspect of sale profit, although the 24-hour-pumping plan has the most oil production, it also has the highest electric charge due to its longest running time, which makes its profit almost the same with 1-hour-pumping plan. And due to the least oil production, the present plan basically has the lowest profit. In addition, with a shallower pump depth and a higher water cut (about 60% in this case), the present plan and 24-hour-pumping plan are likely to have a loss. Obviously it is essential to carry out research of capital expenditure for actual production activities.
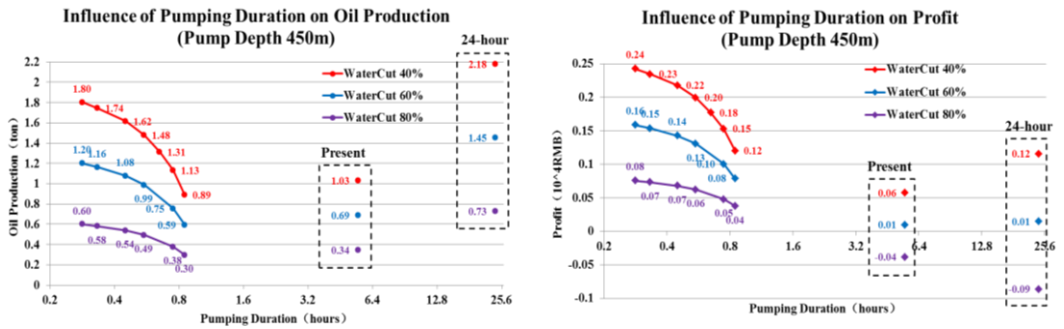
Figure 5. *Influences of Pumping Duration on Cumulative Oil Production and Profit (Pump Depth 450m).*
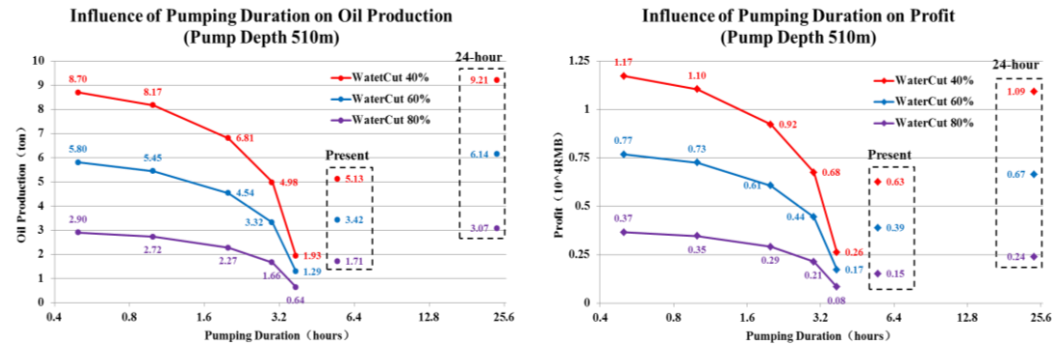
Figure 6. *Influences of Pumping Duration on Cumulative Oil Production and Profit (Pump Depth 510m).*
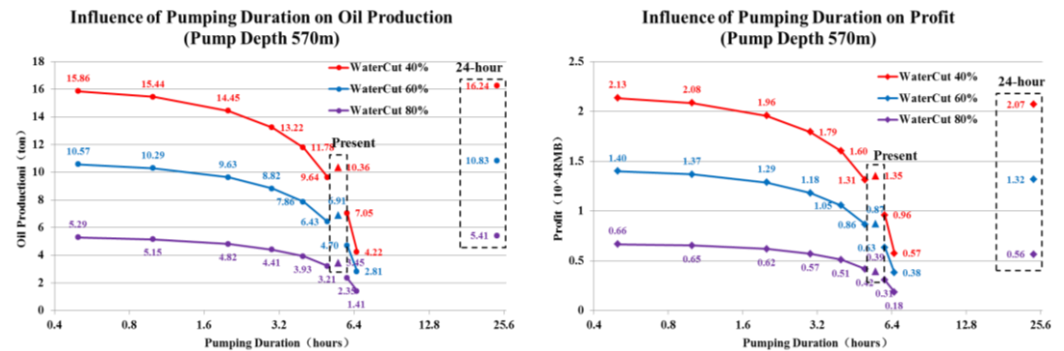
Figure 7. *Influences of Pumping Duration on Cumulative Oil Production and Profit (Pump Depth 570m).*

(2) Influences of Pump Depth on Oil Production and Profit

Reservoir X has an average formation depth of 570m, and the average pump depth of oil wells is 450m, which means that a fluid column of 120m high exists in a well and it contributes to the major proportion of flowing bottomhole pressure. According to the research above, deepening the pump depth can reduce flowing bottomhole pressure, and increasing formation liquid production rate and cumulative oil production. Meanwhile, among the automatic production plans, the profits of 1-hour-pumping plans are always higher than those of 24-hour-pumping, hence here take the 1-

131
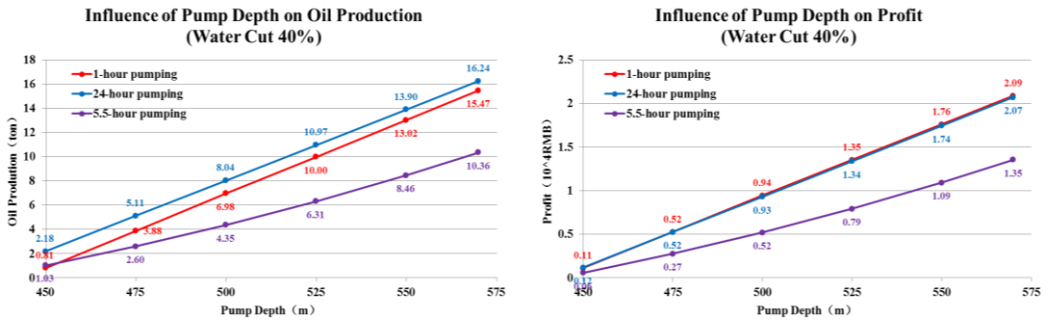
Figure 8. *Influences of Pump Depth on Cumulative Oil Production and Profit (Water Cut 40%).*
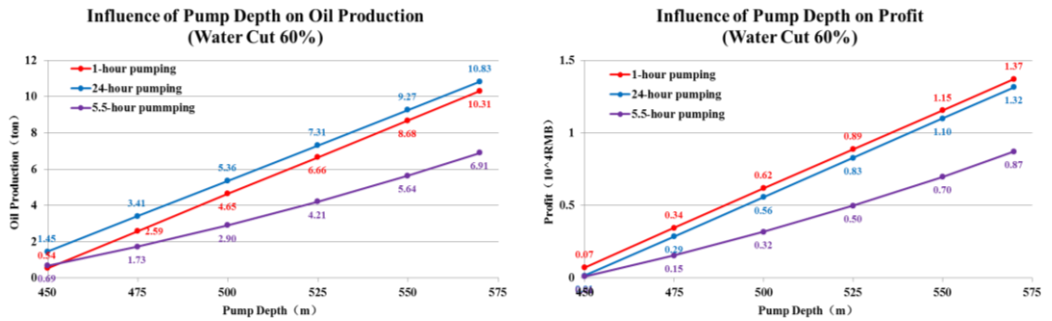
Figure 9. *Influences of Pump Depth on Cumulative Oil Production and Profit (Water Cut 60%).*
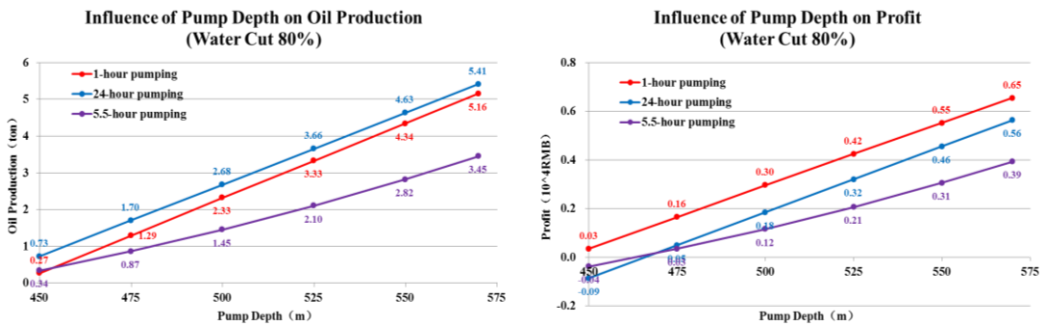
Figure 10. *Influences of Pump Depth on Cumulative Oil Production and Profit (Water Cut 80%).*

hour-pumping plan as a representative of optimized work system. Figure 8, Figure 9 and Figure 10 show the influences of pump depth on cumulative oil production and profit that optimized plan, 24-hour-pumping plan and present plan in various water cut periods. Generally speaking, the oil production and profit of three pumping types increase as pump depth deepens, and reduce as water cut rises. As pump depth is getting deeper, the constant fluid column from well bottom to pump will shorten, which reduces the average flowing bottomhole pressure and increases the average formation liquid production rate. While the rising of water cut will lower the proportion of oil to produced liquid, and add the sewage that needs treatment and expenditure, both of which will reduce the sale profit.

Meanwhile, the figures also show that the oil production and profit of the present plan are almost the lowest, due to its wasted occupation of pumping time and high expenditure on electric charge. The 24-hour-pumping plan has the most oil production, however, its profit doesn't exceed too much over that of 1-hour-pumping plan due to its highest electric charge. Especially when water

132

cut rises, the low efficiency of 24-hour-pumping plan becomes more notable, and the difference of profits between the two pumping plans largens.

4.3. Prediction of Profit Range Influenced by Oil Price and Water Cut

The main objective of studying intermittent pumping plans is that increasing oil production as much as possible within a reasonable scope of capital expenditure, to add the sale profit of oil field. Furthermore, there are also some objective factors that restrict the economic benefit of oil field. Some are optimizable capital expenditures, such as labor, management and equipment. And others are uncontrollable circumstances, such as water cut naturally rising in later period of reservoir development, and volatile oil price. The pumping work system implemented at present will have different economic benefits under various objective factors. Figure 11 shows the profit prediction of 24-hour-pumping plan with various oil price and water cut. As 24-hour-pumping plan is a type of work system that hasn't been optimized at all and has a quite low efficiency, a little adjustment and optimization would make it perform better and more profitable than before. Hence here take 24-hour-pumping plan as the lower limit of profit.
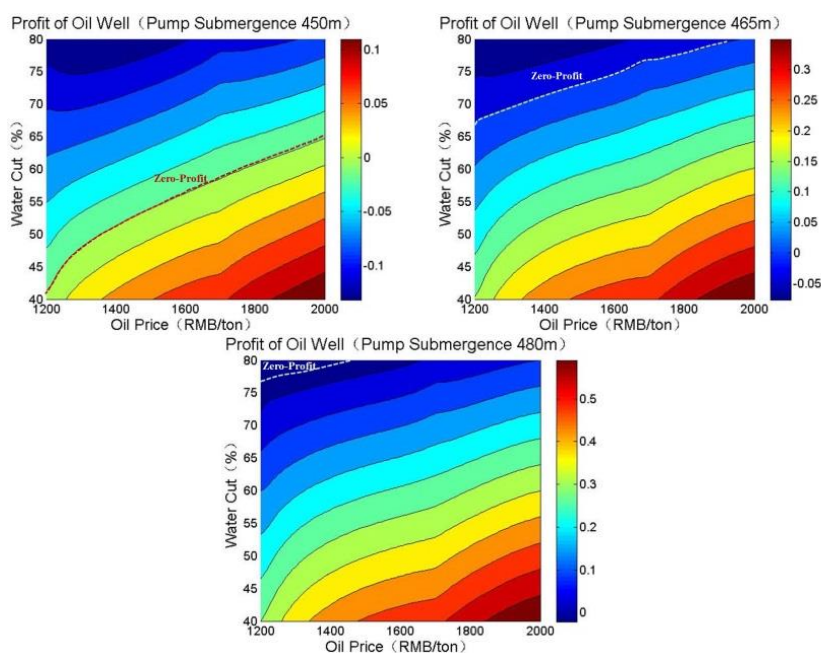
Figure 11. *Influences of Oil Price and Water Cut on Oil Well Profit*

The influences of oil price and water cut on profit can be predicted by the software developed in this work. According to the location of Zero-Profit Line, field workers can clearly see the adaptation of present pumping plan to volatile oil price and water cut rising. Figure 11 also shows that Minus-Profit Range can be diminished by deepening pump depth, which will improve the economic benefit. For the oil wells with maximum pump depth, well shutting down would be an option when oil price falls to or water cut rise to an unprofitable range, or other methods can be carried out to bring oil well back to profit range. As for the oil well that can still deepen pump depth, the economic benefit will be improved by simply doing this. Meanwhile, it can detect the maximum limit of pump depth, and buy some time for making plans of other stimulation methods.

4.4. Safety Check

133

While doing research of pumping plans and prediction of profit, it is also an essential issue that mechanical parameter safety check in actual engineering. Figure 12 shows the sucker rod maximum stress and fatigue strength safety check of all pumping plans that listed in the software.
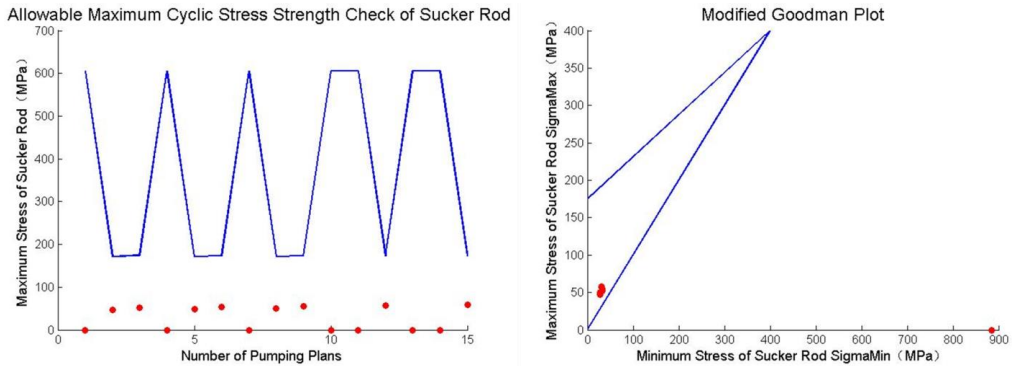
Figure 12. Maximum Stress and Fatigue Strength Check of Sucker Rod

Because of the minor formation depth of reservoir X which is 570m, loads of sucker rod are all not large, and mechanical parameters of all pumping plans are within safe range. Some of calculated results are zero, this is because that when pump submergence of shut down time (point B in Figure 3) happens to be larger than that of restart time (point A in Figure 3) due to combination of pumping unit parameters by software, it would be unreal circumstance and will not be calculated by software.

5. CONCLUSIONS AND RECOMMENDATIONS

(1) In consideration of the interaction between formation flow and fluid column in wellbore, a productivity equation coupling formation flow and fluid column pressure in wellbore is established, which can predict the dynamics of formation liquid production rate and liquid level in wellbore when short of monitoring equipment and well testing data, and in turn can also estimate liquid level according to oil production and pumping time.

(2) A software of intermittent pumping working system optimization of low production oil well is developed. By setting the pump depths of pumping unit start time and shut down time can control the operation of pumping unit, and research of multiple parameter pumping plans can also be processed. The final calculation results contain oil production, sale profit, pumping unit running and shutdown duration, which are convenient to contrast. In addition, economic parameters are included in the software to predict profit ranges of various oil prices and water cuts; as well as mechanical parameters to have safety checks of pumping plans.

(3) Studies of reservoir X reveals that the pumping unit working system implemented at present basically has a lower oil production and profit than other types of intermittent pumping plans, due to its overlong pumping duration and waste of shutdown time to recover some formation pressure. Especially when oil price falls or water cut rises, the present pumping plan is quite likely to have a loss. The 24-hour-pumping plan has the most oil production, however, still has the same problem on sale profit due to its highest electric charge. After contrasted to the former pumping plans, the 1-hour-pumping plan is recommended (shutdown duration is 2 to 5 hours according to the calculation results of the software), which has almost the highest sale profit and is convenient to operate in field.

(4) The profit ranges of various oil prices and water cuts are predicted, indicating that deepening pump depth will improve the sale profit of oil well and enlarge the profit range, which is an effective method to achieve profitability in low oil price or high water cut period.

134

REFERENCES
[1] S. Li, Research of Low Production and Inefficient Oil Well Inflow Performance and Reasonable Intermittent Pumping, Doctoral dissertation, Southwest Petroleum University, 2014.
[2] Y. Meng, X. Li, M. Jiang, D. Feng, T. Zhang, Z. Zhang, Experimental research on three dimensional flow characteristics of multiple horizontal fractures utilizing an innovative experiment apparatus, Arabian Journal of Geosciences 11 (2018) 243. *DOI:10.1007/s12517-018-3589-0*
[3] Z. Peng, X. Li, Improvements of the permeability experiment in coalbed methane, Arabian Journal of Geosciences 11 (2018) 259. *DOI:10.1007/s12517-018-3608-1*
[4] T. Zhao, X. Li, Z. Ning, H. Zhao, J. Zhang, W. Zhao, Pore structure and adsorption behavior of shale gas reservoir with influence of maturity: a case study of Lower Silurian Longmaxi formation in China, Arabian Journal of Geosciences 11 (2018) 353. *DOI:10.1007/s12517-018-3673-5*
[5] W. Zheng, Y. Liu, J. Huang, Y. Liu, J. Chen, Study on the optimal development method for offshore buried hill fractured reservoirs, Arabian Journal of Geosciences 11 (2018) 640. *DOI: 10.1007/s12517-018-3965-9*
[6] J. Ding, S. Yang, T. Cao, J. Wu, Dynamic threshold pressure gradient in tight gas reservoir and its influence on well productivity, Arabian Journal of Geosciences 11 (2018) 783. *DOI: 10.1007/s12517-018-4129-7*
[7] H. Zhu, Research of Intermittent Pumping Law on Low Production and Inefficient Oil Wells of a Block in Yanchang Oilfield, Doctoral dissertation, Xi'an Shiyou University, 2016.
[8] Y. Xiong, Study on Intermittent Oil Pumping Design of Low Pressure Oil Wells, Journal of Southwest Petroleum Institute 03 (1995) 92-96. *DOI:10.3863/j.issn.1000-2634.1995.03.013*
[9] X. Meng, H. Zhang, Quantitative Optimization of the Intermittent Production Pattern of Low Producing Oil Wells and Its Application, Journal of Xi'an Shiyou University(Natural Science Edition) 03 (2006) 38-40+115. *DOI:10.3969/j.issn.1673-064X.2006.03.010*
[10]   Q. Lei, W. Zhao, A Study on Interval Pumping Technique in Stripper Well, Drilling & Production Technology 02 (2001) 28-29+4. *DOI:10.3969/j.issn.1006-768X.2001.02.007*
[11]   R. Tang, Fluid Change Rule after Well-opening to Produce and Oil Well Shutting-in in Pumping Well, Fault-Block Oil & Gas Field 05 (2002) 53-56+92. *DOI:10.3969/j.issn.1005-8907.2002.05.016*
[12]   L. Lu, G. Li, T. Wang, J. Song, Study and Application of Intermitten Production Method System for Low Producing Well, Fault-Block Oil & Gas Field 04 (2004) 75-77+94. *DOI:10.3969/j.issn.1005-8907.2004.04.028*
[13]   M. Zhang, X. Bai, Y. Yao, X. Zhang, Z. Pang, Method for Intermittent Production System in Low Production Well, Drilling & Production Technology 03 (2005) 68-70+118. *DOI:10.3969/j.issn.1006-768X.2005.03.022*
[14]   D. Zhou, Z. Liang, A New Approach for Determing the Reasonable Intermittent Pumping Period for Low Efficiency Well, Drilling & Production Technology 01 (2003) 52-55+3-4. *DOI:10.3969/j.issn.1006-768X.2003.01.017*
[15]   J. Zou, Low Permeability Reservoir Intermittent Production Optimization and Research, Doctoral dissertation, Xi'an Shiyou University, 2013.
[16]   P. Fan, Research and Application of Low Permeability Reservoir Intermittent Production Cycle, Doctoral dissertation, Xi'an Shiyou University, 2013.

135

[17]   H. Gao, Q. Zhu, C. Yang, Y. Liu, Intermittent Intelligence Pumping Unit and Its Application, China Petroleum Machinery 11 (2007) 58-60. *DOI:10.3969/j.issn.1001-4578.2007.11.016*

[18]   K. Palka, J. Czyz, Optimizing Downhole Fluid Production of Sucker-Rod Pumps With Variable Motor Speed, Spe Production & Operations 24 (2009) 346-352. *DOI:10.2118/113186-PA*

[19]   H. Yang, L. Mu, Y. Zeng, et al, Real Time Calculation of Fluid Level Using Dynamometer Card of Sucker Rod Pump Well[C]// International Petroleum Technology Conference, Kuala Lumpur, Malaysia, 2014. *DOI:10.2523/IPTC-17773-MS*

[20]   X. Wang, The Software Development of Sucker Rod Pump Lifting System Condition Analysis and Design, Doctoral dissertation, Yangtze University, 2013.

Calculation of Mass Attenuation Coefficient of Different Types of Cements used in Concrete

Aycan ŞAHİN[1]*, Kadir GÜNOĞLU[2], İskender AKKURT[3]
[1] Akdeniz University, Vocational School of Health Services, Antalya-TURKEY
[2] Isparta University of Applied Sciences, Technical Vocational School, Isparta- TURKEY
[3] Suleyman Demirel University, Science Faculty,Physics Department, Isparta-TURKEY
* aycansahin@akdeniz.edu.tr

ABSTRACT

Cement used as hydraulic binder material especially in cement production consists of natural limestone and clay. In this paper, the mass attenuation coefficients of CEM IV / B (P) 32,5 N type cement commonly used in concrete production were calculated for 511 and 1275 keV gamma energies using GAMOS Monte Carlo simulation code. The results of mass attenuation coefficient obtained were compared with the values measured.

KEYWORDS: Mass attenuation, cement, XCOM, GAMOS

1. INTRODUCTION

The cement industry is one of the basic industries that play an important role in the developing countries. Also, cement is one of the most common structural materials used in constructions such as home, office, hospital, etc. For this reason, investigation of radiation shielding properties of cement have been important.

After discovery of the radioactivity by Becquerel, radiation started to be used in various fields and nowadays it became a part of our life. Employment of radiation, ranging from industry to medicine, brings its hazardous effect and hence radiation protection is developed in parallel with the utilization of radiation.

People are being exposed to increasing amounts of radiation. In order to be protected from radiation, three different criteria are commonly considered. These are time, distance and the shielding. Shielding is the most effective way of radiation protection. An effective shield should cause a large energy loss on a small distance, without emission of more hazardous radiation.

In the present work, mass attenuation coefficients of cement pastes produced using CEM IV / B (P) 32,5 N type cement have been investigated for different gamma energies (511 and 1275 keV) by using GAMOS Monte Carlo simulation code. The calculation results have been compared with the results of measured.

2. MATERIAL AND METHOD

Cement paste was prepared with type of Portland cement which is CEM IV / B (P) 32,5 N and CEN reference sand has been used according to TS EN 196-1 standard.

The photon attenuation coefficients of cement paste have been measured using the gamma spectrometer system containing NaI (Tl) detector coupled to a digital spectrum analyzer (DSPEC LF) which was a full featured 16 K multichannel analyzer on advanced digital signal processing techniques, were recorded on the MAESTRO-32 gamma spectroscopy software [1]. The measurements have been carried out at 511 and 1275 keV which were obtained from 22Na radioactive source.

The schematic arrangement of the experimental setup used in the present study is shown in Figure 1.

137
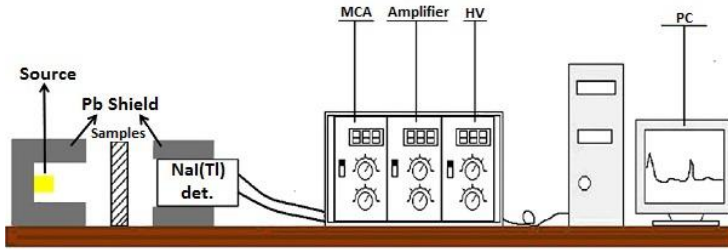
Figure 1. *Schematic view of the experimental setup.*

The photon attenuation coefficients have been evaluated by comparing I and I0, which are the count rates measured by the detector, respectively, with and without the absorber of thickness x.

$$\mu = \frac{1}{x}\ln\left(\frac{I_0}{I}\right) \tag{1}$$

Also in this study, a variant of the famous Monte Carlo package Geant 4 called GAMOS (version 5.1.0) was employed for modeling the geometry of the problem as well as estimating the interaction of source photons [2-4]. The photon was modeled as a point source in a cube of 2 mm directed as a parallel beam toward a collimator having a 0.5 cm opening and made of lead. The beam passed the 0.5 cm thick absorber before reaching the detector which was described as NaI(Tl) material.

3. RESULTS AND DISCUSSION

The mass attenuation coefficient of the cement paste produced using CEM IV / B (P) 32,5 N type cement was calculated by using GAMOS, which is a Monte Carlo simulation code. The simulation results (G) obtained are shown in Figure 1 together with the experimental results (Exp).
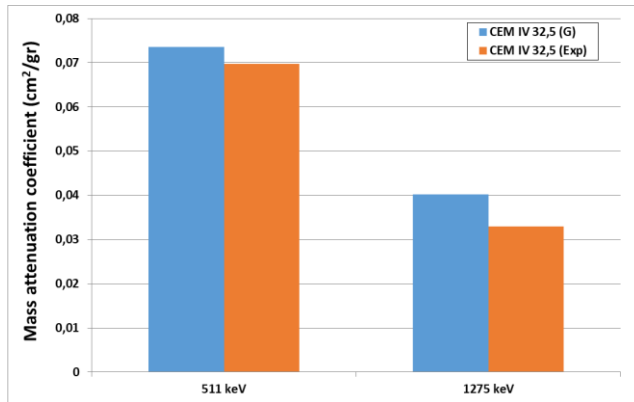
Figure 2. Simulation (G) and experimental (Exp) mass attenuation coefficients

It is clearly seen that the agreement between calculations and measurements are very good. It can be seen that the measured results decrease with increasing photon energy.

REFERENCES

[1]. Akkurt, I., Altindag, R., Günoğlu, K., Sarıkaya, H., 2012. Photon attenuation coefficients of concrete including marble aggregates. Annals of Nuclear Energy 43, 56–60.

138

[2]. Agostinelli, S. et al., Geant4 - A Simulation Toolkit, Nucl. Instrum. Meth. A 2003; 10.1016/S0168-9002(03)01368-8

[3]. Arce P, Rato P, Canadas M. and Lagares, JI. GAMOS: A GEANT4-based easy and flexible framework for nuclear medicine applications. 2008 IEEE Nuclear Science Symposium and Medical Imaging Conference (2008 NSS/MIC), 2008; 10.1109/NSSMIC.2008.4775023.

[4]. Geng, J.P., Cao, T.G., Li, D.F., An, H.L., Han, Y.R., Li, J., Hu, J.S., Li, N.N., Zhan, Y., 2014. Calculation of the physical and microdosimetric parameters of electron and alphaparticle radiation using Monte Carlo simulations. Chin. Phys. Lett. 31(038701_1–038701_3).

Analysis of Cement Sheath Sealing Failure Mechanism During Hydraulic Fracturing

Wei Lian[1], Jun Li[1*], Qian Tao[2] and Yan Xi[3]

[1]China University of Petroleum (Beijing), College of Petroleum Engineering, Beijing, China
[2]Sinopec Engineering and Technology Research Institute, Beijing, China
[3]Beijing University of Technology, Beijing, China
lijun446@vip.163.com

ABSTRACT

The phenomenon of sustained casing pressure (SCP) is widespread during shale gas development process in China. Taking a drilled shale gas well as an example, the finite element model of casing-cement sheath-formation assembly under different spuddings were established based on the shale mechanical parameters profile and the in-situ stress profile, The circumferential / radial stress profile of B annular cement sheath was calculated and the integrity of the cement sheath was judged by Mohr-Coulomb criterion. On this basis, the effects of the cement sheath Young's modulus, pump pressure at the wellhead on the stress profile were analyzed. The results show that: The cement sheath over the first casing shoe prone to circumferential tensile failure, the lower prone to radial compression failure; Reduce the Young's modulus of the cement sheath can reduce the circumferential/radial stress of the cement sheath and the Mohr-Coulomb criterion value. Under different pumping conditions, the circumferential / radial stress of cement sheath and the Mohr-Coulomb critical value are basically parallel. Reducing the pump pressure is beneficial to the integrity of the cement sheath, thus, technical measures should be taken to reduce the cracking pressure of shale during the process of fracturing.

KEYWORDS - *Shale gas, Sustained casing pressure, B annular, Circumferential stress, Radical stress.*

1. INTRODUCTION

Hydraulic fracturing has the characteristics of high pump pressure and large displacement, which poses a threat to wellbore integrity [1-3], the most prominent problem is the wellhead sustained casing pressure (SCP). In the process of shale gas development in the China, there are also significant problems in SCP which cause serious risk of wellhead safty [4], thus it is necessary to analyze the mechanism of SCP during the development of shale gas wells. The analysis of the casing-cement sheath-formation composition has been studied by many scholars, the earliest research was to use the lame's formula to analysis the casing-cement sheath-formation assembly under uniform stress conditions, on this basis, some scholars analyzed the stress state of the cement sheath and the casing under non-uniform stress conditions [5], taking into account the frequent changes in temperature and pressure during the development of oil and gas wells, it is possible to calculate the stress variation of casing and cement sheath by adding the thermal stress term in lame's formula [6]. With the continuous deepening of research, such as referring to casing eccentric, transient thermal-pressure coupling, SAGD, cyclic pressure, it is necessary to conduct comprehensive research on the combination of laboratory test and numerical simulation. Casing eccentric has little effect on its own stress, but great effect on the stress state of the cement sheath, which increases the risk of the tensile failure of the cement sheath [7].

However, all the above studies focused on the integrity of the cement sheath at the location of the production layer, and did not study the integrity of the cement sheath at the non-production layer. According to the definition of SCP, there are two necessary conditions that cause SCP, the first is the existence of high pressure fluid in the formation, the second is the failure of the wellbore barrier [8-11]. The phenomenon of SCP after fracturing in a shale gas well indicates that the

wellbore barrier has failed from the wellhead to the fracturing horizon during the fracturing process. As one of the annulus barriers, if the B annulus cement (cement sheath between tubing and intermediate casing) integrity is destroyed, the formation fluid may migrate upward along the casing shoe and cause SCP. Therefore, it is necessary to study the integrity of cement sheath in the vertical well during fracturing. In this paper, the casing-cement sheath-formation finite element model under different spuddings were established, and the integrity of the cement sheath in the vertical section was judged based on the Mohr-Coulomb criterion, and the sensitivity of the factors affecting the integrity of the cement were analysed lastly.

2. NUMERICAL MODEL ESTABLISHMENT AND VERIFICATION
2.1. Well structure

Take a drilled well as example, there was no casing pressure before fracturing and SCP phenomenon occurred after fracturing, the preliminary conclusion is that the methane gas penetrate along the B annulus cement up to the wellhead that cause SCP, so it is necessary to study the stress state of the cement sheath in the vertical well during the fracturing.

The first-stage conduit is 30 m deep into the hole, the second-stage conduit is 160 m deep into the hole, the surface casing is 940 m in depth and the intermediate casing is 2350 m in depth. The sizes of the casing and bit for each spudding are shown in Table 1. According to the dimensions of the casing and the bit in Table 1, the sizes of the corresponding near-borehole finite element models at different depths of the well can be determined.

Table 1. Casing Size and Bit Size in Each Spudding.

Name	First stage conduct	Second stage conduct	Surface casing	Intermediate casing	Tubing
Inter diameter （mm）	704	482.6	315.32	222.4	118.62
Outer diameter(mm)	720	504	339.7	244.5	139.7
Bit size (mm)	914.4	660.4	444.5	311.2	215.9

2.2. Finite element model

In view of the fact that there are too many grids in the three-dimensional finite element model of the vertical well section that causes low operation efficiency and high time cost, this paper uses the two-dimensional plane strain finite element model instead of the three-dimensional finite element model. The finite element model corresponding to different spuddings were established. The corresponding finite element models for the first-stage conductor, second-stage conductor, and technic casing and product casing are shown in Fig. 1.

(a) First stage conduct   (b) Second stage conduct   (c) First spudding   (d) Second spudding
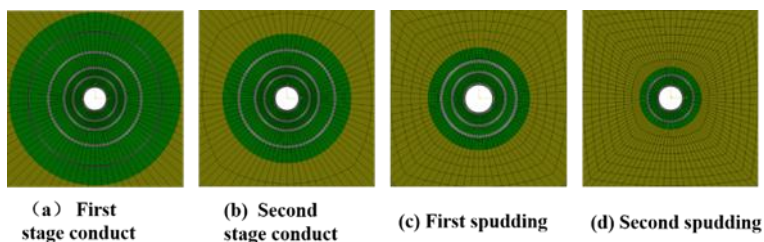
Figure 5. Finite Element Models for Different Spuddings.

The size of the formation is taken as 10 times the size of the wellbore in order to eliminate the influence of the size. The Young's modulus of the casing and the conductor is 210 GPa, the Poisson's ratio is 0.3. The Young's modulus of the cement sheath is 14.3 Gpa and the Poisson's

141

ratio is 0.15, In terms of rock mechanics parameter setting, rock mechanics parameters corresponding to different well depths can be set according to the rock mechanics parameters profile. The displacement of the outer boundary of the formation is constrained. In terms of load setting, since the casing inter pressure and in-situ stress are related to the well depth, the casing inter pressure and in-situ stress can be applied to the model according to the casing inter pressure profile and the in-situ stress profile, and corresponding finite element models with different depth can be obtained in this way.

2.3. Failure criterion

The failure of cement sheath could be mainly divided into tensile failure and compressive failure. Shear failure may also occur when the cement sheath suffers the combination action of tensile stress and compressive stress. When suffering the pure tensile load, the failure of the cement sheath can be judged with the criteria of maximum principal stress. However, the failure of cement sheath is a control of compressive load instead of tensile load once in a while. In such case, the failure of cement sheath under different stress states can be predicted with Mohr–Coulomb failure criteria, with the failure criteria and safety factor of cement sheath shown in Table 2. In the cylindrical coordinate system, $\sigma_1=\sigma_\theta$, $\sigma_3=\sigma_r$, where σ_θ and σ_r are the tangential and radial stresses respectively, MPa.

Table 2. Mohr-Coulomb failure criteria.

Stress interval	Description of interval	Relationship among principal stresses	Failure standard
1	Tension–tension–tension	$\sigma_1 \geq \sigma_3 \geq 0$	$\sigma_1 \geq \sigma_t$
2	Compression–compression–compression	$0 \geq \sigma_1 \geq \sigma_3$	$-\sigma_3 \geq \sigma_c$
3	Tension–compression–compression; Tension–tension–compression	$\sigma_1 \geq 0 \geq \sigma_3$	$\dfrac{\sigma_1}{\sigma_t} - \dfrac{\sigma_3}{\sigma_c} \geq 1$

σ_1 and σ_3 are the maximum and minimum principal stresses, MPa; σ_t and σ_c are the tensile strength and compressive strength of the cement sheath, MPa.

3. CASE STUDY
3.1. In-situ stress profile

The in-situ stress are assumed increases linearly with increasing well depth, in the horizontal section, the vertical stress, maximum horizontal stress and the minimum stress are 51, 65, 44 MPa respectively, so the magnitude of the in-situ stress at different well depths can be calculated as follows.

$$\sigma_H = h \cdot \frac{65}{2450} \tag{2}$$

$$\sigma_h = h \cdot \frac{44}{2450} \tag{2}$$

$$\sigma_V = h \cdot \frac{51}{2450} \tag{3}$$

As shown in Fig. 2, the Young's modulus of rock increases with the depth, and there is a large change in the Young's modulus of the rock near the well depth of 500 m, mainly because the

142

lithologic changes at the interface between Penglaizhen Formation and Xujiahe Formation. The change regulation of Poisson's ratio with the depth is opposite with the Young's modulus, this is because the rock deformability capacity is strong when the rock's Young's modulus is low.
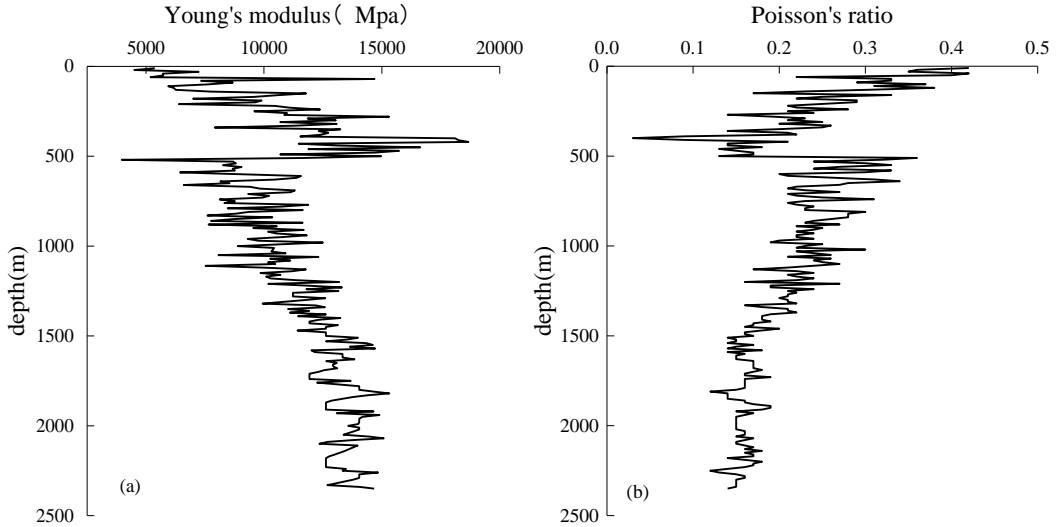
***Figure** 2. Rock Mechanics Parameters Profile.(a) Young's Modulus Variation law, (b) Poisson's Ratio Variation Law.*

3.2. Casing pressure profile
The formula for the effective internal pressure of the casing is as follows:

$$P_{in} = P_{wh} + P_h - \Delta P_s \qquad (4)$$

Where P_{in} is the effective internal pressure of casing, P_{wh} is the wellhead pump pressure, P_h is the hydrostatic pressure of fracturing fluid and ΔP_s is the friction resistance along the well bore, respectively, during the calculation, the wellhead pump pressure is 85 MPa and fracturing fluid density is 1000 kg/m³.

3.3. Results and Discussion
Based on the previous wellbore structure, in-situ stress, rock mechanics parameters profile and effective internal pressure of casing, the circumferential stress, radial stress, and Mohr-Coulomb criterion in different depths of the B annular cement sheath can be calculated. The results were illustrated in Fig. 3.
As shown in Fig. 3, the maximum radial stress of the B annular cement sheath is negative means that the inner wall of the cement sheath is compressed in the radial direction, and the maximum circumferential stress of the B annular cement sheath is positive means that the inner wall of the cement sheath is tensile in the circumferential direction. The maximum radial stress of the cement sheath increases due to the in-situ stress and the effective internal pressure of the casing increase with the depth, and the degree of compression of the cement sheath increases continuously. However, The maximum circumferential stress of the cement sheath decreases as the depth increases, the main reason is that the increase of the in-situ stress with the depth of the well is greater than the increase of the casing inner pressure, the "wrap" effect of the in-situ stress on the near-wellbore assembly is stronger than the "expansion" of the casing internal pressure.

143
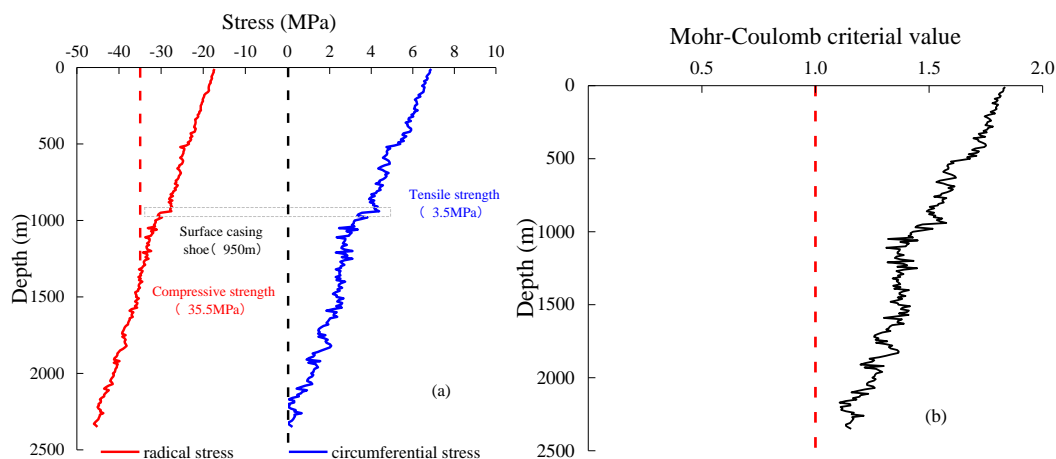
Figure 3. *Stress Profile of Cement Sheath.(a) Maximum Circumferential Stress, Radial Stress Profile,(b) Mohr-Coulomb Criterion Value.*

When the depth is less than the corresponding depth of the first spudding casing shoe, Mohr-Coulomb criterion value is larger than 1, the main form of cement sheath failure is circumferential tensile failure. Compared with the second spudding, the first spudding have one more surface casing and cement sheath, it is difficult to transfer the in-situ stress to the B annular cement sheath to balance the circumferential tensile stress caused by the casing internal pressure. Therefore, the B annular cement sheath over the first casing shoe is prone to circumferential tension failure. When the depth continues to increase, the cement sheath is mainly subjected to radial compressive stress and its value increases continuously, with the risk of radial compression failure.
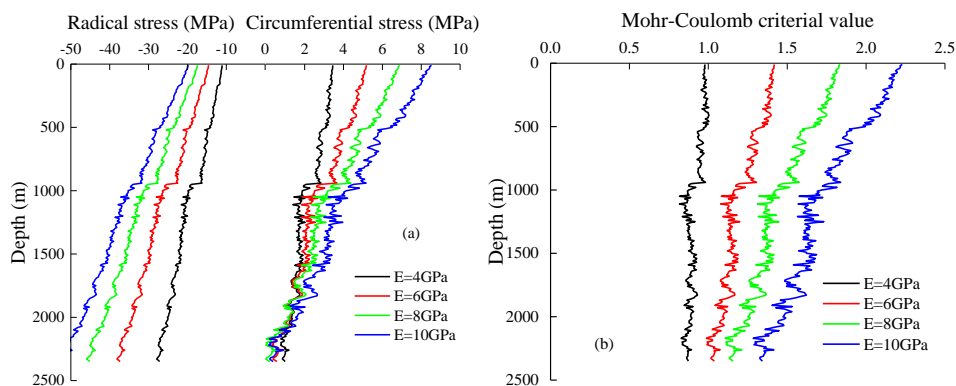
Figure 4. Stress Profile of Cement Sheath Under different Young's modulus.(a) Maximum Circumferential Stress, Radial Stress Profile, (b) Mohr-Coulomb Criterion Value Profile.

3.4. Sensitivity Analysis
The Young's modulus is one of the most important parameters in controlling the integrity of oil and gas wells, It is generally believed that the characteristics of cement sheath should be "high strength, low stiffness", However, the effect of the Young's modulus on the integrity of the cement sheath in the entire straight section has not been studied, keep other parameters unchanged and set the Young's modulus to be 4, 6, 8 and 10GPa, the results are shown in Fig. 4. As can be seen from

144

the Fig. 4, the cement sheath with low Young's modulus can significantly reduce the circumferential stress and radial stress, the circumferential stress under the first casing shoe tends to coincide or even intersect, the circumferential stress over the first casing shoe is more sensitive to the change of Young's modulus. The radial stress changes significantly at the casing shoe, which is mainly due to the different spuddings of the well, resulting in different stress states of the B annular cement. At the same time, it can be seen that the lower the Young's modulus, the more obvious the radial stress reduction. It is necessary to use low Young's modulus cement in the straight well section, especially above the casing shoe, to prevent the cement sheath from yielding. Fig. 4(b) shows that reducing the Young's modulus of cement sheath is also important to reduce the Mohr-Coulomb critical value, especially the judgement value above the surface casing shoe will be significantly reduced, which is conducive to preventing the formation fluid from channeling up the surface casing shoe to the wellhead and causing annulus pressure.

(2) Wellhead pump pressure

Shale rocks have strong heterogeneity and there are great differences in the initiation pressure of shale in different fracturing sections, in the actual fracturing process, the wellhead pump pressure changes greatly. It is necessary to study the stress state of cement sheath under different pump pressure conditions. Setting the Young's modulus and Poisson's ratio of the cement sheath to be 4 GPa and 0.2, wellhead pump pressure are 75, 85, 95, 105 and 115 MPa respectively, the calculation results are shown in Figure. 5.
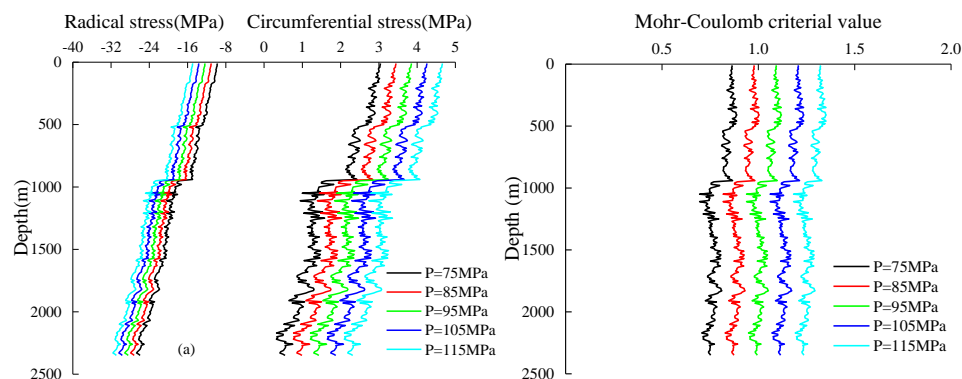
Figure 5. *Stress Profile of Cement Sheath Under different Wellhead Pump Pressure. (a) Maximum Circumferential Stress, Radial Stress Profile, (b) Mohr-Coulomb Criterion Value Profile.*

It can be seen form the Fig. 5(a) and Fig. 5(b) that the circumferential stress, radial stress, and Mohr-Coulomb critical value profile under different wellhead pumping conditions are basically parallel. The greater the pump pressure, the greater the risk of failure of the cement sheath due to circumferential stretching. It is necessary to adopt technical means to reduce the initiation pressure of shale during the fracturing operation to ensure the integrity of the cement sheath.

4. CONCLUSION

(1) Based on the wellbore structure of shale gas wells, the near-wellbore assemblies under different spuddings were established. The radial and circumferential stress profiles of the B annular cement sheath during the fracturing process were calculated, and the Mohr-Coulomb criterion was used for the determination. The results show that: The stress of the cement sheath near the casing shoe will change abruptly during fracturing process, the B annular cement sheath locations are prone to radial compression failure. over the first spudding casing shoe is prone to circumferential tensile failure, and the following

145

(2) Cement sheath with low Young's modulus can reduce the circumferential and radial stress as well as the Mohr-Coulomb judgment value. Therefore, the use of low Yong's modulus cement sheath is beneficial to improve the integrity.

(3) The profile of circumferential/radial stress and Mohr-Coulomb criterion value are basically parallel under different wellhead pump pressure, reducing the internal pressure of the casing is beneficial to the integrity.

ACKNOWLEDGMENTS

REFERENCES

[1]Guo, Xueli., Li, Jun., Liu, Gonghui. et al. Shale experiment and numerical investigation of casing deformation during volume fracturing. Arabian Journal of Geosciences. 22 (2018) 12-16. DOI: 0.1007/s12517-018-4091-4

[2]Saberhosseini, Seyed Erfan., Keshavarzi, Reza. et al. The influence of deviatoric and horizontal differential stress and pore pressure on hydraulic fracture opening by fully coupled 3D cohesive elements method. Arabian Journal of Geosciences. 12 (2019) 12-33. DOI: 10.1007/s12517-018-4222-y

[3]Mao, Xiaolong., Liu, Yuetian., Guan, Wenlong. et al. Experimental and numerical simulation on the influence of anisotropic fracture network deformation to shale gas percolation. Arabian Journal of Geosciences.20 (2018) 11-615.DOI: 10.1007/s12517-018-4222-y

[4]Saunders, P. J., McCoy, D., Goldstein, R. et al. A review of the public health impacts of unconventional natural gas development. Environmental Geochemistry and Health. 40 (2018) 1-57. DOI: 10.1007/s10653-016-9898-x

[5]Mueller, D.T., GoBoncan, V., Dillenbeck, R.L.et al. Characterizing casing-cement-formation interactions under stress conditions: impact on long term zonal isolation. Presented at the SPE Annual Technical Conference and Exhibition, Houston, TX., USA. September 26-29. SPE 90450. DOI: 10.2118/90450-MS

[6]Chen, zhan., Zhang Zhi., Shi Taihe.et al. Mechanism of annular fluid thermal expansion pressure in HTHP sour gas wells. Natur Gas Ind. 30 (2010) 88-90. DOI:10.1016/S1876-3804(11)60008-6

[7]Shahri, M., Schubert, J. J., Amani, M. Detecting and modeling cement failure in high-pressure/high-temperature (HP/HT) wells, using finite element method (FEM). Presented at the International Petroleum Technology Conference, Doha, Qatar. November 21-23. 2005 SPE 10961. DOI: 10.2523/IPTC-10961-MS

[8]Kiran R, Teodoriu C, Dadmohammadi Y, et al. Identification and evaluation of well integrity and causes of failure of well integrity barriers (A review). J Nat Gas Sci Eng. 45 (2017) 511-26. DOI: 10.1016/j.jngse.2017.05.009

[9]Sepp N, Benedikter S, Kofler H, et al. Evaluation of the potential for gas and CO2 leakage along wellbores. SPE Drill complet. 24 (2009) 115-26.DOI: 10.2118/106817-MS

[10]Chu W, Shen J, Yang Y, et al. Calculation of micro-annulus size in casing-cement sheath-formation system under continuous internal casing pressure change. Petrol Explor Dev. 42 (2015) 414-21. DOI: 10.11698/PED.2015.03.16

[11]Feng Y, Li X, Gray KE. Development of a 3D numerical model for quantifying fluid-driven interface debonding of an injector well. Int J Greenhouse Gas Control.62 (2017) 76-90. DOI: 10.1016/j.ijggc.2017.04.008

Numerical Simulation of Rock-breaking Mechanism Under Compound Impact Load

Wei WANG[1*], Gonghui LIU[1,2], Jun LI[1], Chunqing ZHA[2] and Tao HUANG[1]

[1]*China University of Petroleum-Beijing/College of Petroleum Engineering, Beijing, China*
[2]*Beijing University of Technology, Beijing, China*
*1130273144@qq.com

ABSTRACT

Breaking the rock and removal of failed rock are the two primary actions that control drill efficiency. In order to solve the problems of low efficiency of rock breaking and premature failure of PDC bit drilling in hard formation, and further improve the performance of PDC bit, a compound impact drilling technology is put forward. It combines the advantages of axial and torsional impact technology to achieve three-dimensional rock-breaking. With analysis on the structural and operation characteristics of compound impact drilling tool, the finite element model of rock-breaking in single cutter under compound impact load was established, and the mechanism of rock breaking was studied via numerical simulation. The results showed that under the compound impact load, the axial load component can increase the depth of cut, and the shearing action of the tangential load component causes the rock to generate large volume break. Compared with the static load breaking rock, the MSE of compound impact load is reduced by 11.7%.The research results provide a theoretical basis for the field application of the compound impact drilling technology.

KEYWORDS- *Hard formation, Compound impact drilling, Rock breaking mechanism, Numerical simulation*

1.   INTRODUCTION

Polycrystalline Diamond Compact (PDC) bit is the dominant bit-type utilized in oil and gas well drilling today, and its wide application has brought about great economic benefits [1]. However, with proceeding in exploration and development of deep oil & gas, the possibility of drilling hard formations is high, the hardness, drillability and abrasive of the rock encountered are increasing [2, 3]. PDC bit drilling in hard formation has caused serious cutting tooth failure, such as tooth fracture and tooth loss [4], which will greatly reduce rate of penetration and increase drilling cost. Previous studies have indicated that the undesired stick-slip vibration is the main source of PDC bit failure [5-7]. In order to enhance drilling efficiency and prolong the bit service life, various methods to reduce the stick-slip vibration in hard formation have been proposed [8-11]. The torsional impact drilling method is generally considered one of the best approaches for drilling hard rocks. However, torsional impact drilling does not increase the single-stroke of the PDC bit. The compound impact drilling can generate both axial and torsional impacts at the same time, which can reduce the stick-slip vibration while increasing the depth of cut. In the recent years, various compound impact tools are developed for drilling in hard and abrasive formations for oil and gas wells [12, 13]. Previous tests have shown significant ROP enhancement, prolonged bit life and increased single run footage throughout a number of field applications of compound impact drilling tools [14, 15]. In this paper, the working principle and main structural features of the compound impact drilling tool are provided. In addition, the single cutter-rock model under the compound impact load by ABAQUS is established, simulate the rock breaking process under compound impact load and analyze the stress change state and cutting debris formation mechanism during rock breaking process.

147

2. COMPOUND IMPACT DRILLING TOOL

The compound impact drilling tool is a downhole speed-up tool, it is installed in the drill assembly, between the lower part of the neutral point and the drill bit. As shown in Fig.1, a compound impact drilling tool consists of fluidic drive motor and hydraulic vibration module. The motor drives the rotating shaft to rotate, and then distribute high pressure drilling fluid into the hydraulic vibration module. The impact of the tool is created by torsional and axial vibration module which is powered by high pressure drilling fluid.
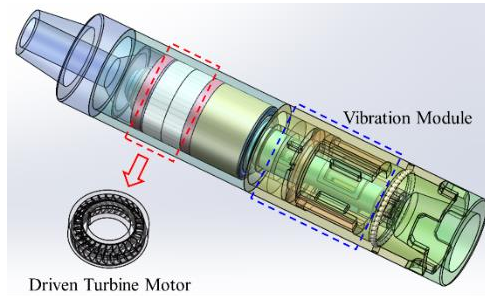
Figure 6. Structure diagram of compound impact drilling tool.

A laboratory test is conducted to verify the feasibility of the compound impact drilling tool. The test results show that the compound impact drilling tool can generate periodic axial and circumferential impact loads at the same time. Moreover, the main parameters of compound impact drilling tool are list on Table1.

Table 1. Main parameters of compound impact drilling tool.

Parameters	Value	Parameters	Value
Outer diameter (mm)	178	Angle of impact(°)	20～50
Length (mm)	800	Impact frequency (Hz)	10～40
Circulating rate (L/s)	15～40	Impact energy (J)	120～600
Operating pressure drop (MPa)	1.0～2.8		

3. DESCRIPTION of FEM MODEL
3.1. Constitutive Model and Failure Criterion

In this study to analyse the rock breaking process, a model is formulated by using the commercial software ABAQUS to simulate rock breaking performances under compound impact load conditions. Considering that a proper plastic constitutive model is the key of accurately simulating the yielding, hardening and damaging process. The Drucker-Prager (D-P) model will be used to simulate the elastic-plastic behaviour of the rock material. The D-P plastic constitutive model, which is widely used in the research of rock-breaking process, not only considers the influence of intermediate principal stress on yielding, but also reflects the expansion caused by shearing. On the meridional plane, the D-P yield criterion should be represented as:

$$q - p \tan \beta - d = 0 \tag{1}$$

Where p is the equivalent compressive stress, q is the deviatoric stress parameter, d is the cohesion of material, β is the slope of the linear yield surface projected on the $p\text{-}q$ stress plane.

148

The parameters of the rock constitutive model are usually obtained by tri-axial tests. Yield surface parameters p and q values calculated from equations (2) and (3) from different confining pressure tri-axial compression test data.

$$p = \frac{1}{3}(2\sigma_1 + \sigma_3) \tag{2}$$

$$q = \sigma_3 - \sigma_1 \tag{3}$$

Since the D-P model is an elastic-plastic model without a damage criterion, chip formation cannot be simulated when only the D-P model is used. In this study, the shear damage criterion will be applied in conjunction with the D-P model with the aim of simulating chip formation phenomena.

3.2. Numerical Model and Boundary Conditions

The FEM of the cutter-rock system as depicted in Figure.3, wherein, diameter of the cutter is 13 mm, thickness of the cutter is 5 mm and back rake angle is 15°, and the rock sample has the size of 80mm (length) by 40mm (width) by 30 mm (depth). The rock is discretized by using C3D8R in ABAQUS, and the top layer with the 6 mm thickness is defined and modeled by a finer mesh. For boundary conditions, fixed constraints are applied to the bottom and sides surfaces of the rock, and surface-surface contact is set between cutter and rock. The initial depth of cut is set to 2 mm and the cutter is assumed to move along the X-direction at a constant speed of 100 mm/s.

During the simulation, a static load exerted by WOB on single cutter is 1500 N, the impact load is 400 N, the impact angle is 30°, and the impact frequency is 30 Hz. The lithology of the rock is set in accordance with sandstone, of which the parameters are listed in Table 2.
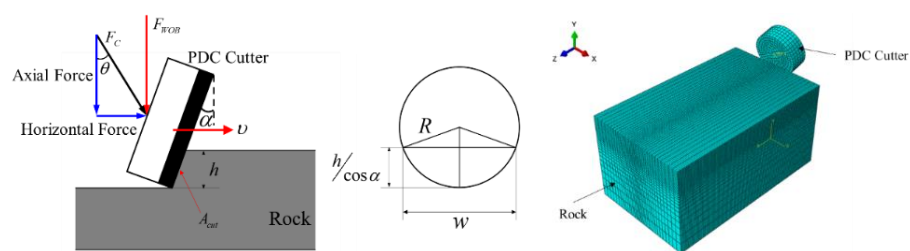
Figure 7. *FEM model of cutter-rock system.*

Table 2. *Material parameters of rock.*

Classification	Compressive strength (MPa)	Tensile strength (MPa)	Young's modulus (GPa)	Poisson ratio	Density (g/cm^3)	Internal friction angle	Cohesion (MPa)
Sandstone	48.53	5.3	16.68	0.214	2.47	40.75°	13.42
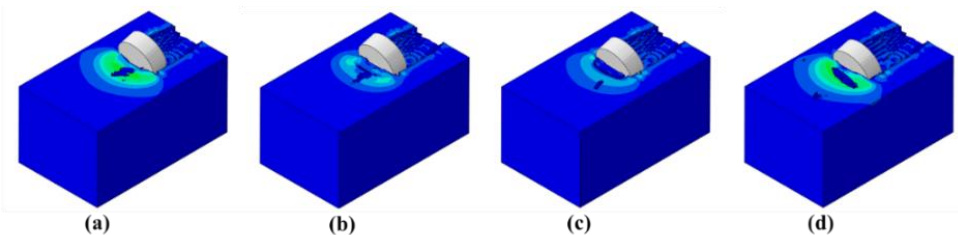
Figure 8. *The formation process of cuttings under compound impact load.*

149

4.　RESULTS AND DISCUSSION

The simulation results of the rock breaking with single cutter under the applications of compound impact load, uniaxial impact load and static load are shown in Figure.4 to Figure.8. Wherein, the magnitude and frequency of uniaxial impact load is equal to the axial component of the compound impact load.

4.1. Cutting Process

Figure.4 shows the simulation results of the cuttings formation in compound impact modes. (a) is the moment that the PDC cutter just has finished its previous impact process. From this moment, the PDC cutter starts compacting and compressing the rock in front of it slowly, the energy accumulates inside the rock. (b) and (c) is the process of compound impact, the internal crack of the rock propagates to the rock surface under impact load, and chunklike cuttings is generated at the front of the PDC cutter. (d) is the moment when the impact is completed, and chunklike cuttings generated in the previous impact process can be observed flying far away. The cutting process of the next compound impact cycle starts.
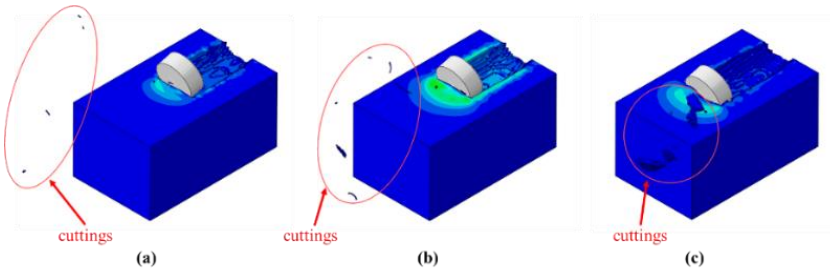
Figure 9. *Comparison of cuttings formation in three cutting modes. (a).static load, (b).uniaxial impact load, (c).compound impact load.*

Figure.5 is the diagram showing the formation of cuttings in three cutting modes. The rock is more prone to large volume rupture under the compound impact load, and the volume of cuttings generated by cutting is significantly larger than the volume of cuttings under static load and uniaxial impact load.

4.2. Cutting Force and Depth of Cut

Figure.6 show the cutting force curves for the three cutting mode. As observable in the simulations, due to the non-continuous chip formation phenomena, the cutting forces exhibit a vibratory nature during the cutting process. Under the compound impact load and uniaxial impact load, the peal value and fluctuation amplitude of the cutting force are obviously higher than the static load. Under the compound impact load, the cutting force fluctuation amplitude is lower than that the uniaxial impact load.

Figure.7 shows the depth of cut (DOC) variation curves in three modes. It can be seen that under the compound impact load and uniaxial impact load, the DOC is greater than that of the static load. The compound impact load coincides with the DOC variation curve of the uniaxial impact load. It indicates that the axial impact load causes an increase in the depth of cutting. Comparing the trend line of cutting force in different modes in Figure.6, it can be seen that with the increase of DOC, the peak value and the fluctuation amplitude of the cutting force increases accordingly, the horizontal component of the compound impact load is beneficial to reduce the fluctuation amplitude of the cutting force.

150
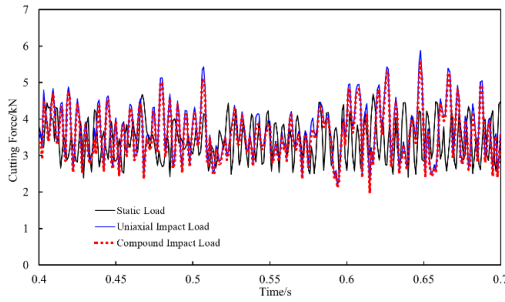
Figure 10. *Cutting force under different modes.*
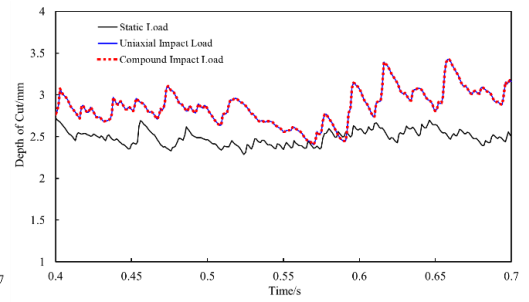
Figure 11. *Depth-of-cut under different modes.*

4.3. Mechanical Specific Energy

Mechanical Specific Energy (MSE) is key factor for evaluating the efficiency of a drilling process. It is defined as the energy required to removing a unit volume of rock. MSE is expressed as:

$$MSE = \frac{W}{V} = \frac{F_{cut}d}{A_{cut}\cos\alpha d} = \frac{F_{cut}}{A_{cut}\cos\alpha} \tag{4}$$

where is the work, is the removed volume of rock, is the cutting force, is the contact area between the cutter and the rock as shown in Figure.3.
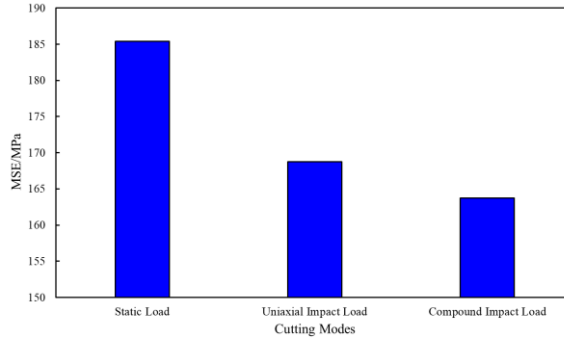
Figure 12. *Evolution of MSE with cutting modes.*

The MSE needed under different cutting modes is shown in Figure.8. Under the compound impact load, the MSE needed to break the rock is 11.7% less than under the static load, and is 2.9% less than the uniaxial impact load.

5.   CONCLUSION

(1). A novel compound impact drilling tool was proposed to mitigate the stick-slip oscillation which is significantly suitable for super hard formations. The result of the laboratory experiment shows that the tool can generate axial and torsional impact simultaneously.

(2).The axial load component can increase the DOC, and at the same time increase the impedance load at the front of the cutter, resulting in an increase in cutting force. The horizontal load component can increase the shear effect of the cutter to the rock which is beneficial to reduce the fluctuation amplitude of the cutting force. The rock is more prone to large volume rupture and the MSE needed is minimum under the compound impact load.

151

REFERENCES
[1] P. Dougherty, et al. Bit Cutter-on-rock Tribometry: Analyzing Friction and Rate-of-penetration for Deep Well Drilling Substrates. Tribology International 77(2014) 178-185. DOI:10.1016/j.triboint.2014.04.003.
[2] Gonghui LIU., et al. New Technology with Composite Percussion Drilling and Rock Breaking. Petroleum Drilling Techniques, 2016. 44(5): 10-15.
[3] M. Azar, et al. Pointing Towards Improved PDC Bit Performance: Innovative Conical Shaped Polycrystalline Diamond Element Achieves Higher ROP and Total Footage. SPE/IADC Drilling Conference & Exhibition, 5-7 March, 2013 Amsterdam-Netherlands.
[4] S. Velvaluri, et al. Middle East Hard/Abrasive Formation Challenge: Reducing PDC Cutter Volume at Bit Center Increases ROP/Drilling Efficiency. SPE/IADC Middle East Drilling Technology Conference & Exhibition, 7-9 October, 2013 Dubai-UAE.
[5] S. Thorsten, et al. Development and Testing of Stick/Slip-Resistant PDC Bits. IADC/SPE Drilling Conference & Exhibition, 4-6 March, 2014 Fort Worth-USA.
[6] M. Fear, et al. The Destruction of PDC Bits by Severe Slip-Stick Vibration. SPE/IADC Drilling Conference, 4-6 March, 1997 Amsterdam-Netherlands.
[7] T. Richard, et al. Influence of Bit-Rock Interaction on Stick-Slip Vibrations of PDC Bits. SPE Annual Technical Conference & Exhibition, 29 September-2 October 2002 San Antonio-Texas.
[8] G. Pelfrene, et al. Mitigating Stick-Slip in Deep Drilling Based on Optimization of PDC Bit Design. SPE/IADC Drilling Conference & Exhibition, 1-3 March, 2011 Amsterdam-Netherlands.
[9] F. Sayid, et al. Drilling Optimisation in Hard and Abrasive Basement Rock Using a Conical Diamond Element Bit. IADC/SPE Asia Pacific Drilling Technology Conference, 27-29 August, 2018 Bangkok-Thailand.
[10] R. Wedel, et al. Mitigating Bit-Related Stick-Slip With A Torsional Impact Hammer. AADE National Technical Conference & Exhibition, 12-14 April, 2011 Houston-USA.
[11] A. Deen, et al. Application of A Torsional Impact Hammer to Improve Drilling Efficiency. SPE Annual Technical Conference & Exhibition, 30 October-2 November, 2011 Denver-USA.
[12] Xiaosong WEN, et al. A Comprehensive Analysis of Compound Impactor Based on Mixed Flow Impeller Drive. International Conference on Computational and Experimental Science and Engineering (ICCESEN 2018), 12-16 October, 2018 Antalya-Turkey.
[13] Shubin LIU, et al. Rock-Breaking Mechanism Study of Axial and Torsional Impact Hammer and its Application in Deep Wells. IADC/SPE Asia Pacific Drilling Technology Conference, 27-29 August, 2018 Bangkok-Thailand.
[14] Chunqing ZHA., et al. Development and Field Application of A Compound Percussive Jet. Petroleum Drilling Techniques, 2017. 45(1): 57-61.
[15] S. Powell, et al., Fluid Hammer Increases PDC Performance through Axial and Torsional Energy at the Bit. SPE Annual Technical Conference & Exhibition, 30 September-2 October, 2013 New Orleans-USA.

Quantification of the Surface Charge Density Using Atomic Force Microscopy by a New Method

Wentong Zhang[*] , Ning Zhengfu, Qing Wang, Biao Zhang, Xiaojun Wu, Hao Lin, Xiwei Gao

Key Laboratory of Petroleum Engineering of the Ministry of Education, China University of Petroleum
*564723729@qq.com

ABSTRACT

The surface charge density can be calculated with the experimental results of Atomic force microscopy (AFM) under the analysis of the Derjaguin–Landau–Verwey–Overbeek (DLVO) theory. Several theoretical models have been applied to establish the relationship between the electrostatic force and surface charge density for a sphere-flat system of AFM. However, the constraint of the fundamental equation which can be applied to describe the relationship between the electrostatic force and surface charge density seems to be neglected. These models can only be used to calculate the value of the surface charge density in low constant potential (<25mV). In this study, we propose a new theoretical model capable of quantitatively measuring the surface charge density without the constraint of low potential (<25mV), presenting a significant improvement in measuring the surface charge density. This study is inspired by the studies of Bharat Bhushan's group in order to expand the application of the method that measure the surface charge density using AFM. The cited experimental AFM results are used to calculate the surface charge density using this theoretical model, the effect of the PH on the surface charge density has also been investigated, then a comparison with the Jing's model is used to demonstrate the advantage of this model. This theoretical model can be applied to accurately measure the surface charge density for identically and differently charged surface without the limit of the low constant potential(<25mV).

KEYWORDS - *Surface charge density; Atomic force microscopy;*

1. INTRODUCTION

Atomic force microscopy has been widely used to image and measure the surface forces, which can be applied to many aspects [1-3]. The relationship of surface forces and separation distance can be obtained between the probe of AFM and selected surfaces of interest. Taken the geometry of AFM tips into consideration, the Derjaguin–Landau–Verwey–Overbeek (DLVO) theory would be established. Then the surface charge density can be calculated with the experimental results of AFM under the analysis of the DLVO theory. Several theoretical models have been applied to establish the relationship between the electrostatic force and surface charge density based on the simplified geometry of the AFM and selected surface, which can measure the surface charge density of sample. However, there still remains some defects for these models. The fundamental equation of these models is only applied to particles of low and constant surface potential, but the surface potentials of the particles can reach very high for constant charge interaction. Thus the constraint of the fundamental equation which has been applied to describe the relationship between the electrostatic force and surface charge density seems to be neglected (<25mV) [4-6]. Therefore, how to accurately measure the surface charge density of the sample of interest needs to be investigated. In this study, we propose a new theoretical model capable of quantitatively measuring the surface charge density without the limit of low potential (<25mV), presenting a significant improvement in measuring the surface charge density. This research is inspired by the studies of Bharat Bhushan's group in order to expand the application of the method that measure the surface charge density using AFM [4-6]. The experimental AFM results which have been cited are used to calculate the surface charge density using a theoretical model, the effect of the PH on the surface charge density is also investigated. Using a quantitative comparison of the model with

153

the Jing's model we identified the model which can best describe the behaviour of surface charge density.

2. A NEW MATHEMATICAL MODEL

2.1. A new model for the relationship between electrostatic force and surface charge density
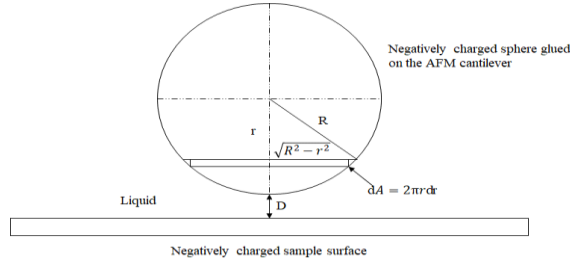
Figure 13. Fig. 1. Geometry of the sphere-flat samples system [4-6].

The eq. (1) can be used to measure the surface charge density only in the condition of low potential (<25mV). However, the limit of the eq. (1) seems to be neglected (<25mV) when the eq. (1) is applied to measure the surface charge density of selected sample of interest.

$$F = \frac{2}{\varepsilon_0 \varepsilon}[\frac{\sigma_1 \sigma_2[(e^{+\kappa D} + e^{-\kappa D})}{(e^{+\kappa D} - e^{-\kappa D})^2} - \frac{\sigma_1^2 + \sigma_2^2}{(e^{+\kappa D} - e^{-\kappa D})^2}] \tag{1}$$

Where σ_1 is the surface charge density for the sphere; σ_2 is the surface charge density for the flat surface; D is the separation distance between the sphere and the flat surface; $1/\kappa$ is the Debye length; ε_0 is the permittivity of the vacuum; ε is the relative dielectric constant of the experimental fluid.

The equation of double layer interaction between a sphere-flat system for two differently charged surface can be described as eq. (2), which is derived by appropriate expressions for the interaction energy between two infinite flat plates. The eq. (2) based on the linear super-position approximation (LSA), which is be the most accurate to describe the electrostatic force between two different charged surface.

$$W = 64\pi R \varepsilon_0 \varepsilon \gamma_1 \gamma_2 (\frac{kT}{ze})^2 \exp(-\kappa D) \tag{2}$$

$$\gamma_1 = \tan(ze\psi_1 / 4kT) \tag{3}$$

$$\gamma_2 = \tan(ze\psi_2 / 4kT) \tag{4}$$

Which leads to an equation of electrostatic force between a sphere and a flat system

$$F = -\frac{dW}{dD} = -\frac{64\pi R \varepsilon_0 \varepsilon \gamma_1 \gamma_2 (\frac{kT}{ze})^2 \exp(-\kappa D)}{dD} = 64\kappa\pi R \varepsilon_0 \varepsilon \gamma_1 \gamma_2 (\frac{kT}{ze})^2 \exp(-\kappa D) \tag{5}$$

154

The eq. (6) can be derived as eq. (5) in the room temperature (298K):

$$\psi_2 = 103 a \tan \frac{F}{9.22 \times 10^{-11} \kappa R \tanh(\psi_1/103) e^{-\kappa D}} \tag{6}$$

The Grahame equation can be simplified further as eq. (7) in room temperature (298K)

$$\sigma = \sqrt{8\varepsilon_0 \varepsilon kT} \sinh(e\psi_0 / 2kT)\{[Na^+]_\infty + [Ca^{2+}]_\infty (2 + e^{-e\psi_0}/kT)\}^{1/2} \tag{7}$$

The relationship between electrostatic force and surface charge density for differently charged sphere and flat surface in 1:1 electrolyte can be obtained through combining eq. (6) and eq. (7).

$$\sigma' = 0.117 \sinh(103 a \tan \frac{F}{9.22 \times 10^{-11} \kappa R \tanh(\psi_1/103) e^{-\kappa D}} / 51.4)[NaCl]^{1/2} \tag{8}$$

3. RESULTS AND DISCUSSION
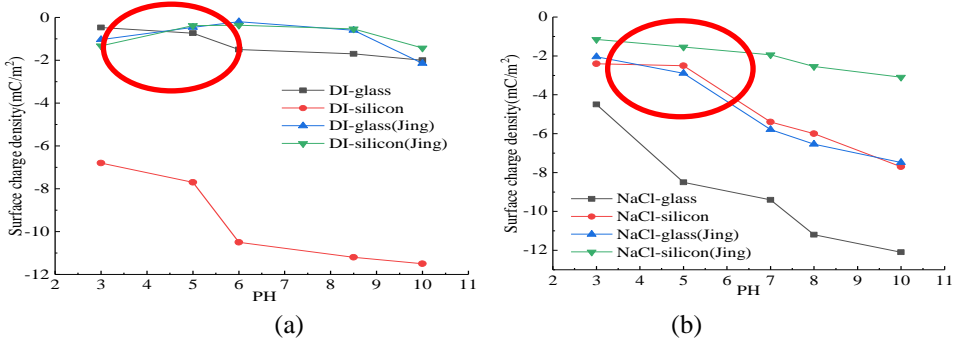
Figure 2. *The relationship between surface charge density and PH of samples (a), by DI water (b) sodium chloride [4-6].*

Jing et al. applies the eq. (1) to investigate the relationship between electrostatic force and the surface charge density for a sphere-flat system of AFM [4-6]. The surface charge density of selected sample of interest can be obtained by fitting the experimental electrostatic force of AFM though integrating eq. (1). The results of the calculated surface charge density are shown in Fig. 2a and Fig. 2b. The Fig. 2a describes the relationship between surface charge density and PH of samples by DI water and the Fig. 2b shows the relationship between surface charge density and PH of samples by sodium chloride. We also present our calculated results in Fig. 2a and Fig. 2b in order to compare with the Jing's model. From the Fig. 2, we have found the calculated surface charge densities of Jing's model are obviously lower than that of the model in this study. This is maybe that Jing's model is based on linear Poisson-Boltzmann (PB) equation, while our model is based on linear super-position approximation (LSA) which is the most accurate process to describe the electrostatic force between two differently charged surface[4-6]. Nevertheless, the calculated surface charge densities approach the values of the Jing's model with the PH ranges from 3 to 5 for borosilicate glass in different fluids. This phenomenon is due to the material of the sphere of AFM is the same as the selected sample (borosilicate glass), then we assume that the amount of surface charge density of the sphere is equal to the selected sample. The surface potentials of the

155

borosilicate glass in different solution are less than 25 mV when the PH ranges from 3 to 5. Jing's model works under the condition of low potential (<25mV). Therefore, the calculated surface charge densities of Jing's model approach that of value in this study when the PH ranges from 3 to 5 for borosilicate glass in different fluids. Furthermore, the other calculated results of Jing's model are very different from that of our model. It is worth to investigate the reason for there is a big difference between two models for one same experimental results. As the previous section has mentioned, the eq. (1) can only be applied to the condition of low potential (<25mV). The surface potentials of the selected samples of interest in different solution are larger than 25 mV when the PH ranges from 5 to 10, which can be found on Table 1, Table 2 and Table 3. Thus, the Jing's theoretical model does not work in this situation. This results in a big difference between the calculated surface charge densities of Jing's model with the values of the model in this study.

4. CONCLUSION

In this study, the surface charge density of selected sample of interest can be measured using atomic force microscopy (AFM) by a new method. Based on the studies of Bharat Bhushan's group, a theoretical model of the relationship between the electrostatic force and surface charge density for a sphere and a flat has been established without the constraint range of surface potential (<25mV). The surface charge density of selected samples of interest are obtained though the theoretical model, then effect of the PH on the surface charge density is also studied. Finally, the theoretical model have been certified by comparing with the Jing's model.

This studies shows that the surface charge density increases with the PH ranging from 3 to 10, the main reason is the dissociation of silanol group. The negative silanol groups would be come into being with the increase of PH, which would result in the increase of the surface charge density. In addition, the PH takes an over advantage on the surface charge density when the difference of solution concentration is less than 1mM.

This model of relationship between electrostatic force and surface charge density for a sphere and a flat surface without the constraint of low potential (<25mV) is certified though the comparison with the Jing' model. Therefore, this study extends the application of the method which can accurately measure the surface charge density of selected sample of interest by AFM.

REFERENCES

[1] Zhao T, Li X, Ning Z, et al. Pore structure and adsorption behavior of shale gas reservoir with influence of maturity: a case study of Lower Silurian Longmaxi formation in China[J]. Arabian Journal of Geosciences, 2018, 11(13): 353. http://dx.doi.org/10.1007/s12517-018-3673-5

[2] Cheng Z, Ning Z, Zhao H, et al. A comprehensive characterization of North China tight sandstone using micro-CT, SEM imaging, and mercury intrusion[J]. Arabian Journal of Geosciences, 2019, 12(13): 407. http://dx.doi.org/10.1007/s12517-019-4568-9

[3] Wu X, Ning Z, Han G, et al. Modified SLD model for coalbed methane adsorption under reservoir conditions[J]. Arabian Journal of Geosciences, 2019, 12(18): 562. http://dx.doi.org/10.1007/s12517-019-4763-8

[4] D. Jing, B. Bhushan, Quantification of surface charge density and its effect on boundary slip, Langmuir 29(23) (2013) 6953-6963. http://dx.doi.org/10.1021/la401168w

[5] D. Jing, B. Bhushan, The coupling of surface charge and boundary slip at the solid–liquid interface and their combined effect on fluid drag: A review, Journal of colloid and interface science 454 (2015) 152-179. https://doi.org/10.1016/j.jcis.2015.05.015

[6] D. Jing, Y. Pan, D. Li, X. Zhao, B. Bhushan, Effect of surface charge on the nanofriction and its velocity dependence in an electrolyte based on lateral force microscopy, Langmuir 33(8) (2017) 1792-1798. http://dx.doi.org/10.1021/acs.langmuir.6b04332

A Comprehensive Study of the Electroviscous Effects on the Transport of Dilute Solutions in Circular Microtubes

Zhilin Cheng[*], Ning Zhengfu, Wentong Zhang, Xiaojun Wu, Shizhen Ke

Key Laboratory of Petroleum Engineering of the Ministry of Education, China University of Petroleum
*zhilin_cheng1992@163.com

ABSTRACT

The investigation of electrokinetic flows in microchannels is important for a wide range of scientific and industrial processes. Through the use of the coupled the Poisson-Nernst-Planck (PNP) and Navier-Stokes (N-S) equations, the transport characteristics of dilute solutions in cylindrical microtubes were presented. The accuracy of this dynamic model was validated by comparing with the results from the Poisson-Boltzmann (PB) model and the experimental measurements. The flow ability of a solution in microtubes under different influencing factors were consequently evaluated. The results demonstrate that the increased flow resistance of deionized water (DW) observed in experiments is mainly owing to the electroviscous effects instead of the formed liquid layers on the solid walls from the unphysical boundary-layer theory. The flow features of fluids in microchannels are determined by multiple factors. Dimensionless apparent viscosity (DAV) of the liquid decreases as the diameter of the microtube gradually increases, this is because the ratio of the electrical double layer (EDL) thickness to the channel diameter becomes smaller. In addition, a decrease in the DAV is found when the ion concentration increases, showing that the fluid flow in microchannels appears to be less impacted by the electroviscous effect in such cases. However, a slight increase in the DAV occurs in the case of the relatively large-sized microtube. Furthermore, the DAV varies non-monotonically with the zeta potential on the solid surface, and there is a critical zeta potential that resulting in the largest DAV. Additionally, we also find that the flow rates of solutions in microchannels with the heterogeneously charged walls are greater than that of the homogeneously charged case, and are very close to the Hagen-Poiseuille (HP) velocities. Thus, it is concluded that the flow-induced resistance can be manipulated by changing the distribution of surface potential on the walls.

KEYWORDS - Electrokinetic flow; Dilute solutions; Poisson-Nernst-Planck model

1. INTRODUCTION

Electrokinetic phenomena is important knowledge, which can be used in many aspects [1-3]. Several surveys on electrokinetic phenomena in microchannels with theoretical models have achieved great progress, these models are always developed based on the simple one-dimensional equations or mathematical approximation techniques and thus have limited applications [4-7]. Numerical methods have been regarded as a promising tool for elaborating the transport features of solutions in microfluidic systems. The applicability of the PB model would be restricted in several cases when the solid surface is heterogeneously charged, the motion of ions cannot be neglected, and the microchannels have overlapped EDLs, The most rigorous approach to describe the ions transport and electrical potential distribution within the EDL is the dynamic Poisson-Nernst-Planck (PNP) equation, which couples the advection and diffusion of ions with the fluid flow and theoretically has wider applications. However, due to the more difficulty in solving the coupled equations, the existing literature on electroviscous flow using the PNP model focuses particularly on the simple one-dimensional slit model. The relevant research on the solutions flowing in cylindrical microchannels is still lacking. Moreover, the electroviscous flow in capillary tubes with nonuniform charged walls is also few reported. This research aims to unravel the

157

pressure-driven flow characteristics of the dilute solutions in cylindrical microtubes using the dynamic PNP model.

2. NUMERICAL METHOD

In this study, we consider the steady-state laminar flow of a binary electrolyte (such as deionized water, incompressible) flow through a cylindrical microtube under pressure-driven conditions, shown in Fig. 1.
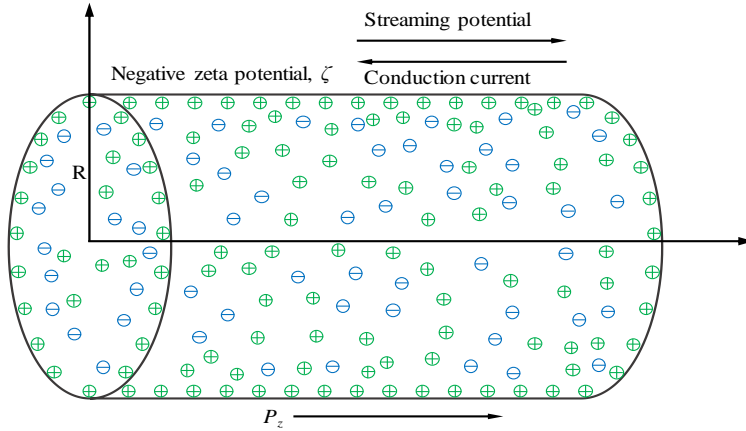
Figure 14. Schematic of the electrokinetic flow of fluids in a capillary [4-6].

2.1. Benchmark

From Fig. 2, It can be seen that the result determined by the PNP equation perfectly matches the PB solutions for two different ζ. In addition, both two numerical solutions agree well with the Debye-Huckel theory when ζ=-10 mV. However, as expected, the PB and PNP solutions slightly depart from the Debye-Huckel one when ζ =-60 mV, this is because the Debye-Huckel approximation is only valid for the low ζ. Overall, by comparing the PNP results with the PB and Debye-Huckel linear solutions, the accuracy of the PNP model is adequately confirmed.
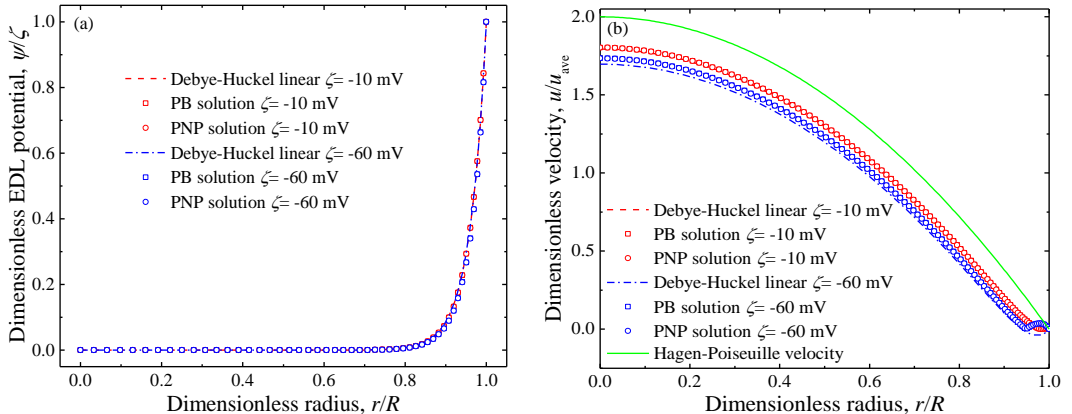
Figure 2. Comparisons of the results from the Debye-Huckel linear method, the PB equation, and the PNP equation when κR=25. (a) the electrical potential distribution; (b) the velocity distribution, where uave represents the average velocity of the fluid.

2.2. Effects of several key influencing factors

158

Fig. 3a depicts the relation between the apparent viscosity of DW and the microtube size. It is found that DAV decreases as the channel diameter increases. This is because the flow resistance resulting from the electroviscous effect is gradually reduced with the increase in the ratio of the channel size to the EDL thickness, shown in Fig. 3b. However, the amplitude of variation in the DAV is apparently diverse under different zeta potentials.
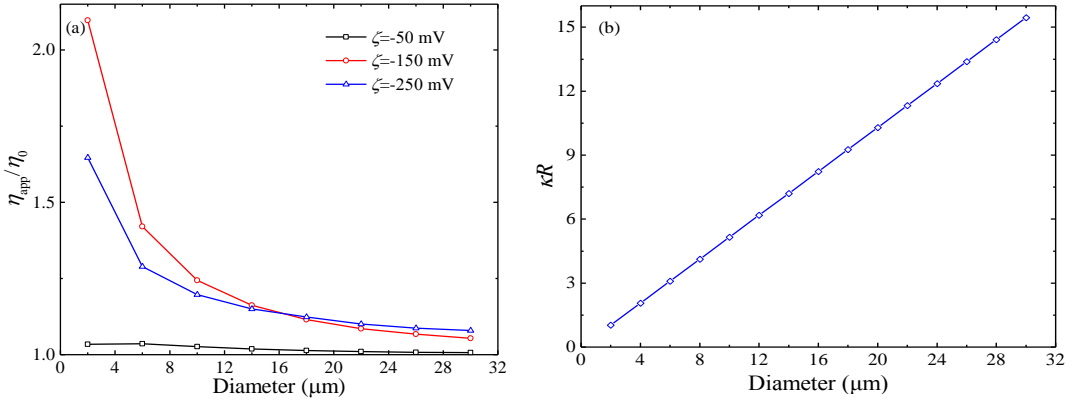
Figure 3. *(a) Variation of DAV as a function of the capillary size for three different zeta potentials. (b) The relationship between the Debye length and the microchannel diameter.*
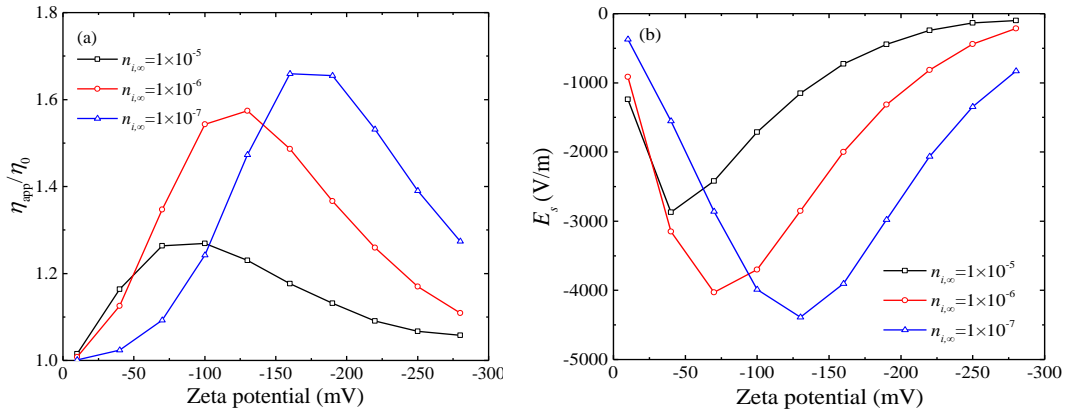
Figure 4. *The effects of zeta potential: (a) variation of DAV as a function of the zeta potential and (b) the generated potential gradient versus zeta potential at different ion concentrations, where the diameter of the microtube is kept as 4 μm, and the pressure gradient is 1 MPa/m.*

It can be shown from Fig.4a that the variations of DAV for different concentrations exhibit a similar trend; specifically, they first show a steep rise until reaching the maximum value, then a rapid decrease with the increasing zeta potential. This nonmonotonic behavior is similar to the previous observations. A possible explanation is that the magnitude of the flow resistance caused by electrokinetic effect is determined by the electrical force term "$\rho_e \times E_s$" and the generated electrical filed E_s has a similar variation trend to that of the DAV as the zeta potential increases (shown in Fig. 4b), while the net charge density basically increases with the increasing zeta potential. Hence, the decrease in the DAV in the large zeta potentials could be because the decreasing E_s dominates the electrical resistance forces compared to the role of the increased ρ_e. Additionally, it is seen that under the same ion concentration the DAV needs a larger zeta potential

159

to obtain the critical value than that of the Es, this could be due to the combined effects of Es and ρe on the induced electrical forces

3. CONCLUSION

The transport behaviors of dilute solutions occurred in microchannels are collectively controlled by multiple influence factors. The EDL becomes thinner as the channel size increases; thus, the fluid flow is less impacted by the electrokinetic force, leading to the gradual decrease in the DAV of the solution. Additionally, in most cases, the DAV shows a monotonical behavior with the ion centration, i.e., the smaller the ion concentration, the larger the DAV. However, in relatively large-sized microtube, the DAV varies non-monotonically with the ion centration, experiencing a slight increase at the larger solution concentrations. Furthermore, the zeta potential has a significant non-monotonical effect on electroviscous flow.

ACKNOWLEDGMENT

REFERENCES

[1] Zhao T, Li X, Ning Z, et al. Pore structure and adsorption behavior of shale gas reservoir with influence of maturity: a case study of Lower Silurian Longmaxi formation in China[J]. Arabian Journal of Geosciences, 2018, 11(13): 353. http://dx.doi.org/10.1007/s12517-018-3673-5

[2] Cheng Z, Ning Z, Zhao H, et al. A comprehensive characterization of North China tight sandstone using micro-CT, SEM imaging, and mercury intrusion[J]. Arabian Journal of Geosciences, 2019, 12(13): 407. http://dx.doi.org/10.1007/s12517-019-4568-9

[3] Wu X, Ning Z, Han G, et al. Modified SLD model for coalbed methane adsorption under reservoir conditions[J]. Arabian Journal of Geosciences, 2019, 12(18): 562. http://dx.doi.org/10.1007/s12517-019-4763-8

[4] Choi Y S, Kim S J. Electrokinetic flow-induced currents in silica nanofluidic channels[J]. Journal of colloid and interface science, 2009, 333(2): 672-678. http://dx.doi.org/10.1016/j.jcis.2009.01.061

[5] Wu J, Cheng L, Li C, et al. Experimental study of nonlinear flow in micropores under low pressure gradient[J]. Transport in Porous Media, 2017, 119(1): 247-265. http://dx.doi.org/10.1007/s11242-017-0882-4

[6] Yoshida H, Kinjo T, Washizu H. Coupled lattice Boltzmann method for simulating electrokinetic flows: A localized scheme for the Nernst–Plank model[J]. Communications in Nonlinear Science and Numerical Simulation, 2014, 19(10): 3570-3590. http://dx.doi.org/10.1016/j.cnsns.2014.03.005

[7] Wang M, Kang Q. Modeling electrokinetic flows in microchannels using coupled lattice Boltzmann methods[J]. Journal of Computational Physics, 2010, 229(3): 728-744. http://dx.doi.org/10.1016/j.jcp.2009.10.006

Experimental and Numerical Study on Motion States of Simulative BHA in Horizontal Wells

Wei Li[1,2], Genlu Huang[1,2], Hongjian Ni[1,2]*, Fan Yu[1,2]

[1]China University of Petroleum (East China), School of Petroleum Engineering, Qingdao, China

[2]Ministry of Education, Key Laboratory of Unconventional Oil & Gas Development (China University of Petroleum (East China)), Qingdao, China

*nihj@upc.edu.cn

ABSTRACT

Motion states of bottom hole assembly (BHA) has a great effect on the efficiency of downhole drilling tools while rotary drilling. In order to research on the motion states of BHA in horizontal wells, a BHA dynamic model was established. The model was used to simulate the motion states of BHA under different rotate speeds, WOB and measuring positions. Meanwhile, an indoor experimental apparatus was built to verify the dynamic model. The results show that the experimental results can match well with the numerical simulation results. The motion states of BHA in horizontal wells can be divided into three kinds, including circular arc swing, "8" swing and dot-like circular motion. Moreover, rotate speed has a promotion on the lateral displacement while WOB have a much smaller effect. Based on the analyses, relevant suggests are given for the drilling engineering. Therefore, the study can help to understand the dynamic characteristics of BHA in horizontal wells and select suitable parameters for drilling.

KEYWORDS - *BHA, motion state, horizontal well, drill string dynamics, simulation experiment.*

1. INTRODUCTION

In horizontal wells, the stress state of drill string is very complex because drill string is strictly confined to narrow wellbore[1-2]. In order to avoid fatigue damage of drill string, it is particularly necessary to research the movement characteristics of drill string under different working conditions, especially lateral vibration. Lateral vibration is considered the main reason that caused the BHA fatigue failure and wear[3]. In horizontal section, kinds of motion states of BHA are proposed in the existing literature[4-5]. However, there is not a basis to distinguish these motion states and the occurrence mechanism has not been revealed.

In order to distinguish kinds of motion states of BHA in horizontal wells and explains the mechanism, a BHA dynamic model was established and an indoor experimental apparatus was designed to verify the numerical results[6]. Meanwhile, some useful suggestions for parametric selection can be obtained through the experimental and numerical analyses. The study can help to understand the dynamic characteristics of BHA in horizontal wells and select suitable parameters for drilling.
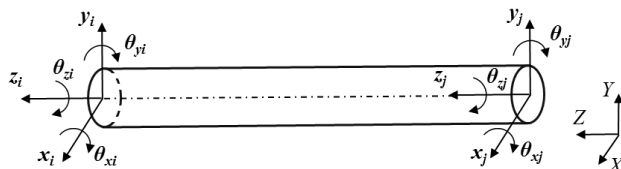
Figure 1. *Nodal displacement vector of drill string element.*

2. MODEL

The whole BHA can be divided into lots of beam elements with 12 degree of freedom (DOF) and a simplified beam element is shown as Fig.1. In the finite element analysis, nodal displacements are

161

generally taken as the unknown variables [7-10]. Drill string dynamics theory is based on Lagrange equation[11-12], and the whole BHA dynamic equation can be obtained by assembling these beam elements:

$$[M]\{\ddot{q}\}+[C]\{\dot{q}\}+[K]\{q\}=\{F\} \tag{1}$$

where $\{q\},\{\dot{q}\},\{\ddot{q}\}$ is nodal displacement, velocity and acceleration of drill string, respectively; $\{F\}$ is external force vector; $[M]$ is mass matrix; $[K]$ is global stiffness matrix; $[C]$ is Rayleigh damping matrix.

3.   EXPERIMENT

It is difficult and unsystematic to carry out a field experiment to research on the motion state of BHA. Thus, an indoor experimental apparatus is designed and built instead of the field experiment, whose schematic diagram is shown in Fig.2. To limit total length of the apparatus, a single pole with 2 m length and 5 mm outer diameter (OD) are chosen as simulative BHA, whose material is PMMA. And a stainless steel tube with 8 mm inner diameter (ID) is used to simulate the wellbore. The test bench is installed on the test support and the change of well inclination can be simulated by changing the installed position of the test bench on the test support. The simulative wellbore is constrained on wellbore supports. Meanwhile, the servo motor can drive the simulative BHA to rotate and a torque sensor is inside the motor. Simulative downhole can provide pressure on the simulative bit and a force sensor is installed to monitor the axial pressure value, which can simulate WOB. Moreover, laser displacement sensors are used to capture the lateral displacement of simulative BHA. Then the sensor data can be saved and displayed on computer.
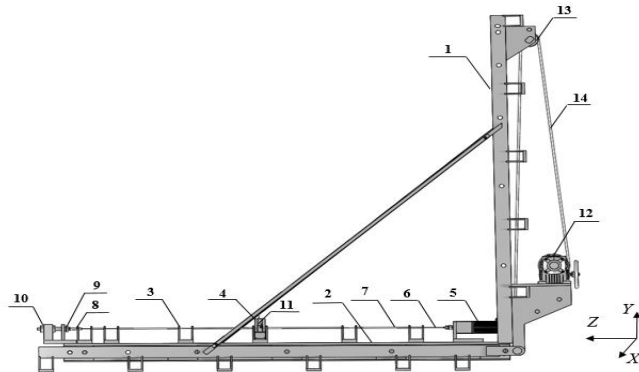
Figure 2. *Schematic diagram of the experimental apparatus. 1- test support; 2- test bench; 3- wellbore support; 4-displacement sensor support; 5- servo motor; 6- simulative BHA; 7- simulative wellbore; 8- simulative downhole; 9- force sensor; 10- loading screw; 11- displacement sensor; 12- turbine reducer; 13- fixed pulley; 14- wirerope.*

4.   RESULT AND DISCUSSION
4.1. Effects of BHA position

In the experiment and numerical simulation, the measuring position is 0.05 m, 0.1 m, 0.3 m and 1.0 m from the drill bit respectively. The rotate speed is 100 r/min and the WOB is 0. Fig. 3 shows the trajectory curve of BHA centre under different measuring positions.

Figure 3. Trajectory curve of BHA center under different positions: (a), (b), (c) and (d) are the experimental results with 1.0 m, 0.3 m, 0.1 m and 0.05 m from the drill bit respectively; (e), (f), (g) and (h) are the numerical simulation results with 1.0 m, 0.3 m, 0.1 m and 0.05 m from the drill bit respectively.

In experiment, the lateral displacement is 1.25 mm, 1.10 mm, 0.70 mm and 0.50 mm respectively in X-direction and 1.10 mm, 0.90 mm, 0.60 mm and 0.40 mm respectively in Y-direction, which means that the lateral displacement decreases with the measuring position far away from drilling bit. In numerical simulation, the results also show the same conclusion. Meanwhile, the motion trajectory of 1.0m and 0.3m like a circular arc, the motion trajectory of 0.1m like a number "8" and the motion trajectory of 0.05m like a small circle or a large point. Thus, the motion state of BHA in horizontal wells can be divided into three kinds, including circular arc swing, "8" swing and dot-like circular motion.

The circular arc swing mainly appears at middle section of BHA, the dot-like circular motion mainly appears at near-bit area and the "8" swing mainly appears at the crossed area of the other two motions. The gravity and tangential friction between BHA and wellbore plays important roles in the motion states. The gravity makes BHA down to lower part of wellbore and the tangential friction makes BHA rotate along right part of wellbore. Thus BHA always rotate at the lower right part of wellbore. The phenomenon just proves the situation of azimuth right drift in drilling field. Moreover, the experimental results can match well with the numerical simulation results, which can proves that the BHA dynamic model is reasonable for analysing the motion states of BHA in horizontal wells.

4.2. Effects of rotate speed

In the experiment and numerical simulation, the rotate speed is taken as 100 r/min, 200 r/min, 300 r/min and 400 r/min respectively, which equals to 25 r/min, 50 r/min, 75 r/min and 100 r/min in drilling engineering. The WOB is 0 and the measuring position is 1.0 m from the drill bit. Fig. 4 shows the trajectory curve of BHA centre under different rotate speeds.

Figure 4. *Trajectory curve of BHA center under different rotate speeds: (a), (b), (c) and (d) are the experimental results with 100 r/min, 200 r/min, 300 r/min and 400 r/min respectively; (e), (f), (g) and (h) are the numerical simulation results with 100 r/min, 200 r/min, 300 r/min and 400 r/min respectively.*

In experiment, the lateral displacement is 1.25 mm, 1.3 mm, 1.35 mm and 1.40 mm respectively in X-direction and 1.10 mm, 1.20 mm, 1.40 mm and 1.60 mm respectively in Y-direction, which means that the lateral displacement increases with the increase of rotate speed. In numerical simulation, the results also show the same conclusion.

Through analyses, rotate speed has a promotion on the lateral displacement. The increase of rotate speed means a shorter time in finishing a single swing. Thus the frequence of frictional contact between BHA and wellbore will be correspondingly improved in a certain time, which can lead to the increase of friction force. Therefore, rotate speed has a promotion on the lateral displacement. In drilling field, in order to keep a small lateral motion of BHA, a lower rotate speed is recommended as well as rotate speed can meet the requirement of rate of penetration (ROP). This can also protect downhole tools from wear damage.

4.3. Effects of WOB

In the experiment and numerical simulation, the WOB is 0 N, 0.23 N, 0.46 N and 0.69 N respectively, which equals to 0, 30 kN, 60 kN and 90 kN in drilling engineering. The rotate speed is 100 r/min and the measuring position is 1.0 m from the drill bit. Fig. 5 shows the trajectory curve of BHA centre under different WOB.

In experiment, the lateral displacement is 1.25 mm, 1.30 mm, 1.30 mm and 1.30 mm respectively in X-direction and 1.10 mm, 1.15 mm, 1.15 mm and 1.15 mm respectively in Y-direction, which means that WOB have no effect on the lateral displacement. In numerical simulation, the results also show the same conclusion. Therefore, the increase of WOB cannot effect lateral motion of BHA under the given condition. Thus WOB have a much smaller effect compared with rotate speed and BHA position. In drilling field, a slightly large WOB is recommended in order to improve ROP.
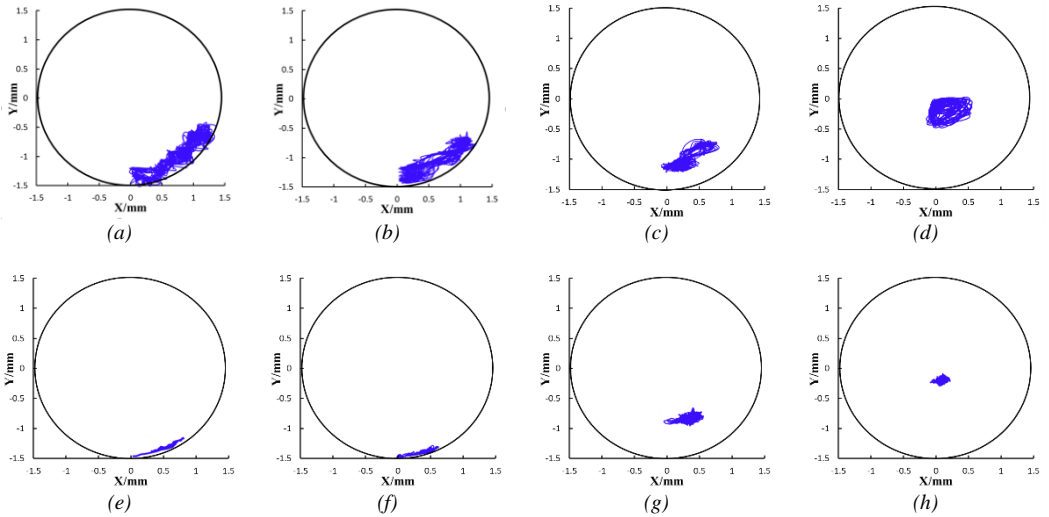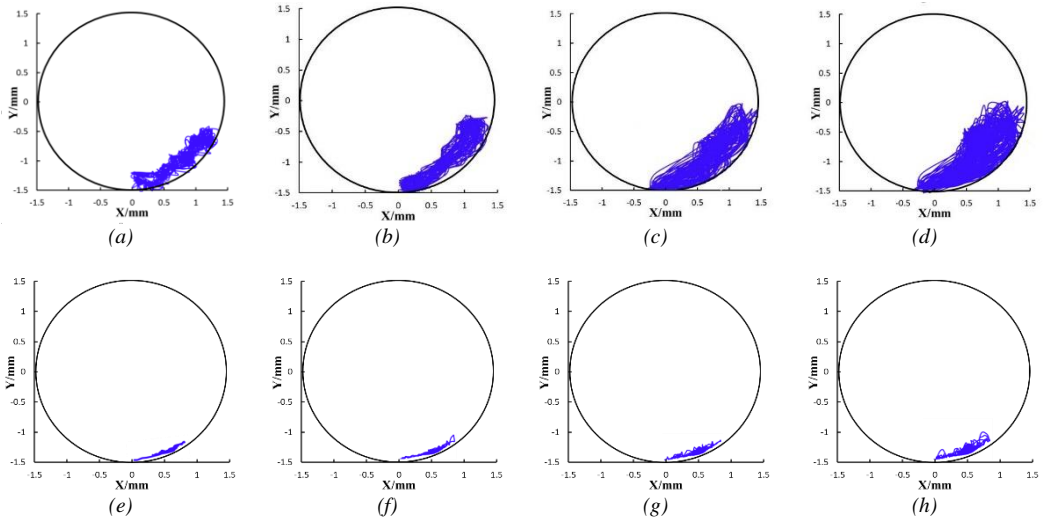
164
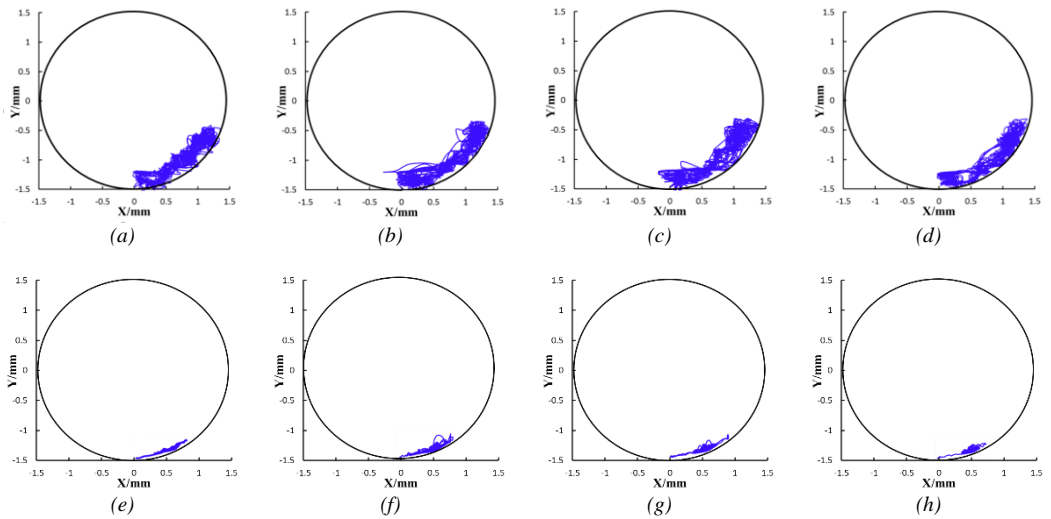
Figure 5. *Trajectory curve of BHA center under different WOB: (a), (b), (c) and (d) are the experimental results with 0 N, 0.23 N, 0.46 N and 0.69 N respectively; (e), (f), (g) and (h) are the numerical simulation results with 0 N, 0.23 N, 0.46 N and 0.69 N respectively.*

CONCLUSION

(1) The numerical simulation results can match well with the experimental results. The motion states of BHA in horizontal wells can be divided into three kinds, including circular arc swing, "8" swing and dot-like circular motion.

(2) The BHA position has a significant effect on the motion states of BHA, the rotate speed has a promotion on lateral displacement, while WOB have a much smaller effect compared with the other two parameters.

(3) From the engineering standpoint, a lower rotate speed is recommended as well as rotate speed can meet the requirement of ROP and it can protect downhole tools from wear damage. Moreover, a slightly large WOB is recommended in order to improve ROP.

ACKNOWLEDGMENT

REFERENCES

[1]. M. Albdiry, M. Almensory. Failure analysis of drillstring in petroleum industry: a review. Engineering Failure Analysis 65, 74-85 (2016). *DOI:10.1016/j.engfailanal.2016.03.014*

[2]. W. Li, G. Huang, Y. Jing, F. Yu, H. Ni. Modeling and mechanism analyzing of casing running with pick-up and release technique. Journal of Petroleum Science and Engineering 172, 538-546 (2019). *DOI:10.1016/j.petrol.2018.09.099*

[3]. W. Zhu, Q. Di. Effect of prebent deflection on lateral vibration of stabilized drill collars. SPE Journal 16 (1), 200-216 (2011). *DOI:10.2118/120455-PA*

[4]. Z. Guan, Y. Jin, Y. Wang. Experimental research on motion states of bottom drilling string in horizontal well. Engineering Mechanics 30(5), 340–345 (2013). *DOI:10.6052/j.issn.1000-4750.2012.06.0467*

165

[5]. D. Shao, Z. Guan, X. Wen, Y. Shi. Experiment on lateral vibration characteristics of horizontal rotary drilling string. Journal of China University of Petroleum (Edition of Natural Science) 37(4), 100–103 (2013). *DOI:10.3969/j.issn.1673-5005.2014.03.010*

[6]. Y. Liu, D. Gao. A nonlinear dynamic model for characterizing downhole motions of drill-string in a deviated well. Journal of Nature Gas Science and Engineering 38, 466–474 (2017). *DOI:10.1016/j.jngse.2017.01.006*

[7]. Z. Lian, Q. Zhang, T. Lin, F. Wang. Experimental and numerical study of drill string dynamics in gas drilling of horizontal wells. Journal of Nature Gas Science and Engineering 27, 1412–1420 (2015). *DOI:10.1016/j.jngse.2015.10.005*

[8]. Y. Bozkurt, M. Barbar, Ö. Özbek. Investigation of Effects of Parameters in Element-Free Galerkin Method for Bending Analysis of Mindlin-Reissner Plates, Acta Physica Polonica A (ICCESEN 2014), Antalya-Turkey. *DOI:10.12693/APhysPolA.128.B-208*

[9]. Z. Akhmetova, S. Zhuzbaev, S. Boranbayev. The Method and Software for the Solution of Dynamic Waves Propagation Problem in Elastic Medium, Acta Physica Polonica A (ICCESEN 2015), Antalya-Turkey. *DOI:10.12693/APhysPolA.130.352*

[10]. V., Kahya, M., Turan. Bending of Laminated Composite Beams by a Multi-Layer Finite Element Based on a Higher-Order Theory, Acta Physica Polonica A (ICCESEN 2016), Antalya-Turkey. *DOI:10.12693/APhysPolA.132.473*

[11]. H. Wang, Z. Guan, Y. Shi, W. Chen, Y. Liu, B. Zhang, D. Liang, X. Wang. Modeling and analyzing the motion state of bottom hole assembly in highly deviated wells. Journal of Petroleum Science and Engineering 170, 763–771 (2018). *DOI:10.1016/j.petrol.2018.07.005*

[12]. Z. Guan, H. Wang, Y. Shi, W. Chen, G. Zhao, J. Wang, G. Cao. Dynamic behavior analysis of push-the-bit rotary steerable bottom hole assembly. Journal of Mechanical Science and Technology 33(4), 1501–1511 (2019). DOI:10.1007/s12206-019-0302-*5*

A New Approach to Enhance Oil Recovery in the Tight Oil Reservoir: Pre-Gas Injection

Deqiang Wang, Linsong Cheng*, Renyi Cao, Junjie Jun, Fuguo Yin

Key Laboratory of Petroleum Engineering of the Ministry of Education, China University of Petroleum, Beijing, China
*lscheng@cup.edu.cn

ABSTRACT

The application of multi-fractured horizontal well has made great progress in the development of tight oil reservoirs. However, the oil production will decrease rapidly and the estimated ultimate recovery is still low in the tight reservoir with low pressure in china when the well is on production using depletion. To improve this situation, the pre-gas injection, which is a process of gas injection and soak before production, is evaluated to analysis the effect. The simulation model, including matrix and fracture, is built to describe the process of gas mass transfer. The pre-gas injection can enhance the pressure of matrix and fracture by gas injection. Gas swept volume can be enhanced after pre-gas injection. Through comparative experiments, it can be found that increasing injection pressure can sweep more oil. The replacement of oil and gas in the soaking well will be completed within 30-60 days. Small fracture spacing increases the contact area between the fracture and the matrix and the oil and gas displacement intensity.

KEYWORDS - *Tight oil; pre-gas injection; Simulation; Soak time*

1. INTRODUCTION

Tight oil is a huge and potential energy. For enhance the low ultimate oil recovery, many scholars have carried out EOR studies. In the experiment study, Cheng and Ding investigate the pore structures and threshold pressure gradient in the tight sandstone [1, 2]. In the simulation study, casing deformation during volume fracturing is investigated [3]. Mao studies the effective stress and modifies the equation[4]. Wang simulates the gas huff-n-puff in Bakken tight oil[5]. Tian builds the compositional model to simulate the gas injection[6]. Luo simulates the miscible and immiscible gas flooding[7]. For the application in the field, surfactant alternating gas injection and cumulative-in-situ-injection-production technology are studied and applied [8, 9]. Huang considers stress sensitivity to analysis the pressure transient[10]. Li summarized the current status of induced seismicity monitoring in the tight oil[11]. Wei analyzes the sensitivity of solution gas re-injection in Baikouquan tight formation[12]. In this paper, the pre-gas injection is proposed and evaluated, which is a process of gas injection and soak before production.

2. METHOD

The characteristics of fracture network in horizontal wells with SRV fracturing are studied by establishing a numerical model with matrix and fracture. According to the contact relation between the fracture and the matrix, the front distance and the distribution of oil saturation in the process of gas intrusion into the matrix are described accurately. ECLIPSE.2011 is adopted to establish the black oil model, and the parameters are shown in TABLE 1.

3. DISSCUSION
3.1. The effect of pressure

The displacement front edge of gas in the matrix increases with the pressure.

Table 15. Parameters and values of numerical simulation

Parameter	Value	Parameter	Value
Initial water saturation in the matrix	0.3	Matrix permeability, mD	0.1
Initial oil saturation in the matrix	0.7	Matrix porosity, 1	0.12
Initial gas saturation in the fracture	1	Fracture permeability, D	2
Pressure in the matrix，Mpa	14.5	Fracture porosity, 1	0.4
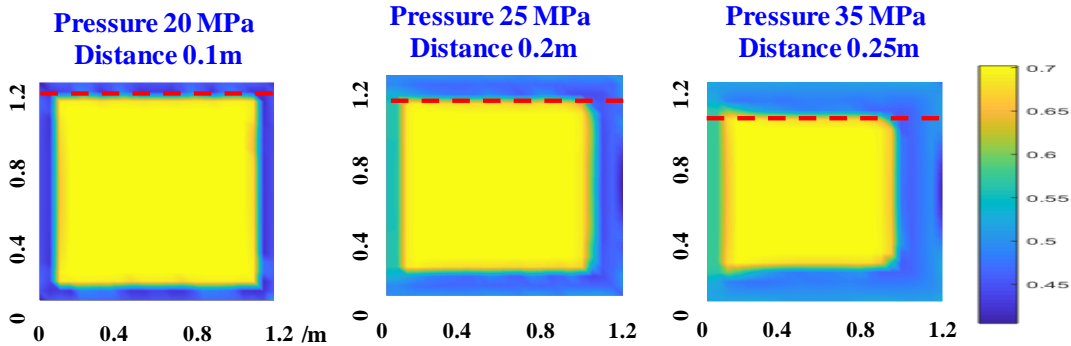
Figure 16. Influence of pressure for pre-gas injection.

3.2. The effect of soak time

In order to optimize the soaking time, it is found that the replacement of oil and gas is completed within 30-60 days through comparative experiment.
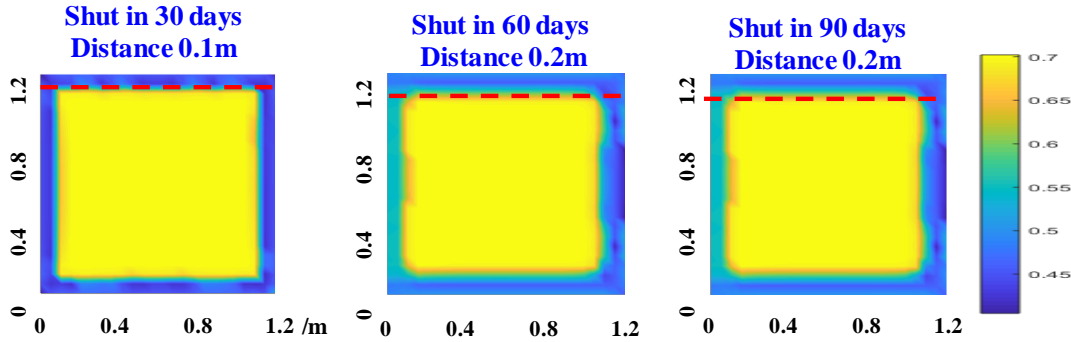
Figure 2. The comparison of soak time

3.3. The effect of cycles

In the first cycle, the gas intrudes into the matrix 0.1m, and the invasion degree increases with the increase of cycles. This is different from the imbibition between oil and water where the oil and gas replacement in the single cycle is limited. However, multiple gas cycles are significant.

168
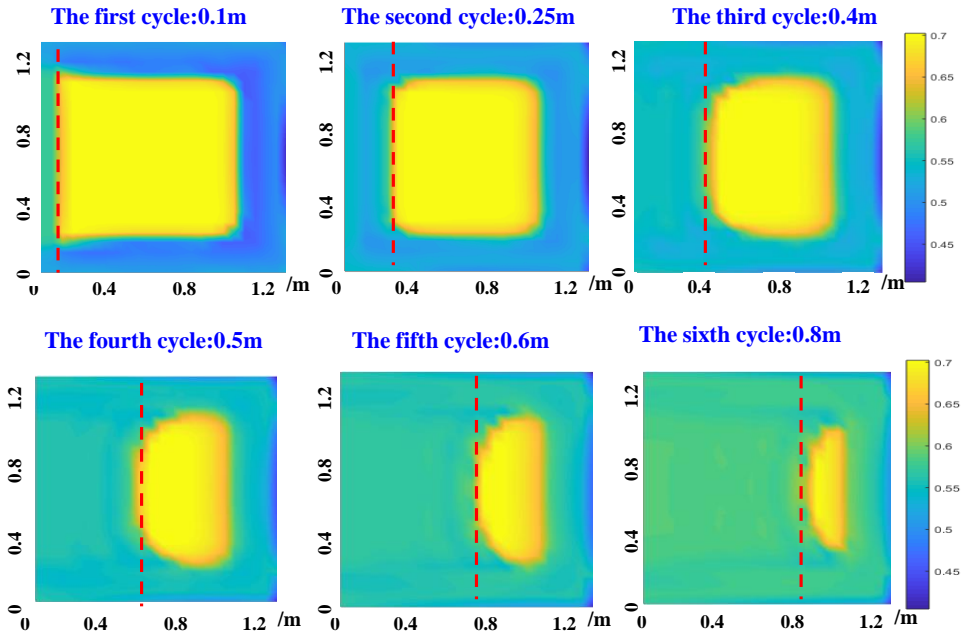
Figure 3. The comparison of cycles

3.4. The fracture spacing

Small fractures spacing increases the contact area between fractures and the matrix and the oil and gas displacement intensity. And the gas function is obvious in the area with more fractures. With the decrease of fracture spacing, the invasion amplitude in the matrix get larger.
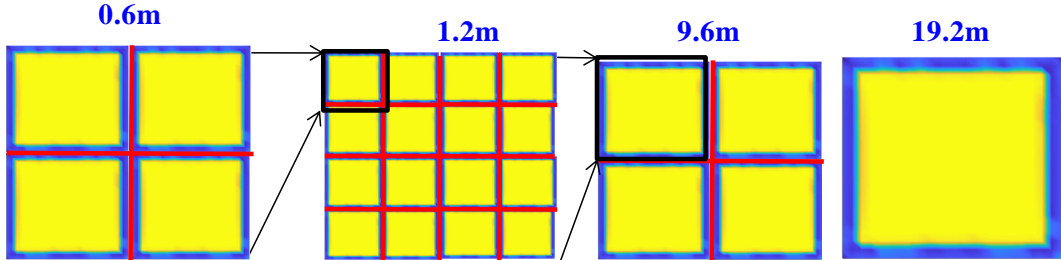
Figure 4. The comparison of fracture spacing

4. CONCLUSION

The pre-gas injection can enhance the pressure of matrix and fracture leading higher sweep efficiency, which is proved by model with fracture and matrix. And higher pressure, more cycles and less fracture spacing are benefit to gas mass transfer.

ACKNOWLEDGMENTS

169
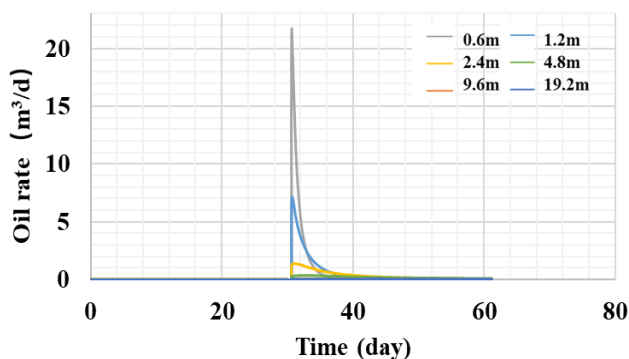
Figure 5. *The comparison of oil rate.*
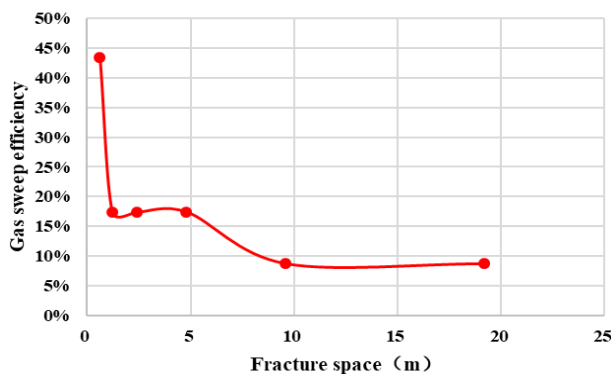
Figure 6. *The comparison of gas sweep effciency.*

REFERENCES
[1] Z. Cheng, Z. Ning, H. Zhao, Q. Wang, Y. Zeng, X. Wu, R. Qi, S. Zhang, A comprehensive characterization of North China tight sandstone using micro-CT, SEM imaging, and mercury intrusion, Arabian Journal of Geosciences, 12 (2019) 407.10.1007/s12517-019-4568-9
[2] J. Ding, S. Yang, T. Cao, J. Wu, Dynamic threshold pressure gradient in tight gas reservoir and its influence on well productivity, Arabian Journal of Geosciences, 11 (2018) 783.10.1007/s12517-018-4129-7
[3] X. Guo, J. Li, G. Liu, W. Lian, Y. Zeng, Q. Tao, X. Song, Shale experiment and numerical investigation of casing deformation during volume fracturing, Arabian Journal of Geosciences, 11 (2018) 723.10.1007/s12517-018-4091-4
[4] X. Mao, Y. Liu, W. Guan, S. Liu, J. Li, A new effective stress constitutive equation for cemented porous media based on experiment and derivation, Arabian Journal of Geosciences, 11 (2018) 337.10.1007/s12517-018-3697-x
[5] L. Wang, W. Yu, Mechanistic simulation study of gas Puff and Huff process for Bakken tight oil fractured reservoir, Fuel, 239 (2019) 1179-1193.https://doi.org/10.1016/j.fuel.2018.11.119
[6] Y. Tian, Y. Xiong, L. Wang, Z. Lei, Y. Zhang, X. Yin, Y.-S. Wu, A compositional model for gas injection IOR/EOR in tight oil reservoirs under coupled nanopore confinement and

geomechanics effects, Journal of Natural Gas Science and Engineering, 71 (2019) 102973.https://doi.org/10.1016/j.jngse.2019.102973

[7] P. Luo, W. Luo, S. Li, Effectiveness of miscible and immiscible gas flooding in recovering tight oil from Bakken reservoirs in Saskatchewan, Canada, Fuel, 208 (2017) 626-636.https://doi.org/10.1016/j.fuel.2017.07.044

[8] P. Ghosh, K.K. Mohanty, Study of surfactant alternating gas injection (SAG) in gas-flooded oil-wet, low permeability carbonate rocks, Fuel, 251 (2019) 260-275.https://doi.org/10.1016/j.fuel.2019.03.119

[9] H. Yu, Z. Yang, L. Luo, J. Liu, S. Cheng, X. Qu, Q. Lei, J. Lu, Application of cumulative-in-situ-injection-production technology to supplement hydrocarbon recovery among fractured tight oil reservoirs: A case study in Changqing Oilfield, China, Fuel, 242 (2019) 804-818.https://doi.org/10.1016/j.fuel.2018.12.121

[10] S. Huang, Y. Yao, S. Zhang, J. Ji, R. Ma, Pressure transient analysis of multi-fractured horizontal wells in tight oil reservoirs with consideration of stress sensitivity, Arabian Journal of Geosciences, 11 (2018) 285.10.1007/s12517-018-3639-7

[11] L. Li, J. Tan, D.A. Wood, Z. Zhao, D. Becker, Q. Lyu, B. Shu, H. Chen, A review of the current status of induced seismicity monitoring for hydraulic fracturing in unconventional tight oil and gas reservoirs, Fuel, 242 (2019) 195-210. https://doi.org/10.1016/j.fuel.2019.01.026

[12] B. Wei, T. Song, Y. Gao, H. Xiang, X. Xu, V. Kadet, J. Bai, Z. Zhai, Effectiveness and sensitivity analysis of solution gas re-injection in Baikouquan tight formation, Mahu sag for enhanced oil recovery, Petroleum, (2019).https://doi.org/10.1016/j.petlm.2019.10.001

Optimization of Gas Injection and Depletion in Tight Reservoir

Deqiang Wang[1], Linsong Cheng[1]*, Lei Song[2], Chenxu Yang[1], Hui Li[1] and Xulin Du[1]

[1]*Key Laboratory of Petroleum Engineering of the Ministry of Education, China University of Petroleum, Beijing, China*

[2]*Changqing Petroleum Exploration Bureau, Xian, China*

*lscheng@cup.edu.cn

ABSTRACT

Tight reservoir reserves are huge and will be an important part of future energy structure. Tight reservoirs have low recovery because of small pore throat. Nowadays, gas injection and depletion development are mostly adopted, and it is of great significance to optimize the two development methods reasonably. For gas injection development, this paper establishes a one-injection-one-production numerical model for the target block and draws a pressure gradient profile. The results show that the gas injection pressure profile is higher than the water injection pressure profile, and the pressure gradient of the gas drive mainstream line is higher than the water drive line, which can better maintain the formation pressure level. For depletion development, this paper establishes the black oil model, conducting multi-factor analysis on reservoir, dissolved gas-oil ratio and other factors. And the boundary chart of dissolved gas-oil ratio and thickness (abundance) is plotted. The results show that when the coupling of the two reaches a certain degree, depletion development achieve better results. For the target block, where the dissolved gas-oil ratio is greater than 90 m^3/m^3 and the thickness is greater than 20 m, can achieve a good development effect. And the well pattern spacing and reasonable working system are studied.

KEYWORDS - *Tight oil, Depletion, Gas flooding, Simulation, Optimization research.*

1. INTRODUCTION

Tight oil is a very important source of energy. However, due to small pore throat and poor physical properties, the ultimate recovery is low [1-3]. Many scholars have carried out relevant research. At present, common development methods include gas injection development and depletion development [4, 5].

Water injection is usually not used because of high injection resistance[6]. And gas injection is considered an effective development method due to its good injection ability. And the experiment and simulation of gas huff-n-puff have been investigated [7, 8].

In addition, depletion development does not require the injection of fluid, which is simple to operate and widely used. For enhancing the ultimate recovery, many measures are adopted and optimized considering mechanism and effective factors [9-12].

In this paper, the applicability of water injection and gas injection is evaluated by numerical simulation of one-injection-one-production, and different main control factors of tight reservoir are evaluated to comprehensively evaluate the applicability of depletion development.

2. EVALUATION of GAS FLOODING

The model is assumed that the reservoir has only three phases of oil, gas and water without considering the influence of temperature and composition. The black oil model with one injection and one production is established and commercial software Eclipse.2011 is adopted.

As shown in the Figure 1, the red curve represents the pressure gradient of gas flooding, and the blue curve represents the pressure gradient of water flooding. It can be seen that under the same conditions, water injection in the near-well zone consumes a lot of pressure resulting in a low pressure gradient in the middle of the formation .A high pressure gradient means more displacement capacity, and therefore gas flooding is more suitable for tight reservoirs.

172
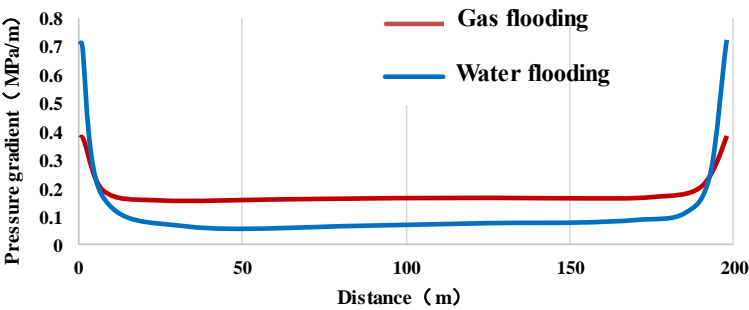
Figure 17. *The comparison of gas flooding and water flooding*

3. EVALUATION of DEPLETION DEVELOPMENT

More practical production processes adopt the depletion development of non-injected fluid, so the black oil model with the following parameters is established to evaluate the factors of dissolved gas, thickness, well pattern and well spacing.

Table 1. *Parameters and values of numerical simulation.*

Parameter	value	Parameter	value
Rock compressibility C_t（MPa^{-1}）	$4*10^{-4}$	Initial gas-oil ratio R_{si}（m^3/m^3）	110
producing pressure drop Δp（MPa）	10	Production gas oil ratio R_p（m^3/m^3）	143
Oil saturation S_o	0.70	oil volume factor B_o（m^3/m^3）	1.25
porosity ϕ	9.1%	Gas volume factor B_g（m^3/m^3）	0.002
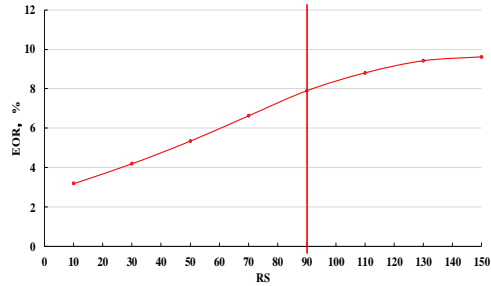
Figure 2. *Recovery for different dissolved gas-oil ratios.*
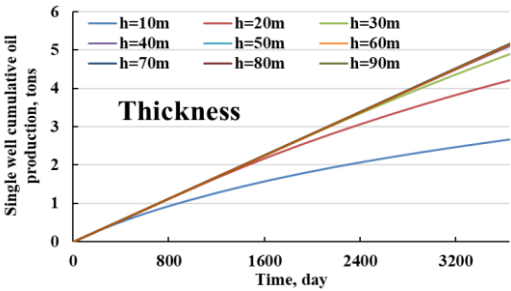
Figure 3. *The oil rate for different thickness.*

The numerical simulation results are shown in Figure 2 and Figure 3. The numerical value represented by color is shown in Figure 4. It is the highest recovery efficiency where dissolved gas-oil ratio is greater than 90 and the reservoir thickness is more than 20 meters.

173

(a)   (b)   (c)
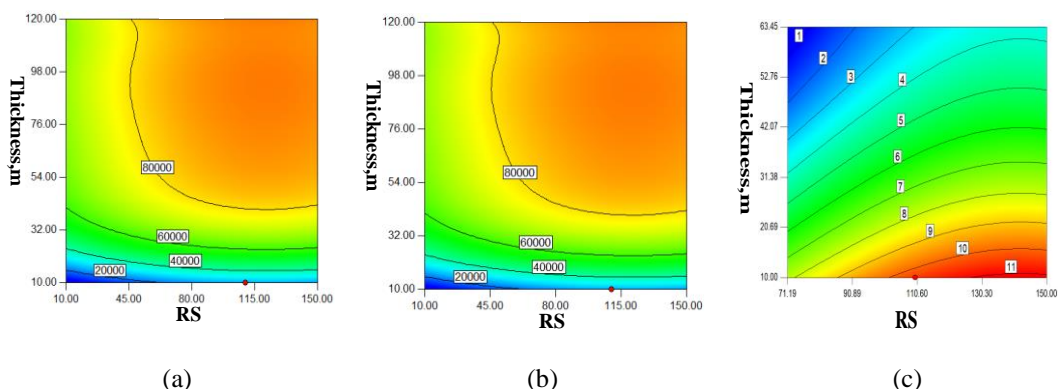
Figure 4. *Influence of thickness and dissolved gas-oil ratio on productivity (a) cumulative yield (b) oil rate (c) recovery.*
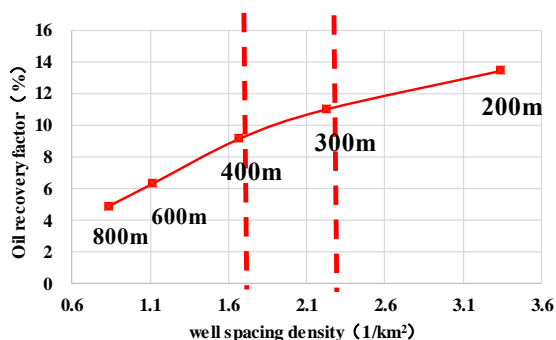
Figure 5. *Recovery curve with pattern density*

As shown in Figure 5, an inflection point occurs at the well spacing of 300-400 meters, which is the recommended horizontal well spacing for depleted development in tight reservoir.

4. CONCLUSION

According to the numerical simulation results, gas flooding has more advantages than water flooding by the comparison of pressure gradient. For depleted development in the target block, 300-400 meters is an appropriate well spacing, especially for reservoirs with the greater than 90 dissolved gas-oil ratio and the more than 20 meters thickness.

ACKNOWLEDGMENTS

REFERENCES

[1] X. Mao, Y. Liu, W. Guan, F. Yueli, Experimental and numerical simulation on the influence of anisotropic fracture network deformation to shale gas percolation, Arabian Journal of Geosciences, 11 (2018) 615.10.1007/s12517-018-3973-9

174

[2] L. Song, Z. Ning, L. Duan, Research on reservoir characteristics of Chang7 tight oil based on nano-CT, Arabian Journal of Geosciences, 11 (2018) 472.10.1007/s12517-018-3842-6

[3] F. Sun, Y. Yao, G. Li, X. Li, Transport zones of oil confined in lipophilic nanopores: a technical note, Arabian Journal of Geosciences, 12 (2019) 136.10.1007/s12517-019-4321-4

[4] L. Zhang, F. Zhou, J. Mou, J. Wang, J. Wang, S. Zhang, Research on sensitivity damage of naturally fractured carbonate reservoirs in Ordos Basin, Arabian Journal of Geosciences, 12 (2019) 595.10.1007/s12517-019-4805-2

[5] W. Zheng, Y. Liu, J. Huang, Y. Liu, J. Chen, Study on the optimal development method for offshore buried hill fractured reservoirs, Arabian Journal of Geosciences, 11 (2018) 640.10.1007/s12517-018-3965-9

[6] L. Cheng, D. Wang, R. Cao, R. Xia, The influence of hydraulic fractures on oil recovery by water flooding processes in tight oil reservoirs: An experimental and numerical approach, Journal of Petroleum Science and Engineering, (2019) 106572.https://doi.org/10.1016/j.petrol.2019.106572

[7] L. Wang, W. Yu, Mechanistic simulation study of gas Puff and Huff process for Bakken tight oil fractured reservoir, Fuel, 239 (2019) 1179-1193.https://doi.org/10.1016/j.fuel.2018.11.119

[8] Y. Tian, Y. Xiong, L. Wang, Z. Lei, Y. Zhang, X. Yin, Y.-S. Wu, A compositional model for gas injection IOR/EOR in tight oil reservoirs under coupled nanopore confinement and geomechanics effects, Journal of Natural Gas Science and Engineering, 71 (2019) 102973.https://doi.org/10.1016/j.jngse.2019.102973

[9] Q. Ma, S. Yang, D. Lv, M. Wang, J. Chen, G. Kou, L. Yang, Experimental investigation on the influence factors and oil production distribution in different pore sizes during CO2 huff-n-puff in an ultra-high-pressure tight oil reservoir, Journal of Petroleum Science and Engineering, 178 (2019) 1155-1163.https://doi.org/10.1016/j.petrol.2019.04.012

[10] J.J. Sheng, Optimization of huff-n-puff gas injection in shale oil reservoirs, Petroleum, 3 (2017) 431-437.https://doi.org/10.1016/j.petlm.2017.03.004

[11] B. Wei, T. Song, Y. Gao, H. Xiang, X. Xu, V. Kadet, J. Bai, Z. Zhai, Effectiveness and sensitivity analysis of solution gas re-injection in Baikouquan tight formation, Mahu sag for enhanced oil recovery, Petroleum, (2019).https://doi.org/10.1016/j.petlm.2019.10.001

[12] J. Guo, L. Tao, F. Zeng, Optimization of refracturing timing for horizontal wells in tight oil reservoirs: A case study of Cretaceous Qingshankou Formation, Songliao Basin, NE China, Petroleum Exploration and Development, 46 (2019) 153-162.https://doi.org/10.1016/S1876-3804(19)30015-1

Transient Pressure and Production Analysis of Fractured Horizontal Well with elliptical SRV in Composite Shale Reservoir

Xulin Du1*, Linsong Cheng1, Jun Chen2 and Jiexi Ma1

1 College of Petroleum Engineering, China University of Petroleum (Beijing), Beijing 102249, China
2 State Key Laboratory of Oil and Gas Reservoir Geology and Exploitation, Southwest Petroleum University, Chengdu 610500, China
*duxulin_cup@foxmail.com

ABSTRACT

This paper establishes a comprehensive flow mathematical model of fractured horizontal well with elliptical SRV in composite shale reservoir considering the mass transfer mechanism of desorption and gas diffusion. The typical curve and production sensitivity of proposed model are analyzed. The unsteady flow caused by concentration difference is considered in matrix, Darcy flow is considered in fractures, and infinite conductivity is considered in horizontal wellbore. This mathematical model can be analytically solved by using Laplace transform, Mathieu function and Stehfest numerical inversion in elliptic coordinate system by introducing the corresponding dimensionless quantity. The results show that the shale gas flow can be divided into 10 flow stages based on the transient pressure curve characteristics. The sensitivity of shale gas productivity is analyzed and the corresponding rules are obtained. The model proposed in this paper has important theoretical significance for the dynamic analysis of fractured horizontal well in shale gas reservoir.

KEYWORDS - *Shale gas reservoir, Elliptical SRV, Composite model, Production analysis.*

1. INTRODUCTION

Shale has the characteristics of low porosity and low permeability [1-2]. At present, with the progress of hydraulic fracturing and horizontal well technology, shale gas production has been effectively improved. Therefore, it is of great significance for petroleum engineers to study the production of fractured horizontal wells, which is one of important approaches for accurate reservoir productivity evaluation and production planning [3-4]. The fracturing not only creates high conductivity fractures, but also connects the natural fractures to form the complex fracture network [5-6]. The high conductivity area formed by hydraulic fracturing is named the stimulated reservoir volume (SRV), and the area without fracturing is the un-stimulated reservoir volume (USRV). At present, a large number of models are used to simulate the production performance of multi-stage fractured horizontal wells with SRV, among which the most widely used are linear flow model and composite model [7-10]. In addition, some scholars adopted the numerical simulation method to simulate the SRV of shale gas reservoir, and carry out sensitivity analysis of relevant parameters and dynamic production prediction [11-12].

The purpose of this paper is to establish a mathematical model of shale gas composite reservoir considering special gas transport mechanisms, introduces the dimensionless variable definition to solve the model, and analyzes the flow law of multi-stage fractured horizontal well with elliptical SRV in composite shale gas reservoir, so as to provide theoretical basis for the dynamic analysis of shale gas reservoir.

2. METHODOLOGY
2.1. Description of the theoretical model

Before deriving the multi-stage fractured horizontal well model for shale gas reservoir, the following assumptions are made: (1) the shale gas reservoir has an elliptical internal and external boundary, in which the top and bottom are closed and the lateral is infinite; (2) the shale reservoir is of equal thickness; (3) the infinite shale reservoir is composed of matrix system and fracture

176

system, in which the fracture system has the anisotropic characteristic; (4) the desorption process of adsorbed gas in matrix can be described by Langmuir isotherm model; (5) the gas in fracture is free gas, and its flow follows Darcy law; (6) the shape of matrix block is spherical, and the gas in matrix exists in two states of adsorbed gas and free gas; (7) the flow of single-phase gas is isothermal, and ignoring gravity and capillary force and so on. Based on the flow mechanism of shale gas and the above assumptions, the actual complex formation conditions are simplified as the physical model of composite reservoir considering elliptical SRV, as shown in Figure 1.
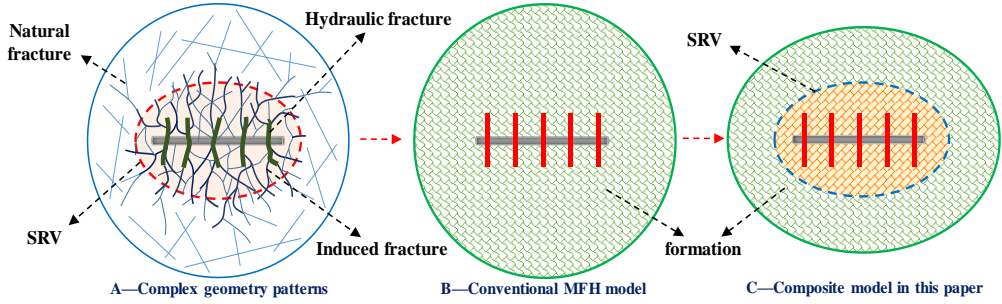
Figure 1. *Physical model of composite shale gas reservoir.*

2.2. Establishment and solution of mathematical model

Under the radial elliptic coordinate, the gas in fracture for inner zone satisfies the following pseudo-pressure diffusion equation, which assumed that the gas diffusion from matrix to fracture follows the second Fick law, and the matrix shape is a sphere:

$$\frac{1}{r}\frac{\partial}{\partial r}\left(k_{fh1}r\frac{\partial \psi_{f1}}{\partial r}\right)+k_{fh1}\frac{1}{r^2}\frac{\partial^2 \psi_{f1}}{\partial \theta^2}+k_{fv1}\frac{\partial^2 \psi_{f1}}{\partial z^2}=\phi_{f1}\mu c_{gf1}\frac{\partial \psi_{f1}}{\partial t}+\frac{2p_{sc}T}{T_{sc}}\frac{3D}{R}\frac{\partial C_m}{\partial r_m}\bigg|_{r_m=R} \quad (1)$$

The instantaneous diffusion of gas follows the second Fick law. By Laplace transformation of the dimensionless unsteady diffusion equation in matrix, the flow in matrix in Laplace space for inner zone can be obtained:

$$K\left[\frac{1}{r_D}\frac{\partial}{\partial r_D}\left(r_D\frac{\partial \overline{\psi_{f1D}}}{\partial r_D}\right)+\frac{1}{r_D^2}\frac{\partial^2 \overline{\psi_{f1D}}}{\partial \theta^2}+\frac{\partial^2 \overline{\psi_{f1D}}}{\partial z_D^2}\right]=\left\{\omega_1 s+\left(1-\omega_1\right)\lambda\alpha\left[\sqrt{\frac{s}{\lambda_1}}\coth\left(\sqrt{\frac{s}{\lambda_1}}\right)-1\right]\right\}\overline{\psi_{f1D}} \quad (2)$$

In the same way as the derivation in inner zone, the comprehensive flow differential equation in outer zone can be obtained:

$$\left[\frac{1}{r_D}\frac{\partial}{\partial r_D}\left(r_D\frac{\partial \overline{\psi}_{f2D}}{\partial r_D}\right)+\frac{1}{r_D^2}\frac{\partial^2 \overline{\psi}_{f2D}}{\partial \theta^2}+\frac{\partial^2 \overline{\psi}_{f2D}}{\partial z_D^2}\right]=\frac{\left\{\omega_2\eta s+\left(1-\omega_2\right)\lambda_2\alpha_2\left[\sqrt{\frac{\eta s}{\lambda_2}}\coth\left(\sqrt{\frac{\eta s}{\lambda_2}}\right)-1\right]\right\}}{\left(1-K\right)}\overline{\psi}_{f2D} \quad (3)$$

It is assumed that the hydraulic fracture is infinite conductivity, and the bottom hole pressure is finally obtained by line source superposition:

177

$$\overline{\psi}_{D1} = \frac{\overline{q_l}}{K}\left[K_0\left(\sqrt{f_1}R_D\right) + I_0\left(\sqrt{f_1}R_D\right)\frac{M\sqrt{f_1}K_1\left(\sqrt{f_1}\right)}{M} \right] \tag{4}$$

The assumptions are as follows: (1) the fractures are perpendicular to the horizontal wellbore; (2) the horizontal well is fully opened; (3) compared with the inflow flux from the hydraulic fracture, the flux in the formation is negligible; (4) the pressure or production in the fracture is a fixed value; (5) the flow conductivity in the horizontal well is infinite.
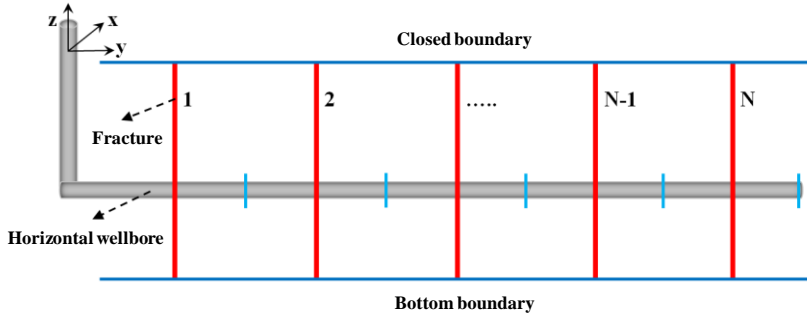
Figure 2. *Physical model of multistage fractured horizontal well.*
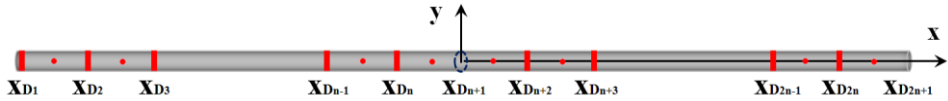
Figure 3. *The superposition of pressure response surface source.*

According to the theory of source function, fracture can be regarded as the surface source in reservoir. Therefore, the pressure response of reservoir is the superposition result caused by continuous surface sources as following:

$$\overline{\psi}_{D1} = \frac{1}{2}\int_{-L_{flD}}^{L_{flD}} \frac{\overline{q}_{LD(\alpha,u)}}{K}\left[K_0\left(\sqrt{f_1}R_D\right) + A_cI_0\left(\sqrt{f_1}R_D\right) \right]d\alpha \tag{5}$$

At the wall of fracture, the pressure in reservoir is equal to that in fracture. The model coupled fracture and reservoir in Laplace space is obtained:

$$\partial\overline{\psi}_{wD} - \frac{1}{2}\int_{-L_{flD}}^{L_{flD}} \frac{\overline{q}_{LD}(\alpha,u)}{K}\left[K_0\left(\sqrt{f_1}R_D\right) + A_cI_0\left(\sqrt{f_1}R_D\right) \right]d_\alpha = \frac{\pi}{KR_{FlD}}\left[x_D\overline{q}_{FlD} - \int_0^{x_D}\int_0^{y}\overline{q}_{LD}d_{x_D}d_c \right] \tag{6}$$

For the constant production in fractured horizontal well, the sum of the production of each fracture should be equal to the total production of the fractured horizontal well. Then, there are the following dimensionless flux normalization conditions in Laplace space:

178

$$\sum_{l=1}^{m} \int_{0}^{l_{FID}} \overline{q}_{LD} d_{x_D} = \frac{1}{u} \tag{7}$$

The certain line source solution can be obtained for each fracture, and the bottom hole pressure of equations can be solved by Gauss elimination method in Laplace space. Then, the dimensionless BHP and dimensionless flux in real space can be solved by Stehfest numerical inversion.

2.3. Type Curves for composite shale reservoir

Typical curves of pressure and pressure derivative of multi-stage fractured horizontal well in composite shale gas reservoir, as shown in Figure 4, can be divided into the following 10 flow stages: (1) the wellbore storage stage: the curve of pressure and pressure derivative coincides with a slope of 1; (2) the early transitional flow stage; (3) the early linear flow stage: the gas flows perpendicular to the fracture near the fracture, and the slope of pressure and pressure derivative is 1/2; (4) the second transitional flow stage: the transition of early linear flow and early radial flow; (5) the early radial flow stage: the pressure derivative curve is constant and the value is $1/(2 \times n)$; (6) the second linear flow stage: the fracture appear obvious interference at this stage; (7) the second radial flow stage: the pressure derivative curve is constant 1/2, which requires a large SRV area; (8) the third transition stage: the transition stage of the second and third radial flow; (9) when the matrix supplies gas to the fracture, there is obvious "concave" in the homogeneous model; (10) the third radial flow stage: the pressure derivative curve is constant and the value is $1/2 \times M$. In the well testing process of shale reservoir, there will be differences in the shape of curves, and some flow stages may be covered up, which depends on the influence of formation parameters and SRV.
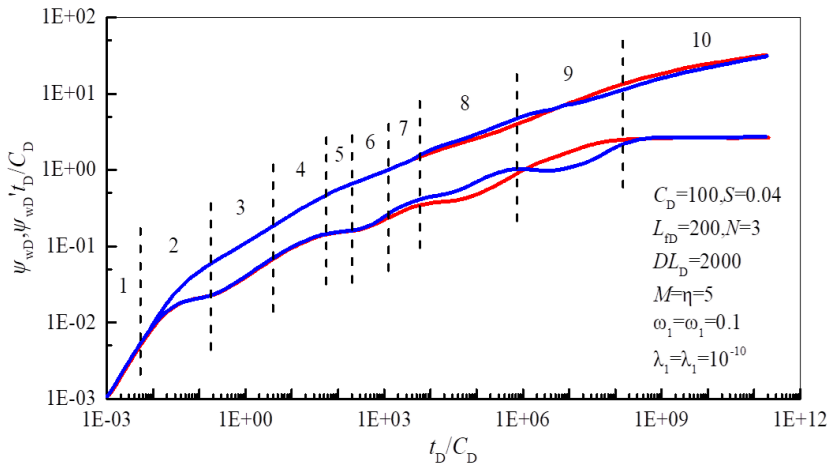
Figure 4. *The type Curves for composite shale reservoir.*

3. PRODUCTION SENSITIVITY ANALYSIS

In this section, the proposed model is adopted for analyzing the sensitivity of productivity and the model parameters are shown in Table 1. Figure. 5 shows the gas production rate and the cumulative gas production under different parameters. It can be seen that the productivity of shale gas well can be increased by increasing the SRV radius and permeability of the internal region. Therefore, the hydraulic fracturing scale can be appropriately increased in the development of shale gas reservoir, the complex fracture network system scale can be increased, and the gas well productivity can be improved. The larger diffusion coefficient, Langmuir volume and Langmuir pressure, the higher productivity of shale gas well.

179

Table 1. *The simulation parameters.*

Properties	Value	Properties	Value
foramation thickness, m	50	Reservoir temperature, K	350
Well radius, m	0.1	Reservoir Pressure, Pa	32×10^6
The fracture half length, m	200	Matrix permeability in inner zone, mD	0.01
fracture spacing, m	70	Fracture permeability in inner zone, mD	50
SRV radius, m	400	Matrix porosity in inner zone, %	0.05
Gas viscosity, Pa·s	0.00002	Fracture porosity in inner zone, %	0.0002
Skin factor	0.01	Matrix compressibility in inner zone, 1/Pa	1×10^{-8}
Wellbore storage coefficient, m^3/Pa	0.01×10^{-6}	Fracture compressibility in inner zone, 1/Pa	35×10^{-11}
Matrix radius, m	10	Matrix permeability in outer zone, mD	0.01
diffusion coefficient, m^2/s	1×10^{-9}	Fracture permeability in outer zone, mD	1
Langmuir volume, m^3/m^3	1	Matrix porosity in outer zone, %	0.05
Langmuir pressure, Pa	2×10^7	Fracture porosity in outer zone, %	0.0001
Gas compression factor	0.89	Matrix compressibility in outer zone, 1/Pa	2×10^{-8}
Bottom hole pressure, Pa	6×10^6	Fracture compressibility in outer zone, 1/Pa	35×10^{-11}

(a) The fracture half-length   (b) The fracture conductivity   (c) SRV radius

(d) Diffusion   (e) Langmuir volume   (f) Langmuir pressure
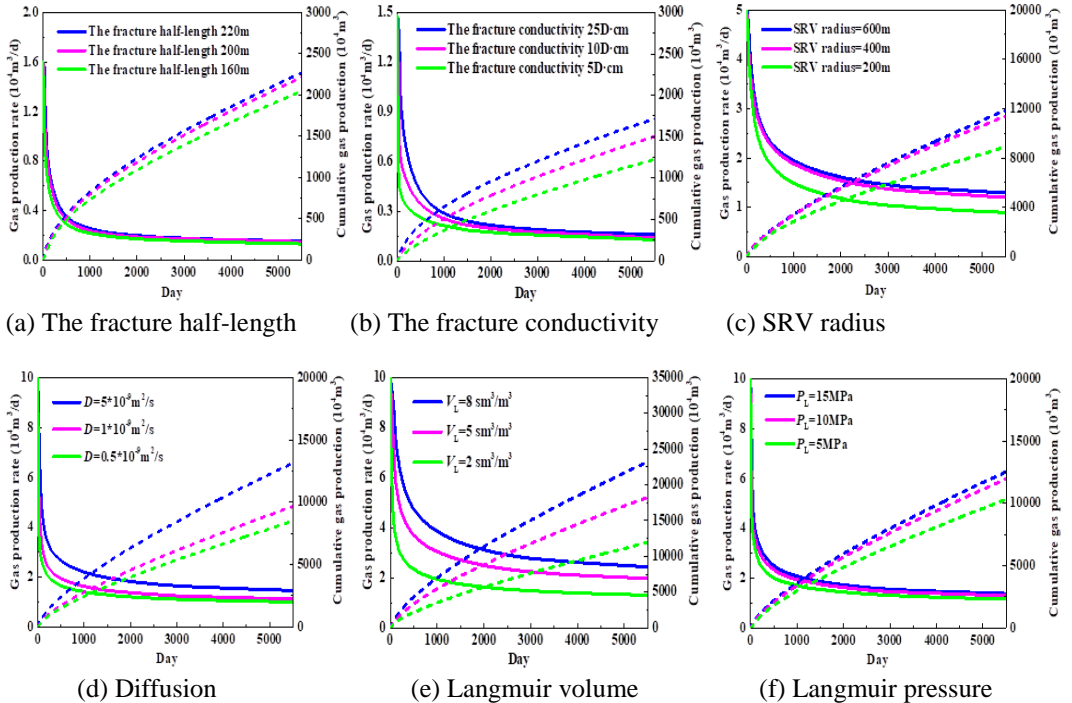
Figure 5. *The production sensitivity analysis.*

180

4. CONCLUSION

In this paper, a composite model based on elliptical SRV and complex transport mechanisms be proposed and can effectively analyze the transient pressure and production of fractured horizontal well in shale gas reservoir. This study can lay a theoretical foundation for further study on the production characteristics, flow mechanism and productivity prediction of fractured horizontal well in shale gas reservoir.

REFERENCES

[1] Zhang J, Huang S, Cheng L, Effect of flow mechanism with multi-nonlinearity on production of shale gas. J Nat Gas Sci Eng 2015; 24: 291-301. 10.1016/j.jngse.2015.03.043

[2] Cao P, Liu J, Leong Y K. A fully coupled multiscale shale deformation-gas transport model for the evaluation of shale gas extraction. Fuel 2016; 178: 103-117. 10.1016/j.fuel.2016.03.055

[3] Pin J, Linsong C, Shijun H, Hongjun L. Transient behavior of complex fracture networks. J Petrol Sci Eng 2015; 132: 1-17. 10.1016/j.petrol.2015.04.041

[4] Bello RO, Wattenbarger RA. Modelling and analysis of shale gas production with a skin effect. J Can Pet Technol 2013; 49(12): 37-48. https://doi.org/10.2118/2009-082

[5] X. Mao, Y. Liu, W. Guan, Experimental and numerical simulation on the influence of anisotropic fracture network deformation to shale gas percolation, Arabian Journal of Geosciences, 11 (2018) 615. https://doi.org/10.1007/s1251

[6] L. Song, Z. Ning, L. Duan, Research on reservoir characteristics of Chang7 tight oil based on nano-CT. Arabian Journal of Geosciences, 11 (2018) 472. https://doi.org/10.1007/s1251

[7] S. Huang, Y. Yao, S. Zhang, Pressure transient analysis of multi-fractured horizontal wells in tight oil reservoirs with consideration of stress sensitivity, Arabian Journal of Geosciences, 11 (2018) 285. https://doi.org/10.1007/s1251

[8] T.A. Blasingame, T.L. McCray, W.J. Lee, Decline curve analysis for variable pressure drop/variable flowrate systems, SPE Gas Technology Symposium, 22-24 January, 1991 Houston-Texas. https://doi.org/10.2118/21513-MS

[9] R. Nie, Y. Jia, Y. Meng, Y. Wang, J. Yuan, W. Xu, New type curves for modeling productivity of horizontal well with negative skin factors, SPE Res. Eval. Eng, 15 (2012) 486-497. https://doi.org/10.2118/163045-PA

[10]　P.M. Adrian, SPE Annual Technical Conference and Exhibition, 26-28 September, 2016 Dubai-UAE. https://doi.org/10.2118/184484-STU

[11]　Jiang J, Younis R, A multimechanistic multicontinuum model for simulating shale gas reservoir with complex fractured system. Fuel 2015; 161: 333-344. 10.1016/j.fuel.2015.08.069

[12]　Rao X, Cheng L S, Cao R Y, An efficient three-dimensional embedded discrete fracture model for production simulation of multi-stage fractured horizontal well. Engineering Analysis with Boundary Elements 2019; 106: 473-492. 10.1016/j.enganabound.2019.06.006

Design of an Apparatus for Measuring Gear Efficiency

İsmail Kaya, Vildan Girişta[*] and Zeynep Parlar

Istanbul Technical University/Mechanical Engineering Department, Istanbul, Turkey
*vgirista@itu.edu.tr

ABSTRACT

Gearboxes are one of the machine elements used in power transmission and changing power axis. Although the efficiency of a single stage in gear pairs is around 97% - 99%, there are additional losses due to various factors as in every machine element. Even the slightest increase in the efficiency of these components results in significant energy savings. In this study, it is planned to create a design that can measure instantaneous power loss while the system is running by measuring input and output power. It is planned to use an electric motor, a gearbox and a centrifugal pump to operate the system under load. A wattmeter shall be connected to the asynchronous electric motor in order to measure the power value at the input. The output power will be measured by the torque transducer located between the output of the gearbox and the input of the centrifugal pump. Thus, only losses in the gearbox will be obtained, and losses in the centrifugal pump and water line will not be allowed to affect the data.

KEYWORDS - *gearbox, efficiency, lubricant.*

1. INTRODUCTION

Gearboxes are most commonly used in order to increase torque of the prime mover and reduce the rotational speed of the output shaft. Gear drives are components of various mechanical systems used in such industries such as refinery, process, construction and mining. In all these industries higher efficiency of mechanical components is always desirable. Especially in passenger vehicles due to importance of fuel economy and environmental concerns, efficiency of gear systems has been gaining importance [1]. Gear manufacturers are constantly improving their design and manufacturing techniques to obtain more efficient gearboxes at lower costs. With good design and manufacturing practice, gear efficiencies of 99% per mesh and better are possible. Efficiency of industrial gear boxes are 1 to 2% power loss per mesh. A three-stage gearbox would have 94 to 97% efficiency [2]. Modern wind turbines transmit up to 5 MW through a gearbox, which has 8 or more gear meshes. Therefore, even small reductions in power loss results in large energy savings [3]. Gearboxes are lubricated with grease or oil. Often, lubrication system improvement is necessary to obtain the highest efficiency [2]. Power loss in a gearbox is related to the chemical properties of the lubricant. In the boundary and mixed lubrication regime, power losses are related to the chemical composition of the additives [4]. Many variations of these lubricants exist with qualities such as: high temperature, extreme pressure, corrosion protection, water resistance etc. These qualities are improved with additives.

In this study, the purpose is to design an experimental system in order to determine the effect of the additive oil to efficiency of the gearbox. Therefore, in order to see the effect of the additive amount in the oil on the friction characteristics, experiments have been carried out on the block on ring system.

2. EXPERIMENTAL SET-UP

Molybdenum disulphide is a widely used lubricant as it maintains its favorable tribological properties up to 400°C in air and up to 800°C in vacuum environment [5]. MoS_2 has a low friction coefficient and it is commonly used as additive in greases and grease like pastes, liquid lubricants such as industrial gear oils and solid film lubricants. In order to see the effect of additives on frictional characteristics of the lubricant, experiments were carried out on a block on ring

182

tribotester (Fig. 1). In block on ring test method a fixed pin is in contact with the ring surface where the contact is in the form of a line so are gear teeth in mesh. A DC Motor with a rotational speed range of $30 - 800$ rpm and force transducer with maximum range $200N$ with $\pm 0,1N$ accuracy is employed. Block is Type 316 Stainless Steel with 12 mm diameter and 18 mm length. Ring is grey cast iron with 65 mm diameter which allows us to have v=$0,20 - 5,45$ m/s sliding speed on counter surface.
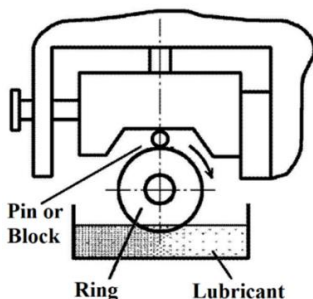
Figure. 1. *Block on ring schematic view.*

Molybdenum disulfide powder additive with particle sizes in range of 2.5-5.0 μm is mixed to SAE 80W-90 gear oil, 1%, 2% and 5% by mass. The lubricant is prepared in ultrasonic bath at 38 kHz frequency and 50°C temperature for two hours. Experiments are carried out under 50 and 75 N normal load and 04, m/s and 0,8 m/s sliding velocity.

3.   EXPERIMENTAL RESULTS
For the results at 50 N normal load, additives lead to lower friction coefficients for all velocity conditions as shown in Fig. 2. However in both speed conditions, 1% and 2% MoS_2 additive had lower friction coefficients than 5% MoS_2 added lubricant. Lowest friction coefficient is obtained with 2% MoS_2 additive for 0,4 m/s sliding velocity. In general MoS_2 additive in the lubricant leaded to lower friction coefficient values. Especially for 0,8 m/s sliding velocity friction coefficient value of 0,03 is obtained. The friction coefficient results obtained in this study, gives an idea about the effect of additives to the lubricants frictional characteristics but it cannot directly determine the effect of additive on the efficiency of a gear pair. Therefore, there is a need for an experimental set-up to monitor this effect on gearboxes.

4.   DESIGN of AN APPARATUS
The purpose is to design a test rig that can measure instantaneous power loss while the system is running by measuring input and output power as shown in Fig. 3. A wattmeter (1) shall be connected to the asynchronous electric motor in order to measure the power value at the input. The input and output torques will be measured by two torque transducers. One (2) will be located between the electric motor and the gearbox, the other (4) will be between the output of the gearbox and the input of the centrifugal pump. Thus, only losses in the gearbox will be obtained, and losses in the centrifugal pump and water line will not be allowed to affect the data. In order to examine the effect of the lubricant on efficiency, viscosity and thermal absorption of the lubricant, will also be measured.

5.   CONCLUSION
MoS2 additive improved frictional characteristics of the lubricant. However high additive rate can have a negative effect on frictional behavior of lubricant. Thus determining the amount of additive has a significant importance. By selecting the reference gear oil, it is aimed to use various additives and determine the amount of additives. The effect of the additives in the lubricant, on gear efficiency will be investigated on the test apparatus.

183
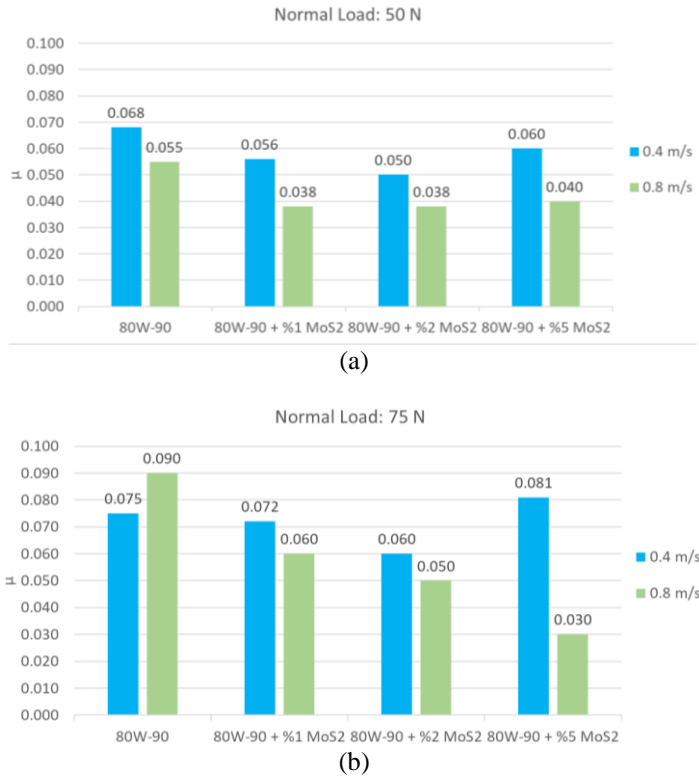
Figure 2. *Experimental results: (a) 50 N normal load conditions, (b) 75 N normal load conditions.*
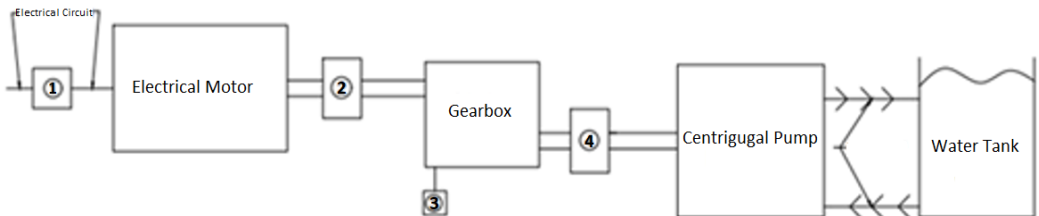
Figure 3. *Test rig design for gearbox efficiency.*

REFERENCES

[1] Petry-Johnson T. T., Kahraman A., Anderson N. E., Chase D. R., (2008) "An Experimental Investigation of Spur Gear Efficiency" *Journal of Mechanical Design*, Vol. 130.

[2] Lynwander, P. (1983) "Gear Drive Systems Design and Application" ISBN: 0-8247-1896-8.

[3] Höhn, B.R., Michaelis, K., Hinterstoisser M. (2009) "Optimization of Gearbox Efficiency" Goriva I Maziva 48 (4): 441-480

[4] Michaelis, K., Höhn, B.R., Doleschel, A. (2009) "Lubricant Influence on Gear Efficiency" Proc.of the ASME 2009 Int. Design Eng. Tech. Conf. & Comp. and Inf. in Eng. Conf.

[5] Lansdown, A. R. (2006). "Molybdenum Disulphide Lubrication" Elsevier

A Monte Carlo simulation: To Determination the Buildup Factor

Faez WAHEED[1]*, Hakan AKYILDIRIM[1] , Kadir GÜNOĞLU[2], İskender AKKURT[1]

[1] Suleyman Demirel University, Isparta-Turkey-2019
[2] Isparta Applied Science University, Isparta- Turkey-2019
*faez_radiophysics@yahoo.com

ABSTRACT

Radiation is important because of the wide variety of application of nuclear physics. In order to perform quality parameter of the measuring system, buildup factor has been calculated by Monte Carlo code program for three life radioactive gamma-ray sources to the wide variety source-detector distance. The minimum value of buildup factor and maximum have been obtained with two conditions, within and without Lead collimators. The results shown that the value of the buildup factor decreases with increasing source-detector distance & with increasing Gamma-ray energy. The results also revealed that there is no scattering photon the value of buildup factor in general at a low level when the geometry structure is built well. While for bad geometry, the detector measured intensity is greater than that described by the main linear attenuation coefficient equation because the scattered photons will be detected as well.

KEYWORDS: Gamma ray, Monte Carlo code program , Buildup factor , Collimator.

6. INTRODUCTION.

NaI(Tl) scintillation detectors are used widely for years since they are low-cost systems, resistant to thermal effects and weather conditions (especially when compared to HPGe detectors) and do not need extra cooling devices. FLUKA is one of the most preferred simulation codes. It uses the Monte Carlo technique to simulate transportation and interaction with the matter of about 60 particles over a wide energy range with high accuracy. FLUKA is used in a wide variety of fields of researches from high energy physics experiments to radiation detector development. FLUKA code uses the well-known Combinatorial Geometry (CG) package to create very complex geometries even a magnetic or an electric field is present [1-5].

7. MATERIALS AND METHODS

7.1. The FLUKA simulations

The simulation of the NaI(Tl) detector by FLUKA code should be modeled with the best possible accuracy because of variations of the detector crystal and surrounding materials dimension influence the photon detection efficiency [6].

7.2. The geometry setting:

The geometry of FLUKA simulation exactly to the practical measurement properties, the physical volume, the mother volume, and sensitive volume were implemented in the word accordingly using (FLUKA 2011.2 x 7, July 2019), routines, as described in FLUKA user manual [1], the description of interaction of incident particle, is important during preparing the input file [7], Figure 1. Illustrate practical geometry put side and pack shielding and covered all by lead shielding to illumination background, Figure 2. Illustrate the geometry structure related to selection configuration..
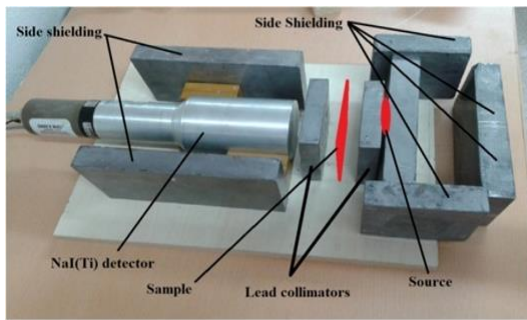
Figure 1. *The experimental configuration.*
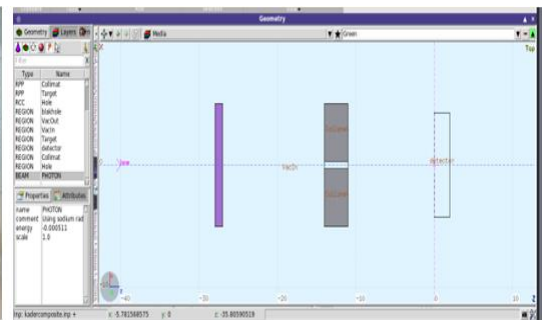
Figure 2. *FLUKA simulation geometry*

8.   RESULTS

The energy absorption buildup factor of the NaI(Tl) detector was obtained using gamma-ray energy emitted by the 137Cs life point radioactive sealed source. The results have been obtained as a function of source-detector distance &energy. there is a great variety of analytical function that is used to describe the energy absorption buildup factor depended on the gamma-ray energy and source-detector distance. It can be seen that the line is the description with the correlation coefficient between the buildup factor energy absorption value and variation source-detector distanc.
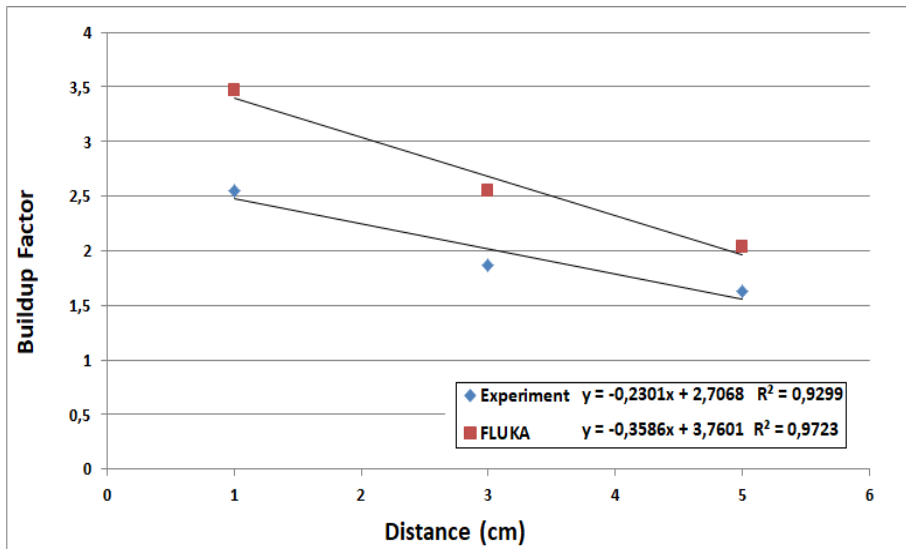
Figure 3. *Buildup Factor as a function of Energy & Distance*

9.   CONCLUSIONS

The FLUKA is a powerful tool for estimating the energy buildup factor of the NaI detector, the applicability of this method depends on the reality input file of the source, geometry, detector. In this study, Energy absorption Buildup factor parameter has been determined experimentally for the 3" x 3" NaI(Tl) scintillation detectors. The impact of source-detector distance to the energy absorption buildup factor was also investigated. It was found from this work that the energy buildup factor depends on source-detector distance, it can be concluded that the variation of buildup factor as a function of the distance.

186

REFFERENCE.

[1]. Ferrari, A., Sala, P. R., Fasso, A., & Ranft, J. (2005). FLUKA: A multi-particle transport code (Program version 2005) (No. INFN-TC-05-11).

[2]. Böhlen, T. T., Cerutti, F., Chin, M. P. W., Fassò, A., Ferrari, A., Ortega, P. G., ... & Vlachoudis, V. (2014). The FLUKA code: developments and challenges for high Energy and medical applications. Nuclear data sheets, 120, 211-214.

[3]. Akkurt, I., Günoğlu, K., Çelik, A., Karakas, M., S ., 2013 . Determination of Gamma Ray Attenuation Coefficients of AL-4% Cu/B4c Metal Matrix Composites at 662, 1173,and 1332 KeV.Bulletin of Materials Science August 2014, Volume 37, Issue 5, pp 1175-1179 First online: 20 September 2014.

[4]. Tekin, H. O. (2016). MCNP-X Monte Carlo code application for mass attenuation coefficients of concrete at different energies by modeling 3×3 inch NaI (Tl) detector and comparison with XCOM and Monte Carlo data. Science and Technology of Nuclear Installations, 2016.

[5]. Tsouflanidis, N., 1983. Measurement and detection of radiation. Mc Graw-Hill, New York.

[6]. Salgado, C. M., Brandão, L. E. B., Schirru, R., Pereira, C. M. D. N. A., & Conti, C. D. C. (2012). Validation of a NaI (Tl) detector's model developed with MCNP-X code. Progress in Nuclear Energy, 59, 19-25.

[7]. Joel, G. S. C., Maurice, N. M., Jilbert, N. M. E., Ousmanou, M., & David, S. (2018). Monte Carlo method for gamma spectrometry based on GEANT4 toolkit: Efficiency calibration of BE6530 detector. Journal of environmental radioactivity, 189, 109-119.

187

Determination of Different Parameters of an Optical Switch Structure with a Metallic Mirror

Fatima BRIK[1*], Abderaouf Fares[1] , Fahima Fares[2] and Kaddour Saouchi[1]
[1]Laboratory of LERCA, University BMA, Department of Electronic, Annaba, Algeria
[2]University Bachir Al Ibrahimi, Department of Electronic, Bourj Bou Arrierig ,Algeria
*Fatimabrik4@gmail.com

ABSTRACT

The objective of this work is to minimize thermal effects in a switch based on a waveguide and Bragg mirror. We propose to replace the Bragg reflector of the optical switch with a metallic mirror which simultaneously serves as a thermostat, and the thickness can be chosen to ensure the rigidity of the device as well as good heat dissipation. This solution has been studied in the case of Fabry-Perot resonators, a thin Bragg mirror can be maintained between the active medium and the metal substrate to ensure the optical optimization of the device. The use of materials of high thermal conductivity is good determinative of heat dissipation. The silver would be the suitable material, since it admits good heat dissipation (value of the refractive index (n = 0.39+i 9.48) at the wavelength λ=0.889μm and its thermal conductivity is $k = 427W. \, m^{-1}K^{-1}$. We use this material to produce our metallic mirror. The performed simulation has optimized the thickness of the guide to obtain the desired characteristics (high reflection coefficient and good contrast).

KEYWORDS- *Switch, thermal effect, Bragg reflector.*

1. INTRODUCTION

The first step towards the processing of all optical information is the realization of the optical components such as: couplers, modulators, filters and switches.The first switches were based on silicon [1-2], were non radiative recombination was contributed to thermal effects. III-V semiconductors (direct gap) are the materials of choice for the realization of these devices [3]. However the experimental study of such a device made of a GaAs film with a grating coupler, and a Bragg mirror as a back reflector has shown that large magnitude thermal effects are present [3-4]. The aim of this work is therefore the optimization of this structure for all optical switching and to improve the performance of the structure; we proposed to replace the Bragg reflector by a metal mirror.

2. THE PROPOSED STRUCTURE

The study of a switch based on a GaAs waveguide has not allowed observing fast switching [4], however the structure seems to be interesting for conditions of minimization of thermal effect. The optical switch is made of an epitaxial film of GaAs, called the active layer, with thickness e_G , on a Bragg reflector made on a periodic stack of layers (31 layers for the whole stack). Light coupling is performed by a diffraction grating etched on the device. The optical properties of this structure have been studied, in the linear regime, both experimentally [3] and modelled [4-5]. To minimize the thermal effect, we propose to replace the Bragg reflector with a metal mirror, serving simultaneously as a thermostat, and whose thickness can be chosen to ensure the rigidity of the device as well as a good heat evacuation, and this by using the substrate report technique [4-6]. The component is technologically feasible according to the current state of the art. The technique of report substrate is an indispensable step for the realization of the metal rear mirror, because these can be carried out only after the epitaxial [4-60]. To ensure a good heat evacuation, the SLID (Solid Liquid Inter-Diffusion) braze allows to obtain solid, homogeneous and stress-free reports over several square centimeters [4-7].

3.   SIMULATION RESULTS

Initially, simulation made it possible to optimize the thickness of the guide and consequently the pitch of grating coupler in order to obtain the desired characteristics (a high reflection coefficient and a good contrast). The use of materials with good high thermal conductivity is crucial for heat removal, Silver, would be the suitable material, since it admits good heat dissipation (value of refractive index (n = 0. 39+i 9.48) at wavelength λ=0.889μm and its thermal conductivity is k = 427(W. m^{-1}K^{-1}).

3.1. Effect of the layer thickness

For a depth of modulation h=0.21μm, we study the evolution of the coefficient of reflexion with the thickness of the guide.
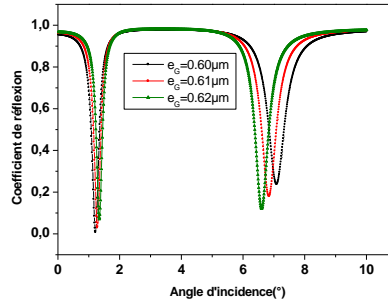
Figure 18. *Variation of the coefficient of reflection of different values of the guide thickness.*

Figure 1, represents the coefficient of reflection for the various values thickness of the guide. According to the simulation results obtained, it has been noted that the thickness of the guide influences the position of resonance and also at the minimum and the maximum of the coefficient of reflexion.

3.2. Effect of modulation depth

Figure 2, represents the coefficient of reflection for a thickness of the guide e_G = 0.60μm and for various values depth of modulation.
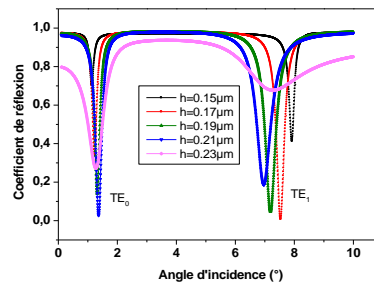
Figure 2. *Reflection coefficient variation of different modulation depth values for the thickness guide of 0.6μm.*

The depth of modulation influences the contrast and the width with middle height. From these results, we can deduce the best compromise: the thickness guide-depth of modulation.

3.3. Spectral response for the optimized metal structure

189

The coefficient of reflection of the compromise found for the structure having of such characteristics is that deferred on the figure 3, it was obtained from ($e_G = 0.60\mu m$; h = 0.21μm; n = 0.39+i 9.48 and K = 4.27W.cm^{-1}.K^{-1}).
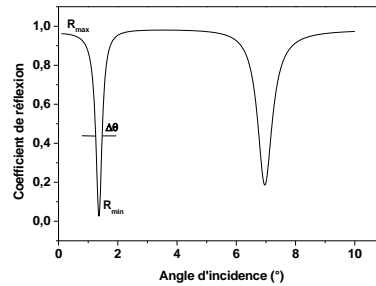
Figure 3. *Reflection coefficient variation of different modulation depth values for the thickness guide of 0.6µm*

According to Figure 3, it can be calculated that:
1.   The coefficient of reflexion Rmax = 0.95, Rmin=0.02.
2.   The width with middle height is $\Delta\theta$ =0.22°.

The use of the metal mirror, gives a slightly weaker reflectivity and a nearly identical to mid-height, width like a Bragg reflector, therefore the thermal effect has reduced.

4.   CONCLUSION

The improvement of the thermal evacuation of our structure requires the use of a metal mirror which has a high thermal resistance, and thus a good thermal stability, ensuring a better operation of the switch.The substrate transfer technique presented allows the sample to be transferred with good homogeneity to a new substrate thanks to the metal solder seal. We have optimized the geometric and physical parameters of such a metallic structure.

REFERENCES
[1] F.Pardo, H.Chelli, A.Koster, N.Paraire, S.Laval, "Experimental and theoretical study of ultrafast optical switching using guided mode excitation in silicon on sapphire", IEEE, Jour. Q.E. 23, 545 1987.
[2] N.Paraire, P.Dansas, A.Koster, M. Rousseau and S.Laval, " Sensitivity and switching contrast optimization in an optical signal processing waveguide structure Optical information technology" ed. S.D. Smith and R.E. Neal (Berlin Springer) 1991.
[3] K.Koynov , N.Paraire, F.Bertrand, R EL Bermil and P Danas " Design and   investigation of semiconductor waveguide structures with grating couplers used as all-optical switches", Journal of optics A: Pure And Applied Optics, 3,26, 2001.
[4] F.Brik, N.Paraire, T.Bouchemat, M.Bouchemt, "Minimization of thermal effects in a waveguide structure optical switch", Applied Physics B Lasers and Optics, vol. 97, pp. 841-847, 2009.
[5] W.S. Capinski, M. Cardona, D.S. Katzer, H.J. Maris, K. Ploog, T. Ruf, "Thermal conductivity of GaAs/AlAs superlattices", Physica B 263-264 530-532, 1999.
[6] N. Cicek Bezir, A.Evcin, H.Okçu, R.Kayali, M.Kaleli, D.A.Aldemir, Effect of Layer Thickness on I-V characteristics of GaInP Nanofibers Fabricated by Electospinning on n-Si Substrates, ICCESEN 2017
[7] A. kudaykulov, A. Zhumadillayeva, Numerical Simulation of temperature Disribution field in beam bulk in the simultaneous presence of heat insaluation, heat flux and heat exchange. Acta Physica Polonica

Experimental Study on Pore Structure Characteristics of the Ultra-Deep Carbonate Gas Reservoir in Northwestern Sichuan

Yuxiang Zhang[1]*, Shenglai Yang[1], Jiajun Li[1], Bei Wang[2], Jianxun Chen[1], Yu Huang[1], and Cheng Zou[1]

[1]*State Key Laboratory of Oil and Gas Resources and Exploration in China University of Petroleum-Beijing, Beijing, China*

[2]*China Petroleum and Natural Gas Co., Ltd. Southwest Oil and Gas Field Branch Exploration and Development Research Institute, Chengdu, China*
*2018312074@student.cup.edu.cn

ABSTRACT

In this paper, the cores of carbonate gas reservoirs are divided into four types by pore and permeability parameters: matrix type, crack type, corroded hole type and crack＆corroded hole type. The pore structure characteristics of the four types of cores are analyzed by high pressure mercury intrusion test. The influence of cracks and corroded holes on the pore structure parameters of ultra-deep carbonate gas reservoirs is summarized.

KEYWORDS – Ultra-deep carbonate, gas reservoir, pore structure, capillary pressure curve.

1. INTRODUCTION

The core appearance description and basic physical property analysis show that the carbonate reservoirs of the Qixia Formation in the Pishuangshi block mainly develop pore pores, caves and cracks. Various pore structures are combined with each other to enhance heterogeneity and form various types of reservoirs. In order to better study the pore-throat structure characteristics of ultra-deep carbonate gas reservoirs, four different types of cores were selected and high-pressure mercury intrusion tests were carried out[1-3], namely matrix type, crack type, corroded hole type and crack＆corroded hole type.

For deep carbonate gas reservoirs, the fractures and karst caves are developed, and the reservoir heterogeneity is strong. It is difficult to study the multi-type pore structure and reservoir permeability by using the porosity classification method[4-6]. Therefore, take whether or not there are karst caves and cracks as the classification criteria, based on the observation of the core surface, the core is initially classified and subjected to high pressure mercury injection experiments. Then, different types of capillary force curves are put together, and the curve characteristics are compared to determine the accuracy of the preliminary classification results.

2. BASIC PHYSICAL PROPERTY ANALYSIS of CORE

Porosity and permeability tests were carried out on 14 rock samples. The porosity test method was used to directly determine the pore volume of rock samples under the low confining pressure of Boyle's law. The permeability was the gas surveying permeability measured by nitrogen at normal temperature and pressure. The porosity and permeability of 14 rock samples are plotted as shown in Fig. 1. The ordinate represents the permeability, the ordinate is the logarithmic coordinate, and the abscissa represents the porosity.

As shown in the figure, the porosity and permeability of the matrix type are small, and the permeability of the crack type is higher than the matrix type due to the development of micro-cracks inside the cores; the porosity of the corroded hole type and the crack＆corroded hole type is higher than the porosity of matrix type and crack type due to the development of the corroded holes inside the cores. Further analysis, the presence of cracks increases the permeability of the rock sample, and the presence of the corroded hole increases the porosity of the rock sample.

191
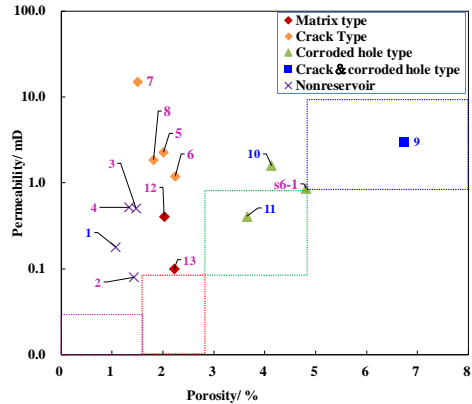
Figure 1. *Core basic physical property test results.*

3. CLASSIFICATION ANALYSIS USING HIGH PRESSURE MERCURY INTRUSION TEST

3.1. Different rock samples

Four rock samples were selected from 14 rock samples representing four different rock types, as shown in Figure 2.

(a) No.3: Matrix type   (b) No.7 Crack type

(c) No.S6-1: Corroded hole type   (d) No.9 Crack&corroded hole type
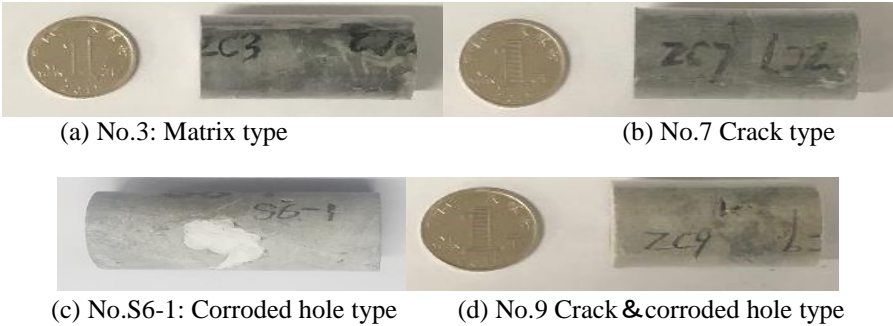
Figure 2. *4 representative rock samples*

3.2. Test results and analysis
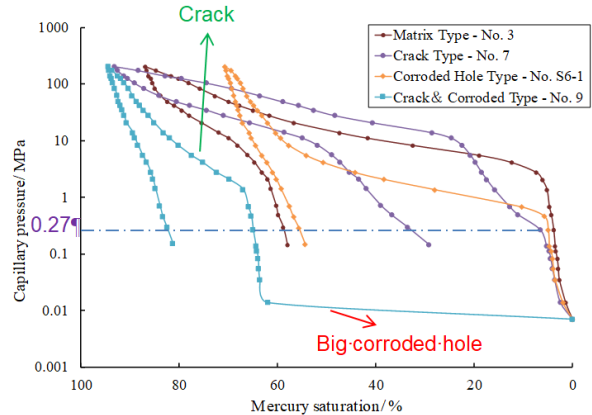
Figure 3. *Comparison of capillary pressure curves of 4 types of rock samples*

192

Table 1. *Summary table of the characteristic values of the capillary pressure curve of 4 types of rock samples*

Pore structure type	Sample number	Permeability K/ mD	Porosity φ/ %	Maximum mercury saturation Smax/ %	Final residual mercury saturation Sr/ %	Ejection efficiency Ew/ %	Drainage pressure Pcd/ MPa	Mercury saturation median pressure Pc50/ MPa
Matrix	3	0.51	1.47	86.9	58	33.3	2.743	15.7
Crack	7	15.16	1.73	93.1	29.1	68.7	0.266	30.4
Corroded hole	S6-1	0.87	4.81	70.6	54.3	23.1	0.466	4
Crack & Corroded hole	9	3.03	6.74	94.4	81.2	54	0.007	0.007

Poremaster PM-33-13 mercury injection apparatus made by Quantachrome company in U.S.A is used in the test whose test pressure ranges from 0.0034MPa to 200MPa. That is, the measured throat radius ranges from 213.7μm to 0.004μm respectively. Figure 3 is the comparison of capillary pressure curves of 4 representative rock samples, and the curve parameters in Table 1 can be calculated from Figure 3. As shown in Figure 3, the middle section of the matrix type curve is not smooth which means the pore size distribution of matrix type is not concentrated. The undistributed pores cause high mercury saturation median pressure. The capillary pressure curve of the crack type showed a large amount of mercury at the 0.27 MPa, corresponding to the existence of a 1.6μm-wide-crack which resulted in the low drainage pressure and high ejection efficiency compared to the matrix type. The mercury saturation median pressure of the crack type is still high because there are also undistributed pores in the crack type. The middle section of the corroded hole type is more smooth and lower than the matrix type and the crack type which means that the pores of the corroded hole type are more distributed and bigger than the matrix type and the crack type. The big corroded hole leads to the low mercury saturation median pressure and the low drainage pressure. The capillary pressure curve of crack & corroded holes exhibits distinct dual-porosity characteristics, with straight segments representing large corroded holes and the latter half representing mercury entering the crack. In the middle of the two sections, the capillary pressure rises rapidly which means the width of the crack is much smaller than the size of the corroded holes.

4.   CONCLUSION

Based on the basic physical property analysis and the high pressure mercury intrusion tests, the effects of cracks and corroded holes on the physical properties of the rock and reservoir characteristics can be summarized. The presence of cracks increases the permeability of the rock sample and increase the ejection efficiency which represents the recovery of the non-wet phase. The presence of corroded holes increases the size of the pore which leads to the large storage capacity of carbonate. Thus, the drainage pressure and mercury saturation median pressure of the rock sample with corroded holes are reduced. Finally the capillary force curve of crack & corroded hole type rock samples can reflect the characteristics of double-porosity media of cracks and corroded holes.

REFERENCES

[1] Ding, J., et al. Dynamic threshold pressure gradient in tight gas reservoir and its influence on well productivity. International Conference on Computational and Experimental Science and

Engineering (ICCESEN 2017), 4-8 October, 2017 Antalya-Turkey. DOI: 10.1007/s12517-018-4129-7

[2] Song, L., et al. Research on reservoir characteristics of Chang7 tight oil based on nano-CT. International Conference on Computational and Experimental Science and Engineering (ICCESEN 2017), 4-8 October, 2017 Antalya-Turkey. DOI: https://doi.org/10.1007/s12517-018-3842-6

[3] Cheng, Z., et al. (2019). A comprehensive characterization of North China tight sandstone using micro-CT, SEM imaging, and mercury intrusion. Arabian Journal of Geosciences 12(13). DOI: https://doi.org/10.1007/s12517-019-4568-9

[4] Wang, L., et al. (2016). Mineral and pore structure characteristics of gas shale in Longmaxi formation: a case study of Jiaoshiba gas field in the southern Sichuan Basin, China. Arabian Journal of Geosciences 9(19). DOI: DOI 10.1007/s12517-016-2763-5

[5] Zhang, L., et al. Research on sensitivity damage of naturally fractured carbonate reservoirs in Ordos Basin. International Conference on Computational and Experimental Science and Engineering (ICCESEN 2017), 4-8 October, 2017 Antalya-Turkey. DOI: https://doi.org/10.1007/s12517-019-4805-2

[6] Zhao, T., et al. Pore structure and adsorption behavior of shale gas reservoir with influence of maturity: a case study of Lower Silurian Longmaxi formation in China. International Conference on Computational and Experimental Science and Engineering (ICCESEN 2017), 4-8 October, 2017 Antalya-Turkey. DOI: https://doi.org/10.1007/s12517-018-3673-5

Numerical Simulation of Water-Induced Fracture in Low Permeability Reservoirs

Chenxu Yang[*], Linsong Cheng , Hui Li , Xulin Du, Junjie Shi and Ming Ma
China University of Petroleum, Beijing 102249, China
*522216016@qq.com

ABSTRACT

Water injection is the main way to supplement formation energy and improve oil recovery in low permeability reservoirs. However, pressure in the near-wellbore zone of the injection well increases gradually due to the poor injection capacity, which will induce the expansion of fractures in the reservoir. The injected water may quickly break through the production well due to the improper placement of the well, reducing the swept volume, increasing the watercut rapidly, and then resulting in a decrease in the recovery of the reservoir. By coupling the embedded discrete fracture model (EDFM) and fracturing pressure, a numerical simulation model for two-dimensional fracture propagation is established by the method of discrete fracture reconstruction. The research shows that fractures will constantly extend to the direction of maximum principal stress when the internal pressure is greater than the fracturing pressure with the increment of water injection and bottomhole pressure under the influence of the current stress field. The water flooding seepage characteristics of the reservoir are changed, and it affects the development effect because of the extension of the fractures. Therefore, the influence of dynamic fractures needs to be considered in the oilfield development process.

KEYWORDS - *water-induced fractures, EDFM, numerical simulation, low permeability reservoirs*

1. INTRODUCTION

There are many low permeability reservoirs in China such as AnSai Oilfield in ChangQing and XinMin Oilfield in JiLin where water injection is a common method to supplement energy and enhance the recovery of the reservoir. Microcracks can usually be found in the low permeability reservoirs. However, some signs indicate that fractures can propagate during water injection. Zhao et al. (2017) gave an example of typical well group in AnSai Oilfield [1], the water content curves show that watercut increases rapidly after a short water-free production period in the direction of maximum principal stress while there is a long water-free production period in the direction of minimum principal stress and the watercut increases slowly on the contrary. Fig 1 shows the well location and water content curves in different directions. Wang et al. (2019) confirmed water-induced fractures by using well-testing analysis, pressure and pressure derivative curves show that the inner radius had an increase of 44 meters after a four-year production [2]. At present, the extended finite element method is one of the most commonly used method to simulate dynamic fractures, which is based on fluid-solid coupling [3-4]. Though XFEM usually has an excellent performance in the simulation of hydraulic fracturing, it shows low efficiency when it comes to long period simulation during the whole period of low permeability reservoirs development. So a proper method should be found to simulate water-induced fractures. Fan et al. (2015) used a dynamic permeability model combined with a dynamic fracture model to simulate the opening and closing of the dynamic fracture [5]. It's an ingenious way to simulate dynamic fractures during water injection, but it is restricted to complex situations. In other words, permeability can only change in a pre-setting direction because of the mesh of grids. The embedded discrete fracture model is commonly used in the simulation of complex fracture networks [6-7]. However, it can't deal with the propagation of the fractures. Our work is to establish an efficient method considering

195

water-induced fractures during long-time water flooding based on EDFM by improving the preprocessing algorithm and finally predict the effect of water drive in different directions.
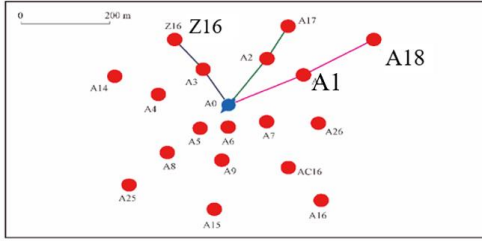
(a) well location
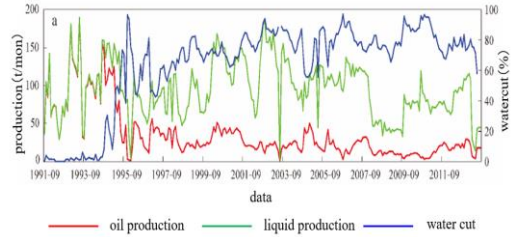
(b) water content curve of A18 well
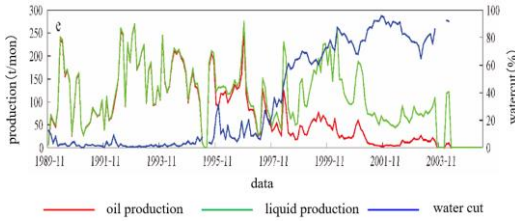
(c) water content curve of Z16 well
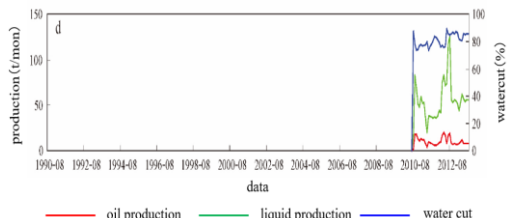
(d) water content curve of A1 well

Figure 19. *Well location and production history curves (Zhao et al. 2017)*
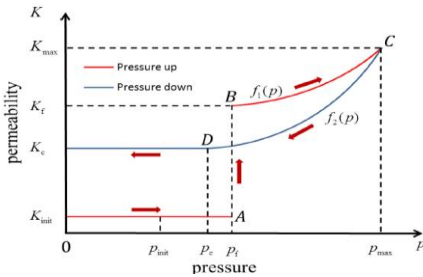
(a) dynamic permeability model
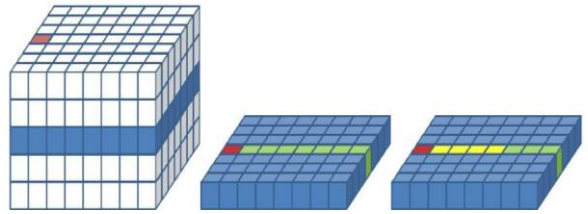
(b) Sketch of the dynamic fracture model

Figure 2. *Dynamic model to simulate water-induced fractures (Fan et al. 2015)*

2. METHOD of SIMULATING DYNAMIC FRACTURES
2.1. Preprocessing Algorithm

Dynamic fracture elements are introduced to simulate the propagation and closure of the water-induced fractures combining with rock failure criterions. If the pressure in the tip of fracture exceeds fracturing pressure, the preprocessing algorithm is recalled to add or change the dynamic fracture elements. The details are: (1) Find fracture tips: Fractures should propagate from fracture tips, so the first thing is to mark all fracture tips. However, fractures are connected to the wells in EDFM, so another thing is to judge if fracture tips belong to injection wells. (2) Add dynamic elements: Once one of the fracture tips meet the failure condition, a dynamic fracture element is connected to the fracture tip. If the fracture propagates for the second time, dynamic fracture element will change to normal fracture element, and another dynamic fracture element is added. (3) Remove virtual elements: A virtual element may appear when a dynamic fracture is connected to the fracture tip. A virtual element can block the transmission between normal fracture elements and dynamic fracture elements. (4) Property matching: After the dynamic preprocessing algorithm

196

is carried out, the property of each fracture elements such as pressure and saturation should be re-correspond.

(a) initial situation   (b) after propagation   (c) simulation resul
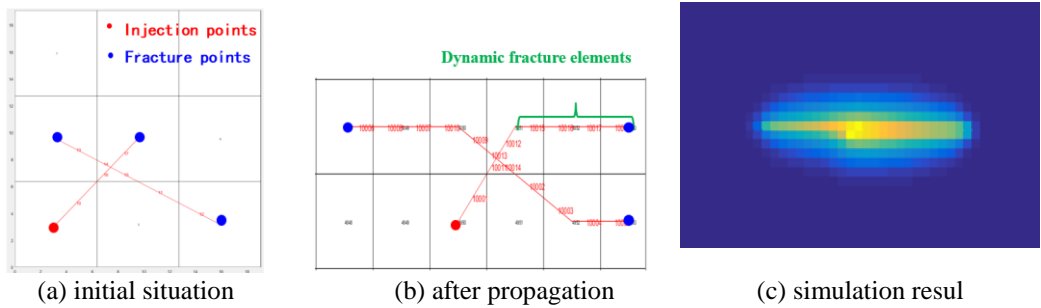
Figure 3. *Pretreatment process of dynamic EDFM model*

2.2. Dynamic EDFM Method

After the dynamic improvement through preprocessing algorithm, dynamic EDFM model is established, the core thought is to add the discrimination part, and recall the dynamic preprocessing algorithm once the fractures are likely to propagate. The framework of the dynamic EDFM model is shown in Fig4.
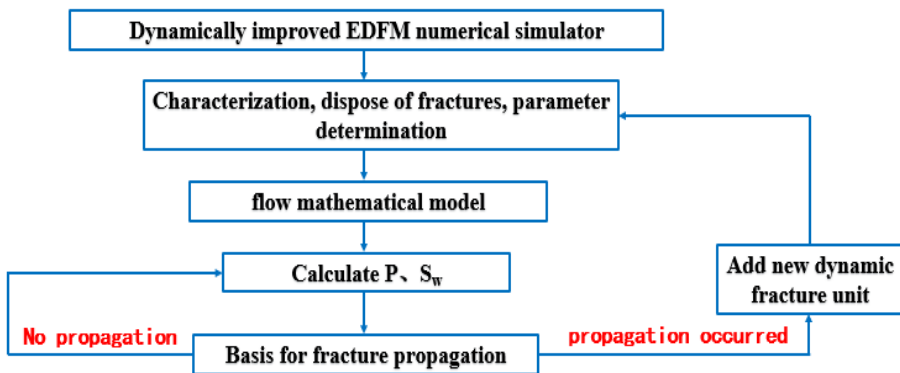
Figure 4. *Pretreatment process of dynamic EDFM model*

2.3. Comparison of EDFM Versus Dynamic EDFM

Fig5 gives a comparison of the pressure field between the EDFM model and dynamic EDFM model which considers the effect of water-induced fractures. Fig6 shows that dynamic fractures significantly influence development effect in different directions because of the in-situ stress and the water content curves have the same law of Fig1.

3. CONCLUSION

(1) Fractures will constantly extend to the direction of maximum principal stress when the internal pressure is greater than the fracturing pressure with the increment of water injection and downhole pressure under the influence of the current stress field.
(2) The dynamic EDFM model is established to simulate the influence of water-induced fractures.
(3) The flow characteristics of the reservoirs during water flooding are changed and they affect the development effect because of the extension of fractures.

197

(a) pressure field simulated by EDFM

(b) pressure field simulated by dynamic EDFM

Figure 5. *Comparison between EDFM model and dynamic EDFM model.*

(a) well location   (b) water content curve of W1

(c) water content curve of W2
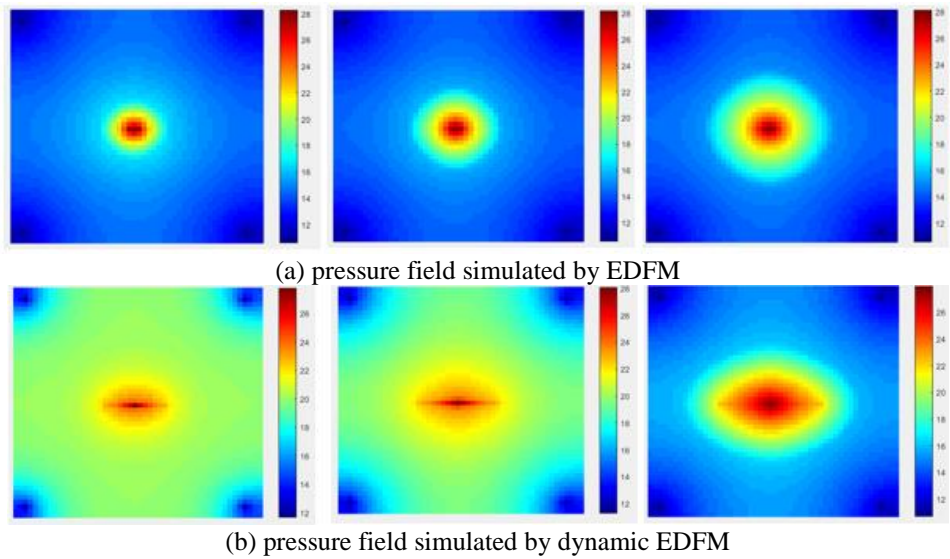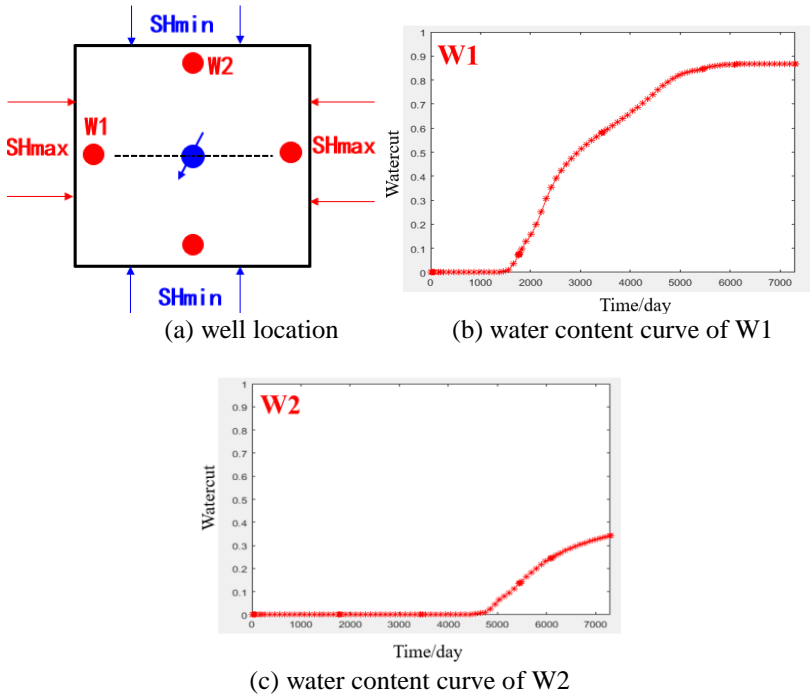
Figure 6. *Comparison between EDFM model and dynamic EDFM model*

REFERENCES

[1] Zhao, X., et al. Characteristics of waterflood induced fracture in low-permeability sandstone reservoirs and its identification methods: A case study from Chang 6 reservoir in W area in

198

Ansai oilfied, Ordos Basin. Oil and Gas Energy 38-6 (2017) 1187-1197. doi:10.11743 /ogg20170620. (in Chinese)

[2] Wang, Y., Cheng, S., et al. A Comprehensive Work Flow To Characterize Waterflood-Induced Fractures by Integrating Real-Time Monitoring, Formation Test, and Dynamic Production Analysis Applied to Changqing Oil Field, China. Society of Petroleum Engineers (2019). doi:10.2118/191370-PA.

[3] Wang, T., Liu, Z., Zeng Q., et al. XFEM modeling of hydraulic fracture in porous rocks with natural fractures. Science China Physics, Mechanics & Astronomy, 60 (2017) : 1-15. http://dx.doi.org/10.1007/s11433-017-9037-3.

[4] Shi, F., Wang, X., Liu, C., et al. An XFEM-based method with reduction technique for modeling hydraulic fracture propagation in formations containing frictional natural fractures. Engineering Fracture Mechanics, 173 (2017) : 64-90. http://dx.doi.org/10.1016/j.engfracmech.2017.01.025.

[5] Fan, T., Wu, S., Zhang, X., et al. A Novel Dynamic Model to Simulate Waterflood Induced Fractures in Low Permeability Reservoirs. Society of Petroleum Engineers (2015). doi:10.2118/176224-MS.

[6] Cao, R., Fang, S., Jia, P., et al. An efficient embedded discrete-fracture model for 2D anisotropic reservoir simulation. Journal of Petroleum Science and Engineering 174 (2018): 115-130. http://dx.doi.org/10.1016/j.petrol.2018.11.004.

[7] Cheng, L., Fang, S., Wu, Y., et al. A hybrid semi-analytical model for production from heterogeneous tight oil reservoirs with fractured horizontal well. Journal of Petroleum Science and Engineering, 157 (2017): 588-603. http://dx.doi.org/10.1016/j.petrol.2017.07.008.

The Range of "Cold Affected Zone" and its Effect on in-situ Stress During Long-Term Water Injection

J.J. Shi[1,2]* (CUPB)

[1] Key Laboratory of Petroleum Engineering of the Ministry of Education, Beijing, China
[2] China University of Petroleum, Beijing, China
*996757751@qq.com

ABSTRACT

Long-term water injection will affect the original temperature distribution of the reservoir because of the temperature of the injected water is often lower than the temperature of the rock. It is necessary to determine the scope of the "cold affected zone" around the injection well and its effect on in-situ stress. In this paper, establishing the corresponding unsteady mass transfer heat transfer mathematical model by analyzing the relationship between material and energy balance in the vertical well injection process. Furthermore, the temperature distribution of the reservoir around the well is obtained. And the vertical well is taken as an example to analyze the influence of the " cold affected zone " on the distribution of in-situ stress. The "cold affected zone" produced by long-term water injection will reduce the in-situ stress. Therefore, it is imperative to define the range of the cold zone and the influencing factors for the subsequent scheme design of water injection and fracturing technology.

KEYWORDS - *Cold affected zone, In-situ stress, Long term water injection.*

1. INTRODUCTION

Replenishing formation energy by water injection is a useful technique in reservoir development. In the long-term water injection development process[1]. The injected water temperature is different from the reservoir temperature. The sensitivity of reservoir physical parameters to temperature requires a precise range of "cold affected zone." After cold water injection, specific additional temperature stress will be generated, which will cause the change of the in-situ stress field. In this paper, aiming at the low temperature zone formed after long-term injection of cold water into the reservoir, a mathematical model considering the thermal convection in the reservoir and the heat conduction with the cap and bottom layer was established and solved, and the range of cold affected zone formed by long-term injection of cold water and its influence on the ground stress were studied.
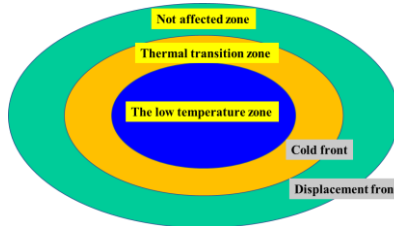
Figure 20. *Temperature distribution after long-term water injection*

200
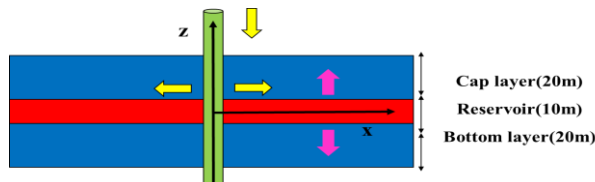
***Figure 2**. Vertical well injection cold fluid model.*

2. MODEL AND PARAMETERS

2.1. Model Assumptions

After the cold fluid is injected into porous media, the heat transfer mode includes direct heat conduction and thermal convection accompanied by the seepage of injected fluid[2]. When the fluid flow velocity in porous media is relatively high, thermal convection plays a significant role. Heat conduction plays a major role in the process of heat transfer with top and bottom impermeable layers. The heat transfer model as shown in Figure 2 is established, and the assumed conditions are as follows:①The reservoir and adjacent layers are homogeneous; ②The fluid flows in one dimension and is incompressible;③The vertical temperature of the reservoir at any horizontal position remains constant; ④Instantaneous thermal equilibrium can be established between the reservoir matrix and fluid(Tm=Tf);⑤The longitudinal flow of fluid in the cap and bottom layer is ignored.

2.2. Mathematical Model and Parameters

According to the above model（Figure 2）, the energy balance equation is established. For reservoir:

$$-v_{inj} \cdot \frac{h}{2} \rho_{inj} \cdot C_{inj} \frac{\partial T_f}{\partial x} + \lambda_m \frac{\partial T_m}{\partial z} = \frac{h}{2} \rho_f C_f \frac{\partial T_f}{\partial \tau}$$

(1)

where, v_{inj}-injection rate; h - reservoir thickness; ρ_{inj} - injection fluid density; C_{inj} -injection fluid specific heat; T_f -reservoir temperature; T_m -cap/bottom rock temperature; λ_m -cap/bottom rock thermal conductivity; ρ_f -reservoir rock density; C_f 为reservoir specific heat, $C_f = \phi C_l + (1-\phi) C_r$, C_l -reservoir fluid specific heat, C_r 为reservoir rock specific heat. τ - time. The first term on the left is the energy change caused by thermal convection, the second term on the left is the heat conduction loss with the cover and bottom layer, and the right term is the cumulative term of energy.

For cap and bottom layer, the equilibrium equation of the incoming and outgoing energies is:

$$\lambda_m \frac{\partial^2 T_m}{\partial z^2} = \rho_m C_m \frac{\partial T_m}{\partial \tau}$$

(2)

where, ρ_m- cap/bottom rock density; C_m -cap/bottom rock density.

Equations (1) and (2) are the established mathematical model of the temperature field. The initial conditions and boundary conditions of the model are given below:

$$\tau = 0, \begin{cases} T_m = T_f = T_{inj}, x = 0 \\ T_m = T_f = T_{ri}, x > 0 \end{cases}$$

(3)

$$x = 0, \quad T_f = T_m = T_{inj}$$

(4)

201

$$x^2 + z^2 \to \infty, \quad T_f = T_m = T_{ri} \tag{5}$$

$$\left(\frac{\partial T_f}{\partial z} + \frac{\lambda_f}{\lambda_m} T_f \right) \Bigg|_{Z=\frac{h}{2}} = \frac{\lambda_f}{\lambda_m} T_m \Bigg|_{Z=\frac{h}{2}} \tag{6}$$

where, T_{inj}-fluid injection temperature, T_{ri}-original formation temperature.

Plane stress problems solve the thermal stress caused by temperature change. The elastic constitutive equation corresponding to radial stress and circumferential stress caused by temperature change is as follows[3]:

$$\sigma_r = \frac{-E}{1-\mu^2} \left(\varepsilon_r + \mu \varepsilon_\theta \right) + \frac{E\alpha\Delta T}{1-\mu} \tag{7}$$

$$\sigma_\theta = \frac{-E}{1-\mu^2} \left(\varepsilon_\theta + \mu \varepsilon_r \right) + \frac{E\alpha\Delta T}{1-\mu} \tag{8}$$

where, σ_r - Radial stress caused by temperature change; σ_θ-Circumferential stress caused by temperature change; E -Young's modulus; μ -Poisson's ratio; ε_r -radial strain; ε_θ -circumferential strain α -thermal expansion coefficient. Define the following four dimensionless variables [4]:

$$x_D = \frac{4\lambda_m \pi R^2}{h^2 \rho_{inj} c_{inj} v_{inj}}, \quad \tau_D = \frac{4\lambda_m}{h^2 \rho_f C_f} \cdot \tau, \quad \lambda = \frac{\rho_f c_f}{\rho_m c_m}, \quad z_D = z \cdot \frac{2}{h} \tag{9}$$

The above mathematical model can be solved as follows:

$$T_m = T_{ri+erfc} \left(\frac{x_D + |z_D| - 1}{2\sqrt{\lambda(\tau_D - x_D)}} \right) \cdot U(\tau_D - x_D) \tag{10}$$

$$T_r = T_{ri+erfc} \left(\frac{x_D}{2\sqrt{\lambda(\tau_D - x_D)}} \right) \cdot U(\tau_D - x_D) \tag{11}$$

$$\sigma_r = \frac{E\alpha}{r^2} \int_a^r \Delta \mathrm{Tr} \, dr - \frac{E}{1-\mu^2} \left[(1+\mu)A - (1-\mu)\frac{B}{r^2} \right] \tag{12}$$

$$\sigma_\theta = -\frac{E\alpha}{r^2} \int_a^r \Delta \mathrm{Tr} \, dr - \frac{E}{1-\mu^2} \left[(1+\mu)A + (1-\mu) + \frac{B}{r^2} \right] + E\alpha\Delta T \tag{13}$$

202

where, $A = -\dfrac{(1+\mu)\alpha}{b^2}\displaystyle\int_a^b \Delta Tr\,dr$, $B = \dfrac{(1+\mu)a^2}{1-\mu}A$, $U(\tau_D - x_D) = \begin{cases} 0,(\tau_D - x_D) \le 0 \\ 1,(\tau_D - x_D) > 0 \end{cases}$

The radial stress and circumferential stress are converted to the stress in orthogonal coordinates by coordinate transformation:

$$\begin{bmatrix} \sigma_x & \sigma_{xy} \\ \sigma_{xy} & \sigma_y \end{bmatrix} = L\begin{bmatrix} \sigma_r & \sigma_{n\theta} \\ \sigma_{r\theta} & \sigma_\theta \end{bmatrix}\mathbf{L}^{\mathrm{T}} \quad \mathbf{L} = \begin{bmatrix} \cos\theta & -\sin\theta \\ \sin\theta & \cos\theta \end{bmatrix}$$

(14)

Table 1 shows the parameters used in this case.

***Table 1.** Parameters used in this case*

Thermal conductivity of Reservoir [W/m/°C]	2.5	Density of fluid [kg /m³]	1000	Poisson ratio	0.25	specific heat capacity of Fluid [J/Kg/°C]	4182	Injection flow rate [m³ /s]	0.002	Coefficient of thermal expansion [1/°C]	3×10⁻⁶
Thermal conductivity of Cap/Bottom layer [W/m/°C]	3	Rock density of Reservoir[kg /m³]	2700	Young modulus [GPa]	20	specific heat capacity of Oil [J/Kg/°C]	2200	Oil saturation[%]	60	borehole radius [m]	0.2
specific heat capacity of Cap/Bottom layer[J/Kg/°C]	800	Rock density of Cap/Bottom layer [kg /m³]	3000	well control radius [m]	100	Original reservoir temperature[°C]	80	Injection temperature（well bottom）[°C]	40	Porosity [%]	20

3.   RESULTS AND DISCUSSION

The temperature distribution along the well diameter after different injection time is shown in Figure 3 and Figure5(a).With the increase of time, the advance speed of the low-temperature zone gradually slows down. Figure 4 shows the longitudinal temperature distribution in half of the reservoir. The temperature distribution in the z-direction at x=5m at different times is shown in Figure 5(b). With the increase of time, the heat exchange between the reservoir and the cap /bottom layer is more. Figure 5(c) shows the effect of the injection rate on radial temperature distribution.
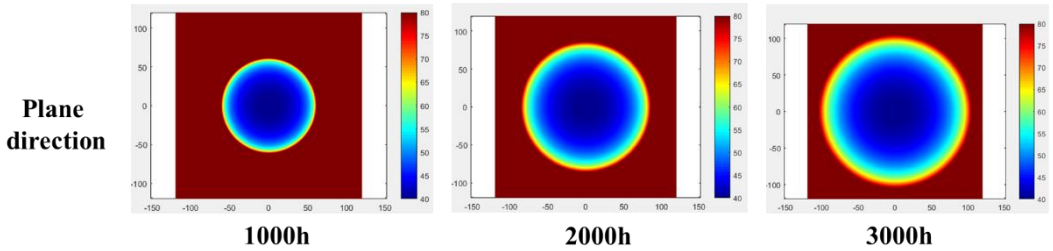
Figure 3. *Temperature distribution in XY plane at different times*
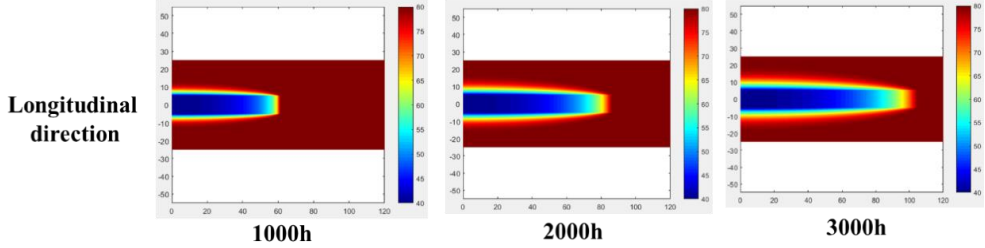
Figure 4. *Temperature distribution in XZ plane at different times*
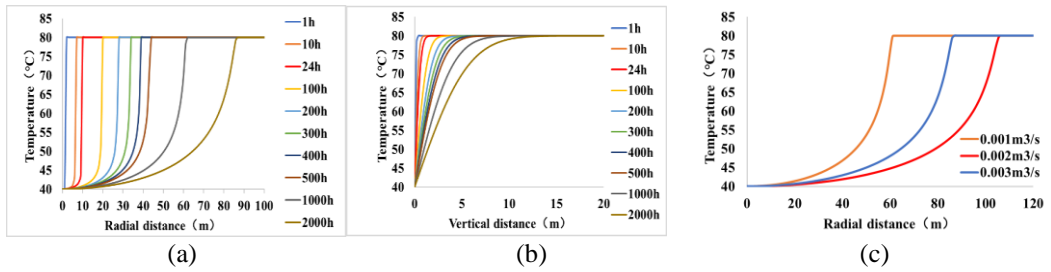
Figure 5. *Radial temperature and vertical temperature change with distance, time , injection rate*

The temperature change and the in-situ stress change are shown in Figure 6,   Maximum reduction of in-situ stress is 3.11MPa in the x-direction and 6.40MPa in the y-direction. The decrease of ground stress in the region with the biggest temperature change is most substantial. The in-situ stress shift will affect the design of the water injection and fracturing process[5].
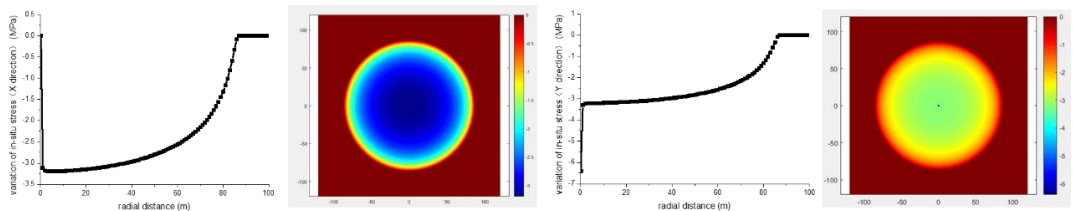
Figure 6. *Variation distribution of in-situ stress in XY plane (2000h)*

4.   CONCLUSION

In this paper, we studied the changes in reservoir temperature and ground stress caused by long-term water injection, and obtained the following findings:

204

(1)The scope of the "cold affected zone" is positively correlated with injection velocity and time.
(2)With the increase of time, the increased rate of "cold affected zone" gradually slows down.
(3)Long-term injection of cold water will cause in-situ stress reduction.

REFERENCES

[1] Mahdi Abbasi.Analytical model for convection-conduction heat transfer during water injection in fractured geothermal reservoirs with variable rock matrix block size, Geothermics,2017(69), 1-14, http://dx.doi.org/10.1016/j.geothermics.2017.04.002.

[2] Sayantan Ganguly, M.S. Mohan Kumar, Analytical solutions for movement of cold water thermal front in a heterogeneous geothermal reservoir, Applied Mathematical Modelling, 2014.2(38), 451-463, http://dx.doi.org/10.1016/j.apm.2013.06.031.

[3] Sun Jin, Deng Jingen, Yu Baohua, et al. Effect of reservoir temperature on in-situ stresses during water injection development[J]. China Offshore Oil and gas,2016,28(4):100-106. DOI:10.11935/j.issn.1673-1506.2016.04.016.

[4] Lauwerier H A.The transport of heat in an oil layer caused by the injection of hot fluid ［J］. Applied Scientific Research 1955(5) : 145-150. http://dx.doi.org/10.1007/BF03184614.

[5] Chao Zhou, Xiaodong Wu, Hui Li, Zongxiao Ren, Yinan Xin. Influence of In-situ Stress Distribution on Selection of Fracturing Fluid Backflow Technology. ICCESEN-2015(347) DOI: 10.12693/APhysPolA.130.347.

Investigation of Mechanical Properties of Hybrid Composites Produced with Glass Prepreg and Basalt Fiber

Yalçın BOZTOPRAK*, Remzi YILDIZ, Eda YENİAY, Ömer Faruk SEZGİN
Marmara University, Technology Faculty Metallurgical and Materials Engineering Department, Istanbul, Turkey
*yboztoprak@marmara.edu.tr

ABSTRACT

Glass reinforced epoxy based composite structural parts offer design, machining, performance and cost advantages according to metals. Advantages of glass reinforced materials include fracture toughness, impact resistance, strength-to-weight ratio, high corrosion resistance and improved fatigue properties are important for practical applications.

Recently, basalt fibers have been used as a good natural material instead of glass fibers. Because basalt is derived from rocks and it has been experimentally proven that basalt fibers are harmless to human health and bioinert. Basalt fibers are produced as short and continuous filaments by melting basalt rocks at high temperatures. By improving the process technology of basalt fibers, the new generation basalt fibers show positive performance characteristics such as sound insulation properties, excellent heat resistance (better than glass), chemical resistance and low water absorption.

In this study, hybrid composite materials were produced by using glass prepreg and basalt fiber with hot press method at suitable temperature and pressure and mechanical properties of the obtained composite materials were investigated. Improvement in mechanical properties was observed with basalt fiber reinforcement. Therefore, it is recommended to use in applications requiring higher mechanical properties.

KEYWORDS - *Basalt fiber, Glass prepreg, Hybrid composites*

1. INTRODUCTION

Today, composite materials are used in many different fields. The composite materials comprise three components: the matrix, the reinforcement material and the interface (between the matrix and the reinforcement). Flexible materials that act as load carriers in composites and are at least 20 times the length of their cross-section are generally referred to as fibers [1]. Various fiber types such as glass fiber, carbon fiber, basalt fiber are used as reinforcement material. Glass fiber is the most widely used fiber type in fiber reinforced polymers. Glass fiber is composed of Silica (SiO_2-Silicon dioxide), except for other metal oxides in small pieces. The glass prepreg is obtained by impregnation with the resin layer of the glass fiber. Prepregs are easy to stack, cut to desired sizes and easy to shape.

Natural fibers appear to be low cost, lightweight and apparently environmentally superior than synthetic fibers used in composites. [2] Natural fiber composites are likely to be environmentally superior to synthetic fiber composites in most cases for the following reasons: (1) natural fiber production has a lower environmental impact than synthetic fiber production; (2) natural fiber composites have higher fiber content for equivalent performance, further reducing the contaminant base polymer content; (3) light-weight natural fiber composites, especially in automotive applications, increase fuel efficiency and reduce emissions during the use of the component; and (4) incineration of natural fibers at the end of its life, resulting in recovered energy and carbon credits.[3]

Basalt is a magmatic rock which is abundant in the world. Basalt fiber is a unique product derived from basalt rock, a natural substance from frozen lava-derived volcanic rocks. In terms of

mechanical and physical properties, basalt fiber has attracted attention due to its high elastic modulus, high strength, corrosion resistance, high temperature resistance and light weight.

Glass prepreg impregnated with epoxy resin and basalt fiber were used in this study. Epoxy resin prepreg was preferred because of its high mechanical properties, good environmental strength, chemical resistance and high toughness[4]. Hybrid composite materials were produced by using glass prepreg and basalt fiber with hot press method at suitable temperature and pressure. Mechanical properties of the obtained composite materials were investigated.

2. EXPERIMENTAL SECTION
2.1. Materials

The glass prepregs used in this study were obtained from Kordsa and the basalt fiber was supplied from Spinteks.

A prepreg consists of a combination of a matrix (or resin) and fiber reinforcement. Prepregs are fiber-reinforced resins that harden under heat and pressure to form extremely strong but light components. Prepregs are produced to provide fast production and time saving. Only the prepreg resin was used as the resin by the manufacturer to obtain a strong bond between the prepreg and the fiber. Composite sheets are produced as layer by layer as follows.

G0= 14 layer glass prepreg
G1= 3 GP + 1B + 3 GP
G2= 2GP + 1B + 2GP + 1B + 2GP
G3= 2GP + 1B + 2GP + 1B + 2GP + 1B + 2GP + 1B + 2GP
G4= 3GP + 1B + 3GP + 1B + 3GP

GP = Glass Prepreg
B   = Basalt Fiber

2.2. Preparation of The Composite Samples

Firstly, prepregs and basalt fabrics were cut to dimensions of 300x300 mm. Subsequently, the surface of the flat molds was coated with a polymeric film to easily remove the samples from the mold. The cut prepreg and basalt fibers were placed layer by layer on the flat mold and the materials between the 2 molds were held in a hot press under 7 bar pressure up to 140°C. Then, at 140°C, the composite plate was kept to cure at the time specified in Table 1. Subsequently, the composite plate were removed from the mold after the mold temperature was lowered by cooling with water. These procedures were performed for each sample. The produced samples were placed in a post-cure oven at 155 degrees and kept for 2 hours. After this process, the composite plates were cut with CNC router to obtain test samples according to standards.

Table 1. Process parameters

Sample	Holding Time in Hot Press (minute)	Press Pressure (bar)	Thickness of The Obtained Samples (mm)
G_0	30	7	4.5
G1	60	7	2.5
G2	60	7	2.8
G3	60	7	5.9
G4	60	7	4.25

Composite plates were subjected to NDT test (ultrasonic test) to determine whether adhesion was good and whether delamination occurred between the layers . According to NDT test, there was no delamination between glass prepreg and basalt fibers.

2.3. Wear Morphology

Wear testing is used to determine the abrasion resistance of materials used where it is in contact with other materials or where it is subject to friction. Wear test was carried out in Pin On Disk Tester in according to ASTM G-99 standard at a weight load of 250 g at a speed of 72 rpm. The wear resistance is calculated from the weight value lost by the wear of the material placed in a rotating device.

2.4. Impact Test

Impact test was performed using Izod unnotched test method to determine the impact strength of the composite samples. Unnotched specimens were tested using Zwick B5113.30 Izod Impact Device with a 21.6 J Izod impact hammer according to the ISO 180 standard.

2.5. 3 Point Bending Test

Flexural strength of the composite laminates were determined via 3-point bending tests with a test speed of 2 mm/min on a Zwick Z010 universal tensile device. Tests were performed according to EN ISO 14125 standart. Specimen sizes were 80x10x4 and 5 samples were used for each group. Span to depth ratio was hold as 16:1.

2.6. Hardness Test

Hardness test is a type of mechanical test which is done to learn the hardness of the materials and to have information about the machinability. Hardness was performed according to "Shore D" test method.

3. RESULTS AND DISCUSSION

According to the test results, it is understood that all samples have good wear resistance. When we compare the G2 and G4 samples with the same amount of basalt fibers (Table 2), it was seen that the wear resistance increased with increasing prepreg amount.

Table 2. *Weight loss of samples*

Sample	Weight Loss (gr)
G0	0.00027 ± 0.00007
G1	0.00017 ± 0.00007
G2	0.00027 ± 0.00017
G3	0.00020 ± 0.0001
G4	0.00023 ± 0.00007

When G1 and G3 are compared in Table 3. the impact strength increases with the increase in the number of basalt fibers. When G2 and G4 samples are compared. it is seen that impact strength decreases with increasing prepreg number. It is seen that the impact resistance increases with the addition of basalt fiber but the impact strength decreases as the number of glass prepreg increases in parallel.

Table 3. *Results of Izod impact test*

Sample	Izod Impact Strength (kJ/m^2)
G0	312.85
G1	92.74

G2	324.78
G3	239.84
G4	45.23

When we compare G2 and G4 samples. it was found that the flexural strength of G2 sample was higher than G4 sample. It was determined that the flexural strength decreased with increasing amount of prepreg. This is thought to be due to the fact that glass fiber reduces the flexibility of the material. It is understood from the Table 4. that the effect of basalt fiber on bending strength is less.

Table 4. *Flexural strength values of samples*

	Elasticity Modulus (MPa)	Flexural Strength (MPa)
G0	41020	1160
G1	19980	201.6
G2	46100	1280
G3	21540	920.8
G4	16700	219

Table 5. shows the increase in hardness with the addition of basalt fiber. Basalt fiber increased the hardness of the samples because it has a hard structure. When G2 and G4 were compared. it was observed that as the amount of prepreg increased. hardness decreased. It was observed that the hardness remained in a certain range in all basalt fiber reinforced samples.

Table 5. *Table of hardness values of samples*

	Hardness
G0	73.27 ± 1.27
G1	73.44 ± 2.93
G2	73.77 ± 1.23
G3	73.77 ± 1.77
G4	73.55 ± 1.55

4. CONCLUSION

Glass prepreg and basalt fiber reinforced epoxy composite sheets were produced successfully by hot press method. It is seen in the literature that the mechanical properties of basalt fibers are good. It has been observed that glass prepregs have increased wear resistance. impact strength and hardness by reinforcing with basalt fiber. This result is due to the fact that basalt fiber is a hard material and has good mechanical properties. Basalt fiber reinforced glass prepreg epoxy composites can be used easily where friction and wear are involved. Basalt fiber reinforcement will reduce the cost of composite materials. Basalt fiber reinforced composites can be used in various fields such as aerospace. automotive and transportation [5].

REFERENCES
[1] Kalpakjian S.. Steven R Schmid.. Manufacturing Engineering and Technology. International edition. 4th Ed. Prentice Hall. Inc. 2001. ISBN 0-13-017440-8.

209

[2] Vive D.. Garima M.. Kyong Y.. Soo-Jin P.. David H.; A Short Review On Basalt Fiber Reinforced Polymer Composites. Composites Part B: Engineering. 73. 166-180. 2015. https://doi.org/10.1016/j.compositesb.2014.12.011

[3] S.VJoshi. L.TDrzal. A.KMohanty. S.Arora. "Are Natural Fiber Composites Environmentally Superior To Glass Fiber Reinforced Composites?". Composites Part A: Applied Science and Manufacturing. 35. 3. 371-376. 2004. https://doi.org/10.1016/j.compositesa.2003.09.016

[4] Jamshaid H. Mishra R. A Green Material From Rock: Basalt Fiber–A Review. The Journal of The Textile Institute. 1-15. 2015. https://doi.org/10.1080/00405000.2015.1071940

[5] Qiang L.. Montgomery T. S.. Richard S. P.. Anne-Marie M.. Investigation of Basalt Fiber Composite Mechanical Properties for Applications in Trasnportation. Polymer Composites. 27. 1. 41-48. 2005. https://doi.org/10.1002/pc.20162

Oxidation-Reduction Reactions Of Quinone And Hydroquinone In The Alkaline Condition On The Graphite Electrodes

S.S. Yegeubayeva[*], S.T. Almagambetova, S.S Konyratbekova, A.Zh. Altmyshbayeva
Almaty Technological University, Almaty, Kazakhstan,
Satbayev University, Almaty, Kazakhstan
* salamat.egeubaeva@mail.ru

ABSTRACT

By method of reading of cyclic potentiodynamic polarizing curves the oxidation-reduction reactions in the system of $C_6H_4O_2$-$C_6H_4(OH)_2$, at the different concentration of quinone and hydroquinone on the graphite electrodes are investigated.It was shown, that in alkaline solutions at cyclic polarization the processes of oxidation and reduction of quinone and hydroquinone took place reversible.

KEYWORDS: *potential, quinine, hydroquinone, a graphite electrode, a polarizing curve.*

1. INTRODUCTION

Earlier in works [1,2], possibility of formation of electromotive power in «red-ox» system "quinine-hydroquinone" on graphite electrodes at a difference of temperatures in electrode spaces was shown. In our works [3] was shown, that in base of processes of formation of electromotive forces at the difference of temperatures in the electrode spaces represented the reversible oxidation-reduction electrochemical reactions which took place on the graphite electrodes.

2. EXPERIMENTAL

Potentiodynamic polarizing measurements were spent on the potentiostat "Autolab PGSTAT 302 N" (fig.1 a), in the temperature-controlled three-electrode cell (fig.1 b).

a)   b)
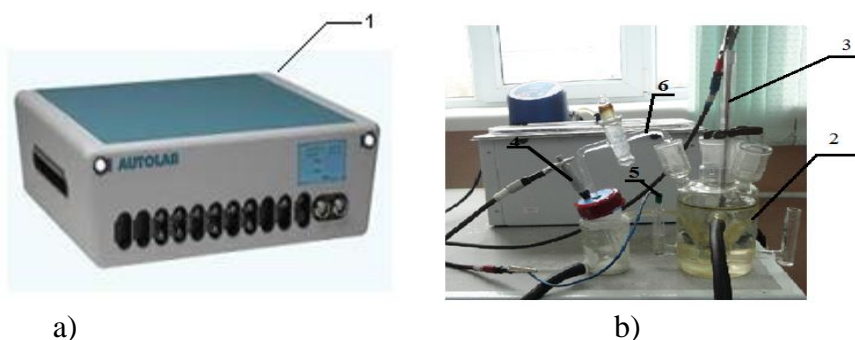
Figure1. *a) – General view of installation for carrying out of potentiodynamic polarizing curves : 1-potentiostat "AutolabPGSTAT 302 N"; b) - electrochemical cell; 3- graphite electrodes; 4- reference electrode; 5- auxiliary platinum electrode; 6- electrolytic bridge.*

The measurements were carried with respect to silver chloride reference electrode in a saturated solution KCl (E=+203 mV). Platinum plate was used as a counter electrode.
A typical example of reversible redox reactions were the reactions in the system "quinone-hydroquinone" which were studied in detail by Muller Baumberger [4].

$$C_6H_4O_2 + 2H^+ + 2\bar{e} \rightleftarrows C_6H_4(OH)_2 \quad E^0 = 0{,}69 \text{ V} \tag{1}$$

211

Standard potential of the system was equal "plus" 0,69V and was described by the equation

$$E_{xr} = E_0 + 2,303 \frac{RT}{2F} lg \frac{a_x a_{H+}^2}{a_{\Gamma X}} \tag{2}$$

According to [5,6] for the polarographic reduction of quinones two waves were observed, and on the basis of this phenomena a number of authors have suggested the formation of radical anions in the reduction of many quinones, for example, duroquinone, α-oksifenazon, N-methyl-α-oksifenazin and a number of other.

Study of polarographic reduction of quinones which carried out by Vavzonek [4] showed that indeed a result of joining of an electron to a molecule of quinone the ion-radical - semiquinone was appeared, according to the reaction:
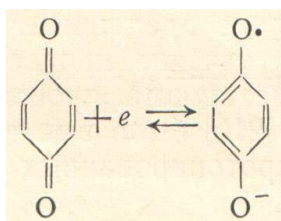
This radical, joined by a second electron, formed a dianion
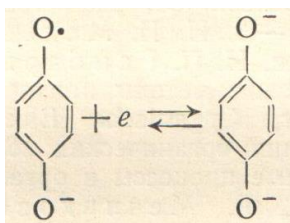
which adjoining the protons from the the solvent formed a hydroquinone
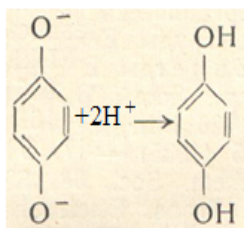
In the work, the polarization curves of the redox system $C_6H_4O_2$-$C_6H_4 (OH)_2$ were recorded in an aqueous solution of sodium hydroxide with a concentration of 100g /l in the potentiodynamic regime.

3. RESULTS AND DISCUSSION

As it was clear from the polarogram curves (Fig. 2, curve 1), in a background solution of sodium hydroxide except currents of oxygen release any other waves were not observed. In Figure 2 (curves 2-4) the anodic polarization curves at different concentrations of hydroquinone were

212

presented. As can be seen from a polarogram curve, at the potential sweep in anode direction two weakly expressed successive waves of oxidation in the field of potentials "minus" 200 mV and "plus" 1000 mV were revealed, and after that oxygen was allocated at the potential "plus" 1500 mV by reaction (4):

$$2OH^- - 2e \rightarrow 1/2O_2 + H_2O \tag{4}$$

V=100mV/s; t=25^{0}C: 1) background-100 g/l NaOH; 2) hydroquinone, g/l:2-1.0; 3-5.0; 4-10.0.
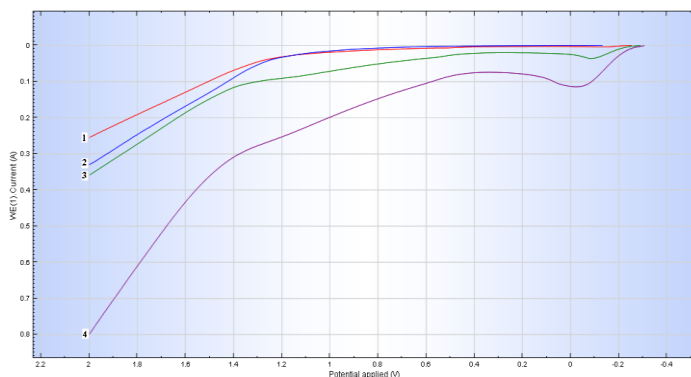
Figure 2*. The anodic polarization curves of the graphite electrode in a solution of sodium hydroxide at various concentrations of hydroquinone*

At the displacement from the equilibrium potential in the cathodic direction on the polarogram curves (Figure 3.4) there were two hardly detectable waves of the quinone reduction to hydroquinone, flowing through the reverse reaction (1), and then a current of hydrogen allocation on reaction (5) was observed :

$$2H_2O + 2e \rightarrow H_2 + 2OH^- \tag{5}$$
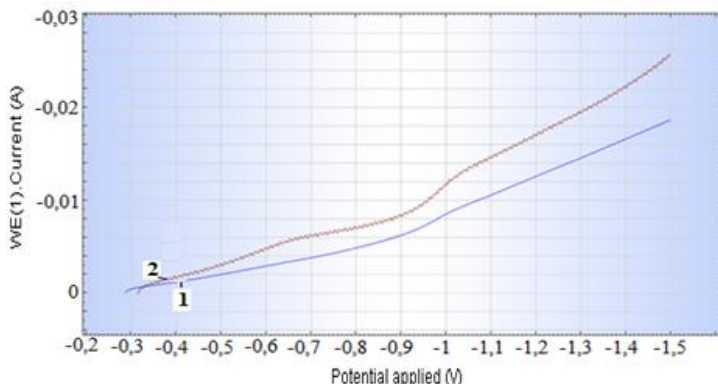
Fiure 3. *Cathodic polarization curves of the graphite electrode in an alkaline solution at different concentrations of the quinone*

V= 100 mV/s; t=25 ºC;a background -100 g/l NaOH+quinone,g/l:1-1.0; 2-5.0

For a more detailed understanding of the mechanism of the reversible reaction were obtained the cyclic potentiodynamic polarization curves of the graphite electrode in the presence of 5 g/l solution of hydroquinone in 100 g/l of sodium hydroxide.

As seen in Figure 5, at the anode-cathode cyclic polarization in the anodic direction were observed two current maximum oxidation of hydroquinone to quinone in the potential "minus" 200 mV and "plus" 1000 mV, then the current of oxygen evolution at the potential "plus" 1500mV took place.

At displacement of potential to the opposite cathode direction were also observed two waves of reduction of quinone to hydroquinone in the field of potentials "plus" 400 mV and "minus" 200 mV, then there was an allocation of hydrogen on the graphite electrode.
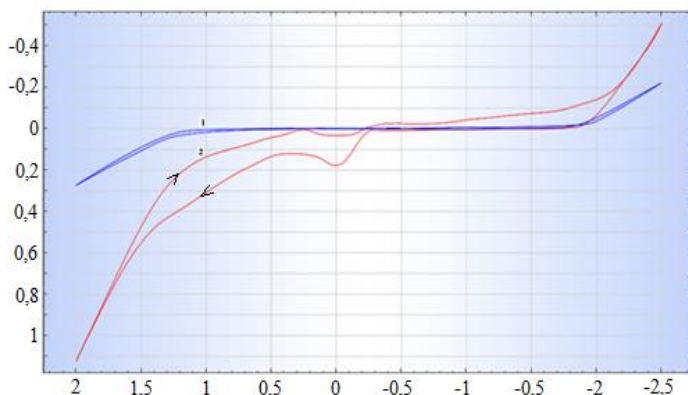
Figure 4. *Anode - cathode cyclic potentiodynamic polarization curve of a graphite electrode in a solution of sodium hydroxide in the presence of hydroquinone*

V=100mV/s, t=25^{0}C; 1) a background -100 g/l NaOH; 2) a background -100 g/l NaOH +5 g/l hydroquinone;

At polarogram curves (Figure 5) obtained by the polarization of the graphite electrode in the anode - cathode direction in the presence in the electrolyte of 5 g/l quinone and 5 g/l of hydroquinone two oxidation wave of reduction of $C_6H_4(OH)_2$ to $C_6H_4O_2$ and current of allocation of oxygen were observed. At displacement of the electrode potential in the cathodic direction two successive waves of reduction of quinone to hydroquinone and hydrogen evolution also were observed.
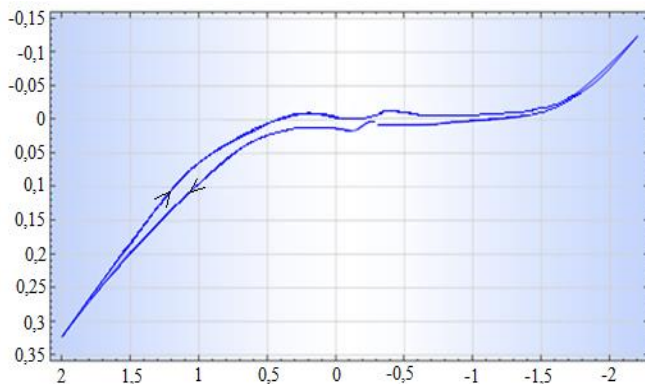
Figure 5. *The anode - cathode cyclic potentiodynamic polarization curve of a graphite electrode in a solution of sodium hydroxide in the presence of the quinone and hydroquinone*

214

V=100mV/s, t=25^{0}C; a background – 100 g/l NaOH+ 5 g/l hydroquinone+5g/l quinone;

4. CONCLUSION

Thus, we investigated for the first time the processes of oxidation and reduction in the system "quinone-hydroquinone" in an alkaline solution in the graphite electrode by record method of potentiodynamic cyclic polarization curves and we revealed that the balance $C_6H_4O_2$-$C_6H_4(OH)_2$ was reversible.

REFERENCES
[1]. S.S. Yegeubayeva, A.B. Bayeshov, , A.K. Bayeshova. *Acta Physica Polonica A*. Vol. 128 (2015). No. 2-B. p. 455.
[2]. A.B. Bayeshov, S.S. Yegeubayeva, A.K. Bayeshova, M.Zh. Zhurinov. *Journal of Chemical Sciences* 2014. V. 12(2). – P. 456
[3]. A.B. Bayeshov, S.S. Yegeubayeva, A.K. Bayeshova. *Reports of NAN RK*, 2013, **3**, p.   28.
[4]. A.P.Tomilov, S.G.Mairanovskii, M.Ya.Phioshin, V.A.Smirnov. *M., Chemistry*, 1968,   p. 592.
[5]. L. Michaelis, M. Schubert, R. Reber, J. Kuck, S. Granick. *J. Am. Chem. Soc*., **60**, 1938, p.1678.
[6]. L.Mikhaelis. *ONTI*, 1936, p.130.

Investigation of the Producibility of Monolithic Insulation Plate Using Raw Perlite

Metin DAVRAZ[1*], Ali Ekrem AKDAĞ[2], Murat KORU[3], Yunus Emre DELİKANLI[4], Şemsettin KILINÇARSLAN[5], Mehmet ÇABUK[6]

[1]*Isparta University of Applied Science, Senirkent Vocational School, Dep. of Construction, Isparta-TURKEY*
[2]*Isparta University of Applied Science, Technology Faculty, Dept. of Mechanical Engineering, Isparta-TURKEY*
[3]*Isparta University of Applied Science, Vocational School of Technical Science, Isparta-TURKEY*
[4]*Isparta University of Applied Science, Senirkent Vocational School, Dep. of Machinery, Isparta-TURKEY*
[5]*Suleyman Demirel University, Engineering Faculty, Dept. of Civil Engineering, Isparta-TURKEY*
[6]*Isparta University of Applied Science, Senirkent Vocational School, Dep. of Chemistry, Isparta-TURKEY*
*metindavraz@isparta.edu.tr

ABSTRACT

The production of monolithic thermal insulation plate (monoper) was investigated by using raw perlite in this study. In the research, raw perlite powder as filling material and also sodium hydroxide and foaming additive were used as chemical additive. Changes in the properties of monoper samples with increasing foam additive ratio were investigated. Pore sizes of monoper samples were examined by SEM microscope and thermal conductivity coefficients were measured by heat flow meter method. Density changes were determined according to sintering temperature and time of monoper samples, and expansion coefficients were calculated. In addition, the mathematical relationship between apparent density and thermal conductivity coefficient for monoper samples has been demonstrated.

KEYWORDS – Raw perlite, Monolithic Insulation Plate, Thermal Conductivity

1. INTRODUCTION

Nowadays, energy production technologies are continuously updated and alternative methods are developed to meet the increasing energy consumption in industry and housing. Perlite is a naturally occurring dense glassy volcanic rock and it expands at suitable temperature and gains a porous structure. When perlite in special forms having a certain grain size is heated at temperatures in the range of 900 - 1100°C, it expands about 7-25 times of its original volume. Its structure contains 2-6% crystal water. Also, Perlite is not dissolved in water and is not decayed. It is chemically inert in many environments [1].

Thermal conductivity coefficient (λ) of a "thermal insulation material" should be less than 0.065 W/mK according to ISO and CEN standards [2]. When the thermal conductivity coefficient of the insulation material decreases, its resistance to heat transfers increases [3].

2. MATERIAL AND METHODS

In this study, the production of monolithic - thermal insulation material using raw perlite was investigated. For this purpose, the production of monolithic and ultra-lightweight perlite sheets (monoper), raw perlite as the main material, sodium hydroxide as the melting material and foaming agent (FA) were used. Raw perlite (RP) form Ankara region (in Turkey) was used in the study.

The components of monoper samples were given in Table 1. 25 M NaOH solutions (SH) were used in all samples and 2% foaming agent (FA) of the mass of the mixture was added to the NaOH solution. The prepared mixtures were pressed in a 30 mm diameter steel cylinder mold and dried in a microwave oven until constant mass. The dried samples were sintered in a 25 L ash furnace at 850°C for 10 minutes.

Table 1. *The component ratios of monoper samples.*

Sample	% RP	% FA	% SH
1	80	0.00	20.00
2	79.5	0.50	20.00
3	79	1.00	20.00
4	78.5	1.50	20.00
5	78	2.00	20.00

The masses of the expanded monoper samples after sintering were weighed with 1/100 g precision scales and their volumes were determined.

The 40 mm cube (3 pieces) for compressive strength (σ_{10}) test, and 60 mm diameter and 25 mm thickness cylinder samples for thermal conductivity measurement were prepared from sintered samples. The compressive strength of the samples in accordance with TS EN 826 standard at 10% strain and their thermal conductivity in accordance with TS EN 12667 standard was determined [4, 5]. Thermal conductivity measurements were performed with Fox 50 device according to heat flow meter method at SDU DEYMAM. In addition, SEM analysis of the optimum monoper sample was carried out at Innovative Technologies Research Center of Suleyman Demirel University (SDU YETEM).

3. RESULTS

Primarily, the samples were exposed to 850°C for 10 min to determine optimum %RP and, %FA ratios. After the sintering, samples were cooled to room temperature (cooling rate of 5 °C/min). The volumes of the monoper samples obtained at this stage were determined and their apparent densities were calculated. All of the results obtained from the experiments are given in Table 2.

Table 2. *Mechanical, Physical and Thermal test results*

Sample	m (g)	V (cm³)	D (kg/m³)	□ (kPa)	□ (mW/mK)
1	16.68	19.41	859	1635	136
2	16.51	46.26	357	895	83
3	16.42	54.27	303	713	69
4	16.47	69.49	237	584	63
5	16.28	85.32	191	510	52

As shown in Figure 4, density of the monoper samples sintered at 20% SH ratio and 850°C, decreased with increasing FA ratio. According to the results in Figure 1, the optimum FA ratio is 2%.

217
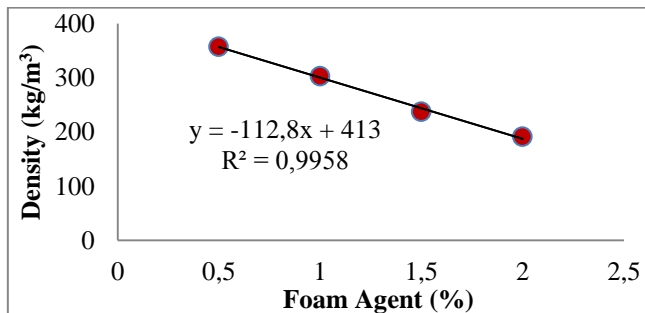
Figure 1. *Change of density according to FA ratio (850 ℃ and 20% SH)*

Cubic samples with 40x40x40 mm dimensions were prepared by cutting from the monoper samples having the most suitable parameters. The average compressive strengths of 3 samples were correlated with their density and the results were given in Figure 2.
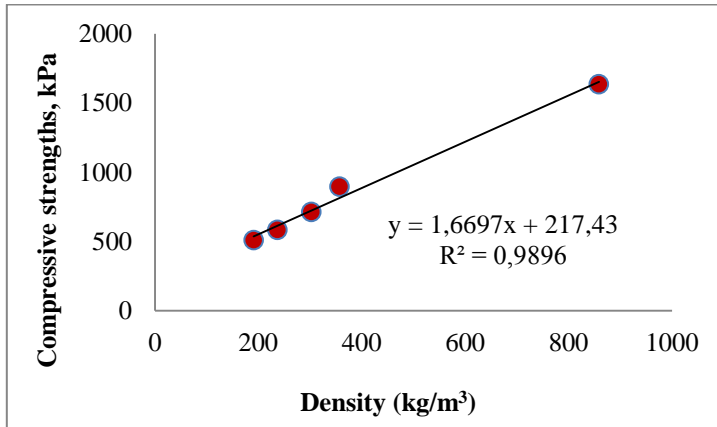
Figure 2. *Density-compressive strength relationship for monoper samples.*

According to the Figure 2, there was a linear relationship between density-compressive strength in monoper samples (R^2 = 0.989). In addition, the changes in the density-dependent thermal conductivity coefficients of the monoper samples were examined in Figure 3. Similar to the density-compressive strength relationship, there was a similar relationship between density and thermal conductivity. As the density of monoper samples increased, thermal conductivity coefficients increased linearly.
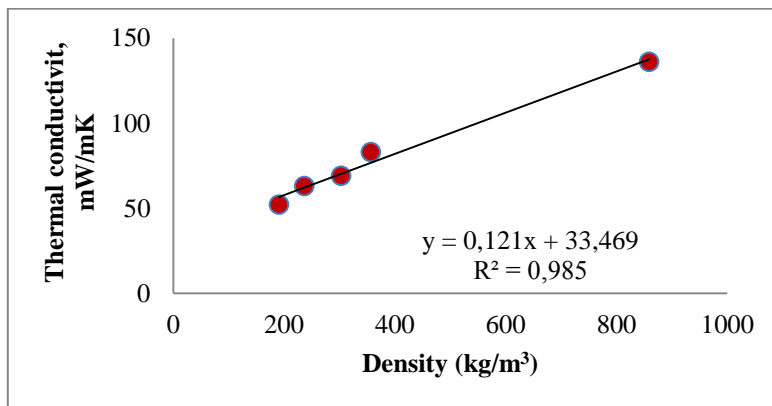
Figure 3. *Density-thermal conductivity relationship for monoper samples.*

In addition, pore structures, sizes and cell wall thicknesses were examined in SEM images of the sample1 at different magnifications (Figure 4). As shown in SEM image at 150x magnification that the pore distribution was homogeneous and has a closed pore structure.

4. CONCLUSION

In this study, the Producibility of a monolithic thermal insulation plate from raw perlite with lightweight, sufficient strength and low thermal conductivity properties was investigated.

218
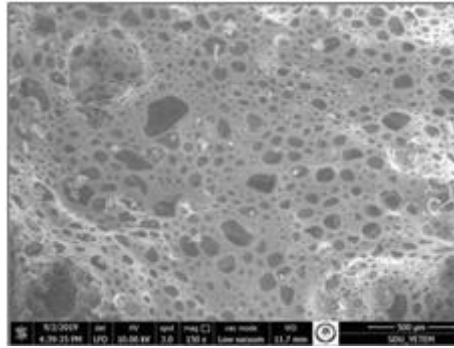
Figure 4. *SEM images at 150x magnification of Monoper sample*

When the results of the study were evaluated,

-Optimum monoper sample sintered at 850°C for 10 min has a density of 191 kg/m^3, compressive strength of 510 kPa and thermal conductivity was 52 mW/mK.

- Improvements were observed in the samples as the foam agent ratio increased.

- It was been found that there is a high correlation between foam agent ratio and density, compressive strength and thermal conductivity.

ACKNOWLEDGEMENTS

REFERENCES

[1] M. Davraz, Ş. Kılınçarslan, The Effect of Plasters with Perlite Aggregate to the Energy Saving in Buildings. 2nd International Davraz Congress, Isparta, Turkey, 2014.

[2] G. Wypych, Functional Fillers: Chemical Composition, Morphology, Performance, Application, Chemtec Publishing, p. 48, Toronto, Canada, 2018.

[3] TS 825, 2013, Thermal Insulation Requirements for Buildings, Turkish Standard Institute, Ankara, Turkey.

[4] TS EN 826, Thermal Insulating Products for Building Applications-Determination of Compression Behaviour, Turkish Standard Institute, Ankara, Turkey, 2013.

[5] TS EN 12667, Thermal Performance of Building Materials And Products - Determination of Thermal Resistance by means of Guarded Hot Plate and Heat Flow Meter Methods - Products of High and Medium Thermal Resistance, Turkish Standard Institute, Ankara, Turkey, 2003.

[6] M. Kelly, Glass mineral fibre and rockwool, Solas Further Education and Trainin Authority, Rev. 2.0, Dublin, 2014.

[7] D. Shuting, , The Properties Research of The Rockwool Used for Energy Saving, New Building Materials, 5, China, 2013

[8] K. Arı, Production of Wall Bricks with Infills and Comparison of Thermal Conductivity Coefficients. Department of Civil Engineering, Institute of Natural and Applied Sciences, University of Çukurova, Adana, PhD Thesis, 2009.

[9] T. Uygunoğlu, , A. Keçebaş, LCC Analysis for Energy-Saving in Residential Buildings with Different Types of Construction Masonry Blocks. Energy and Buildings, 43(9), 2077-2085, 2011.

[10] M.S. Al-Homoud, Performance Characteristics and Practical Applications of Common Building Thermal Insulation Materials. Building and Environment 40, p. 353–366 , 2005.

The Effect of Different Parameters on Strength Properties of Glulam Timber Beams

Şemsettin KILINÇARSLAN*, Yasemin ŞİMŞEK TÜRKER
Suleyman Demirel University, Department of Civil Engineering, Isparta,Turkey
*semsettinkilincarslan@sdu.edu.tr

ABSTRACT

Wood is one of the oldest known materials of construction, and it is the only naturally renewable building material. For many centuries, wood has been a natural material of construction for homes and other buildings, for bridges and waterfront structures, for poles and pole frame, for electric and telephone lines, and many other uses. Modern technology has increased the durability of wood, spurred a host of new wood products such as plywood, particleboard, and other panel products, largely removed the laminations of size and from through the glue-laminating process, and developed improved fastness with greater load-carrying capacity.

Glued laminated timber (glulam) is an engineered wood product made from sawn lumber lamina glued together in horizontal layers. Glulam timber is one of the most commonly used materials for civil engineering applications. It is well-known that glulam beams performance depends on its length, strength, width and different properties of the laminae. In addition, glulam beam properties are influenced by various characteristics such as wood species, moisture, number of layers, type of glue. For a composite material, one of the main advantages is that its properties can be designed. In this study, the effect of different number of layer, laminate thickness and wood type on mechanical strengths of glulam timber beams was investigated. As a result, it was found that these parameters had an effect on modulus of elasticity. The design of glulam beams used in the construction of wooden structures is of importance in terms of sustainability, economy and environment.

KEYWORDS – *Glulam, Beam, Modulus of Elasticty*

1. INTRODUCTION

Wood is one of the oldest building materials used by mankind [1-3]. As a building material, wood continues to be a building material that is used in many areas thanks to its superior physical and mechanical properties such as its durability despite its lightness in its structure, its warm grip in cool winter and easy to be dismantled and assembled [4]. Disadvantages of wood material such as durability and very variable properties can be reduced by lamination technology (Glulam = glue laminated timber, laminated timber) [1]. The properties of wood material vary according to their directions, they may have natural defects and some unwanted formations occur during growth. Therefore, it is very difficult to predict the behaviour of wooden elements under different loads [5]. These natural defects and formations can be reduced by the use of elements such as glued laminated timber (Glulam). Glulam is especially used as a structural element in the construction of wooden structures [6].

Glued laminated timber began to be used in the late 1800s [7,8]. This materials largely were used during and after World War II [7-9]. When synthetic resins suitable for outdoor or indoor use began to be used, casein glue was most commonly used until the 1970s. There is an increase in the use of glued laminated timber in both buildings and bridges. Structures that are not applicable using only sawn timber have proved practical and successful in using glued laminated timber [7]. Structural composite timber is used in lieu of timber in various applications and manufacture of other engineered wood products, such as prefabricated wood I-beams, to take advantage of the engineering design values higher than those of sawn timber [10]. Laminated timber has been used for many years as a structural element in the construction of structures. Glulam elements are

220

generally produced in timber with a thickness of 19-50 mm and a length of 1.5-5 m. In glulams, joining is made with finger jointing in the longitudinal direction. The timber used is glued parallel to each other [11]. Glulam material has some superior properties compared to normal timber. The first of these superior properties is high strength. The material to be laminated can be selected carefully. For this reason, the glulam material to be produced can be produced in perfect and desired size. One of the most important issues is that existing defects cause less damage to the material produced and are distributed along the length of the produced element. With this production, the effects of the defects are minimized and give higher values than the rupture modulus values of the sawn timber evenly. Wood materials with different strength classes are used in layers that will be exposed to high stress. Low quality wood type is used in beam elements and inner layers while high quality wood type is used in the pull axis. The second superior feature of glulam material is that it produces materials with high moment of inertia. With the destruction of our forests today, it is very difficult to obtain long sawn timber. Therefore, being able to produce materials of the desired size is among the superior properties of glulam material. The third superior feature of laminated timber is that it can provide longer passage of clarity. For example, high-span (500 ft length) arched roof constructions are made with the use of glulam materials. The fourth superior feature of glulam material is the ability to prevent deformation and control. The fifth feature is that it can be produced in various cross-sectional sizes. The sixth superior property of the laminated material is its high fire resistance. In addition, the cost of this material is lower than the cost of materials used in steel and reinforced concrete structures [7].

Mohammad et all. (2011) [12] , In their study titled ''Bending Strength Properties of Glued Laminated Timber from Selected Malaysian Hardwood Timber'', they aimed to evaluate the flexural resistance behaviour of glulam produced using wood species belonging to different resistance groups. In this study, bending strength behaviour of glulam produced from selected Malaysian tropical timber was investigated. Before glulam production, all timber was visually rated for durability properties according to MS 1714: 2003. The lumber used was dried to the required moisture content (8 to 15%). Phenol Resorcinol Formaldehyde (PRF) adhesive and hardener from Dynea NZ Limited (Prefere 4001-2 and Prefere 5837) were used to laminate glulam beams. Glulam beams were prepared according to MS758. The tests were performed on four simple support beams isolated according to the procedure set out in BS EN 408: 2003. The flexural strength of the glulam and the bending strength values of the glulam materials were compared with the permissible force value for the timber under bending according to MS 544 Part 3. The glulam beams are 150x300x6000 mm in size. It consists of 10 layers and each timber is 30 mm thick. Although samples from different strength groups were used in the study, it was determined that there was no significant difference in bending strength values. The maximum load bearing capacity of the produced glulam beams is above the limit value and therefore it has been determined that these materials are suitable for structural purposes.

Frese and Blab (2005) [13] investigated the flexural strength values of glulam materials produced from beech. Glulam beams (47 piece) were produced and these beams were studied. For this purpose, they made mechanical classification in grading of lamellae. The beams were tested according to EN 408. The bending test results showed that the bending resistance reached 44.5 N / mm^2. According to the results of bending test, they made modelling of finite elements. This model was developed especially for estimating the flexural strength of glulam beams produced from beech. As a result of the study, it was determined that the experimental data and the results of the analytical study were correlated with each other.

2. MATERIAL AND METHODS

The effect of different layer number and layer thickness was investigated on mechanical strength of glulam beams. Glulam beams used in the study were obtained from Antalya Nasreddin Forest Products Company. Pine timber was used for glulam production. Timbers were conditioned in a

221

chamber to an environment of 65 ± 5% relative humidity and 20 ± 2°Ctemperature. After the conditioning period, the mean equilibrium moisture content was determined as almost 12 % was determined. Modulus of elasticity (MOE) of glulam beams was obtained using three point static bending tests device.

Five beams, h mm high, with h/4 thickness lamellae (three glue lines); more five beams with six lamellae of h/6 mm in height each (five glue lines) and another five beams with 8 lamellae of h/8 mm in height each (seven glue lines) were produced. Schematic view of glulam beams divided into three different groups according to layer number and thickness is given in Figure 1.
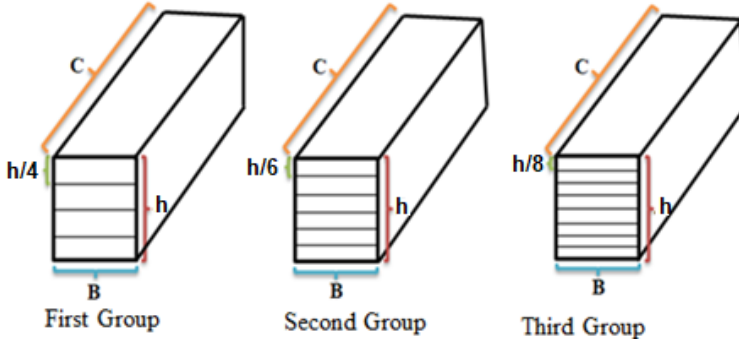
Figure 1. *Schematic view of glulam beams belonging to three different groups*

As shown in Figure 1, the width, length and height of the glulam beams belonging to three groups are the same. However, the layer number and thickness of the samples belonging to these 3 groups are different from each other. Static bending tests of the beams were performed in the apparatus given in the schematic view in Figure 2.
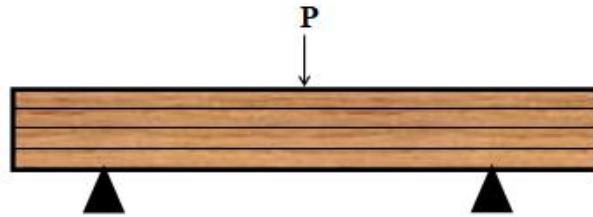
Figure 2. *Schematic view of static bending test apparatus*

Modulus of elasticity (MOE) of glulam beams were obtained using three point static bending tests device located at Suleyman Demirel University DEYMAM. The device automatically measures the modulus of elasticity of the material.

3. RESULTS

In the study, experiments were performed on the device given in Figure 3 and the modulus of elasticity of the glulam beams was determined automatically with this device. Modulus of elasticity values of three different series are given in Figure 4.
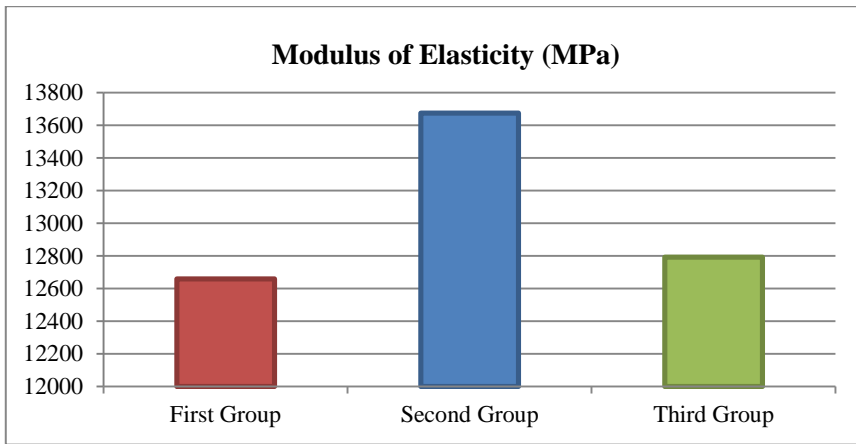
Figure 4. *Modulus of elasticity of glulam beams belonging to three different groups*

It is seen in the graph that the increase in layer thickness and number does not change proportionally with the elasticity modulus values. Icimoto et all. (2016) [14] investigated the effect of layer number and thickness on elasticity modulus and hardness values of glulam material. In their study, they stated that the number and thickness of layers do not affect the resistance and hardness values of glulam beams. The first group had the lowest modulus of elasticity; the second group had the highest modulus of elasticity, whereas in the third group, the values of elasticity decreased again. For this reason, it is necessary to perform a test to determine the strength values of all produced beams.

4. CONCLUSION

Results obtained in this study can led to conclude that variation of lamellae thickness (h/4, h/6, h/8) or glue lines number did not influence significantly on in stiffness and bending strength. While the lowest elasticity modulus values were observed in the samples with the highest layer thickness (h/4), approximately the same result was reached in the samples with the highest layer thickness (h/8). However, it is seen that the modulus of elasticity value of the sample with a medium thickness (h/6) is the highest.

As a result, when the findings obtained in the study are examined, the elasticity modulus values of the h/4 thickness samples are approximately the same as the h/8 thickness samples, it offers the following advantages:

- ✓ The smaller the number of layers, the smaller the amount of adhesive used, and the lower the cost of the adhesive.
- ✓ Due to the small number of layers, the processes required for the preparation of the layers used in beam production will be reduced.
- ✓ As the number of layers is low, the labor required during glulam production will be less and easier joining will be provided.

On sustainability issues, that configuration with four lamellae or three glue lines are the best solution among experimental conditions investigated. However, as it is seen in the study, it has been found that layer thickness and number and elasticity modulus values are not related. For this reason, the strength values of all produced materials should be tested. According to the results obtained, the number and thickness of the layers should be determined by performing analytical studies.

REFERENCES
[1] A. André, Fibers for strengthening of timber structures. Technical Report. Luleå University of Technology. Department of Civil and Environmental Engineering Division of Structural Engineering, 2006.
[2] C. Gürer, H. Akbulut, G. Kürklü, Recycling in the construction industry and re-evaluation of different building materials as a source of raw materials. Industrial Raw Materials Symposium, Izmir, 28-36., 2004.
[3] E. Bostancıoğlu, E., Düzgün Birer, Ecology and the Future of the wood material in wood-Turkey. Uludag University Journal of Faculty of Engineering and Architecture, 9(2), 2004.
[4] M.M. Uzunoğlu, M. Emiroğlu, T. Kap, Y., Yuca, Experimental and Numerical Investigation of Wood Frame Systems. 5th International Symposium on Advanced Technologies (IATS'09), 13-15 May, Karabük, Turkey, 2009.
[5] J. Jacob, O.L.G. Barragan, Flexural strengthening of glued laminated timber beams with steel and carbon fiber reinforced polymers. MSc thesis, Chalmers University of Technology, Gothenburg, 2010.
[6] I. Glišović, B. Stevanović, M. Todorović. Flexural reinforcement of glulam beams with CFRP plates. Materials and Structures, 49(7), 2841-2855, 2016.
[7] J. J. Stalnaker, E. C. Harris. Structural Design in Wood (Second Edition). Massachusetts: Kluwer Academic Publishers, 11-12, 17-18, 157-159,305, 1999.
[8] H.J. Dagher, B. Abdel-Magid, R. Lindyberg, J. Poulin, S. Shalter. Staticbending test result of Douglas-fir and western hemlock FRPreinforced glulambeams. AEWC Report No.98-4, University of Maine AEWC Center, Orono, Marine,U.S.A, 1998.
[9] P. Dutko, S. Steller, B. Kozelouh, Research into and experience of the use of finger-joints in timber structures in Czechoslovakia. In Production, Marketing and Use of Finger-Jointed Sawnwood (pp. 35-47). Springer, Dordrecht, 1982.
[10] N. M. Stark, Z. Cai, C. Carll. Wood-Based Composite Materials, Panel Products, Glued-Laminated Timber, Structural Composite Lumber, and Wood–Nonwood Composite Materials. In R. J.Ross (Ed.), Wood handbook—Wood as an engineering material. Madison, WI: U.S.: Department of Agriculture, Forest Service, Forest Products Laboratory, pp. 11-1,11-2,11-17,11-20, 2010.
[11] E. R. Thorhallsson, G. I. Hinriksson, J. T. Snæbjörnsson. Strength and stiffness of glulam beams reinforced with glass and basalt fibres. Composites Part B: Engineering, 115, 300-307, 2017.
[12] W. H. W. Mohamad, M. A. Razlan, Z. Ahmad. Bending strength properties of glued laminated timber from selected Malaysian hardwood timber. Int. J. Civ. Environ. Eng, 11(4), 7-12, 2011.
[13] M. Frese, H. J. Blaß. Beech glulam strength classes. In International council for research and innovation in building and construction Working Commission W18-Timber Structure-Meeting Thirty-Eight, 2005.
[14] F. H. Icimoto, C. C. Neto, F. S. Ferro, L. B. de Macedo, A. L. Christoforo, F. A. R. Lahr, C. C. Júnior. Influence of lamellar thickness on strength and stiffness of glued laminated timber beams of Pinus oocarpa. International Journal of Materials Engineering, 6(2), 51-55, 2016.

Automatic Segmentation Trend ARIMA Model for Coalbed Methane Production Forecast

Hongli Wang[1*], Suian Zhang[1], Hongxing Huang[2], Hongzhao Peng[2], Zengping Zhao[2], Zhihong Nie[2] and Dong Chen[2]

[1]China University of Petroleum-Beijing, Beijing, China

[2]China United Coalbed Methane National Engineering Research Center Co., Ltd., Beijing, China

*15210870454@163.com

ABSTRACT

Nowadays, huge quantities of coalbed methane (CMB) well production data have been saved in fields' data base, which declare that industry of CBM enter the age of Big Data. The traditional gas production data analysis method, such as decline curve and type curve, doesn't perform well for complex production condition. So, we proposed an automatic Segmentation Trend ARIMA Model for CBM production forecast, which based on the production data and is more robust for the complex production condition. CBM production data is time series data, so we choose the most popular time series data mining model Auto Regressive Integrated Moving Average (ARIMA) model as basic model. In general, ARIMA models is denoted by the notation ARIMA (p, d, q), where p denotes the order of the autoregressive (AR), d expressed differentiation, and q express order of the moving average (MA). We use time series cross validation and gradient descent to estimate the parameter automatically. To make the model more robust to complex production condition we decompose the production series based on the segmentation and trend feature of CBM production, and implement the model for each piece.

We use 10 set of CBM well data to evaluate the new model and compare with the type cure and decline cure method. The regression model generated by new model can achieve a mean accuracy of 95.7% by calculating r-square. The mean forecast accuracy can achieve 97.8% for a short time.

KEYWORDS – *Coalbed Methane, Gas Production Forecast, ARIMA model.*

1. INTRODUCTION

Under the conditions of the original coalbed methane **(CBM)** reservoir, the methane reserves in coal seam as an adsorbed state. Due to the unique characteristics of the adsorption state of CBM, the prerequisite for the production of CBM is the transformation from adsorption state to free state, which process is called desorption. Based on the theory of CBM adsorption, the production process of CBM is divided into "water drainage - pressure drop - methane desorption - methane diffusion - methane seepage" [1]. The essence of CBM well production is to reduce the bottomhole flow pressure through water drainage, reducing pressure of reservoir, so that the adsorbed coalbed methane can desorb, and provide the CBM production.

The production forecast of CBM well plays a critical role in the process of CBM development. At present, the methods for predicting the productivity of CBM wells mainly include numerical simulation method, Arps Decline curve method and typical curve method. Due to the complicated development process of coalbed methane and the low accuracy of coal seam property data, the prediction accuracy of reservoir numerical simulation technology is poor. In the production process of CBM wells, the production conditions are changeable, and the steady decline stage often does not appear in the later stage of production like conventional oil or gas reservoirs. The method of decline curve is only applicable to coalbed methane wells with stable decline in the later stage. Geological factors and drainage control will affect the production of coalbed methane wells. Sometimes several wells in a single well group will also exhibit different production characteristics, which reduces the adaptability of the typical curve method.

225

Autoregressive Integrated Moving Average (**ARIMA**), a typical time series analysis method, can extract both strong trend information and the randomness of CBM wells production process. In view of the influence of various factors of the productivity of CBM wells and the large difference between wells, the actual production data of coalbed methane wells in the Baiyanghe mining area of Fukang, Xinjiang, China, and establishes was used to build an ARIMA modelling method to predict coalbed methane production. The time series cross-validation technique was added to make the model achieve the effect of automatic optimization and fitting to improve the accuracy of CBM prediction.

2. AriMA MATHMATICAL MODEL

An ARIMA model is often noted ARIMA (p, d, q), which represent three parts: Autoregressive part, Moving Average part and Integrated part.[2]

2.1. Autoregressive Model （AR）

time series is said to follow an autoregressive (AR) model of order p if the current value of the series can be expressed as a linear function of the previous values of the series plus a random shock term. The general equation of an autoregressive model of order p, AR(p), can be written as :

$$x_t = \phi_1 x_{t-1} + \phi_2 x_{t-2} + \ldots + \phi_p x_{t-p} + \varepsilon_t$$

Where:

ϕ_1 , ϕ_2 , …, ϕ_p : the autoregressive model parameters.

2.2. Moving Average Model （MA）

The moving average (MA) model describes a time series that is a linear function of the current and previous random shocks (ε). The random shocks are also called errors, residuals or a white noise process. A time series, x_t, is said to be a moving average process of order q, MA(q), if

$$x_t = \varepsilon_t - \theta_1 \varepsilon_{t-1} - \theta_2 \varepsilon_{t-2} - \ldots - \theta_q \varepsilon_{t-q} \qquad (2)$$

Where:

x_t : the current value of time series data;

ε_t , ε_{t-1} , …, ε_{t-q} : the current and previous errors or random shocks;

θ_1 , θ_2 , …, θ_q : the moving average model parameters.

2.3. Autoregressive Moving Average Model (ARMA)

While the AR and MA models can be used for many data sets, they are not adequate for some data, and a more general set of models is needed. The autoregressive moving average (ARMA) models contain both AR and MA processes. Alternatively, a time series x_t is said to follow an

226

autoregressive moving average model of orders *p* and *q*, ARMA(*p*, *q*), if x_t satisfies the following difference equation.:

$$x_t - \phi_1 x_{t-1} - \phi_2 x_{t-2} - \ldots - \phi_p x_{t-p} = \varepsilon_t - \theta_1 \varepsilon_{t-1} - \theta_2 \varepsilon t - 2 - \ldots - \theta_q \varepsilon_{t-q}$$

2.4. Autoregressive Integrated Moving Average Model (ARIMA)

To model a given time series with the ARMA process, the series must be stationary. This means that both the expected values of the series and its auto covariance function are independent of time. In addition, the series must have stabilized variance and constant mean.

Most time series are nonstationary but some can be transformed to a stationary series by differencing. This process is often used to remove the trend, seasonality, and periodic variations of the series, thus rendering the nonstationary time series stationary. The differenced time series, w_t , can then be analysed and modelled like any other stationary time series. After modelling the differenced time series, the output series is transformed back to the original raw data, x_t , by reversing the order of differencing. Inclusion of differencing in the formulation of the ARMA model results in the autoregressive integrated moving average (ARIMA) model. An ARIMA model predicts a value in a response time series as a linear combination of its own past values, past errors, and current and past values of other time series. The order of an ARIMA model is usually denoted by the notation ARIMA (*p*, *d*, *q*), where p is the order of the autoregressive component, d the order of the differencing, and q the order of the moving-average process. Therefore, all models discussed previously are subsets of ARIMA models. Mathematically, the ARIMA model is written as:

$$w_t = \mu + \frac{\theta(B)}{\phi(B)} \varepsilon_t \tag{4}$$

where

w_t : the response series or a difference of the response series;

μ: a constant or intercept;

B: the backshift operator (i.e. $Bx_t = x_{t-1}$),

$\phi(B)$: the autoregressive operator, represented as a polynomial in the backshift operator, $\phi(B) = 1 - \phi_1 B - \ldots - \phi_p B^p$;

θ(B) = the moving-average operator, represented as a polynomial in the backshift operator: $\theta(B) = 1 - \theta_1 B - \ldots - \theta_q B^q$;

ε_t : the random error or shock

3. DATA PREPROCESSING
3.1. Data source

227

The data used were obtained from China United Coalbed Methane National Engineering Research Center Co., Ltd. The typical CBM well X-1 was in Baiyanghe Block, Xinjiang, China. Well X-1's production data curve was shown in *Figure 1*:

Noise and erroneous data are generated due to people mistake and sensor fault in the production process, which will affect the performance of ARIMA model mainly basing on time series trends. Therefore, before the production capacity prediction, the production data needs to be preprocessed, mainly including outlier identification and data cleaning.
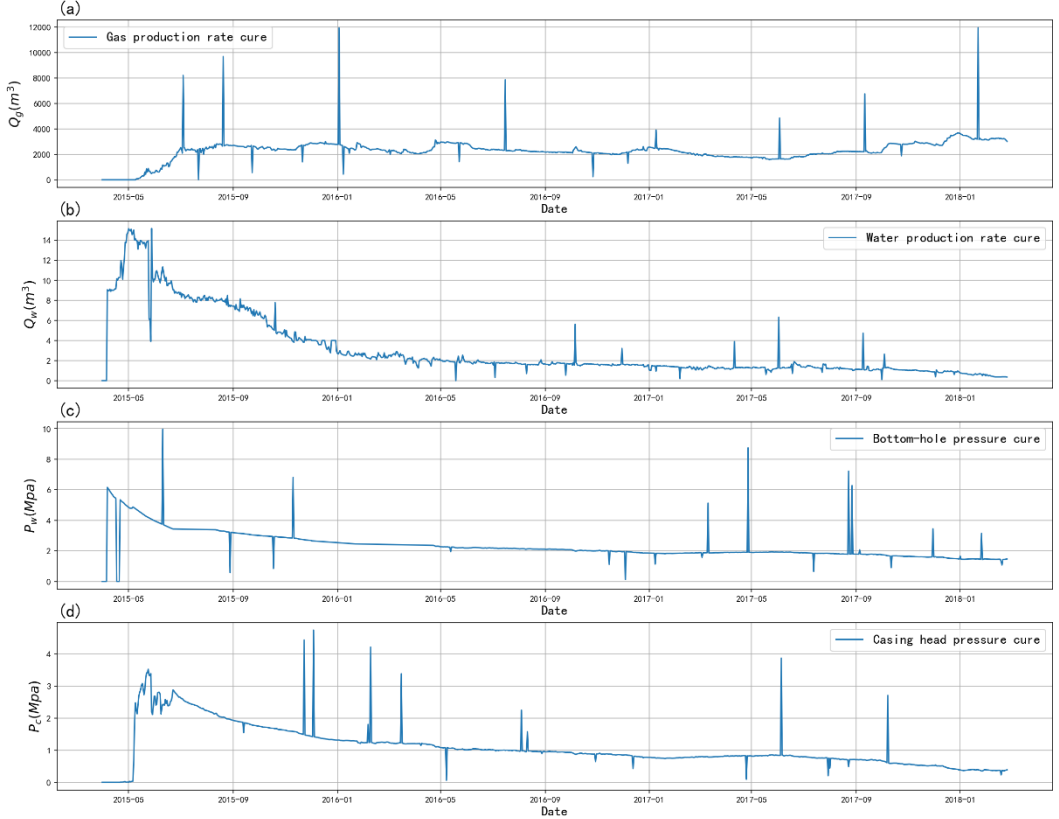
Figure 1. *The raw production data of well X-1*

3.2. Outliers Detection and Data Cleaning

the Holt-Winters method, which is a three-exponential smoothing algorithm, is often used as the outlier detection method for time series data, which considers the trend, level and seasonal of the data. The common CBM production data is not seasonal, so double exponential smoothing can be used. The formula for double exponential smoothing is as follows:

$$\ell_t = \alpha x_t + (1-\alpha)(\ell_{t-1} + b_{t-1})$$
$$b_t = \beta(\ell_t - \ell_{t-1}) + (1-\beta)b_{t-1} \tag{5}$$
$$x_{x+1} = \ell_t + b_t$$

Where:

228

ℓ_t : The level component of the data;

b_t : The trend component of the data;

α : A weight for smoothing moving average value;

β : A weight for exponential smoothing.

The red points in Figure 2 are the outliers detected by double exponential smoothing method. The red dotted lines are the conference intervals of 95%.

Figure 2. *Outliers detected by double exponential smoothing method*

The ARIMA model mainly uses gas production data, so we can use the water production, flow pressure and casing pressure data for the outliers of the gas production data. If outliers are generated at the same time point, we use the moving average and the maximum likelihood estimation method for interpolation cleaning. The cleaned data is shown in *Figure 3*.

229
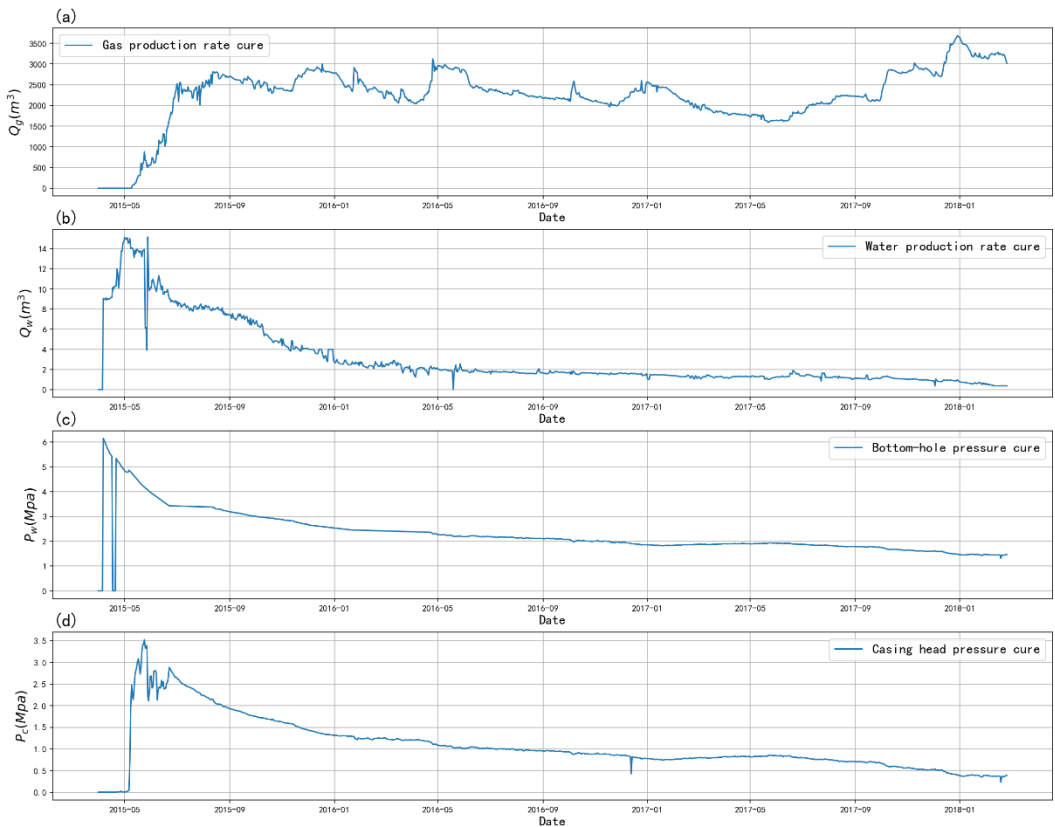
Figure 3. *Production data curve after data cleaning*

4.   AUTOMATIC ARIMA MODELING METHODOLOGY
4.1. Model Identification

The manual process of using ARIMA to forecast involves five stages: visualizing the time series; stationarizing the series, plotting autocorrelation and partial autocorrelation (ACF/PACF) charts and find optimal parameters; building the ARIMA model and making predictions. [3]

4.1.1.   Visualizing the time series

Firstly, by visualizing the time series data, it can be determined whether the data used has an overall trend, whether there is seasonality and which model to use. By observing the daily gas production data of the coalbed methane well in Figure 4 (a), it is found that some random factors such as human factors and geological factors make the trend of daily gas production not obvious, such as the impact of secondary fracturing and well shut. And the cumulative gas production in Figure 4 (b) shows a trend. At the same time, we can observe that there is no seasonality. The daily gas production is the first-order difference of the cumulative gas production. For the ARIMA model, the data stability needs to be increased by difference, so the use of the two has the same meaning.

230
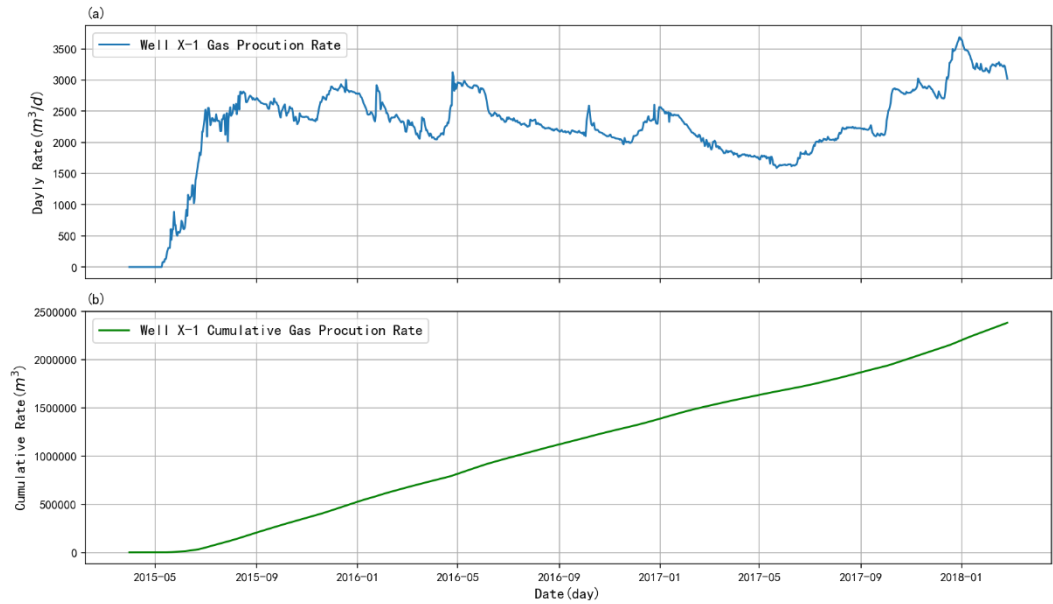
Figure 4. *Well X-1 Gas daily and cumulative production rate*

4.1.2.   Staionarizing the data

It is important for building the ARIMA model that the time series data is stationary, which means

the mean, variance and the covariance of the tth term and $(t+i)^{th}$ term should not be a function of time. Dickey-Fuller test was used to check the stationarity of the cumulative production data, and ***Figure 5*** shows that the cumulative production data is not stationary.
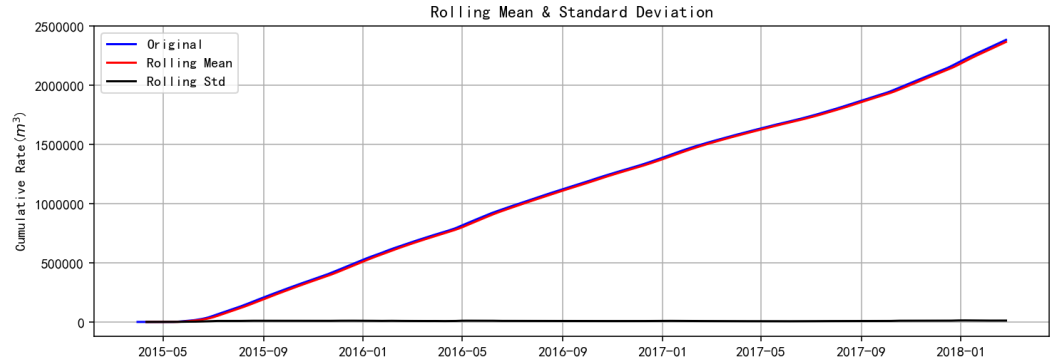
Figure 5. *The rolling mean and standard deviation of the cumulative production data*

To make the data stationary is through taking the difference of the data. First order of cumulative rate is the daily rate, which is not stationary either, so more order difference was taken. ***Figure 6*** (c) shows that the second order of the data (the first order of the daily rate data) is stationary enough.

231
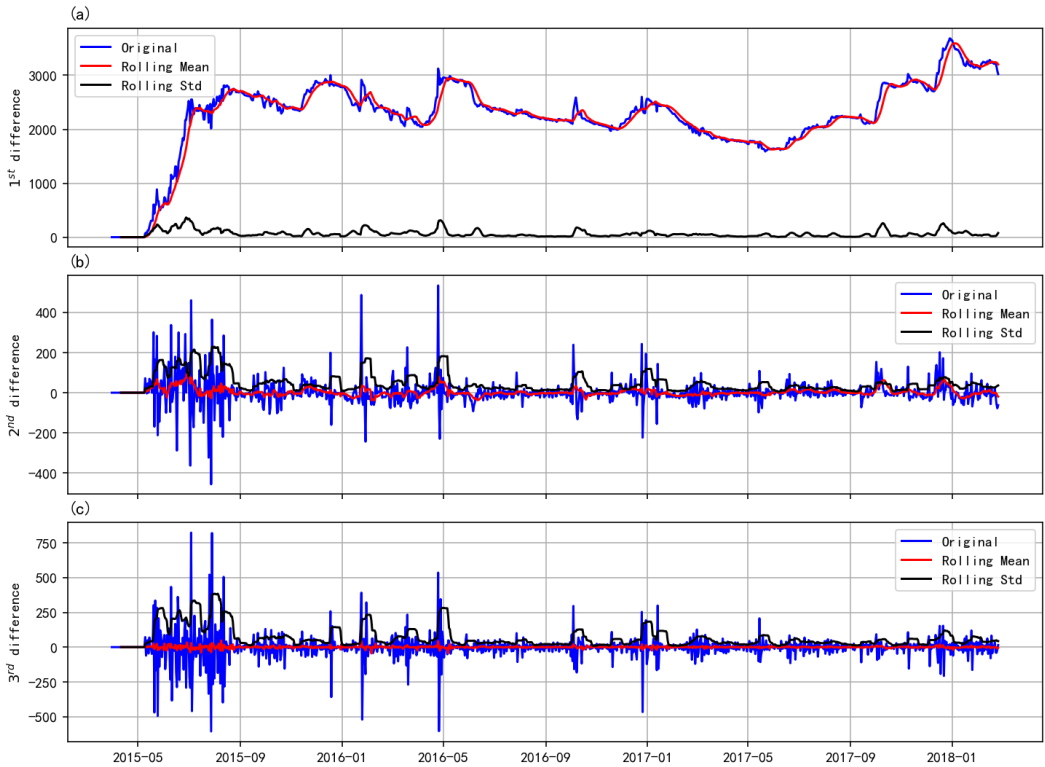
***Figure 6.** Difference of production data*

4.1.3. **Estimating optimal parameters**

First-order difference and second-order difference of the daily gas data were used to plot the ACF and PACF charts. ***Figure 7*** shows the ACF plot of the first order difference of daily production data. A rapid decrease in the ACF plot indicates that the series is stationary. The partial autocorrelation function measures the degree of association between time series observations when the effect of other time lags on the response time series is held constant. The PACF is an extension of ACF and is used to examine serial dependencies for individual lags. ***Figure 8*** shows the ACF plot of the first order difference of daily production data. However, the partial autocorrelation function has more significant lags.

Identifying the ARIMA (p, d, q) model:

d the order of integration, which means number of differences needed to make the series stationary, is 1;

p is that the current series values depend on its previous values with some lag. From the PACF chart in ***Figure 7***, it is 0, which is the biggest significant lag;

q refers the current error depends on the previous with some lag. From the ACF chart in ***Figure 7***, it is also 0 with the same logic.

232
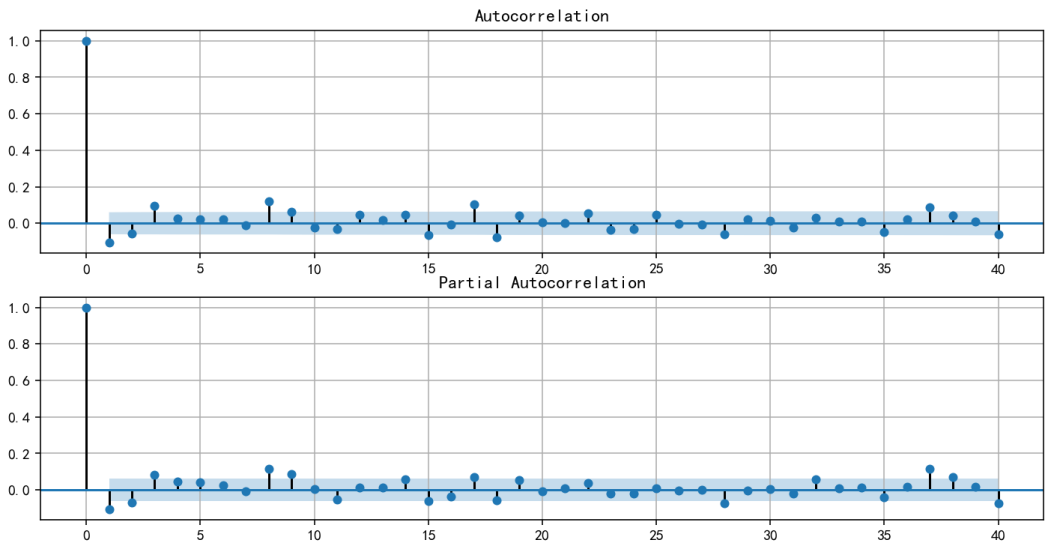
Figure 7. *Autocorrelation plots of first difference of daily production data*
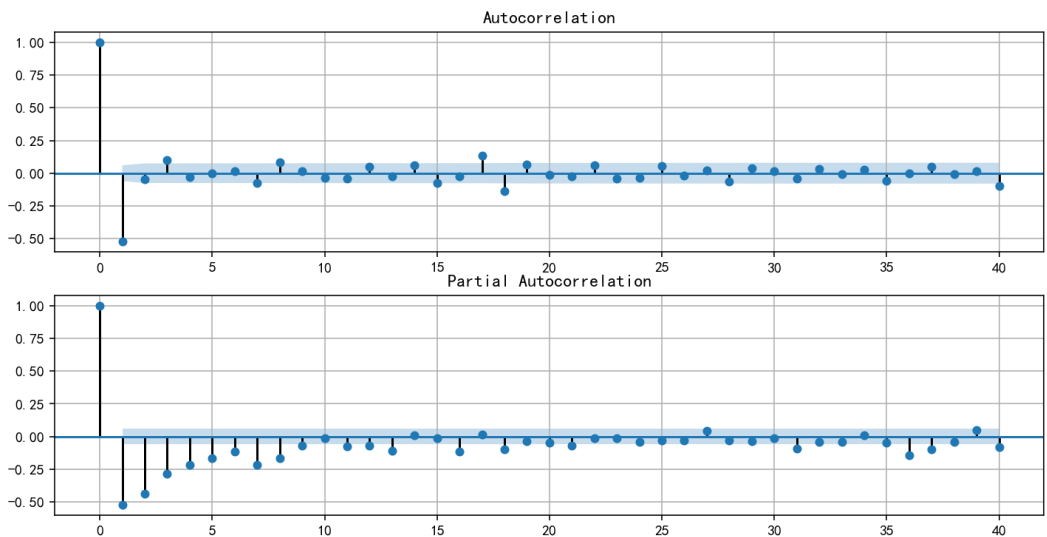
Figure 8. *Autocorrelation plots of second difference of daily production data*

4.1.4.   Building the ARIMA Model

The estimation of optimal parameters of ARIMA is very subjective, so we used different combinations of parameter to estimate and choose the optimal. The parameters were estimated using function minimization procedures, so that the sum of squared residuals is minimized.
The result and accuracy of the model will be discussed in next sector.

4.2. Automatic Model Identification

In order to reduce the subjectivity of manual judgment and improve the accuracy of the model, it can estimate model parameters automatically. Firstly, the squared residuals were chosen as the loss function for the task., then a cross-validation method was used to evaluate the given model

233

parameters, calculate the gradient. Traditional cross-validation method will lose the dependency of time series data, so we use a time series cross-validation method. Training model on a small segment of production data from the beginning to some time, then making predictions for the next t steps, and calculate an error. Then, we expand training sample to $t+n$ value, make predictions from $t + n$ until $t+2n$, and move the test segment of production data until the last available date. As shown in **Figure 9**, we have as many folds as *n* will fit between the initial training sample and the last observation.
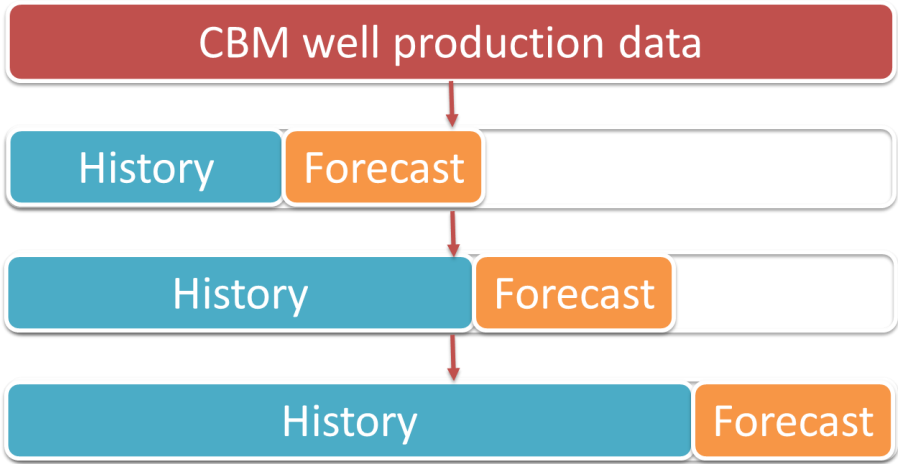
Figure 9. *Time series cross validation for CBM well production data*

5.   RESULTS AND DISCUSSION

Figure 10 presents the raw production data and the linear interpolation by ARIMA model. A very good match can be observed, making the time series very representative of the original production data.
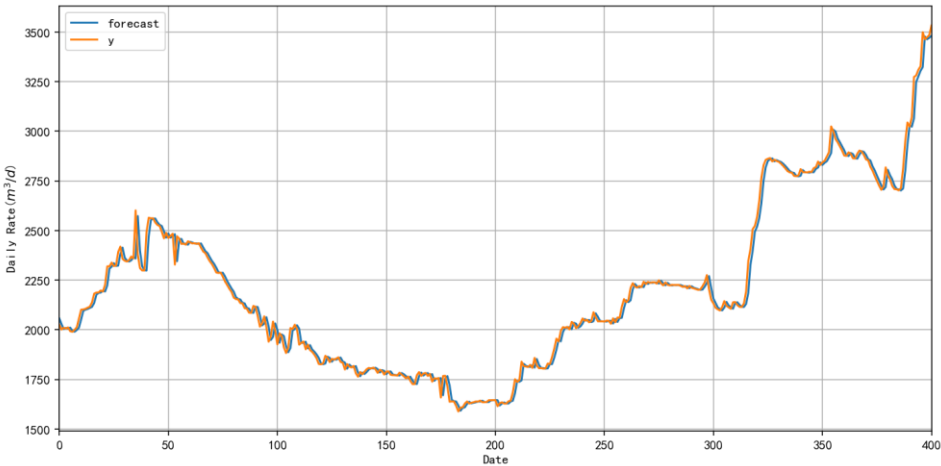
Figure 10. *The regression cure made by ARIMA model*

234

The curve shown in Figure 11 was used to compare ARPS decline curve method with ARIMA model. After comparing two models, predictions were made for 160 days. The accuracy of ARIMA was 98.9%, and of Decline Curve was just 68.03% respectively. It's obvious that ARIMA (0,1,0) performs better that Decline Curve Analysis. More importantly the ARIMA predict the right trend.
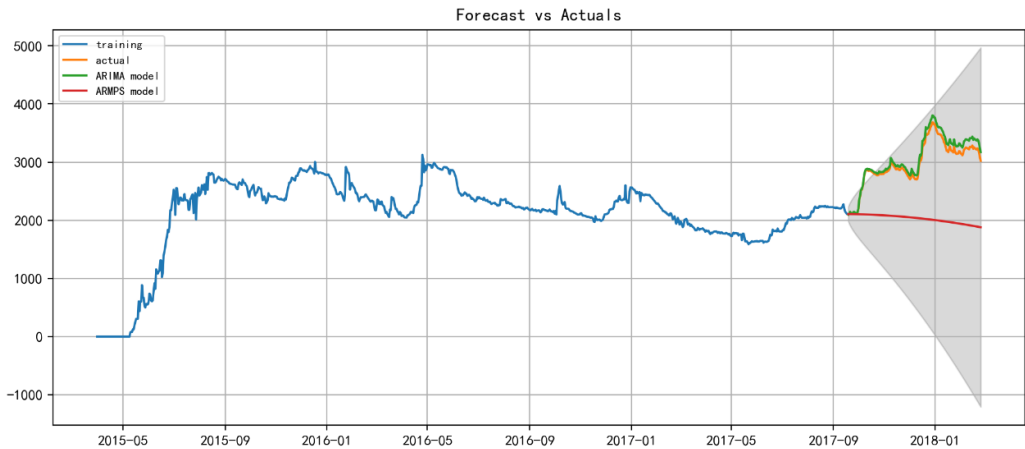
Figure 11 *Comparation between ARPS and AEIMA model*

Figure 12. *Prediction model of Well X-1 gas production rate*

6. CONCLUSION

- We developed ARIMA models for CBM well in Baiyagnhe block, Xinjiang, China, to predict CBM production. For its high accuracy in short time forecast, it can be used to guide the operation.
- The ARIMA model not only can extract the overall trend information of whole production, but also obtain some non-pure random information with relevant properties.
- For the production data with two peaks like the Well X-1 well in the Baiyanghe block, it is more suitable to use the ARIMA model for prediction by increasing the periodic method.

235

REFERENCES

[1] Zhang Sui'an, Qin Peng. Study on interference well test technology between coalbed methane wells. Coal Science and Technology. DOI：*10.13199/j.cnki.cst.2015.12.016*.

[2] Olominu, O., & Sulaimon, A. A. (2014, August 5). Application of Time Series Analysis to Predict Reservoir Production Performance. Society of Petroleum Engineers. DOI: *10.2118/172395-MS*

[3] Al-Fattah, S. M. (2005, January 1). Time Series Modeling for U.S. Natural Gas Forecasting. International Petroleum Technology Conference. DOI:*10.2523/IPTC-10592-MS*

[4] Mohammad Fuad, I. I., Rosli, L. H., & Husni, H. (2019, November 11). Application of Hybrid ARIMA – Decision Tree Algorithm in Reservoir Pressure Surveillance. Society of Petroleum Engineers. DOI:*10.2118/197762-MS*

[5] I. Akkurt, A. Elkhayat, The effect of barite proportion on neutron and gamma-ray shielding, Annals of Nuclear Energy 51 (2013) 5-9. *DOI:10.1016/j.anucene.2012.08.026*

[6] Laboratory Signals, Systems. Signal Processing Deployment in Power Quality Disturbance Detection and Classification. International Conference on Computational and Experimental Science and Engineering (2016). DOI: *10.12693/APhysPolA.132.415*

[7] Z. Cömerta, A.F. Kocamaz. Comparison of Machine Learning Techniques for Fetal Heart Rate Classification. International Conference on Computational and Experimental Science and Engineering (2016). DOI: *10.12693/APhysPolA.132.451*

[8] A.S. Yüksela, Ş.F. Çankaya. Design of a Machine Learning Based Predictive Analytics System for Spam Problem. International Conference on Computational and Experimental Science and Engineering (2016). DOI: *10.12693/APhysPolA.132.500*

[9] M. Djendel, O. Allaoui. Characterization of Alumina–Titania Coatings Produced by Atmospheric Plasma Spraying on 304 SS Steel. International Conference on Computational and Experimental Science and Engineering (2016). DOI: *10.12693/APhysPolA.132.538*

[10] O. İpek, B. Gürel. Numerical Investigation on Hydrodynamic Combustion and NOx Emission Behavior in 8 MW Circulating Fluidized Bed. International Conference on Computational and Experimental Science and Engineering (2016). DOI: *10.12693/APhysPolA.132.553*

236

Determination of Glandular Dose in Mammography

Şeyda AŞCI[1], Kadir GÜNOĞLU[2*], İskender AKKURT[1], Umit KARA[3],
[1] Suleyman Demirel University, Science Faculty,Physics Department, Isparta-TURKEY
[2] Isparta University of Applied Sciences, Technical Vocational School, Isparta- TURKEY
[3]Suleyman Demirel University, Vocational School of Healt Services, Isparta-TURKEY
*[*kadirgunoglu@isparta.edu.tr](mailto:kadirgunoglu@isparta.edu.tr)*

ABSTRACT

Medical imaging technologies are changing and developing together with developing technology. The use of radiation in the field of health is realized in two ways as diagnosis and treatment. Ionized and non-ionized radiation used for diagnostic purposes is used to detect the problematic tissue or organ by obtaining anatomical and physiological image of the patient. Radiotherapy takes its place in medicine for treatment purposes. Diagnostic radiology includes x-ray, computed tomography (CT), magnetic resonance (MRI), ultrasonography (USG) and mammography. In this study, glandular dose rates were measured experimentally in patients between 40 and 45 years of age in mammography units, which are frequently used in the screening and diagnosis of breast cancer in hospitals.

KEYWORDS - *Radiation, Mammography, radiological dose*

1. INTRODUCTION

Today, radiation has become a part of human life and manifests itself in different areas. Recently, medical imaging technologies in the world are changing and developing together with the developing technology. The use of radiation in the field of health is realized in two ways. These are diagnosis and treatment. Of these, the ionized and non-ionized radiation used for diagnosis is used to detect the problematic tissue or organ by obtaining the anatomical and physiological image of the patient. Radiotherapy takes its place in medicine for treatment purposes. Diagnostic radiology includes x-ray, computed tomography (CT), magnetic resonance (MRI), ultrasonography (USG) and mammography.

One of these methods, mammography, is intended to have high soft tissue contrast and shows the structural changes in the breast by using low dose X-ray and allows the examination of soft tissues [1-2]. Mammography has a very important place today for the best detection of breast cancer among all imaging and diagnostic methods.[3-4].

The aim of this study was to calculate the glandular dose of patients aged 40 to 45 years during mammography, which is commonly used in hospitals, according to breast thickness.

2. MATERIAL AND METHOD

Mammography is an X-ray of the breast using a low radiation dose. Breast is also the best tool for the detection of both malignant and benign tumors that positively assist human health. Mammography is the only imaging method that is most effective and safe for breast cancer screening.

This study was carried out with the patients who were examined using Mammomat Inspiration (Siemens, Erlangen, Germany) model mammography with anode / filter combination W / Rh in Necmettin Erbakan University Meram Medical Faculty Hospital Radiology Department. The study included data from 14 patients who were diagnosed as breast cancer between the ages of 40-45, underwent surgical intervention and were screened. Craniocaudal (CC) and mediolateral-oblique (MLO) positions were given to the patient to obtain as clear a view as possible on mammographic examinations. Breast compression was performed to the extent allowed by the device using

237
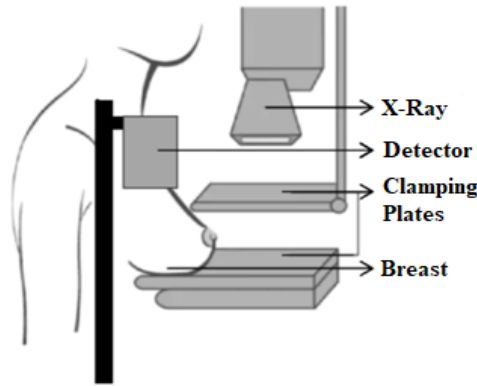
Figure 1. *Experimental measuring area*

automatic clamping plates. Then, with the automatic dose control, mammography was performed at the exposure values determined by the device according to the breast structure of the patient. Polimaster brand PM 1405 model detector was used for measurements. During the measurements, the detector was placed as close to the patient as possible at the breast level, as shown in Figure 1 [5]. Parameters such as age, weight, height, compressed breast thickness in right-left craniocaudal, mediolateral oblique positions, tube voltage (kV), tube current (mAs), force applied to the breast, inlet dose and glandular dose were recorded separately for all patients undergoing mammography.

Table 1. *Experimental parameters and glandular dose values*

Weight (kg)	Height (m)	Age	Force (N)	Position	Tube Voltage (kV)	Tube Current (mAs)	Breast Thickness (mm)	Inlet Dose (mGy)	Glandular Dose (mGy)
58	1,67	40	187	RCC	28	90,1	51	2,7	1,16
73	1,49	45	168	RCC	28	104,7	49	3,2	1,19
76	1,6	41	114	RCC	28	67	45	2	0,81
75	1,6	40	183	RCC	27	68,8	49	1,8	1,02
54	1,51	44	104	RCC	28	69,4	49	2,1	0,79
85	1,5	44	181	RCC	30	107,2	54	4,2	1,19
58	1,61	42	186	RCC	28	82,3	46	2,5	0,98
75	1,74	42	183	RCC	29	99,7	52	3,4	1,2
88	1,65	45	171	LMLO	30	113,4	58	4,5	1,2
65	1,62	43	186	LCC	29	73,7	52	2,5	0,89
53	1,5	43	95	RCC	27	54,9	42	1,4	0,76
58	1,6	45	185	RCC	27	51,9	34	1,4	0,69
74	1,59	42	184	RCC	29	144,8	69	5,1	1,56
87	1,65	40	130	RCC	29	68,8	50	2,4	0,85
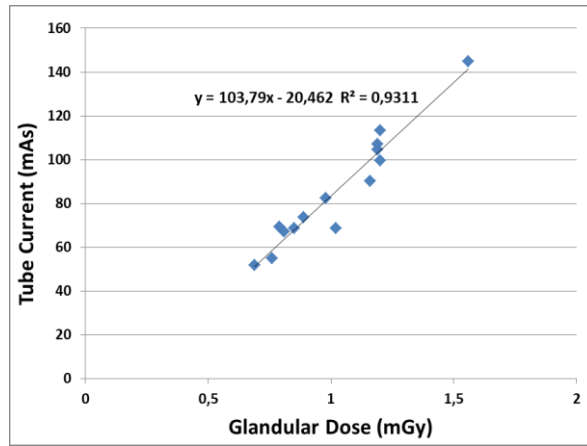
Figure 2. Relationship between glandular dose and tube current (mAs).

3.   RESULTS AND DISCUSSION

In this study, breast mammary glandular dose was measured experimentally in 14 patients who were diagnosed as breast cancer between the ages of 40-45 and underwent surgical intervention. The obtained glandular dose values are given in Table 1.

The relationship between glandular dose values and tube current (mAs) is shown in figure 2. It can be seen from figure 2 that as the tube current (mAs) value increased, the glandular dose value also increased. The relationship between glandular dose values and breast thickness (mm) is shown in figure 3. It can be seen from figure 3 that as the breast thickness (mm) value increased, the glandular dose value also increased.
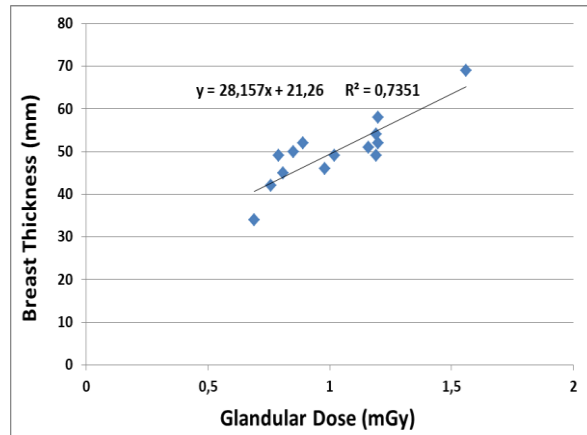
Figure 3. Relationship between glandular dose and breast thickness (mm)

In this study, the experimental glandular dose of a mean 50 mm breast was measured as 1.0 mGy. It was concluded that experimental glandular doses obtained according to the limit dose value of 2.5 mGy for 50 mm breast specified in Euref protocol were low [6].

REFERENCES

[1].   Sancak, İ.T., (Ed.), 2015. Temel Radyoloji. Güneş Tıp Kitabevleri, s.737-738, Ankara.

239

[2]. Arıbal, E., 2014. Mamografi Fiziği ve Dijital Mamografide Yeni Çözümler. Ulusal Radyoloji Teknisyenleri Kongresi ve MR Fizik Kursu, 15-18 Mayıs 2014, Antalya, 83-84.

[3]. Topuz, E., Aydıner, A., Dinçer, M., 2003. Meme Kanseri. Nobel Tıp Kitabevleri, s.1-146, İstanbul.

[4]. Oyar, O., 2008. Magnetik Rezonans Görüntüleme (Mrg)'Nin Klinik Uygulamaları Ve Endikasyonları. Harran Üniversitesi Tıp Fakültesi Dergisi, 5(2), 31-40.

[5]. Canadian Cancer Society, 2019. Mammography. http://www.cancer.ca/en/cancer-information/diagnosis-and-treatment/tests-and-procedures/mammography/?region=qc

[6]. Euref (European Reference Organisation for Quality Assured Breast Screening and Diagnostic Services), 2017. European protocol fort the quality control of the physical and technical aspects of mammography screening. Four Edition. 117.

Misalignment Tolerance in Free Space Optical Interconnects

Nedal Al-Ababneh

Department of Electrical Engineering, Jordan University of Science & Technology, Irbid, Jordan
*nedalk@just.edu.jo

ABSTRACT

This paper describes the use of tapered, or apodized, apertures which may be employed in future free space optical interconnects to mitigate the effects of misalignment. We use the Gaussian aperture as an example. We show that the misalignment tolerance improves and the reduction of the signal to crosstalk ratio caused by the misalignment is still within the practical ranges. Simulation results are also presented to show the claimed improvement.

KEYWORDS - *Diffraction, free space optical interconnects, Gaussian aperture.*

1. INTRODUCTION

Misalignment of different optical components in the future free space optical interconnects (FSOIs) as a result of manufacturing or installation reasons is considered as one of the limiting issues that affect the design and performance of (FSOIs) system [1]–[8]. Therefore, studying the impact of misalignment on FSOIs systems and introduce methods to mitigate and reduce its effect is essential in these optical systems. In fact, the misalignment of different optical components in (FSOIs) increases the optical crosstalk that is already exists in these systems. Therefore, methods to deal with crosstalk and at the same time increase the system tolerance to misalignment are required. Most of the methods considered to deal with crosstalk and misalignment were based on introducing models and formulas for the crosstalk of the misaligned optical system then use these formulas and models to optimize the crosstalk. For example, in [9]–[11] a modified mode expansion method to model and optimize the crosstalk in misaligned FSOIs is presented. In [12], a method using Hermite–Gaussian beam model and generalized Collins diffraction theory was presented to quantify the diffraction in a misaligned FSOIs system with finite aperture. In [13], a crosstalk model for a misaligned apertured lens based FSOIs system based on the generalized diffraction integral formula for treating the propagation of a Laguerre–Gaussian (LG) beam through slightly misaligned FSOIs in cylindrical coordinate system was introduced. An approximate analytical formula of the light irradiance is derived for an apertured slightly misaligned FSOIs system by expanding the aperture function as a finite sum of complex Gaussian functions. Using this formulism, the overall crosstalk was estimated and optimized. In [14] a method that uses a micro lens with a Gaussian transmittance profile is used to reduce crosstalk.

The work in this paper is built on the work presented in [14]. In this paper, we show that the use of a micro lens with Gaussian profile increase the misalignment tolerance in lens based free space optical interconnects is. To best of the authors' knowledge the use of lens apodization to increase the system' tolerance to misalignment and at the same time reduces the crosstalk in FSOIs systems has not yet been investigated.

2. OPTICAL FIELDS IN UNAPERTURED MISALIGNED

Consider the FSOIs system shown in Fig. 1. This optical system consists of VCSELs array, transmitter microlens array, and detectors array. The VCSELs array is placed at the front focal length of the transmitter microlens f_t. The distance between detector array and microlenses array is denoted by l. s_x is the misalignment of the microlens with respect to the optical axis of the FSOIs system.
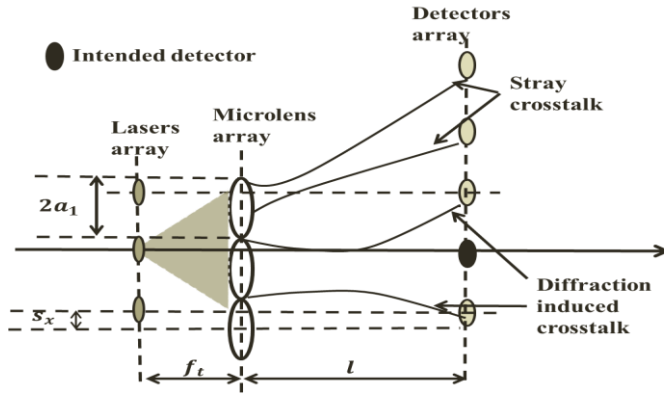
Figure 1. *Misaligned lens-based FSOIs.*

To find the field distribution at the detectors plane we use the generalized diffraction integral formula in cylindrical coordinate system assuming paraxial approximations. Based on this formula the optical field at an output plane can be related to an input optical field propagating misaligned linear optical system by [15]

$$E_2(\rho_2,\theta_2) = \frac{ik}{2\pi b}\int_0^\infty\int_0^{2\pi} E_1(\rho_1,\theta_1)\exp\left[-\frac{ik}{2b}\rho_2'^2\right]\exp\left[\frac{ika}{2b}\rho_1^2\right]$$
$$\times\exp\left[\frac{ik\rho_1}{b}\rho_2''\cos(\theta_1-\phi)\right]\rho_1 d\rho_1 d\theta_1 \tag{1}$$

$$\rho_2'^2 = d\rho_2^2 + g\rho_2\cos\theta_2 + h\rho_2\sin\theta_2 \tag{2}$$
$$\rho_2''^2 = (\rho_2\cos\theta_2 - e/2)^2 + (\rho_2\sin\theta_2 - f/2)^2 \tag{3}$$

$$\phi = \tan^{-1}\left(\frac{\rho_2\sin\theta_2 - f/2}{\rho_2\cos\theta_2 - e/2}\right) \tag{4}$$

ρ_1,θ_1 and ρ_2,θ_2 are the cylindrical coordinates of input and output planes respectively. $E_1(\rho_1,\theta_1)$ is the input optical field, $k = 2\pi/\lambda$ is the wave number and λ is the wavelength. *a*, *b*, *c*, and *d* are the transfer matrix elements of the aligned optical system and e, f, g, and h are the misalignment parameters. For the FSOIs system under consideration (Fig. 1) the transfer matrix elements are:

$$a = 1 - (l/f_t), \quad b = l, \quad c = -1/f_t, \quad d = 1 \tag{5}$$

and the misalignment parameters are:

$$e = 2\frac{l}{f_t}s_x \quad, f = 0, \quad g = 0, \quad h = 0 \tag{6}$$

242

Assuming a LG beam model for the FSOIs of Fig.1, $E_1(\rho_1, \theta_1)$ is the optical field distribution of the LG beam in the cylindrical coordinate system at the front surface of the microlens and is given by [10]

$$E_1(\rho_1, \theta_1) = \left(\sqrt{2}\, \frac{\rho_1}{\omega_1} \right)^m \exp\left[-\frac{\rho_1^2}{\omega_1^2} \right]$$
$$\times L_p^m\left[\frac{2\rho_1^2}{\omega_1^2} \right] \times \exp[-im\theta_1]$$

(7)

L_p^m is the Laguerre polynomial with mode orders p and m. ω_1 the beam radius at the front surface of the transmitter microlens and is given by is

$$\omega_1 = \omega_0 \sqrt{1 + \frac{\lambda^2 f_t^2}{\pi^2 \omega_0^4}}$$

(8)

ω_0 is the waist radius of the LG beam emitted from the VCSEL. Substituting (7) into (1) and using (5) and (6) after performing tedious integration, we can obtain the optical field at the detectors array of the unapertured FSOIs system as

$$E_{2u}(\rho_2, \theta_2) = \left(\frac{ik}{2l} \right)^{m+1} \exp[-im\theta_2] \exp\left[\frac{ik}{2l} \rho_2^2 \right]$$
$$\times \left[\frac{ik[1-(l/f_t)]}{2l} + \frac{1}{\omega_1^2} \right]^{-m-p-1} \left[\frac{ik[1-(l/f_t)]}{2l} - \frac{1}{\omega_1^2} \right]^p$$
$$\times \left[\frac{\sqrt{2}}{\omega_1} \sqrt{(\rho_2\cos\theta_2 - 2s_x/f_t)^2 + (\rho_2\sin\theta_2)^2} \right]^m$$
$$\times \exp\left[\frac{-k^2\left[(\rho_2\cos\theta_2 - 2s_x/f_t)^2 + (\rho_2\sin\theta_2)^2\right]}{4l^2\left(\frac{ik[1-(l/f_t)]}{2l} + \frac{1}{\omega_1^2} \right)} \right]$$
$$\times L_p^m\left[\frac{k^2\left[(\rho_2\cos\theta_2 - 2s_x/f_t)^2 + (\rho_2\sin\theta_2)^2\right]}{2\omega_1^2 l^2\left(\frac{k^2[1-(l/f_t)]^2}{4l^2} + \frac{1}{\omega_1^4} \right)} \right]$$

(9)

Equation (9) is closed form formula for the optical field irradiance at the detector array for the LG beam propagating through a slightly misaligned unapertured lens based FSOIs system shown in Fig. 1. This equation will be used to estimate the crosstalk.

3. MISALIGNED FSOIS WITH GAUSSIAN CIRCULAR APERTURE

In this section, we assume the presence a circular aperture with Gaussian transmission profile at the plane of the microlens. Let $H(\rho_1)$ the circular Gaussian aperture function with a_1 radius

243

$$H(\rho_1) = A(\rho_1)G(\rho_1) = \begin{cases} G(\rho_1) & \rho_1 \leq a_1 \\ 0 & \rho_1 \succ a_1 \end{cases}$$

(10)

$$G(\rho_1) = \exp\left[-\frac{\rho_1^2}{\omega_a^2}\right]$$

(11)

ω_a is the width of the Gaussian aperture. Again, by expanding $A(\rho_1)$ in terms of finite number of complex Gaussian functions, we write $H(\rho_1)$ as [16], [17]

$$H(\rho_1) = \sum_{n=1}^{N} C_{1n} \exp\left(-\left[\frac{C_{2n}}{a_1^2} + \frac{1}{\omega_a^2}\right]\rho_1^2\right)$$

(12)

Substituting (12) into (1) and performing the integral, we obtain

$$\mathrm{E}_{2g}(\rho_2,\theta_2) = \left(\frac{ik}{2l}\right)^{m+1} \exp[-im\theta_2]\exp\left[\frac{ik}{2l}\rho_2^2\right]$$

$$\times \left[\frac{\sqrt{2}}{\omega_1}\sqrt{(\rho_2\cos\theta_2 - 2s_x/\mathrm{f}_t)^2 + (\rho_2\sin\theta_2)^2}\right]^m$$

$$\times \sum_{n=1}^{N} C_{1n}\left[\frac{ik[1-(l/f_t)]}{2l} + \frac{C_{2n}}{a_1^2} + \frac{1}{\omega_a^2} + \frac{1}{\omega_1^2}\right]^{-m-p-1}$$

$$\times \left[\frac{ik[1-(l/f_t)]}{2l} + \frac{C_{2n}}{a_1^2} + \frac{1}{\omega_a^2} - \frac{1}{\omega_1^2}\right]^{p}$$

$$\times \exp\left[-\frac{k^2\left[(\rho_2\cos\theta_2 - 2s_x/\mathrm{f}_t)^2 + (\rho_2\sin\theta_2)^2\right]}{4l^2\left(\frac{ik[1-(l/f_t)]}{2l} + \frac{C_{2n}}{a_1^2} + \frac{1}{\omega_a^2} + \frac{1}{\omega_1^2}\right)}\right]$$

$$\times L_p^m\left[\frac{k^2\left[(\rho_2\cos\theta_2 - 2s_x/\mathrm{f}_t)^2 + (\rho_2\sin\theta_2)^2\right]}{\frac{2l^2}{\omega_1^2} - 2\omega_1^2 l^2\left(\frac{ik[1-(l/f_t)]}{2l} + \frac{C_{2n}}{a_1^2} + \frac{1}{\omega_a^2}\right)^2}\right]$$

(13)

Equation (13) is an approximate analytical relation for the optical field distribution of the LG beam propagating through misaligned FSOIs system with circular Gaussian aperture. In fact, this relation provides a convenient way for estimating the crosstalk in a slightly misaligned FSOIs system taking into account the effect of finite aperture of the microlens.

4. CROSSTALK CALCULATION

To estimate the crosstalk, we consider Fig. 2. Two types of optical crosstalk are considered. The first type is the stray crosstalk which can be seen as the fraction of the transmitted power from the intended source that transmit to other detectors through neighboring microlenses as shown in

244

Fig.2. The stray crosstalk power can be found as the total power received by all neighboring detectors from the light coming through neighboring microlenses assuming only the intended source is on. In this case, we can estimate the stray crosstalk power for the different apertures by

$$P_{c1} = P_{c11} + P_{c12} = 4\iint_{\Omega_1} |E_1(\rho_1,\theta_1)|^2 \rho_1 d\rho_1 d\theta_1$$
$$+ 4\iint_{\Omega_2} |E_1(\rho_1,\theta_1)|^2 \rho_1 d\rho_1 d\theta_1$$

(14)

In (14), P_{c11} and P_{c12} are the crosstalk noises received by the intended detector from the neighbor and next neighbor VCSELs respectively. Ω_1 and Ω_2 are the areas covered by neighbor and next neighbor transmitted microlens, respectively. The second crosstalk type is diffraction induced crosstalk comes from the overlap between the intended detector aperture and the diffracted light beams from other VCSELs through other transmitted microlens. The total diffraction induced crosstalk power received by the intended detector can be found as

$$P_{c2} = P_{c21} + P_{c22} = 4\iint_{\Omega_3} |E_2(\rho_2,\theta_2)|^2 \rho_2 d\rho_2 d\theta_2$$
$$+ 4\iint_{\Omega_4} |E_2(\rho_2,\theta_2)|^2 \rho_2 d\rho_2 d\theta_2$$

(15)

P_{c21} and P_{c22} are the crosstalk noises received by the detector from the neighbor and next neighbor detectors respectively. Ω_3 and Ω_4 are the areas covered by neighbor and next neighbor detectors, respectively. The signal power is the power received by the intended detector as given by

$$P_s = \iint_{\Omega} |E_2(\rho_2,\theta_2)|^2 \rho_2 d\rho_2 d\theta_2$$

(16)

Ω is the area covered by intended detector. After estimating the signal and the crosstalk for the FSOIs system, the SCR could be determined. In our model, no detector preamplifier is used and the crosstalk noise resulting from stray light at transmitted microlens, light diffraction from apertures, and misalignment are included. Using (18)-(22), the SCR ratio can be determined as

$$SCR = \frac{P_s}{P_{c1} + P_{c2}}$$

(17)

5. NUMERICAL SIMULATIONS

The following parameters are used in our simulations: for the VCSEL λ=0.850 μm and ω$_0$= 3 μm; for the transmitter microlens the focal length and the diameter are 720 μm and 250 μm, respectively. The interconnection length is 2.5 mm. Fig. 2 shows the SCR versus detector radius for the aligned FSOIs system with uniform hard edge aperture and Gaussian aperture. The radius of the uniform hard edge aperture is 125 μm. The width of Gaussian aperture is 125 μm. It is clear that the SCR for the FSOIs system with Gaussian aperture is larger than that of the system with no aperture. In the case of the unapertured system the SCR is 25, while it increases to 93 in the case of the Gaussian aperture. Furthermore, the optimum detector radius for the Gaussian aperture

245

system is smaller than that of both FSOIs systems with uniform hard edge aperture. For maximum SCR, the optimum detector radii for for the FSOIs systems with uniform hard edge aperture and Gaussian aperture are 23 µm, and 14 µm, respectively. The existence of such optimum can be explained by considering the design formula used to model the crosstalk. In this paper, we consider the diffraction induced cross talk and the stray light crosstalk. The diffraction induced crosstalk depends on the detector size while the stray crosstalk depends on the microlens size. For a given microlens radius, the stray crosstalk is constant and overwhelms the diffraction crosstalk at small detector size. In this case, the decrease of the SCR as the detector size decreases is due to the decrease in the signal power. For large detector size, the diffraction crosstalk is dominant and increases with the detector size. Fig. 3 shows the SCR versus detector-to-lens radius ratio for the apertured FSOIs system with a misalignment of 10 µm for the microlens in x-direction. The SCR decreases with misalignment. The optimum SCR is deceased to 18.5 for the system with Gaussian aperture and to 7.5 for the system with the uniform aperture. Moreover, the optimum detector radius decreases with increasing the misalignment to tolerate the decrease in the SCR.
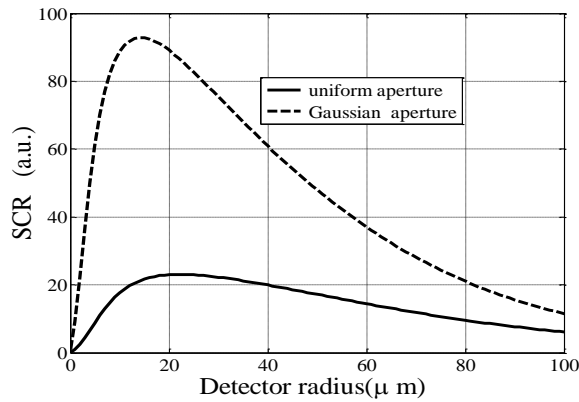
Figure 2. SCR versus detector size for the aligned FSOIs systems using uniform and Gaussian apertures.
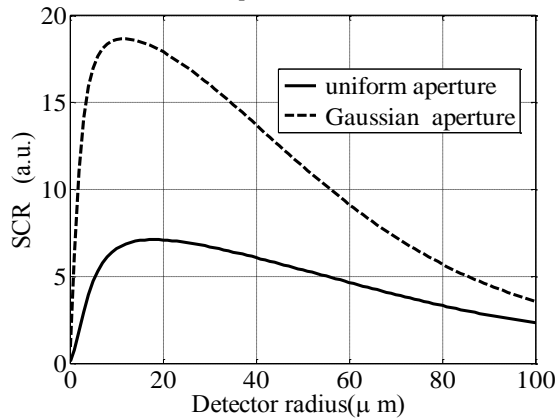
Figure 3. SCR versus detector radius for the misaligned FSOIs system using uniform and Gaussian apertures. Misalignment is 10 µm.

6. CONCLUSION

We have analyzed a misaligned free space optical interconnects system employing apodized aperture. A novel diffraction model has been proposed using the generalized diffraction integral formula Assuming Gaussian. Based on the proposed diffraction model and using some the derived

formulas, the signal-to-crosstalk ratio has been estimated and used as the performance measure. Our numerical results have shown that the effect of misalignment can be reduced using apodized aperture for the optical system.

REFERENCES

[1] N. Al-Ababneh, "Misalignment analysis of lensless free-space optical interconnects," *Opt. Eng.*, 2006. http://dx.doi.org/10.1117/1.2212907

[2] J. Chou *et al.*, "Rotational optical alignment for array based free space board-to-board optical interconnect with zero power hold," in *Proceedings of the IEEE International Conference on Micro Electro Mechanical Systems (MEMS)*, 2010. http://dx.doi.org/10.1109/MEMSYS.2010.5442283

[3] N. Al-Ababneh, "Crosstalk in misaligned free space optical interconnects: Modelling and simulation," *Int. J. Electr. Comput. Eng.*, 2019. http://dx.doi.org/10.11591/ijece.v9i3.pp1620-1629

[4] N. S. F. Ozkan, W. L. Hendrick, P. J. Marchand, and S. C. Esener, "Misalignment tolerance analysis of free-space optical interconnects via statistical methods," *Appl. Opt.*, 2002.

[5] A. Mansour, R. Mesleh, and M. Abaza, "New challenges in wireless and free space optical communications," *Opt. Lasers Eng.*, 2016. http://dx.doi.org/10.1364/AO.41.002686

[6] A. G. Kirk, "Free-space optical interconnects," *Springer Ser. Opt. Sci.*, 2006. http://dx.doi.org/10.1007/978-3-540-28912-8_13

[7] E. Bisaillon *et al.*, "Free-space optical link with spatial redundancy for misalignment tolerance," *IEEE Photonics Technol. Lett.*, 2002. http://dx.doi.org/10.1109/68.980535

[8] H. P. Kuo *et al.*, "Free-space optical links for board-to-board interconnects," *Appl. Phys. A Mater. Sci. Process.*, 2009. http://dx.doi.org/10.1007/s00339-009-5144-z

[9] N. S. Petrović and A. D. Rakić, "Modeling diffraction in free-space optical interconnects by the mode expansion method," *Appl. Opt.*, 2003. http://dx.doi.org/10.1364/AO.42.005308

[10] F. C. F. Tsai, C. J. O'Brien, N. S. Petrović, and A. D. Rakić, "Analysis of optical channel cross talk for free-space optical interconnects in the presence of higher-order transverse modes," *Appl. Opt.*, 2005. http://dx.doi.org/10.1364/AO.44.006380

[11] F.-C. F. Tsai, N. S. Petrovic, and A. D. Rakic, "Comparison of stray-light and diffraction-caused crosstalk in free-space optical interconnects," in *Photonics: Design, Technology, and Packaging*, 2004.

[12] W. Hu, X. Li, J. Yang, and D. Kong, "Crosstalk analysis of aligned and misaligned free-space optical interconnect systems," *J. Opt. Soc. Am. A*, 2010.

[13] N. Al-Ababneh, "Crosstalk in misaligned free space optical interconnects: Modelling and simulation," *Int. J. Electr. Comput. Eng.*, vol. 9, no. 3, 2019.

[14] N. Al-Ababneh, "Crosstalk reduction in free space optical interconnects systems using microlenses with Gaussian transmittance," *Opt. Commun.*, vol. 318, 2014.

[15] S. A. Collins, "Lens-System Diffraction Integral Written in Terms of Matrix Optics*," *J. Opt. Soc. Am.*, 1970.

[16] D. Ding and Y. Zhang, "Notes on the Gaussian beam expansion," *J. Acoust. Soc. Am.*, 2004.

[17] J. J. Wen and M. A. Breazeale, "A diffraction beam field expressed as the superposition of Gaussian beams," *J. Acoust. Soc. Am.*, 1988.

A Breif Review on Atmospheric Radiation Dose Estimations

Zuhal Er[1]* and Iskender Akkurt[2]

[1] *Department of Physics Eng., Faculty of Science and Letters, Istanbul Technical University, Istanbul, Turkey*
[2] *Suleyman Demirel University, Physics Department, Isparta-Turkey*
*erzuh@itu.edu.tr

ABSTRACT

Objectives of this study can be listed as: one is to review the existing evaluations with new technological studies in the radiation applications, second is to manufacturing most (securely) safely radiation applications, third is to define the radiation doses for the scientific new studies and for the recent technologies. Furthermore, this study is focused to define suitable materials choosing with respect to radiation shielding cases. Finally, our observations will be reflections to propose new innovations for mobile radiation detections or applications. This proceeding study is give briefly summaries about atmospheric radiation doses with some figures.

KEYWORDS- *Nuclear Propulsion, Atmospheric Radiation Exposure Doses, Nuclear Ships and Submarines.*

1. INTRODUCTION

Motivation of the study is coming from that reality which there is atmospheric radiation exposure cases and improving material options with new technological investments. On the other hand, some experimental radiation studies cannot prepared or be carry out initial experiments at place without opportunities of a laboratory as can be done for photon-based techniques (X-rays, NMR, IR, Raman, etc). Furthermore, technological innovations service new and mobile laboratory opportunities are placed with adding radiation to the atmospheric radiation in a human life. In an atomic explosion, the radiation is particularly harmful. But the neutronic flash does not last. Free neutrons have an half-life of about 12 minutes. They are generally absorbed by matters before decaying. Energy storage, transport, conversion all benet from radiation research are the reality of today's life. The investigation of properties of new energy storage materials rely heavily on neutron scattering. Suitable storage materials are analysed in operation do using neutrons, for instance for transportation. Neutron scattering can help improve lithium batteries. The development of superconductors for energy transport relies on information from neutron scattering. In photovoltaics and solar energy research, neutrons are used to study the performance of solar cells [1, 2, 3].

2. RADIATION DOSES

When cancer treatment is needed, people have a lot to think about and understand such as natural backqround, artificial radiation cases, etc.. Radiation facilities are divided into areas where they can be controlled, controlled and classified as uncontrolled. National regulatory authorities have established exposure limits for these areas. All passengers in commercial aircraft flying above 26,000 ft. (7924.8 m) will typically experience some exposure in this aviation radiation environment. For our purposes which is comparing extraterrestrial radiation knowhow with to terrestrial radiation, the sources of radiation in Earth space are separated into four categories [2, 4,5]:

• Plasma

248

- • Trapped Particles
- • Solar Particles
- • Galactic (Cosmic) Rays
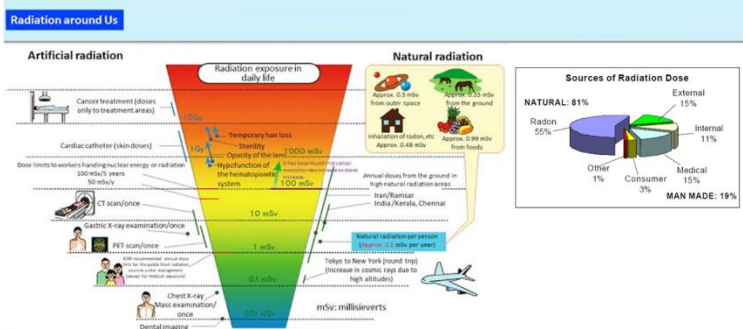
Figure 1. *Comparision of Exposure Doses (Simplified Chart) [1].*
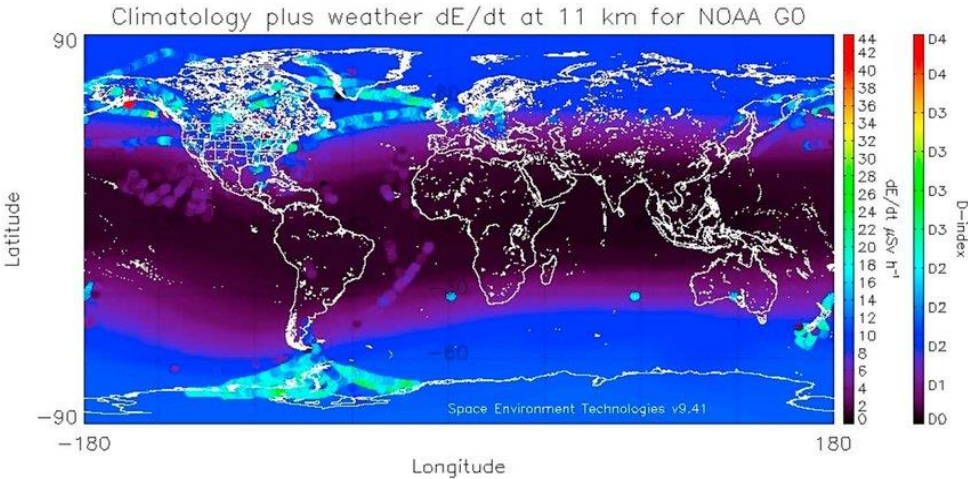
Figure 2. *Global Magnetometric Evaluations [7,8].*

Another environmental factor is the geomagnetic field which strongly influences plasma/particle motions and locations. A geomagnetic storm is the result of solar storm particles being injected into the Earth's magnetic field. Geomagnetic storms have been directly correlated to the incidence of spacecraft charging [6, 7, 8]. Countless materials are produced every day to make our life easier. Cars, planes, trains, turbines, cosmetics, laundry deter- gents, drugs, all are improved both in efficiency, quality and price thanks to information provided by neutron experiments. Furthermore, developing advanced materials that support new technologies depends on scientists' ability to manipulate their properties at the atomic level, and neutron science is a key to these efforts. Industrial innovation and competiveness rely on fundamental knowledge provided by neutrons on the behavior of molecules, or the determination of inner stresses to develop components with higher performance.

3. Results and Discussions

In this study, for the radiation safe, different cases were briefly evaluated with the reviews. Our evaluations are given by the figures in the literatures. The Figure 3 represents a human in the

natural radiation reality evaluation. The extraterrestrial and terrestrial radiation doses evaluations in the literatures are illustrated in the Figure 4.
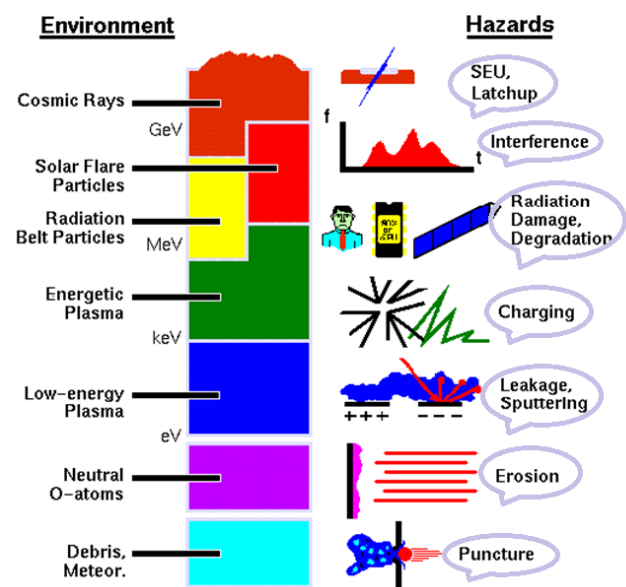
Figure 3. *Radiation in the Environment and its effects [1].*
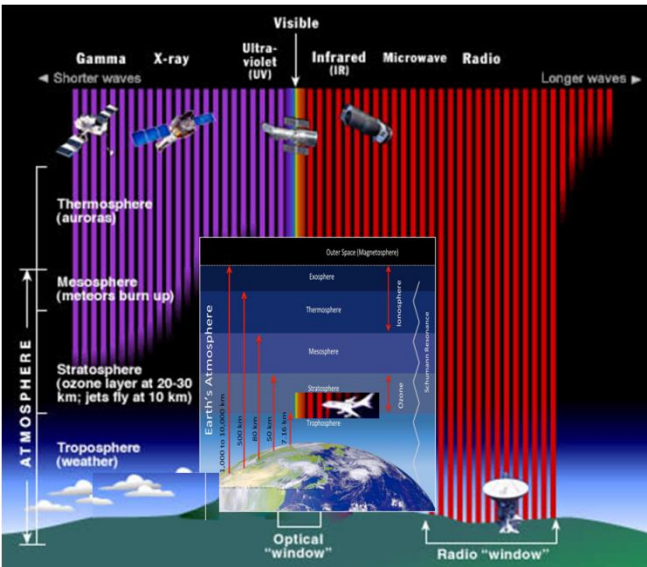
Figure 4. Extraterristrial and Terristrial Evaluations

5 CONCLUSION

This study has contributed to multidisciplinary assessments for new low - energy nuclear reaction imaging techniques designed to detect the presence of "special nuclear materials" - gun - grade uranium and plutonium - in cargo containers arriving at ports.

REFERENCES

[1]Wallace Friedberg and Kyle Copeland, Ionizing Radiation in Earth's Atmosphere and in Space Near Earth, Final Report, Federal Aviation Administration

[2] C. Brunoa, C. Dujarric, n-space nuclear propulsion, February 2013, Acta Astronautica 82(2):159–165. DOI: 10.1016/j.actaastro.2012.08.022

[3]   IEAE, The Role of Nuclear Power and Nuclear Propulsion in the Peaceful Exploration of Space, Vienna, 2005.

[4] David A. Schauer, Otha W. Linton, National Council on Radiation Protection and Measurements Report Shows Substantial Medical Exposure Increase, 01November 2009, https://doi.org/10.1148/radiol.2532090494.

[5] J. M. Clem, G. De Angelis, P. Goldhagen, J. W. Wilson, New calculations of the atmospheric cosmic radiation field—results for neutron spectra, Radiation Protection Dosimetry, Volume 110, Issue 1-4, 1 August 2004, Pages 423–428, https://doi.org/10.1093/rpd/nch175.

[6] The United States Nuclear Naval Propulsion Program, Departmant of Energy and Department of Navy, Julay 2016. https://carrierdisposaleis.com/Portals/carrierdisposaleis/ files/Gray_Book_U.S._Naval_Nuclear_Propulsion_Program_July_2016.pdf

[7] UNSCEAR (United Nations Scientific Committee on the Effects of Atomic Radiation)

[8] Report 2008 and ICRP (International Commision on Radiobiological Protection) Report 2007

New Approach to Detecting of Micro Surface Defects on Metallic Materials Using Bacteria Based Liquid Penetrant

Melise KARATAY KUTMAN[1]*, F.Zumrut BIBER MUFTULER[1], Ozge KOZGUS GULDU[1], Coşkun HARMANSAH[2]

[1] *Ege University, Department of Nuclear Applications, Institute of Nuclear Sciences, Bornova-IZMIR, TURKEY,*

[2] *Ege University, Ege Vocational School, Bornova-IZMIR, TURKEY*

*melisekaratay35@gmail.com

ABSTRACT

This study focuses on detecting micro cracks on the surface of the metallic components using Escherichia Coli (E.coli) bacteria as a liquid penetrant. Usage of bacteria based penetrant offers flexibility to liquid penetrant test with the advantages of using environmentally friendly chemicals and less steps for testing. Within this context, E.coli bacteria was conjugated with a fluorescent dye that Fluorescein Isothiocyonate (FITC). Thus, a luminescent E. coli bacteria was first prepared. Then, images of based penetrant applied to the surface of the test material were taken by fluorescence microscopy imaging by Olympus BX53 microscope. The performance of the fluorescently labeled bacteria was compared with that of a commercial penetrant. The second stage of the experimental studies, E.coli was radiolabeled with Technetium-99m (99mTc). After being radiolabeled bacteria, radiolabeling yield were calculated from radioactivity measurements which were taken with CdTe detector. The experimental studies showed that FITC-conjugated E.coli materials.

KEYWORDS - *Non Destructive Testing (NDT), 99mTc Radiolabeled, Escherichia Coli (E.coli), Liquid Penetrant (LP).*

1. INTRODUCTION

Bacteria are a group of single-cell microorganisms which they are typically several micrometers in length and have various shapes. Bacteria are present in every environment on earth. Some types can grow in soil, seawater, in the depths of the ocean, in the earth's crust, in the skin, in the intestines of animals, in radioactive wastes. Therefore, bacteria are used in many different fields in the industry because of their rapid growth and easy manipulation.

Recently, a number of researches and studies have been carried out in order to bring new approaches to conventional NDT techniques for the requirements of the industry. On the other hand, micro-scale components and their applications are rapidly becoming a part of the manufacturing process. Defects on these products can not be inspected by conventional NDT techniques. The increase in micro-scale manufacturing technology has resulted in significance trends in research and development of new methods for surface and sub-surface defects detection [1-5].

Liquid penetrant inspection is widely used to check the presence of the surface cracks in any products from the automotive industry to critical parts of the aircraft industry. For many years, this method is a simplistic standard to verify the usability of the raw materials, processed part or parts used in service [6]. The number of studies conducted on penetrant inspection techniques over the years. One of the important contributions to the literature was made by Mahendran et al. They present a methodology to visualize flaws by the naked eye using nanofluids in ferromagnetic material [7]. Siores et al studied the potential use of magnetotactic bacteria in NDT applications. This study has shown that the bacteria can be used as a penetrant for detecting very small cracks in materials [8]. In the literature, one of the remarkable studies is performed by Santos et al. In this

research, they presented a new NDT technique based on bacterial cell films to inspect micro surface cracks. Their experiments showed that bacterial cells can be used as a dye penetrant to reveal very small surface defects in stainless steel and aluminum alloy [9,10]. Recently, the use of bacteria-based applications for different forms and purposes in the industry is becoming more common. This increase has brought a new perspective on the use of bacteria for NDT techniques.

The aim of this study is to present a new bacteria as penetrant to inspect very small surface cracks. For the purpose of this, E.coli bacteria conjugated with FITC fluorescent dye for fluorimetric imaging and were radiolabeled with Technium-99m (99mTc) radioisotope. E.coli bacteria are preferred because of biosafety Level-1. 99mTc is the most common radioisotope used in medical diagnostic. It has been preferred for its properties such as short half-life and low gamma energy. This study is focused mainly on detecting small size surface defects using with fluorimetric methods and radiation measurements. In this paper, we studied the potential use of E.coli bacteria for the detection of small surface cracks on the metal parts.

2. MATERIALS AND METHODS

E.coli bacteria was conjugated with Fluorescein isothiocyanate (FITC) according to literature [11-12]. FITC-labeled E.coli bacterial suspension as a penetrant was applied to the surface of the test parts. The penetrant remains on the test part for a predetermined time (dwell time), here five minutes. After deposition of the E.coli bacterial suspension, each surface defect on the test sample was observed by fluorescence microscopy using an Olympus BX53 microscope. Table 1 column A are enlarged views of 4x in the test pieces under the fluorescence microscope.

In the second stage, E.coli bacteria were radiolabeled with Technetium-99m (99mTc) and applied to test samples and radioisotopic measurements were taken by the CdTe detector. Radioactivity measurements from these locations were performed by the CdTe detector as shown in Table.1 column B. The 99mTc radionuclide was chosen because of its short half-life and low gamma energy. On the other hand, E.coli bacteria were preferred because of their biosecurity Level-1. This feature is very important for human and environmental health [13].

Commercial penetrant is used to detect surface cracks in red penetrant metal or non-metal materials by making them visible in daylight without causing any damage to the material under examination. It is a water-washable penetrant with high contrast red-pink color, sensitivity level 1-2, Type II method A-C [14]. As shown in Table 1 column C, a commercial penetrant was used for quality control purposes.
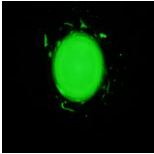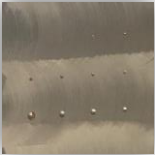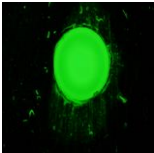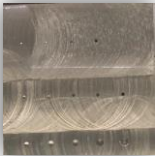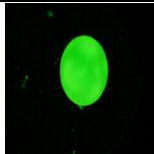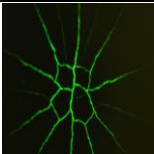
In this study, all experiments were performed on four test samples. Test pieces are aluminum alloy and commonly used in engineering applications. Defects on test pieces were artificially produced using CNC milling machine to make indentations of different sizes. This works are done by Ege University Ege Vocational School Machine Department. The PSM-5 Panel is a standart reference test specimen including 5 different test sections.

In this study; the use of bacteria as a liquid penetrant for non-destructive testing was investigated to inspect small surface defects on the test pieces. As a result of fluorimetric and radioisotopic measurements, FITC conjugated E.coli bacteria were able to detect surface defects in reference test pieces. Radiolabeled bacteria were used as a tracer to find the location where surface defects were intense. Experimental results showed that surface cracks ranging in depth from 0.25 to 0.75 mm in test pieces were successfully detected.

3.CONCLUSION

This study introduces a new approach to inspect small surface cracks using E.coli bacterial suspension. The obtained results from experiments also showed that FITC conjugated and radiolabeled with 99mTc E.coli bacteria were appropriate for examination of the surface defects. Moreover, experimental studies in this work may contribute to existing literature. The results from radioisotopic measurements and fluorescence imaging studies are consistent with each other.

Table 1. *Some surface defects detected for different penetrants in the test pieces under study.*

	A	B	C
	Inactive measurements	**Radioactive measurements**	**Commercial penetrant**
Test Material 1		15.53±0.94	
est Material 2		18.40±0.56	
Test Material 3		22.46±0.61	
PSM-5 Panel		NA	

REFERENCES

[1] Z. Deng, Y. Sun, Y. Yang, Effects of surface roughness on magnetic flux leakage testing of micro-cracks, Measurement Science and Technology, 28.4: 045003, DOI:10.1088/1361-

254

6501/aa57e1, 2017.

[2] C. Xu, X. Gong, W. Zhang, An Investigation on Eddy Current Pulsed Thermography to Detect Surface Cracks on the Tungsten Carbide Matrix of Polycrystalline Diamond Compact Bit, Applied Sciences, 7.4: 429, DOI:10.3390/app7040429, 2017.

[3] H. Khong, M.A. Amde, J. Ceesay, Application of laser shearography for detecting microcracks in concrete, 1st International Conference on Recent Advances in Concrete Technology, Washington, DC USA, Date: SEP 19-21, 2007.

[4] Daneshvar K. and Dogan B., Application of quantum dots as a fluorescent-penetrant for weld crack detection, Materials at High Temperatures, 27.3: 179-182.179-182pp., 2014.

[5] Y. Shi, L. Zhang, L. Cai, Detection of surface breaking on cylinder material using surface acoustic wave generated by scanning laser source, In: High-Power Lasers and Applications V. International Society for Optics and Photonics, p. 78431B, DOI:10.1117/12.869382, 2010.

[6] C.A.C Alba, Image acquisition and processing in an attempt to automate the fluorescent penetrant inspection, mechanical engineering, PhD Thesis, École de technologie supérieure, 2011.

[7] V. Mahendran and J. Philip, Nanofluid based optical sensor for rapid visual inspection of defects in ferromagnetic materials, Applied Physics Letters, 100.7:073104, , DOI: 10.1063/1.3684969, 2012.

[8] E. Siores, A.S. Lamb, L.M. Swallow, Bacterial magnetic particles for applications in NDT&E, detection of flaws and cracks in sample materials. In: Proc. 17th world Conf. Nondestruct. Test. p. 25-28, 2008.

[9] T.G. Santos, R.M. Miranda, C.C.C.R. Carvalho, A new NDT technique based on bacterial cells to detect micro surface defects, NDT & E International, 63:43-49, DOI: 10.1016/j.ndteint.2014.01.006, 2014.

[10] T.G. Santos, R. M. Miranda, F. Nascimento, L. Quintino, P. Vilaça, C.C. de Carvalho, Surface discontinuity detection using bacterial suspensions. Welding in the World, 59(5), 723-730. DOI:10.1007/s40194-015-0249-9, 2015.

[11] N. Nakamura, G.J. Burgess, K. Yagiuda, S. Kudo, T. Sakaguchi and T. Matsunaga, Detection and removal of escherichia coli using fluorescein isothiocyanate conjugated monoclonal antibody immobilized on bacterial magnetic particles, Analytical chemistry, 165.15: 2036-2039, DOI:10.1021/ac00063a018, 1993.

[12] S. Santra, H. Yang, D. Dutta, J.T. Stanley, P.H. Holloway, W. Tan and R.A. Mericle, TAT conjugated, FITC doped silica nanoparticles for bioimaging applications, Chemical communications, 24: 2810-2811, DOI:10.1039/b411916a, 2004.

[13] S.O.F Diniz, B.M. Resende, E.A. Nunan, C.J.R Simal, V.N. Cardoso, 99mTechnetium labelled Escherichia coli, Applied radiation and isotopes, 51(1), 33-36, DOI:10.1016/s0969-8043(98)00185-7, 1999.

[14] Ultramat, 'Penetrant ve Developer', http://ultramat.com.tr/ (access time: 16 Oct. 2017).

Synthesis and Characterization of ICG Loaded Silica Nanoparticles for Detection of Sentinel Lymph Node

Ahmet BILGI[2], Ozge KOZGUS GULDU[1], Emin Ilker MEDINE[1], Hazal TOSUN[1], Dilek TASKIRAN[3], Mustafa Cosan TEREK[2]

[1]*Ege University, Institute of Nuclear Sciences, Department of Nuclear Application, Izmir - TURKEY*
[2]*Ege University, School of Medicine, Department of Obstetrics and Gynecology, Izmir - TURKEY*
[3]*Ege University, School of Medicine, Department of Physiology, Izmir – TURKEY*
*ozgekzgs@gmail.com

ABSTRACT

In this study, mesoporous silica nanoparticles (MSN) as a multifunctional biocompatible probe were used. Solution-based synthesis method was used that followed by structure directing agent removal. MSN samples were characterized by Scanning Electron Microscopy (SEM), Dinamic Light Scattering (DLS) and Fourier Transform Infrared Spectroscopy (FTIR) analyzes. As a result of DLS and SEM analyzes, it was found that MSN were synthesized homogeneous size and dispersity, the average size of 36-58 nm.

Fluorescent dyes are encapsulated into MSN in order to provide optical imaging. Indocyanine green (ICG) used as the fluorescent dye was encapsulated to MSN and endowed relatively durable fluorescence characteristic. Encapsulation of such kind of dyes with silica nanoparticles contributes to their long-term monitoring in vivo, increases their chemical stability and biocompatibility, and significantly reduces their damping and degradation.

All experimental results suggest that ICG/MSN can be used for in vivo applications and imaging.

KEYWORDS - Indocyanine green (ICG), Silica nanoparticles, Sentinel lymph node.

1.INTRODUCTION

Sentinel lymph node detection is an emerging practice that is increasingly prevalent in oncologic surgery. A lymph node is a tumor nodule that is marked as a sentinel lymph node. Determining sentinel lymph nodes is an application that avoids unnecessary and over-invasive procedures in oncologic patients, reduces the additional morbidity rate associated with surgery in the patient, and uses daily routines as a procedure that serves the completion of the minimum necessary surgeon. Sentinel lymph node detection applications are performed on gynecologic oncology with methylene blue and indocyanine green (ICG) molecules, and sensitivities for determining the sentinel lymph node range from 70% to 90% in various studies.

Imaging techniques are crucial for early tumor detection and treatment. Fluorescence imaging technology provides clear results in biological and medical applications. New generation probes show tissue weakening and autofluorescence from non-targeted tissue by reducing off-target residues in the NIR region (650-900 nm).

Early diagnosis of cancer is very important for the success of cancer treatment. Early detection of cancer is inadequate with traditional methods. To nanotechnological developments, nanoscale materials can be used to detect cancerous tissues by gaining magnetic and optical properties.

MSN has great potential in improving the drug yield of water-insoluble and poorly permeable drugs. There has been great potential in the implementation of MSN as targeted drug delivery vehicles for anti-cancer drugs [1]. MSN has been recognized as a good drug carrier due to its easy synthesis, morphology, pore size, good stability and diversity of surface functionality [2].

256

The physiological and physical properties of ICG were first described by Fox and Wood in 1960. It has been widely used by cardiologists for cardiac flow studies since the 1960s. Since a sulfate group is attached to each polycyclic moiety, it becomes molecularly hydrophilic. It exhibits an emission maximum of around 800 nm [3].

2   MATERIALS AND METHODS
2.1   Synthesis of Mesoporous Silica Nanoparticles (MSN)

N-cetyltrimethylammonium bromide (CTAB) and triethanolamine (TEA) were used for mesoporous structure of silica nanoparticles (MSN). 1 g CTAB and 70 TEL TEA were placed in a three-necked flask and mixed for 1 hour. At the end of the period, 1.5 mL of tetraethyl orthosilicate (TEOS) was added dropwise and stirred for a further 1 hour. The resulting white mixture was allowed to cool for a while. After cooling, it was washed twice with 20 mL of ethanol to remove any unreacted material. APTES (3-Aminopropyltriethoxysilane) was used to modify the surface of MSN with amine groups. The synthesized MSNs were stirred under reflux for 12 hours at 80 °C in 50 mL ethanol and 1 mL APTES. MSN-NH2 was obtained. Precipitated nanoparticles Fourier Transform Infrared Spectroscopy (FTIR) was performed for structure analysis. The relevant FTIR results are given in Figure 1.

Peak (cm^{-1})	Strecht
3400–3600	SiO-H
2195	-CH-
1180	Si-O-Si
960	Si-O-Si
630	Si-O-Si
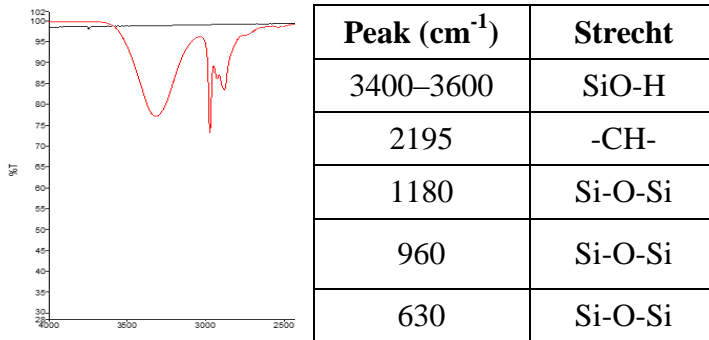
Figure 1. FTIR spectrum of MSN and peak stretches

In the spectrum of the prepared sample, Si-OH groups and Si-O bond were found in 460 cm-1 and 967 cm-1 bands respectively as in previous studies [4, 5].

The hydrodynamic diameter was 76.38 ± 28.16 and monodisperse by DLS. The hydrodynamic diameters of synthesized MSN found by DLS analysis are consistent with the literature. [6].

Size and surface morphology analyzes of MSN were examined by taking SEM images at Ege University MATAL. As a result of the analysis, the presence of nanoparticles with a diameter of 36-58 nm was observed (Figure 2). The size and shape were harmonic with literature [7, 8].

257
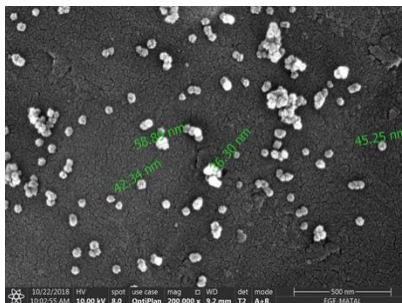
Figure 2. *SEM image of MSN*

2.2   Determination of ICG loading capacity on MSN

1mg/mL ICG aqueous solution was prepared. 100 µg ICG and 5 mL of ultra-pure water were added over 5 mg of MSN-NH2-DTPA and stirred at room temperature for 4 hours.

After loading the ICG, washing was carried out 3 times with distilled water. The supernatants obtained after each wash were collected. ICG standard solutions were prepared and a calibration graph was created. Supernatants obtained after washing with standard solutions were measured spectrophotometrically at a wavelength of 800 nm and the loading capacity was calculated.

Loading capacity as a result of ICG upload to MSN 77.11% ± 1.50 It was found as. This shows that mesoporous structures have a high level of attitude towards ICG. After loading ICG into MSN, the amount of ICG released from the nanoparticle was calculated. ICG release calculated within 24 hours 34.01% ± 1.97. After 24 hours, the amount of ICG loaded in the sample was 50.88% ± 1.95.

3.   CONCLUSION

In this study MSN-NH2-DTPA-ICG was synthesized by chelating MSN with DTPA. As a result, MSNs were chelated with DTPA and loaded into ICG into a fluorescent molecule. All these results are thought to contribute to the creation of new diagnostic and especially the creation of sentinel lymph node imaging systems.

REFERENCES

[1] V. Mamaeva, J. M. Rosenholm, L. T. Bate-Eya, L. Bergman, E. Peuhu, A. Duchanoy, C. Sahlgren, Mesoporous silica nanoparticles as drug delivery systems for targeted inhibition of Notch signaling in cancer. Molecular Therapy (2011) 19(8), 1538-1546. DOI. 10.1038/mt.2011.105.

[2] F. Tang, L. Li, D. Chen, Mesoporous silica nanoparticles: synthesis, biocompatibility and drug delivery. Advanced materials (2012) 24(12), 1504-1534. DOI. 10.1002/adma.201104763.

[3] S. L. Owens, Indocyanine green angiography. The British journal of ophthalmology (1996) 80(3), 263. DOI. 10.1136/bjo.80.3.263.

[4] M. Qasim, J. Ananthaiah, S. Dhara, P. Paik, D. Das, Synthesis and characterization of ultra-fine colloidal silica nanoparticles. Advanced Science, Engineering and Medicine (2014) 6(9), 965-973. DOI. 10.1166/asem.2014.1578.

[5] S. Santra, P. Zhang, K. Wang, R. Tapec, W. Tan, Conjugation of biomolecules with luminophore-doped silica nanoparticles for photostable biomarkers. Analytical chemistry (2001) 73(20), 4988-4993. DOI. 10.1021/ac010406+.

[6] L. Qiao, X. Wang, Y.Gao, Q. Wei, W. Hu, L. Wu, Q. Wang, Laccase-mediated formation of mesoporous silica nanoparticle based redox stimuli-responsive hybrid nanogels as a

multifunctional nanotheranostic agent. Nanoscale (2016) 8(39), 17241-17249. DOI. 10.1039/C6NR05943K.

[7] Y. Zhang, Z. Zhi, T. Jiang, J. Zhang, Z. Wang, S. Wang, Spherical mesoporous silica nanoparticles for loading and release of the poorly water-soluble drug telmisartan. Journal of Controlled Release (2010) 145(3), 257-263. DOI. 10.1016/j.jconrel.2010.04.029.

[8] C. Tao, Y. Zhu, X. Li, N. Hanagata, Binding of CpG oligodeoxynucleotides to mesoporous silica nanoparticles for enhancing delivery efficiency. Microporous and Mesoporous Materials (2015) 204, 91-98. DOI. 10.1016/j.micromeso.2014.11.007.

Investigation of Foaming Additives and Usage Rates for the Production of Ultra-Light Foam Glass

Metin DAVRAZ[1]*, Ali Ekrem AKDAĞ[2], Murat KORU[3], Şemsettin KILINÇARSLAN[4], Yunus Emre DELİKANLI[5], Mehmet ÇABUK[6]

[1]*Isparta University of Applied Science, Senirkent Vocational School, Dep. of Construction, Isparta-TURKEY*
[2]*Isparta University of Applied Science, Vocational School of Technical Science, Isparta-TURKEY*
[3]*Isparta University of Applied Science, Technology Faculty, Dept. of Mechanical Engineering, Isparta-TURKEY*
[4]*Suleyman Demirel University, Engineering Faculty, Dept. of Civil Engineering, Isparta-TURKEY*
[5]*Isparta University of Applied Science, Senirkent Vocational School, Dep. of Machinery, Isparta-TURKEY*
[6]*Isparta University of Applied Science, Senirkent Vocational School, Dep. of Machinery, Isparta-TURKEY*
** metindavraz@isparta.edu.t*r

ABSTRACT

In this study, production possibilities of foam glass having a apparent density of < 200 kg/m3 from waste glass powders ground to grain size <150 µm were investigated. In the research, glass powders obtained from waste window glasses and waste soda bottles were used as fillers, and sodium silicate, silicon carbide, carbide and glycerin were used as foaming agents. The samples were sintered in an ash oven at 875 °C for 25 minutes and then cooled at 10 °C / min. The volumes of the foam glass samples obtained were determined, their masses were measured with precision scales and then their density was calculated. The pore diameters and morphology of the samples were examined by scanning electron microscopy. The compressive strengths of glass foam samples were tested and thermal conductivity coefficients were measured by heat flow meter method. As a result, the chemical structure of the waste glass, optimum foaming additives and their proportions were determined for the production of ultra-light foam glass.

KEYWORDS: Foam Glass, Foaming Additive, Apparent Density, Thermal Conductivity

1. INTRODUCTION

Porous glass foams, which are thermal insulation and sound-insulation materials, have attracted great attention and are applied in many areas such as buildings, high temperature applications and defense areas [1]. Glass foams have excellent features such as, low density, low thermal conductivity, fireproof, etc. Foam glass is usually produced using gas-releasing materials called foaming agents [2].

The most important properties of the foam glass produced are density, thermal conductivity and mechanical strength. The relative density of the foam glass (ρrel) is the ratio of the bulk density (ρb) containing the pores to the powder density (ρ) which is the density of the solid forming the walls of the cells. It has been proved that the compressive strength of the foam glass increases with increasing relative density [3].

In this study, it is aimed to produce foam glass with sufficient strength and low thermal conductivity. Moreover, the effects of different auxiliary foaming agents on density, compressive strength and thermal conductivity of foam glass produced from waste soda and window glass were investigated.

2. MATERIALS AND METHODS

In this study, firstly, the effects of various types of foaming agents (FA) used together with sodium silicate on the physical and mechanical properties of glass foam (GF) samples were investigated. Soda bottle glass (WGP A) and window-glass (WGP B) were used as waste glass powder (WGP). The waste glasses were broken in the jaw crusher, grinded in a ball mill and then sieved to a particle size of $\leq 150 \square$m. Chemical properties of WGPs were determined by XRF method in Afyon Kocatepe University Technology Research and Application Center (AKU TAUM) Laboratory and given in Table 1.

Table 1. Chemical analyses of WGP

Component	WGP·A	WGP·B
SiO_2	65,68	68,44
Al_2O_3	2,53	1,40
CaO	13,25	10,59
Fe_2O_3	0,94	0,31
MgO	3,51	4,39
Na_2O	12,30	13,75
K_2O	0,57	0,47
Others	0,60	0,39
LOI	0,61	0,26

The main foaming agent used in the production of GF is sodium silicate (SS; Na2SiO3). Silicon carbide (SiC), carbide (CaC2), and glycerin (GLS; C3H8O3) were used as auxiliary foaming agent. The densities of all solid raw materials were determined by gas pycnometer (Micromeritics Accupyc II 1340) according to ASTM D 5550-06 standard [4]. Furthermore, WGP particle size and specific surface area were measured with Bettersizer device in AKU TUAM. The physical properties of WGPs and FAs are given in Table 2.

Table 2. The physical properties of WGP and Fas

Raw Material	Density(kg/m^3)
WGP-A (<150 μm)	2545
WGP-B (<150 μm)	2506
SiC	3214
CaC_2	2440
SS	1357
GLS	1258

In the first stage of GF sample production, waste glass, glass water and foaming agents were mixed in certain proportions (Table 3). The mixture was compressed in a 30 mm diameter cylinder mold and dried in a microwave oven until it reached constant mass. The dried samples were sintered in an ash furnace (25 L) at 875oC for 25 minutes. The temperature rise of the ash furnace was set to 10oC/min. The cooling rate of sintered samples was set to 20oC/min up to 600oC and then to 2oC/min. The masses of the GF samples were weighed with a precision scale of 1/100 g and their volumes were determined with the help of fine silica sand. The samples prepared in the second stage were sintered in a 200x100x100 mm steel mold in an ash furnace with 500 L at 875oC for 25 min. From each GF sample produced at this stage, 3 pieces of 40 mm cubes for compressive strength ($\square$10) test and 60 mm diameter and 25 mm thickness cylindrical specimens were prepared for thermal conductivity test. The compressive strength of the samples (at 10% strain) was determined in accordance with TS EN 826 [5] standard and their thermal conductivity

was determined in accordance with TS EN 12667 [6] standard. Thermal conductivity measurements were performed with Fox 50 device according to heat flow meter method.

Table 3. Components of the samples

Sample No	WGP		SS	FA	
	Type	%	%	Type	%
1	A	83	15	Glycerin	2
2	A	83	15	SiC	2
3	A	83	15	Carbide	2
4	B	83	15	Glycerin	2
5	B	83	15	SiC	2
6	B	83	15	Carbide	2

3. RESULTS

In order to determine the optimum type of WGP and auxiliary FA, the volumes of the GF samples produced in the first stage were determined and then their density was calculated. SiC and carbide agent used as foaming agent with waste soda glass failed and production was not realized. Therefore, the results of soda glass and glycerin agent samples are given in the table. Obtained results were given in Table 4. After the sintering, samples were cooled to room temperature (cooling rate of 5 °C/min). The volumes of the monoper samples obtained at this stage were determined and their apparent densities were calculated. All properties of the samples were given in Table 5.

Table 4. Densities of GF samples produced

Sample No	Mass (g)	V (cm³)				D (kg/m³)
		1	2	3	Avg.	
1	21,2	62,56	62,86	62,35	62,59	339
4	21,5	102,55	103,15	103,69	103,13	208
5	22,2	65,01	64,55	63,13	64,23	345
6	21,6	43,12	42,13	41,15	42,13	513

Table 5. Mechanical, Physical and Thermal test results

Sample	σ (kPa)	λ (mW/mK)
1	570	94
4	515	64
5	794	79
6	1074	98

4. CONCLUSIONS AND DISCUSSIONS

In this study, it was aimed to produce foam glass by using waste soda glass and waste window glass, sodium silicate and foam agent. Glycerin, SiC and carbide were used as foaming agents.

262

As a result; waste soda glass was successful only if glycerin foaming agent was used, but compressive strength and thermal conductivity values gave worse results than waste window glass. The best result of the glass foam samples produced from waste window glass gave glycerin foam agent. In this example, both the density and compressive strength and thermal conductivity values were better than those produced with other foaming agents.

ACKNOWLEDGEMENT

REFERENCES

[1] E. Bernardo, R. Castellan, S. Hreglichb, I. Lancellottic, Sintered sanidine glass-ceramics from industrial wastes, J. Eur. Ceram. Soc. 26 (15), 3335-3341, doi.org/10.1016/j.ceramint.2007.10.019, 2006.

[2] G. Scarinci, G. Brusatin, E. Bernardo, Glass foams. Cellular Ceramics: Structure, Manufacturing, Properties and Applications, Wiley-VCH, 158-176, 2006.

[3] L. J. Gibson, M. F. Ashby, Cellular solids: structure and properties, Cambridge university press, 1999.

[4] ASTM D 5550-06, Standard Test Method for Specific Gravity of Soil Solids by Gas Pycnometer, ASTM International, West Conshohocken, PA, 2006.

[5] TS EN 826, Thermal Insulating Products for Building Applications-Determination of Compression Behaviour, Turkish Standard Institute, Ankara, Turkey, 2013.

[6] TS EN 12667, Thermal Performance of Building Materials And Products - Determination of Thermal Resistance by means of Guarded Hot Plate and Heat Flow Meter Methods -Products of High and Medium Thermal Resistance, Turkish Standard Institute, Ankara, Turkey, 2003.

[7] G. Brusatin, E. Bernardo, G. Scarinci, Production of foam glass from glass waste, In Sustainable Waste Management and Recycling. Proc. of the International Conference Organized by the Concrete and Masonry Research, Kingston University, London, UK, Thomas Telford Publishing, 67-82, 2004.

[8] J. S. Morgan, J. L. Wood, R. C. Bradt, Cell size effects on the strength of foamed glass, Materials Science and Engineering, 47(1), 37-42, 1981.

[9] D. M. Abdel Alim, Production and characterization of foam glass from container glass waste (MSc dissertation, The American University in Cairo AUC), 2009.

[10] F. Méar, P. Yot, R. Viennois, M. Ribes, Mechanical behaviour and thermal and electrical properties of foam glass, Ceramics international, 33(4), 543-550, 2007.

A Fractional Order Diabetes Model with Atangana-Baleanu Derivative

Sümeyra UÇAR[*], Necati ÖZDEMİR
Balıkesir University, Department of Mathematics, Balıkesir, Turkey
*sumeyraucar@balikesir.edu.tr

ABSTRACT

In this work, we aim to study some existence results for a diabetes model and its complications which are enlarged by Atangana-Baleanu derivative defined with Mittag-Leffler kernel. Benefiting from the fixed point theory and Picard-Lindelof approach, we present a comprehensive analysis of the gained outcomes.

KEYWORDS - *Fixed point theory, fractional calculus, mathematical model.*

1. INTRODUCTION

In the last few decades, fractional calculus plays an important role to characterize many problems in physics, biology, medicine, control theory etc. For this reason, there are several fractional derivatives such as Riemann-Liouville (RL) and Caputo operators which are the most conventional ones [1-11]. Even though these derivatives describe real world phenomena as more accurately than the integer order derivatives, the singularity arising from their kernel functions leads to many weaknesses. In order to overcome these weaknesses, Atangana and Baleanu [12] has been introduced Atangana-Baleanu (AB) derivative which is a new non-singular derivative with Mittag-Leffler kernel. In this work, we study a diabetes model in term of the newly-defined AB derivative.

Here, we deal with a classical diabetes model and its complication introduced by [13] of the following integer order form:

$$\frac{dD(t)}{dt} = I - (\lambda + \mu)D + \gamma C,$$

$$\frac{dC(t)}{dt} = I + \lambda D - (\gamma + \mu + \upsilon + \delta)C,$$

where I shows the emergence of diabetes mellitus, D indicates the no of diabetics with no complications at time t, C stands for the no of diabetics with complications. γ indicates the ratio of healing complications, μ indicates the ratio of natural mortality, υ shows the ratio where diabetic patients with complication converts critically disabled, λ denotes the probability of a diabetic person spreading a complication and δ stands for the mortality ratio because of complications. Regarding $N(t) = C(t) + D(t)$, we find

$$\frac{dC(t)}{dt} = -(\lambda + \theta)C + \lambda N,$$

$$\frac{dN(t)}{dt} = I - (\upsilon + \delta)C - \mu N,$$

where $\theta = \gamma + \mu + \upsilon + \delta$ with the initial conditions $C(0) = C_0$, $N(0) = N_0$.

2. BASIC DEFINITIONS AND PRELIMINARIES

In this part, we give some fundamental definitions which are useful in the succeeding chapters.

Definition 1 *Let* $a < b$, $g \in H^1(a,b)$ *be a function and* $\sigma \in [0,1]$. *Then AB derivative in Caputo type of order* ζ *of* g *is given by [12]*

$$_a^{ABC} D_t^\sigma \left[g(t) \right] = \frac{B(\sigma)}{1-\sigma} \int_a^t g'(x) E_\sigma \left[-\sigma \frac{(t-x)^\sigma}{1-\sigma} \right] dx,$$

where $B(\sigma)$ is a normalization function with $B(0) = B(1) = 1$.

Definition 2 *Let* $a < b$, $g \in H^1(a,b)$ *be a function and* $\sigma \in [0,1]$. *Then AB derivative in RL type of order* σ *of* g *is given by [12]:*

$$_a^{ABR} D_t^\sigma \left[g(t) \right] = \frac{B(\sigma)}{1-\sigma} \frac{d}{dt} \int_a^t g(x) E_\sigma \left[-\sigma \frac{(t-x)^\sigma}{1-\sigma} \right] dx.$$

Definition 3 *The fractional integral associated to the AB fractional derivative is given by [12]:*

$$_a^{AB} I_t^\sigma \left[g(t) \right] = \frac{1-\sigma}{B(\sigma)} g(t) + \frac{\sigma}{B(\sigma)\Gamma(\sigma)} \int_a^t g(\lambda)(t-\lambda)^{\sigma-1} d\lambda.$$

3. DIABETES MODEL WITH FRACTIONAL ORDER

In this section, we rearrange the diabetes model given in [13] in terms of AB derivative:

$$_0^{ABC} D_t^\sigma \left(C(t) \right) = -(\lambda + \theta)C + \lambda N,$$
$$_0^{ABC} D_t^\sigma \left(N(t) \right) = I - (\upsilon + \delta)C - \mu N.$$

with the initial conditions $C(0) = C_0$, $N(0) = N_0$ and where $_0^{ABC} D_t^\sigma$ is AB derivative in Caputo type.

The above system is equivalent to the followings:

$$C(t) - h_1(t) = \frac{1-\sigma}{B(\sigma)} \left\{ -(\lambda + \theta)C(t) + \lambda N(t) \right\}$$

$$+ \frac{\sigma}{B(\sigma)\Gamma(\sigma)} \int_0^t (t-\lambda)^{\sigma-1} \left\{ -(\lambda + \theta)C(t) + \lambda N(t) \right\} d\lambda,$$

$$N(t) - h_2(t) = \frac{1-\sigma}{B(\sigma)} \left\{ I - (\upsilon + \delta)C(t) - \mu N(t) \right\}$$

$$+ \frac{\sigma}{B(\sigma)\Gamma(\sigma)} \int_0^t (t-\lambda)^{\sigma-1} \left\{ I - (\upsilon + \delta)C(t) - \mu N(t) \right\} d\lambda.$$

Iteratively, the above can be given as

$$C_0(t) = h_1(t),$$

265

$$N_0(t) = h_2(t).$$

and

$$C_{n+1}(t) = \frac{1-\sigma}{B(\sigma)} \times \left\{ -(\lambda+\theta)C_n(t) + \lambda N_n(t) \right\}$$

$$+ \frac{\sigma}{B(\sigma)\Gamma(\sigma)} \int_0^t (t-\lambda)^{\sigma-1} \left\{ -(\lambda+\theta)C_n(t) + \lambda N_n(t) \right\} d\lambda,$$

$$N_{n+1}(t) = \frac{1-\sigma}{B(\sigma)} \times \left\{ I - (\upsilon+\delta)C_n(t) - \mu N_n(t) \right\}$$

$$+ \frac{\sigma}{B(\sigma)\Gamma(\sigma)} \int_0^t (t-\lambda)^{\sigma-1} \left\{ I - (\upsilon+\delta)C_n(t) - \mu N_n(t) \right\} d\lambda.$$

For a large value of n, if we take the limit we hope to get the exact solution of equation. Finally, the system (4) has a unique set of solution.

4. USING PICARD-LINDELOF METHOD TO PROVE THE EXISTENCE OF SOLUTIONS

Here, we state the operator of the following form:

$$n_1(t,C) = -(\lambda+\theta)C(t) + \lambda N(t),$$
$$n_2(t,N) = I - (\upsilon+\delta)C(t) - \mu N(t),$$

where n_1, n_2 are contraction with reference to the functions C and N. Let

$$M_1 = \sup_{C[a,b_1]} \left\| n_1(t,C) \right\|,$$

$$M_2 = \sup_{C[a,b_2]} \left\| n_2(t,N) \right\|.$$

where

$$C[a,b_1] = [t-a,t+a] \times [x-b_1, x+b_1] = A \times B_1,$$
$$C[a,b_2] = [t-a,t+a] \times [x-b_2, x+b_2] = A \times B_2.$$

We apply Banach-fixed point theorem using the metric on $C[a,b_i]$ $(i=1,2)$ with the norm:

$$\left\| f(t) \right\| = \sup_{t \in [t-a,t+a]} \left| f(t) \right|.$$

(11)

Now, we consider Picard's operator

$$\varphi : C(A, B_1, B_2) \to C(A, B_1, B_2)$$

given by

266

$$\varphi X(t) = X_0(t) + X(t)\frac{1-\sigma}{B(\sigma)} + \frac{\sigma}{B(\sigma)\Gamma(\sigma)}\int_0^t (t-\lambda)^{\sigma-1} F(\lambda, X(\lambda))d\lambda$$

where

$$X(t) = \begin{bmatrix} C(t) & N(t) \end{bmatrix}^T,$$

$$X_0(t) = \begin{bmatrix} C(0) & N(0) \end{bmatrix}^T,$$

$$F(t, X(t)) = \begin{bmatrix} n_1(t, C(t)) & n_2(t, N(t)) \end{bmatrix}^T.$$

Suppose that the following inequality satisfied

$$\|X(t)\| \le \{b_1, b_2\}.$$

(13)

We think

$$\|\varphi X(t) - X_0(t)\| = \left\| \frac{1-\sigma}{B(\sigma)} F(t, X(t)) + \frac{\sigma}{B(\sigma)\Gamma(\sigma)}\int_0^t (t-\lambda)^{\sigma-1} F(\lambda, X(\lambda))d\lambda \right\|$$

$$\le \frac{1-\sigma}{B(\sigma)}\|F(t, X(t))\| + \frac{\sigma}{B(\sigma)\Gamma(\sigma)}\int_0^t (t-\lambda)^{\sigma-1}\|F(\lambda, X(\lambda))\|d\lambda$$

$$\le \frac{1-\sigma}{B(\sigma)} M + \frac{\sigma}{B(\sigma)} Ma^\sigma$$

where $M = \max\{M_1, M_2\}$. Let $b = \max\{b_1, b_2\}$ and $a < \dfrac{b}{M}$. So, we have

$\|\varphi X(t) - X_0(t)\| < aM < b.$ Also, we get the following

$$\|\varphi X_1 - \varphi X_2\| = \sup_{t \in A}|X_1 - X_2|.$$

Then, we obtain

$$\|\varphi X_1 - \varphi X_2\| = \left\| \frac{1-\sigma}{B(\sigma)}\big(F(t, X_1(t)) - F(t, X_2(t))\big)\right.$$

$$\left. + \frac{\sigma}{B(\sigma)\Gamma(\sigma)}\int_0^t (t-\lambda)^{\sigma-1}\big(F(\lambda, X_1(\lambda)) - F(\lambda, X_2(\lambda))\big)d\lambda \right\|$$

$$\le \frac{1-\sigma}{B(\sigma)} q\|X_1(t) - X_2(t)\|$$

$$+ \frac{\sigma q}{B(\sigma)\Gamma(\sigma)}\int_0^t (t-\lambda)^{\sigma-1}\|X_1(\lambda) - X_2(\lambda)\|d\lambda$$

267

$$\leq \left(\frac{1-\sigma}{B(\sigma)} q + \frac{\sigma q a^{\sigma}}{B(\sigma)\Gamma(\sigma)} \right) \|X_1(t) - X_2(t)\|$$

$$\leq aq \|X_1(t) - X_2(t)\|$$

with $q < 1$. Since F is contraction, we get $aq < 1$; and thus φ is a contraction. Finally the system (4) has a unique set of solution.

5. CONCLUDING REMARKS

Diabetes mellitus plays a leading role in the occurrence of many fatal diseases and is a very common type of disease all over the world. For this reason, researchers in several disciplines use mathematical models of diabetes ([13,14] and references therein). In this study, we prove the existence of solutions for a fractional diabetes model and its complications by means of fixed point theory.

REFERENCES

[1] N. Özdemir, D. Karadeniz, B.B. Iskender, Fractional optimal control problem of a distributed system in cylindrical coordinates, Physics Letters A 373 (2009) 221-226. *DOI: 10.1016/j.physleta.2008.11.019*

[2] N. Özdemir, O.P. Agrawal, B.B. Iskender, D. Karadeniz, Fractional optimal control of a 2-dimensional distributed system using eigenfunctions, Nonlinear Dynamics 55 (2009) 251-260. *DOI: 10.1007/s11071-008-9360-4*

[3] F. Evirgen, N. Özdemir, Multistage adomian decomposition method for solving NLP problems over a nonlinear fractional dynamical system, Journal of Computational and Nonlinear Dynamics 6 (2010) 6pages. *DOI: 10.1115/1.4002393*

[4] D. Baleanu, K. Diethelm, E. Scalas, J.J. Trujillo, Fractional calculus models and numerical methods. World Scientific, 2012.

[5] F. Evirgen, Analyze the optimal solutions of optimization problems by means of fractional gradient based system using VIM. An International Journal of Optimization and Control: Theories & Applications (IJOCTA) 6 (2016) 75-83. *DOI: 10.11121/ijocta.01.2016.00317*

[6] Z. Hammouch, T. Mekkaoui, Circuit design and simulation for the fractional-order chaotic behavior in a new dynamical system. Complex & Intelligent Systems 4 (2018) 251-260. *DOI:10.1007/s40747-018-0070-3*

[7] H.M. Başkonuş, T. Mekkaoui, Z. Hammouch, H. Bulut, Active control of a chaotic fractional order economic system, Entropy 17 (2015) 5771-5783. *DOI: 10.3390/e17085771*

[8] E. Uçar, N. Özdemir, E. Altun, Fractional order model of immune cells influenced by cancer cells, Mathematical Modelling of Natural Phenomena 14 (2019) 12pages. *DOI: 10.1051/mmnp/2019002*

[9] N. Özdemir, M. Yavuz, Numerical Solution of fractional Black-Scholes equation by using the multivariate Pade approximation, Acta Physica Polonica A 132 (2016) 1050-1053. *DOI: 10.12693/APhysPolA.132.1050*

[10] D. Baleanu, A. Fernandez, On some new properties of fractional derivatives with Mittag-Leffler kernel, Communications in Nonlinear Science and Numerical Simulation 59 (2018) 444-462. *DOI: 10.1016/j.cnsns.2017.12.003*

[11] S. Uçar, E. Uçar, N. Özdemir, Z. Hammouch, Mathematical analysis and numerical simulation for a smoking model with Atangana-Baleanu derivative, Chaos, Solitons & Fractals 118 (2019) 300-306. *DOI: 10.1016/j.chaos.2018.12.003*

268

[12] Atangana A, Baleanu D. New fractional derivatives with non-local and non-singular kernel: theory and applications to heat transfer model. Thermal Science 20 (2016) 763-769.

[13] A. Boutayeb, E. H. Twizell, K. Achouayb, A. Chetouani, A mathematical model for the burden of diabetes and its complications. BioMedical Engineering OnLine 3 (2004). *DOI: 10.1186/1475-925X-3-20*

[14] J. Singh, D. Kumar, D. Baleanu, On the analysis of fractional diabetes model with exponential law, Advances in Difference Equations, 231 (2018). *DOI: 10.1186/s13662-018-1680-1*

269

Feasibility of Gravity Drainage Process in Offshore Heavy Oil Reservoirs with Bottom Water

Cheng WANG[1*], Liguo ZHONG[1], Tongchun HAO[1], Jian ZOU[2] and Qiuxia WANG[2]

[1]*China University of Petroleum(Beijing), Beijing, China*
[2]*Tianjin Subcompany of CNOOC, Tianjin, China*
* sygc156@163.com

ABSTRACT

Developing heavy oil economically from reservoirs containing bottom water is one of the most challenging technical problems in Bohai offshore oilfield. Gravity drainage shows economic potential of developing heavy oil from reservoirs where recovery is limited by water coning. In this paper, gravity drainage performance, including SAGD and MFAGD (multiple thermal fluids assisted gravity drainage), in heavy oil reservoir with bottom water was numerically studied. Results indicated that gravity drainage can produce heavy oil reservoirs with bottom water effectively, and water produced from the aquifer can be greatly reduced by operating the production wells at pressure close to that of the aquifer and increasing the distance between the production well and the oil-water interface. The cumulative oil recovery varied from 44% (water-oil volume ratio is 10) to 66% (no bottom water) of OOIP. The thickness of the bottom water and the well configurations had a significant effect on the cumulative oil recovery. The optimal way to develop heavy oil reservoirs with bottom water is SAGD-MFAGD, which means SAGD first, and then switch to MFAGD when the steam chamber reach to the top of the reservoir.

KEYWORDS - *Gravity drainage, Offshore heavy oil, Bottom water, Numerical simulation*

1. INTRODUCTION

Developing and producing heavy oil economically from reservoirs containing bottom water is one of the most challenging technical problems in Bohai offshore oilfield [1, 2]. Gravity drainage, which use parallel horizontal wells, with horizontal production wells near the bottom of the reservoir and horizontal injection wells near to the top of the reservoir, shows economic potential of developing heavy oil from reservoirs where recovery is limited by water coning.

In this paper, gravity drainage performance, including SAGD and MFAGD (multiple thermal fluids assisted gravity drainage) [3-5], in heavy oil reservoir with bottom water was numerically studied. The study compared the characteristics of SAGD and MFAGD at different stages, and investigated the effects of steam injection rate and pressure, gas-water ratio (in MFAGD), bottom water thickness, and the location of the wells. Thereafter, a set of numerical simulations were performed to optimize the best way to develop heavy oil reservoirs with bottom water.

2. NUMERICAL MODEL

On the basis of the LD5-2N offshore oilfield geological characteristics, a numerical simulation model with bottom water was established using CMG STARS thermal simulator. The numerical simulation model is shown in Fig. 1, and the basic parameters are listed in Table 1. This reservoir model has a 101×10×30 grid system, and the grid spacing is 1 m, 30 m, and 1 m, respectively. There are 2 horizontal wells in this model and both of the horizontal wells have a 300 m horizontal wellbore.

Table 1. *Basic physical parameters of numberical simulation*

| Items	Value	Items	Value
Mid depth of reservoir (m)	1015	Thickness of the reservoir (m)	30
Initial reservoir pressure (MPa)	10	Porosity	0.33
Viscosity of heavy oil at 51℃ (mPa·s)	20380	Horizontal permeability (mD)	3000
Initial oil saturation	0.68	Kv/Kh	0.8
Initial reservoir temperature (℃)	51	Length of horizontal well (m)	300
Solution gas oil ratio (m³/m³)	8	Diameter of horizontal well (m)	0.185
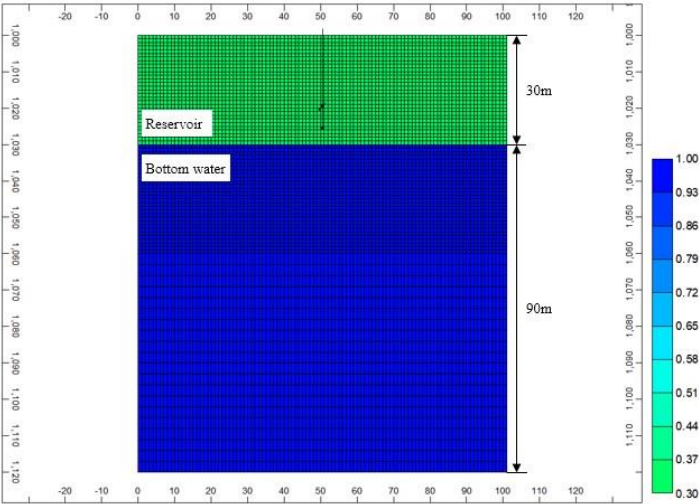
Figure1. *The reservoir numberical model*
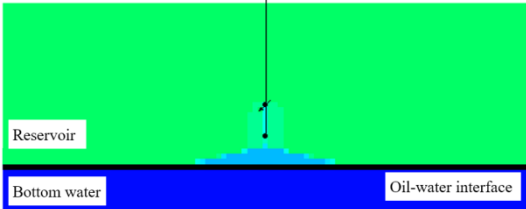
3. RESULTS AND ANALYSIS

Gravity drainage can produce heavy oil reservoirs with bottom water effectively, and water produced from the aquifer can be greatly reduced by operating the production wells at pressure close to that of the aquifer and increasing the distance between the production well and the oil-water interface.

271

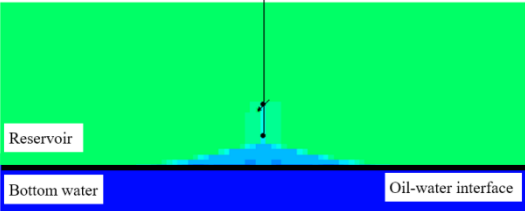***Table 2.*** *Volume of water coning in different numberical simulations*

Development mode	Oli water volume ratio	Distance between production well and the oil-water interface	Volume of water coning
SAGD	3	5m	4500m^3
SAGD	5	5m	8400m^3
SAGD	10	5m	16500m^3
SAGD	10	10m	8100m^3
SAGD	5	7m	5400m^3
SAGD	5	10m	2700m^3
MFAGD	5	5m	7200m^3
MFAGD	10	5m	11500m^3
MFAGD	10	10m	6300m^3
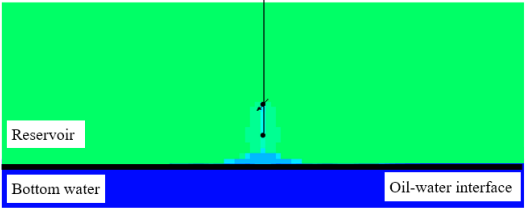
SAGD with oil water volume ratio of 3   SAGD with oil water volume ratio of 5

SAGD with oil water volume ratio of 10   MFAGD with oil water volume ratio of 5
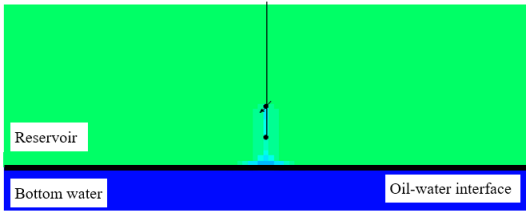
Figure 2. *Water coning in different numerical simulations*

The cumulative oil recovery varied from 44% (water-oil volume ratio is 10) to 68% (no bottom water) of OOIP. The thickness of the bottom water and the well configurations had a significant effect on the cumulative oil recovery. The optimal way to develop heavy oil reservoirs with bottom water is SAGD-MFAGD, which means SAGD first, and then switch to MFAGD when the steam chamber reach to the top of the reservoir. This investigation could be a reference for the successful design of gravity drainage process in offshore heavy oil reservoirs with bottom water.

Figure. 3 *- The oil rate and oil recovery of SAGD and SAGD-MFAGD*

4. CONCLUSIONS

Based on the basic geological parameters of LD5-2N block in Bohai offshore oilfield, a series of numerical simulation studies have been carried out, and the following conclusions can be obtained:

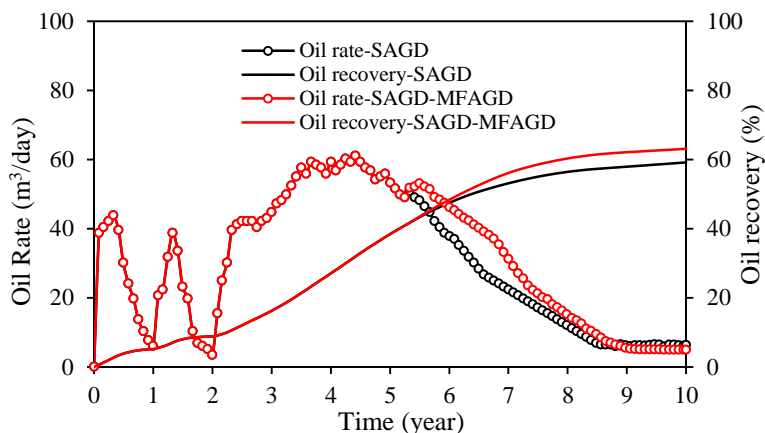1. The existence of bottom water could reduce the ultimate recovery of SAGD by about 11% - 24% of the OOIP. The thickness of the bottom water and the well configurations had a significant effect on the cumulative oil recovery.

2. The volume of water coning decreases obviously with the increase of distance between production well and the oil-water interface.

3. The optimal way to develop heavy oil reservoirs with bottom water is SAGD-MFAGD, which not only can redce water coning, but also can increase oil recovery by 3.94% compared to SAGD.

REFERENCES

[1] Wehunt CD, Burke NE, Noonan SG, Bard TR. Technical Challenges for Offshore Heavy Oil Field Developments. Paper OTC 15281 presented at the Offshore Technology Conference, Houston, Texas, USA, 5-8 May 2003. *DOI: dx.doi.org/10.4043/15281-MS*

[2] Giuggioli A, De Ghtto G. Innovative Technologies Improve The Profitability Of Offshore Heavy Oil Marginal Fields. Paper SPE 30014 presented at the International Meeting on Petroleum Engineering, Beijing, RP China, 14 – 17 November, 1995. *DOI: dx.doi.org/10.2118/30014-MS*

[3] Liu XH, Zhang FY, Huang K, Cui DY, Huang YH, Miu FF. Discussion about the thermal recovery of NB35-2 offshore heavy oilfield. Reservoir evaluation and development. 2011, 1(1-2): 61-63. *DOI：10.13809/j.cnki.cn32-1825/te.2011.z1.011*

[4] Zhong LG, Dong ZX., Hou JR, Li YQ, Sun YT, Zao L, Lu W, Qin F. Investigation on Principles of Enhanced Offshore Heavy Oil Recovery by Coinjection of Steam with Flue Gas. Paper SPE 165231 presented at the SPE Enhanced Oil Recovery Conference, Kuala Lumpur, Malaysia, 2-4 July 2013. *DOI: dx.doi.org/10.2118/165231-MS*

[5] Liu D, Zhao CM, Su YC. New Research and Application of High Efficient Development Technology for Offshore Heavy Oil in China, Paper OTC 23015-MS presented at the Offshore Technology Conference, Houston, Texas, USA, 30 April-3 May 2012. *DOI: dx.doi.org/10.4043/23015-MS*

Effect of Oblique Light Incidence and cavity length on band-gap properties of One Dimensional Photonic Crystals

Bouras MOUNIR *, Charik HAOUARİ, Fouad BERRABAH

Département d'Electronique, Faculté de Technologie, Université
Mohamed Boudiaf de M'sila, BP.166, Route Ichebilia, M'sila 28000, Algeria
*mouno_25000@yahoo.fr

ABSTRACT

We have investigated the optical properties of one-dimensional photonic crystals composed of multilayer thin films having the form (AB) 7, where A=Si and B=Air for the oblique light incidence and with defect layer. The selection of Si and Air is that because of their wide applications like beam splitting, high reflecting mirrors and antireflection coating. The properties of the structure are simulated using the Rigorous Coupled Wave Analysis (RCWA) method. The bandgap of the photonic crystal was also calculated. It is found that the bandgaps exist in the region (700–1900 nm). Similar crystal oblique light incidence and with central air defect by changing the position and with defect, respectively, in different orders was also studied. It is found that both position and width depend on the incidence angle and defect parameters.

KEYWORDS - *Photonic Crystals, Bandgap, (RCWA) method, defect layer, Transmission Spectra.*

1. INTRODUCTION

The photonic crystals are periodicities of dielectrics that can control the propagation of electromagnetic wave traveling through them [1-3]. The frequencies of the electromagnetic waves traveling through the photonic crystals are classified into allowed modes and photonic bandgaps. The allowed modes are with high transmission ratio where the photonic bandgaps are with zero transmission. One-dimensional photonic crystal could be defined as Bragg's mirror or multilayer thin film. In 1917, Lord Rayleigh showed the details of the optical characteristics of the multilayer thin film [4]. The one-dimensional photonic crystal is consisting of layers of different dielectric constants that are stacked on each other as shown in Figure 1. There are other structural types, namely two and three-dimensional photonic crystals. The two-dimensional photonic crystal has a periodicity along two of its axes and it is homogenous along the third axis. The three-dimensional photonic crystal has also photonic bandgaps and defect modes. The electromagnetic wave in this type of the photonic crystal is localized in all three dimensions [5, 6]. PhC have been used in a wide range of applications such as bend waveguides, filters, sensors, lasers, amplifiers, and resonators [7, 8]. In this work, will be a 1D photonic crystal (multilayer thin film), having the structure (AB) 7 , which means that there is a consequence of 7 unit cells, and each unit cell is formed of two layers (A=Si and B=Air). A central air defect width in this system will be by changing in different orders through the structure of the system. The simulations were carried out using RCWA method.

2. STRUCTURE DESIGN

A 1D photonic crystal consists of periodic Si layers intermediated with air gaps as shown in Figure 2. The thickness of the Si layers is assumed to be 100 nm and the width of the air gaps is 200 nm. The refractive index and the dielectric constant of the Si material are given by the double term exponential equation formula [9]:

275

n_Si=112e^(-0.01028 λ)+3.753e^(-0.00005769 λ)   (1)

The refractive index of Air n_Si=1. Due to the huge contrast between the refractive indices (or dielectric constant s) of the Si and air, the generated photonic band gap is wide as shown in the band structure Figure 2.
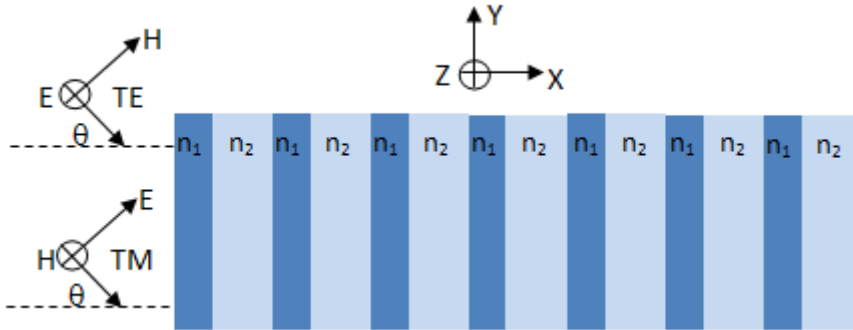
Figure 1. *The system of 1D photonic crystal with the incident electromagnetic wave with angle incidence "θ" in both TE and TM modes.*

The transmission spectral curves in Figure 2 show that there are two photonic bandgaps. The first photonic bandgap is in the visible region with range (482 nm - 641 nm) with bandgap width Δλ=159 nm. The second photonic bandgap is in the NIR region from 850 nm to 1750 nm with bandgap width Δλ=900 nm.
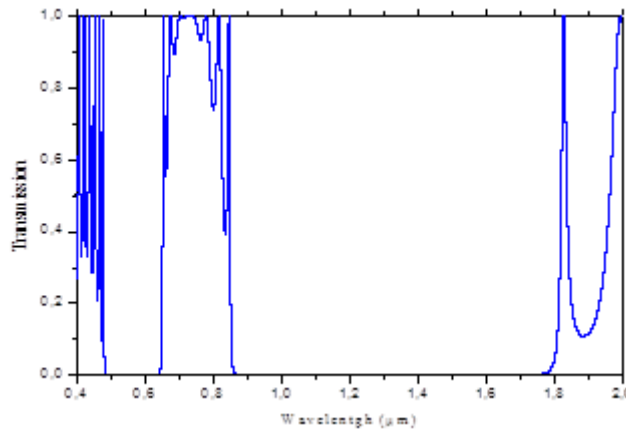
Figure 2. *Transmission spectrum curve of (Si/Air)7 1D photonic crystal.*

3. RESULTS AND DISCUSSIONS

This section presents the influence of the oblique light incidence and with central air defect by changing the position and with defect, respectively, on the photonic band gap properties in order to predict the largest photonic bandgap structures for telecommunications applications. The numerical tools used for our simulations are based on the Rigorous Coupled Wave Analysis (RCWA) (RSoft Design Group, DiffractMode, Inc. 200 Executive Blvd. Ossining, NY 10562).

3.1 Effect of the oblique light incidence

276

In this section, we investigate the optical properties of one-dimensional PC in the case of oblique light incidence and provide the theoretical analysis of the photonic bandgap behavior as a function of the angle of incidence.

Figure 3 (a). *Transmittance versus wavelength for different values of angle incidence of one-dimensional photonic crystal (1D PhCs)*
Figure 3 (b). *Variation of the photonic bandgap width as a function of angle incidence of one-dimensional photonic crystal (1D PhCs)*

Figure 3 (a) reports the variations of the photonic bandgap width as a function of wavelength for the same values of angle of light incidence. From results we can observe th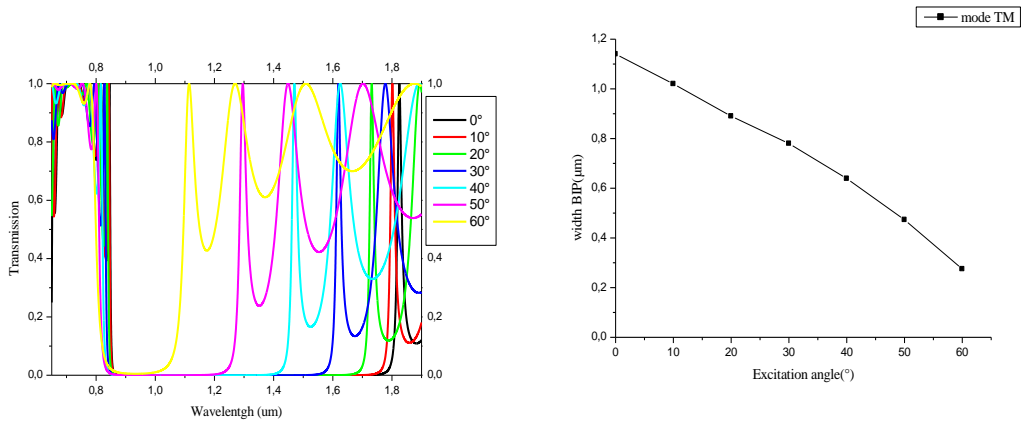at the size of photonic bandgap was varying like a laniary function with angle of light incidence θ. In the other hand, the bandwidth is maximum for D=1μm at θ=0°. Figure 3 (b) shows the results of transmission spectrum of TE mode for seven values of angle of light incidence. The results demonstrate clearly that more the angle of light incidence increases, the bandwidth decreases, and the medium wavelength λ0 increases from 0.92μm for θ=60° to 1.34μm for θ=0°.

3.2 Effect of the central air defect width
In this part, the effect of the central air defect width, as shown in Figure 4 (a), on the transmission and on the allowed modes appearing in the photonic bandgap region. As shown in Figure 4 (b), there are different allowed modes appear within the region of the photonic bandgap of Si/Ai photonic crystal when the central air defect width (D) is changed from 500 nm up to 900 nm with a step of 100 nm. Due to the high contrast between the refractive indices of Si and air central defect of 1D photonic crystal, defect modes appear, and the position of which depends on the width of air defecting layer (D). As the central defect width D changes, the transmission of the traveling electromagnetic wave through the defected region will be changed.

4.   CONCLUSION
An analysis of the 1D photonic band gap of Si and Air has been presented, using RCWA
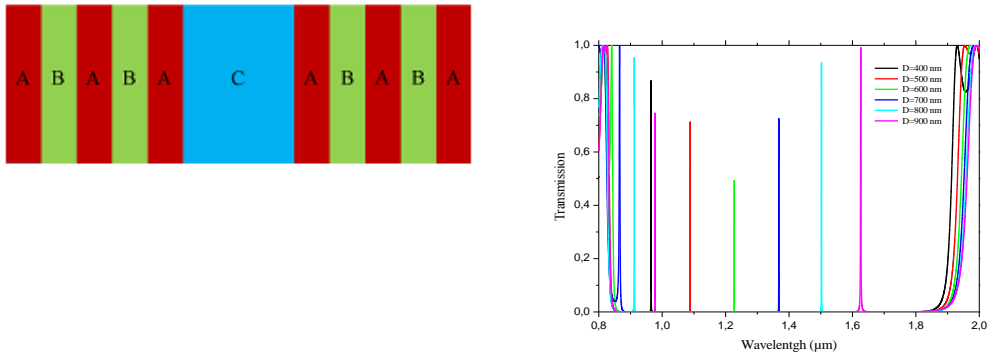
Figure 4 (a). *Central air defect inside the Si walls intermediated with air gaps as 1D photonic crystal defect*

Figure 4 (b). *Transmission curve of Si/Air photonic crystal with a central air defect of variable width of 500, 600, 700, 800, and 900 nm. Therefore, by using this simpler design, we can be easily fabricated as part of silicon-based photonic integrated circuits designed for operation in the near-IR wavelength range.*

simulation to provide theoretical prediction that certain structures geometries can lead to modify and tune the photonic band structures. Our results show that the for oblique light incidence and with defect layer have a great influence on the position and the width of PBG, and by changing the cavity length, the wavelength of the cavity mode can be shifts towards the higher wavelengths. An additional benefit of this approach is that it is compatible with standard microfabrication techniques, facilitating their incorporation into integrated optical systems.

References

[1] J. D. Joannopoulos, S.G. Johnson, J. N. Winn, R. D. Meade, Photonic Crystals Molding the Flow of Light, Princeton University Press, Princeton, New Jersey, 2007.

[2] B. E. A. Saleh , M. C. Teich, Fundamental of Photonics, 2nd edition, Wily Interscience, 1991.

[3] F. Shanhui, P. R. Villeneuve, and J. D. Joannopoulos, Journal of Applied Physics, 78 (1995) 1415-1418. http://dx.doi.org/10.1063/1.360298

[4] N. Çiçek Bezir, A. Evcin, R. Kayali, M.K. Özen, G. Balyaci, Comparison of Pure and Doped TiO2 Thin Films Prepared by Sol-Gel Spin-Coating Method, 132 (2016) 620. DOI:10.12693/APhysPolA.132.620

[5] B. Aktas, M. Albaskara, S. Yalcin, K. Dogru, Optical Properties of Soda-Lime-Silica Glasses Doped with Eggshell Powder, 132 (2016) 422. DOI: 10.12693/APhysPolA.132.442

[6] Lin SY, Chow E, Johnson SG, Joannopoulos JD. Opt. Lett. 25 (2000) 1297–1299. http://dx.doi.org/10.1364/OL.25.001297

[7] A. Hocini, J. Nanophoton. 10 (2016) 016007. http://dx.doi.org/10.1117/1.JNP.10.016007

[8] S. Salleh, H.F. Abdul Amir, A. Kumar Tiwari, F. Pien Chee, Collision Cascade and Spike Effects of X-ray Irradiation on Optoelectronic Devices, 130 (2015)93. DOI:10.12693/APhysPolA.130.93

[9] http://www.luxpop.com.

Research on Injection-Production Relationship Analysis Method Based on Data Mining

T. XIE[1], H. LIN[1], Z. H. LI[1], H. Y. TUO[1], L. G. ZHONG[2], T. C. HAO[2]

[1]*State Key Laboratory Offshore Oil Exploitation, CNOOC China Limited, Tianjin Branch, Tianjin, China;*
[2]*China University of Petroleum, Beijing, China*
*linhai10@cnooc.com.cn

ABSTRACT

Influenced by the surrounding injection and production wells, the formation near the infill adjustment wells is in abnormal pressure state. During drilling and completion operations, complex situations and accidents such as leakage and overflow are prone to occur. In order to accurately predict formation pressure recovery during shutdown and adjustment of peripheral injection wells, the distribution law and main influencing factors of formation pressure during shutdown and adjustment of injection wells are studied by combining physical simulation experiment with numerical simulation. A correlation estimation method of injection and production wells based on data mining is proposed, and the shutdown modulation degree of peripheral injection wells during drilling and completion of infill adjustment wells is formulated. The application of six infilling adjustment wells in PL19-3 oilfield in Bohai Sea shows that the correlation method of injection-production wells and the shutdown degree of water injection wells around infilling adjustment wells proposed in this paper can effectively ensure the safety of drilling and completion operation and the effect of reservoir protection, and have good application and popularization value.

KEYWORDS - *Infill Adjustment Well, Pressure Controlled Drilling, injection-production Relationship.*

1. INTRODUCTION

When the adjustment wells are drilling and completion, affected by the surrounding geological conditions and the production of injection-production wells, it is easy to cause the near-well zone to be in an over-pressure or under-pressure state, thus causing complicated situations and accidents[1-4]. The pressure can be controlled by adjusting the surrounding injection wells to reduce the operation risk. Therefore, the understanding of the adjustment law of the adjustment well pressure when the surrounding injection wells are closed is an important prerequisite for the formulation of the injection and production well adjustment scheme[5-7].

In this paper, the variation law of formation pressure and the main influencing factors of injection-production wells under geological conditions are studied. The correlation data of injection-production wells is used to predict the correlation of injection-production wells. On this basis, the influence of adjustment well pressure is preferred. The water injection well was shut down, and the encryption and adjustment of the surrounding water injection well modulation degree table during the drilling and completion of the well was established, and good results were obtained in the field application.

2. EXPERIMENTAL SIMULATION

In order to study the effect of shut-in injection wells on the pressure recovery rate of the adjustment wells at the core scale, a two-dimensional plane core model with homogeneous and heterogeneous artificial cementation with pressure collection and saturation monitoring (Table 1, Figure 1) is used to carry out the injection and production well shutting experiments. The

279

variation of well pressure under homogeneous and heterogeneous conditions are shown in Figure 2.

Table 1. *The basic parameters of the homogeneous two-dimensional model.*

size	80cm×80cm×4.5cm		
porosity	0.28	permeability	1000mD
Production well	8	Injection well	1
pressure tap	10	Electrode point	82
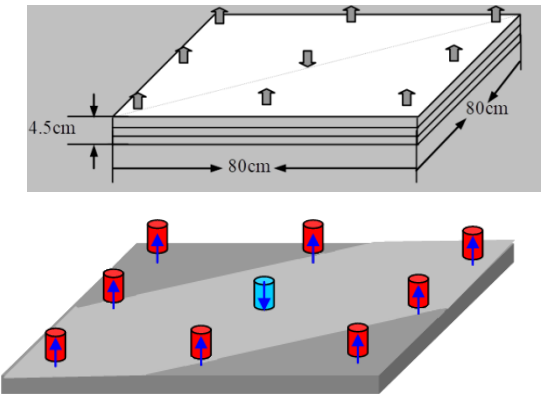
Figure 1. *Schematic diagram of physical experiment model.*

The results show that: (1) The lower the permeability of the model 、 the higher the viscosity of the crude oil and the higher the pressure of the waterflooding model can cause the more obvious the pressure drop after shutting down (Fig. 2); (2) The more the water injection flow rate decreases large can cause the greater the pressure regulation is reduced; (3) the well pattern is the main factor affecting the pressure, the pressure recovery rate is faster after the horizontal injection well is closed; (4) the pressure distribution of the homogeneous model is more uniform, after the adjustment The model pressure recovery is also uniform; (5) The heterogeneous model has little effect on the pressure transmission of the shut-in pressure inside and outside the channel; (6) In the early stage of water injection in the heterogeneous model, the greater the difference in permeability can cause the faster the shut-in pressure recovery.

Figure 2. *Schematic diagram of physical experiment model.*

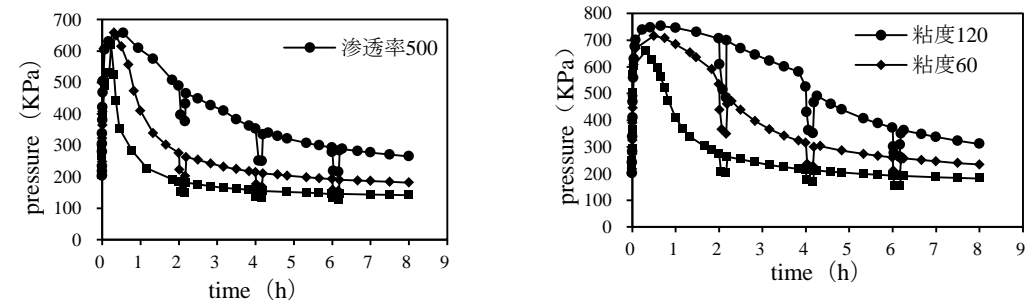According to the above experimental simulation results, the formation pressure of the encrypted adjustment well is affected by the joint injection well and the production well. Adjusting the surrounding injection wells during well drilling is an important measure to ensure the safety drilling and drilling and completion quality of the adjustment wells. However, considering the problem of oilfield production efficiency, it is preferred to adjust the injection wells that have a great influence on the adjustment well pressure. This paper proposes a method to directly predict the correlation of injection-production wells based on the production dynamic data of water injection wells and production wells, so as to facilitate the selection of water injection wells that need to be shut down.

3. INJECTION-PRODUCTION RELATIONSHIP ANALYSIS METHOD

The relationship between the injection well and the production well is determined by the water injection index of the injection well and the production index of the production well, and the influence of perforation data and formation pressure on the injection-production relationship is considered. Using the Kalman filter algorithm [8-9], the discretization of the water injection index is characterized by a digital signal filtering process, which is characterized by a discretionary water injection index step change and duration. For the production fluid index response sample, equation (1) is used to estimate the injection-production relationship between the injection well and the production well (or well group):

$$R_{ji}^{IP} = \frac{\Delta q_{ti}^c}{\Delta I_{ti}} = \frac{\int_{t_{ji}}^{t_{ji}+\Delta t_{ji}} \Delta q_j(t)}{\int_{t_i}^{t_i+\Delta t_i} \Delta I_j(t)} \approx \frac{\sum_{t_{ji}}^{t_{ji}+\Delta t_{ji}} \Delta q(t)}{\sum_{t_{ji}}^{t_{ji}+\Delta t_{ji}} \Delta I_j(t)} , i=1,2,\cdots,m \tag{4}$$

Where is the injection-production relationship between the injection well and the production well (or well group), and   is the injection volume change at a certain time in the injection well, when the sample data is the daily injection amount, it is the time of the day. And the change in the daily injection amount is the sum of the amount of change in the injection amount per day.

In the sample of the injection well water injection index step change and the production well production index response obtained by the digital signal filtering treatment, on the one hand, the production fluid index response caused by the increase or decrease of the production well itself is removed, and on the other hand, the influence of the time lag of the injection well response is removed.

4. FIELD APPLICATION

According to the law of pressure change after the water injection well is adjusted, combined with the correlation analysis results of the injection and production wells, the different water injection pressures and different well spacings for an oil field are formulated. The adjustment of the surrounding water injection and closing degree during the well drilling and completion operation is shown in the table 2. The encryption and adjustment drilling technology mentioned in this paper has been applied to the three-port encryption adjustment wells of the C, D and E platforms in an oilfield in Bohai. The shut-in scheme is shown in Table 3. Through the reasonable adjustment of the surrounding injection wells, the three wells did not have complicated conditions such as overflow and leakage during the drilling and completion operation, and the reservoir protection effect was good.

Table 2. *Injection shutting-in system table of infill adjustment wells.*
Measures distance

measures	distance (m)	wellhead pressure (MPa)	Time (d)
Shut-in	<200	<4	1~4
		>4	3~6
	200~375	<5	1~4
		>5	3~6
Reduce injection 1/2	375~500	4~8	2~6
		>8	4~8
	>500	4~8	5~10
No measures	>500	>8	/

Table 3. *The shut-in scheme of the water injection well around the adjustment well.*

Adjustment well	Injection well	distance (m)	wellhead pressure (MPa)	water rate (m^3/d)	measures
D03ST03	D02ST03	240	5	430	2d/Reduce injection
	D08	600	8	580	No measures
	D09ST01	887	6	350	No measures
E54ST01	E51	426	8.1	1260	5d/Reduce injection
	E55	300	7.8	860	5d/Reduce injection
C05ST01	C07ST1	291	7.2	1800	2d/Reduce injection

5. CONCLUSION

1) The experimental results show that the reservoir permeability heterogeneity and well pattern well type are the main factors affecting the pressure recovery of the adjustment well. When the water content in the formation near the adjustment well is high, the pressure recovery of the water injection well is faster. Therefore, the water injection well with good connectivity to the adjustment well is the main target.

2) A method for directly determining the connectivity relationship by using the surrounding water injection wells and production well production dynamic data is established. Combined with the change law of the adjustment well pressure after the injection wells are closed under the injection and production conditions, the modulation adjustment degree of the surrounding water injection adjustment well is established. It has great significance for the safety of drilling and completion operations and the improvement of oilfield production.

REFERENCES

[1]ZHANG Fengjiu, LUO Xianbo, LIU Yingxian, et al. Research on overall encryption adjustment technology of offshore oil field. Engineering Sciences, 2011, 13(5):34-40. DOI: 10.3969/j.issn.1009 -1742.2011.05.006

282

[2]JIANG Wei. Research and practices of re-infill drilling technology for offshore close-spaced cluster-well pads. Natural Gas Industry, 2011, 31(1):69-72. DOI:10.3787/j.issn.1000-0976.2011. 01.015

[3]WANG Gongjun, WANG Dongmei. Estimation of formation pressure by logging data. Foreign logging technology, 2011(4):71-72. DOI: CNKI:SUN:GWCJ.0.2011-04-039

[4]WANG Gongjun, WANG Dongmei. Calibration and standardization of logging curves. Inner Mongolia petrochemical industry, 2009, 35(10):98-99.DOI: CNKI:SUN:NMSH.0.2009-10-048

[5]SUN Chao, GAO Jing, WANG Xiaobo, YAO Zhongyi. Formation pressure analysis technology based on logging data. Drilling and production technology, 2008(S1):1-5+113.DOI: 10.3969/j.issn. 1006-768X.2008.z1.001

[6]ZHANG Yunzhen, ZHANG Yaoyin. Infill well, adjust well formation pressure and parameter identification and fitting. Journal of oil, 1994, 15(3):76-83. DOI: 10.1007/BF02943584

[7]YAO Yuedong, LI Xiangfang. Dynamic and static methods for prediction and adjustment of well formation pressure. Oil drilling technology, 2009, 37(4):32-34. DOI:CNKI:SUN:SYZT.0.2009-04-013

[8]YAO Yuedong, Ge Jiali, Wei Junzhi. Study on seepage law of low permeability reservoirs. Petroleum exploration and development, 2001(04):73-75+11-2. DOI: 10.3321/j.issn:1000-0747. 2001.04.022

[9]HAN Dexin. Distribution law of shallow gas layer in the south of daqing placanticline and prediction of formation pressure in adjustment well area. Northeast petroleum university, 2007. DOI:10.7666/d.y1224968

A Drilling Method of Adjustment Wells Pressure Management Based on Injection-Production Data Mining

L. ZHANG[1], H. LIN[1], P. DOU[1], P. H. DONG[1], L. G. ZHONG[2], T. C. HAO[2]

[1]*State Key Laboratory Offshore Oil Exploitation, CNOOC China Limited, Tianjin Branch, Tianjin,China;*
[2] *China University of Petroleum, Beijing, China*
*zhanglei134@cnooc.com.cn

ABSTRACT

Due to the influence of surrounding injection and production Wells, leakage and overflow are easy to occur during drilling and completion of infill adjustment Wells. In this paper, a new method of setting the shut-in scheme is proposed: using data mining method to judge high-correlation Wells for accurate shut-in instead of general shut-in. Firstly, the correlation between injection and production Wells is simulated by using the index of water injection and production. Then, Extended Kalman Filter (EKF) is used to build a model to predict the correlation of injection-production Wells, and the high correlation Wells is defined as shut-in objects after multi-well correction. Finally, the high correlation Wells is classified by the water cut, pressure, daily flow rate and well spacing data to determine shut-in time and pressure recovery criteria. This method was applied in drilling and completion of 10 adjustment Wells in Bohai oilfield. Compared with the geological data, the accuracy of correlation prediction of injection-production wells is more than 85%. Finally, by classifying the injection wells, the shut-in time was determined and the wellhead pressure of the injection Wells was controlled to be less than 4 MPa to ensure the safety of the drilling and completion of the adjustment Wells. No shut-in and adjustment measures are taken for low-correlation wells, so that when a single adjustment well is drilled and completed, more than 5000 m3 of low-correlation injection wells are injected around it, which improves the development efficiency.

KEYWORDS - Data Mining, Adjustment Wells, Accurate Shut-in.

1. INTRODUCTION

Affected by the surrounding injection and production wells, the encryption and adjustment of wells during drilling and completion operations are prone to complex situations such as leakage and overflow[1-4]. Generally, the general control method is adopted to close all injection and production wells within 500m from the adjustment well to ensure safe operation. This paper proposes a method for formulating the adjustment scheme of the surrounding wells based on the data mining of injection and production. Apply data mining methods to find high-correlation wells for precise closure instead of general closure. The method focuses on the injection-production wells with large correlations with the adjustment wells, and carries out precise adjustments. Under the premise of ensuring the safety of drilling operations, the impact of adjusting well completions on oilfield development is minimized, and the production efficiency of oilfields is improved.

2. RESEARCH METHODS

2.1 Injector-Producer Relationships

For the first time, Feilong Liu et al[5-7]. combined the extended Kalman filter with the injector-producer relationships(IPR), and used the water injection rates and production rates. Based on this to predict the injector-producer relationships, this paper considers using water injection index and production index combined with extended Kalman filter to calculate the injector-producer relationships.

284

Data such as perforation data of surrounding injection wells, production dynamic data, and dynamic stress tests were collected for research. Firstly, the water injection index and the liquid production index are calculated as the research objects of the injection-production well correlation.

$$I = \frac{(Q_1 / d_1)}{P_h + P_g - P_z - P_o} \tag{5}$$

Where I is the water injection index, and   is water injection rates, and   is effective perforation thickness, and   is Wellhead pressure, and   is Liquid column gravity in the wellbore, and   is Tubing resistance, and   is Mean formation pressure.

$$P = \frac{(Q_2 / d_2)}{P_o - P_w} \tag{2}$$

Where is the production index, and   is Bottom hole pressure.

Using the response of the production well index of the production well when the water injection index of the injection well is changed within a certain period of time (usually 1 year) to estimate the relationship between injection and production, the IPR value of the injection-production relationship can be expressed as:

$$IPR = \frac{\Delta P}{\Delta I} \tag{3}$$

Applying the extended Kalman to calculate the value of IPR,

$$IPR = \frac{\Delta P}{T\Delta I} = \frac{f(r,k)\int_0^\infty h(t)dt}{T} \approx f(r,k)\sum_{n=0}^\infty h(n) = \frac{\gamma z^{-1} f(r,k)}{(1-\alpha z^{-1})^2} \approx f(r,k)H(z)\big|_{z=1} = \frac{\gamma f(r,k)}{(1-\alpha)^2} = \frac{\gamma'}{(1-\alpha)^2} \tag{4}$$

2.2 Design shut-in scheme

After the multi-well joint correction, the high-correlation wells are identified as the key targets. High-correlation wells were classified by data such as water cut, pressure, daily flow rate and well spacing data to determine shut-in time and pressure recovery criteria.

3.   FIELD APPLICATION

Taking a production blocks of oilfield as an example, the water injection index and the liquid production index of well near the adjustment well are calculated, and IPR are calculated and shown in Table 1. The IPR calculation results are represented on the well map as shown in Fig.1. The production conditions of the injection wells near the adjustment well are shown in Table 2. The wellhead pressure curve of the injection well near the adjustment well during the shut-in period is shown in Figure 2. Based on the calculation results of IPR and the actual shut-in pressure drop law of the injection well, the shut-in scheme of the water injection well around the adjustment

Table 1. *The IPR calculation results.*

| Producing well	IPR mean	Normalization	Date	Result
A11ST1	9.5756	0.4710	2017.9.1-2018.9.1	strong
A14ST4	7.5482	0.3713	2017.9.1-2018.9.1	strong
A17ST3	1.3879	0.0682	2017.9.1-2018.9.1	strong
A23ST4	0.6853	0.0337	2018.6.18-2018.9.1	moderate
A08ST3	0.4748	0.0233	2017.9.1-2018.8.28	weak
A15ST3	0.3362	0.0165	2017.9.1-2018.9.1	weak
A22ST6	0.170009	0.0083	2017.9.1-2018.9.1	weak
A18ST4	0.148697	0.0073	2017.9.1-2018.9.1	weak
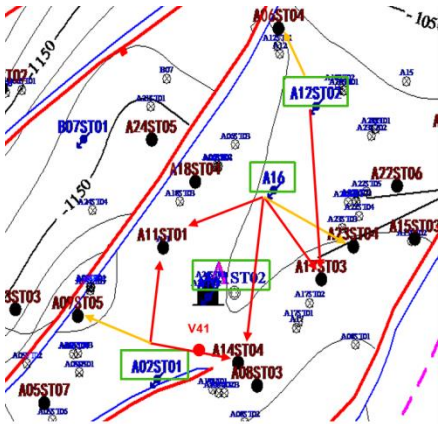
Figure 1. *IPR calculation results on the well map.*

well was established, as shown in Table 3. A02ST1 well has high IPR, close to the distance to be drilled, and the pressure drop at the wellhead is slow. It is recommended to reduce the injection 5 days before drilling to ensure that the wellhead pressure is lower than 4MPa; A16 well has high IPR. However, the distance is slightly farther. It is recommended to drill down to reduce the injection 3 days before drilling. The A12ST2 well has low correlation and long distance, so it is recommended not to adjust. According to the shutdown plan for on-site application, the drilling process is safe and smooth, and the drilling system meets the operation requirements. Compared with the traditional shut-in system, it can inject more water by about 7000m3.

286

Table 2. *The production conditions of the injection wells.*

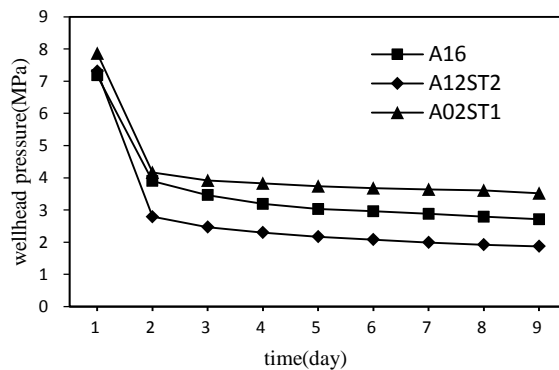| Injection well	Years	wellhead pressure (MPa)	water rate (m³/d)	Average water content	distance (m)	Wellhead pressure drop rate	IPR
A02ST1	15	7.87	1850	96%	164m	slow	strong
A12ST2	6	7.31	1220	83%	765m	fast	weak
A16	15	7.18	1460	90%	498m	medium	strong

Figure 2. *The wellhead pressure recovery of the injection well.*

Table 3. *The shut-in scheme of the water injection well around the adjustment well.*

Injection well	distance (m)	wellhead pressure (MPa)	water rate (m³/d)	measures
A02ST1	164	7.9	1850	5d/Reduce injection
A12ST2	765	7.3	1220	No measures
A16	488	7	1460	3d/Reduce injection

At present, more than 20 wells have been applied in the Bohai field, complex fault block reservoir and strong bottom water reservoir. The IPR of injection and production wells is calculated by using the water injection index and liquid production index of more than 350 groups of injection and production wells. Comparing the calculation results with the geological data, the accuracy of the correlation prediction results of the injection wells reached more than 85% .

The original "shut-in 15 days before drilling into the target zone within the distance of 400-600m Wells" was optimized to "drop injection or shut-in 5 to 10 days before drilling into the target zone according to injection-production relationship", which not only ensured safe offshore drilling, but also significantly reduced the impact on oilfield development effect.

287

4 CONCLUSION

Based on the understanding of the influence law of the correlation of complex pressure wells under injection-production condition, this method forms a new method of estimating injection-production relationship based on injection-production data, and establishes a regulation system of injection-production wells around the adjustment well based on injection-production relationship estimation and shut-in pressure drop law. By closing the wells with high correlation of regulating injection-production, the influence of adjusting well drilling and completion on oilfield development can be minimized on the basis of ensuring operation safety.

REFERENCES

[1]ZHANG Fengjiu, LUO Xianbo, LIU Yingxian, et al. Research on overall encryption adjustment technology of offshore oil field. Engineering Sciences, 2011, 13(5):34-40. DOI: 10.3969/j.issn.1009 -1742.2011.05.006

[2]ZHU Binglan, CHENG Yuanfang, XIE Xiandong. Research and application of formation pressure prediction method for adjustment Wells. Complex oil and gas reservoirs, 2011, 04(2):68-71. DOI: CNKI:SUN:FZYQ.0.2011-02-021

[3]ZHAO Shaowei, FAN Baitao, ZHONG Liguo, et al. Research and application of pressure prediction and control technology for infill adjustment wells during injection-production operations. China Offshore Oil and Gas, 2017, 29(1):99-104. DOI:10.11935/j.issn.1673-1506. 2017.01.015.

[4]ZHAO Changsheng，TAO Benzao. Kalman Filtering of Linear System with Colored Noises. GEOMATICS AND INFORMATION SCIENCE OF WUHAN UNIVERS, 2008, 33(2):180-182. DOI:10.3969/j.issn.1671-8860.2007.10.009

[5]B. Vaferi, V. Salimi, D. Dehghan Baniani, A. Jahanmiri, S. Khedri. Prediction of transient pressure response in the petroleum reservoirs using orthogonal collocation. Journal of Petroleum Science and Engineering, 2012, 98-99.DOI:10.1016/j.petrol.2012.04.023

[6]Zhao H, Kang Z, Sun H, et al. An interwell connectivity inversion model for waterflooded multilayer reservoirs. Petroleum Exploration and Development, 2016, 43(1):106-114. DOI:10.1016/ S1876-3804(16)30012-X

[7]Xie X, Zhao H, Kang X, et al. Prediction method of produced polymer concentration based on interwell connectivity. Petroleum Exploration and Development, 2017, 44(2):286-293. DOI: 10.1016/s1876-3804(17)30032-0